Design of Ti-Mo-Nb-Zr alloys with low elastic modulus using cluster-plus-glue atom model

by

Mampai Lereto Raganya

A Doctoral Research theses submitted in fulfilment of the requirements for the degree of

DOCTOR OF PHILOSOPHY

in

ENGINEERING METALLURGY

in the

Faculty of Engineering and the Built Environment

at the

UNIVERSITY OF JOHANNESBURG

SUPERVISOR: Prof Ronald Machaka
CO-SUPERVISOR: Dr Babatunde Obadele & Prof Mamookho Makhatha

August 2020

Dedication

I dedicate this thesis to the angel in heaven, my late mum, Isah Raganya.

Declaration

I, **Mampai Lerato Raganya**, hereby declare that this doctoral research thesis is wholly my own work and has not been submitted anywhere else for academic credit either by myself or another person. I understand what plagiarism implies and declare that this proposal is my own ideas, words, phrase, arguments, graphics, figures, results and organisation except where reference is explicitly made to another's work. I understand further that any unethical academic behaviour, which includes plagiarism, is seen in a serious light by the University of Johannesburg and is punishable by disciplinary action.

Signed… ……..... Date…17/09/2020……

Acknowledgement

Firstly, I would like to give my gratitude to God. I would never have put this document together without you by my side.

I would also like to sincerely thank my supervisors Prof. Ronald Machaka, Dr Babatunde Obadele and Prof. Mamookho Makhatha for their guidance and supervision throughout my Ph.D. study.

Many thanks to Prof Makhatha, you have generally taught me a lot about ethics. Your leadership skills are incomparable.

I would also like to acknowledge the National Research Foundation (South Africa), the University of Johannesburg (UJ), the Council for Scientific and Industrial Research (CSIR) and the Department of Science and Innovation (DSI) for financial support.

I would also like to express my gratitude to Nthabiseng Moshokoa, for assisting me with my experimental work and the knowledge you shared throughout my study.

Special thanks go to the Lusanda Fikeni and Ntswaki Nyakeni for always being helpful in the labs by assisting me with experimental work.

Big thanks also to Dr Clive Oliphant at the National Metrology Institute of South Africa for his assistance with the EBSD analysis.

I would also like to acknowledge the staff at Mintek, CSIR and University of Pretoria (UP) for their technical support.

Lastly, I would like to thank my family, friends and colleagues for bearing with me when I was pressurized by titanium and its alloys.

To my Godsend grandmother, Violet, thank you for raising me, for your everlasting support and encouragement. The journey is almost over.

List of Publications

1. M. L. Raganya, N. M. Moshokoa, B. Obadele, P. A. Olubambi, and R. Machaka, "The microstructural and mechanical characterization of the β-type Ti-11.1Mo-10.8Nb alloy for biomedical applications," *IOP Conf. Ser. Mater. Sci. Eng.*, vol. 655, no. 1, 2019, doi: 10.1088/1757-899X/655/1/012025
2. L. Raganya, N. Moshokoa, B. A. Obadele, P. A. Olubambi, and R. Machaka, "Investigation of the tensile properties of heat treated Ti-Mo alloys," Mater. Today Proc., Jul. 2020, doi: 10.1016/j.matpr.2020.05.782.
3. L. Raganya, N. Moshokoa, B. A. Obadele, P. A. Olubambi, and R. Machaka, "Study of the microstructure and crystal orientation of as-cast Ti-10.2Mo-19.5Nb alloy," Mater. Today Proc., Jul. 2020, doi: 10.1016/j.matpr.2020.05.785.
4. N. Moshokoa, L. Raganya, B. Obadele, P. Olubambi, and R. Machaka, "Effects of Mo content on the microstructural and mechanical properties of as-cast Ti-Mo alloys," *IOP Conf. Ser. Mater. Sci. Eng.*, vol. 655, no. 1, 2019, doi: 10.1088/1757-899X/655/1/012015
5. N. Moshokoa, L. Raganya, B. A. Obadele, R. Machaka, and M. E. Makhatha, "Microstructural and mechanical properties of Ti-Mo alloys designed by the cluster plus glue atom model for biomedical application," 2020.
6. N. Moshokoa, L. Raganya, B. Obadele, E. Makhatha, and R. Machaka, "Influence of solution treatment on the phase evolution and tensile properties of binary Ti-Mo alloys" SAIMM, August 2020
7. L. Raganya, N. Moshokoa, B. A. Obadele, E. Makhatha, and R. Machaka, "Study of the microstructure and mechanical properties of heat treated Ti–Mo alloys," Materials Characterization., Feb. 2021
8. L. Raganya, N. Moshokoa, B. A. Obadele, E. Makhatha, and R. Machaka, "Microstructure and mechanical properties of Ti-Mo-Nb alloys designed using the cluster plus-glue-atom model," Journal of Advanced Manufacturig Technology, Feb. 2021

Abstract

This study is aimed at designing a series of metastable β-type Ti-Mo-Nb-Zr alloy series with low elastic moduli as potential alternatives for conventional orthopaedic implant materials including 316L stainless steel, cobalt-chromium and Ti6Al4V. The most important concerns associated with these materials during long term implantation are cytotoxicity and stress-shielding effect resulting from the imbalance of the elastic moduli with those of the human bone, which can cause bone resorption and implant failure.

The alloys in this were designed using a synergic combination of approaches (cluster-plus-glue-atom model cluster formula $[(Mo)(Ti_{14-x}Zr_x)]Ti_yNb_z$ and β stability predicting theories including molybdenum equivalence, d-electron theory and average electron concentration ratio) instead of using trial-and-error method with no fundamental basis, which is time-consuming and costly during manufacturing.
For the identification of the phase constituents, X-ray diffraction analysis was carried out, whereas the microstructural characterization was performed using the scanning, electron microscopy, and optical microscopy and electron backscatter diffraction techniques. The mechanical properties including microhardness, tensile properties, bending properties and compressive properties were also investigated.

The microstructures of the as-cast alloys characterized by the OM, SEM XRD and EBSD generally exhibited primary BCC β phase and secondary precipitates of the orthorhombic martensitic α" and athermal ω phase. High microhardness was observed in alloys containing one Nb glue atom due to the large amount of the ω phase, which induced precipitation hardening effect on the β matrix. Generally, the addition of Nb_2 to Nb_3 glue atoms and/ or the Zr cluster shell atom resulted in higher tensile and yield strengths, while Nb_1 glue atom resulted in the lowest elastic modulus. All the as-cast alloys failed in a brittle manner. No significant difference in the bending strengths of the as-cast alloys was revealed. However, Nb_2 glue atoms resulted in the lowest bending modulus, while Nb_1 glue atom and/ or Zr_1 cluster shell atom exhibited ductile properties. The highest compressive and yield strengths were obtained at Nb_1 and/ Zr_1 atoms, while Nb_2 atoms resulted in the lowest compressive modulus.

Generally, solution treated alloys precipitated larger volume fractions of the secondary phases than the AC alloys. The tensile strength and elongation at rupture were generally enhanced, whereas the yield strength was decreased. A general increase in the elastic modulus was also observed, meanwhile the elastic admissible strain was considerably high. The ductility of the alloys was improved, while the bending modulus was generally reduced after solution treatment. Experimental findings the *Moeq* and e/a ratio approaches overestimated the β-stabilizing effect of alloying elements Mo, Nb and Zr in the designed multicomponent alloy. In the case of the d-electron theory approach, an overestimation of the β-stabilizing effect of the Mo and Nb was observed in the TMN alloys, respectively. Meanwhile, the β-stabilizing effect of Mo, Nb and Zr in TMNZ alloy was underestimated.

The accuracy of the theoretical prediction tools with reference to the experimentally obtained results in the alloys was evaluated. The *Moeq* and *e/a* ratio approaches overestimated the β-stabilizing effect of Mo and Nb in all the Ti-Mo-Nb alloys, and Mo, Nb and Zr in the Ti-Mo-Nb-Zr alloy. In the case of the d-electron theory approach, an overestimation of the β-stabilizing effect of Mo, and Mo and Nb was observed in all the Ti-Mo-Nb alloys, respectively. Meanwhile, the β-stabilizing effect of Mo, Nb and Zr in Ti-Mo-Nb-Zr alloy was underestimated.

The microstructural and mechanical characteristics have indicated the feasibility of the combinatorial use of the cluster-plus-glue-atom model and β-stability predicting approaches to design metastable β-type Ti-Mo-Nb(-Zr) alloys with low elastic modulus for orthopaedic applications. The superior mechanical properties of the designed alloys, obtained in the absence of thermo-mechanical processing, indicate that these alloys can be suitable candidates for orthopaedic applications.

List of acronyms and abbreviations

SYMBOL	DESCRIPTION
α	the alpha
α'	hexagonal martensitic alpha
α"	Orthorhombic martensitic alpha
Al	Aluminium
β	Beta
BCC	Body-centred cubic
Bo	Bond order
Co-Cr-Mo	Cobalt-Chromium-Molybdenum
CP Ti:	Commercially pure Titanium
Fe	Iron
Cu:	Copper
e/a:	Valence electron concentration
EBSD	Electron Backscatter Diffraction
GPa	gigaPascal
kV	Kilovolt
mA	milliampere
Md	d-orbital energy level
Mn	Manganese
Mo	Molybdenum
Mo Equivalence	*Moeq*
Nb	Niobium
OM	Optical Microscopy
SEM	Scanning Electron Microscopy
Si	Silicon
Sn	Tin
Ta	Tantalum

SYMBOL	DESCRIPTION
TEM	Transmission electron microscope
Ti	Titanium
XRD	X-ray diffractometry
316L SS	316 low carbon stainless steel
V	Vanadium
W	Tungsten
Zr	Zirconium

Table of Contents

Dedication i

Declaration ii

Acknowledgement iii

List of Publications iv

Abstract v

List of acronyms and abbreviations vii

List of Figures xii

List of Tables xvii

1.0 Introduction 1

1.1 Background of Research 1

1.2 Problem Statement 2

1.3 Research Questions 2

1.4 Research Motivation 3

1.5 Research Objectives 3

1.6 Significance of the study 4

1.7 Research Methodology 4

1.8 Delimitation 6

1.9 Ethical statement 6

1.10 Conclusion 6

1.11 Structure of the thesis 6

2 Chapter 2: Literature Review 8

2.1 Metallic biomaterials 8

2.2 Conventional orthopaedic biomaterials and their limitations 11

2.3 Ti and its alloys 12

2.3.1 Effects of alloying elements on Ti 12

2.3.2 Classification of Ti and its alloys 13

2.3.3 Limitations of Ti and its alloys in orthopaedic applications 13

2.3.4 Metastable beta (β) titanium alloys 14

2.3.4.1 Ti-X binary alloys 16

2.3.4.2 Multicomponent β Ti alloys 19

3 Methodology 37

3.1 Introduction 37

3.2 Alloy Design 37

3.2.1 Selection of alloying elements 37

3.3 Design Model 37

3.3.1 Ti-Mo binary alloys 37

3.3.2 Ti-Mo-Nb(-Zr) multicomponent alloy system 39

- Cluster-plus-glue-atom model 39

3.4 Starting Materials 43

3.5 Fabrication of Specimen 44

3.5.1 Casting 44

3.5.2 Solution Treatment followed by Quenching 45

3.6 Microstructural Characterization methods 47

3.6.1 Preparation of specimen 47

3.6.2 Optical Microscopy 47

3.6.3 X-ray diffraction 47

3.6.4 Scanning electron microscopy 48

3.6.5 Electron Back-Scatter Diffraction (EBSD) 48

3.7 Mechanical testing 49

3.7.1 Micro-Vickers Hardness Testing 49

3.7.2 Tensile Testing 50

3.7.3 Compression Testing 51

3.7.4 Bending Testing 52

4 Results and discussion 53

4.1 Structure and Properties of the Binary Alloys 53

4.1.1 Phase analysis of AC and ST Ti-Mo binary alloys 53

4.1.2 Optical Microscopy analysis 57

4.1.3 Scanning electron microscopy (SEM) characteristics 60
4.1.4 EBSD results 65
4.1.5 Comparison of Experimental Phase Observations with the theoretical Predictions 68
4.1.6 Summary of findings 70
4.2 Effect of microstructure on the mechanical properties of Ti-Mo alloys 70
4.2.1 Microhardness Results 70
4.2.2 Tensile properties 73
4.2.2.1 Fracture surfaces 75
4.2.2.2 **Elastic Modulus** 77
4.2.3 Elastic admissible strain 82
4.2.4 Bending Properties 84
4.2.5 Compressive properties of the alloy series 89
4.3 Effect of Nb and Zr on the microstructural evolution of $[Mo(Ti_{14-x}Zr_x)]Nb_yTi_z$ alloy series. 91
4.3.1 Phase analysis of AC and ST designed alloys. 91
4.3.2 Microstructural Characteristics 98
4.3.2.1 Optical Microscopy Observations 98
4.3.2.2 Scanning electron microscopy observations 102
4.3.2.3 EBSD results 105
4.3.3 Summary of findings 113
Comparison of microstructural observations with the theoretical predictions 114
4.4 Effect of microstructure on the mechanical properties 116
4.4.1 Micro-hardness Test Results 116
4.4.2 Tensile tests results 120
4.4.3 Bending test results 135
4.4.4 Compression test results 143
5 Conclusion and Recommendations 147

5.1 Conclusions 147
5.2 Contribution to knowledge 149
5.3 Recommendations 150

List of Figures

Figure 1-1. Flow diagram (methodology).....5
Figure 2-1: a) Hip and b) Knee joint replacements. (Source: *https://www.sharanhospital.com/index.html?v=139)*.....9
Figure 2-2: – Various causes for failure of implants that leads to revision surgery [20]. 11
Figure 2-3. Effects of alloying elements on Ti. (Source: http://www.dierk-raabe.com/titanium-alloys/).....13
Figure 2-4: Schematic phase diagram of titanium alloys with the decomposition products of the β-phase [32]. 15
Figure 2-5. a) Ti-rich corner of the Ti-Mo binary phase diagram. The [β/(α+β)] boundary line shows a fairly rapid drop, the slope of which (the dotted line) is taken as a measure of the b-stabilization capability of Mo. b) The Schematic plot for the slope calculation, i.e., slope = (T1 T0)/C1 [61]. 21
Figure 2-6. Microstructural evolution of Ti alloys after quenching with respect to the e/a ratio scale [60].....22
Figure 2-7: Schematic variation of elastic modulus with electron/atom (e/a) ratio in binary Ti alloys [53]. 23
Figure 2-8. Alloying parameters, (a) bond order, Bo and (b) d-orbital energy level, Md. In (a), ϕM and ϕX are the atomic orbitals of M and X, and Bo is proportional to the overlap population between them. 24
Figure 2-9: Cluster models used fo calculations a) BCC luster and b) HCP cluster. 25
Figure 2-10: Phase stability change with alloying elements [62].....26
Figure 2-11: Extended Bo-Md diagram of different Ti alloys [62].....27
Figure 2-12: 1st-neighbour rhombic-dodecahedral cluster consisting of two sub-shells covering the eight nearest neighbours (yellow balls) and the six nearest neighbours (green balls). The orange ball represents the cluster centre atom. The outer shell, consisting of twelve atoms (blue balls), are locations of the glue atoms [71].....28
Figure 2-13. TEM images of Ti-39.5Ta-28Zr-2.5Nb a) bright-field image, b) selected area electron diffraction pattern and c) dark field image derived from the ω spots circled in (b) [59]. 30
Figure 2-14. TEM images of Ti-45Ta-18.4Hf-10Zr: a) bright-field image, b) the corresponding selected area electron diffraction of a).....31

Figure 2-15. Bright-field TEM image of solution-treated (ST) Ti-33Nb-4Sn specimen (a) and the corresponding electron diffraction pattern (b). The bright-field image displays typical martensite structure. 33
Figure 2-16: Biological safety of metals (a): cytotoxicity of pure metals, and (b): relationship between polarization resistance and biocompatibility of pure metals, Co–Cr alloy and stainless steels [73]. 36
Figure 3-1: Bo-Md phase stability map [92] 39
Figure 3-2. CN14 rhombic dodecahedron as the cluster in BCC structure [70]. 40
Figure 3-3: Bo-Md phase stability map [94] 42
Figure 3-4: a) Scanning electron microscopy and b) particle size distribution analytical apparatus 43
Figure 3-5: SEM micrographs of as-received powders (a) CP Ti. (b) Mo, (c) Nb and (d) Zr. 44
Figure 3-6: Arc remelting furnace. 45
Figure 3-7: Schematic diagram displaying the solution treatment procedure. 46
Figure 3-8. a) Electropolishing apparatus and b) optical microscope. 47
Figure 3-9: XRD equipment. 48
Figure 3-10: EBSD equipment 49
Figure 3-11: Vickers microhardness tester 50
Figure 3-12. Schematic dimensions of the tensile specimen. 51
Figure 3-13: Instron™ 1342 model apparatus 51
Figure 4-1: XRD patterns of the AC Ti-Mo binary alloys. 54
Figure 4-2. XRD patterns of the ST Ti-Mo binary alloys. 55
Figure 4-3: Comparison of the XRD patterns of AC and ST a) Ti-8Mo, b) Ti-10Mo and c) Ti-15Mo binary alloys. 57
Figure 4-4: Optical micrographs of AC a) Ti-8Mo, b) Ti-10Mo and Ti-15Mo alloy specimens. 58
Figure 4-5: Optical micrographs of ST a) Ti-8Mo, b) Ti-10 and Ti-15Mo binary alloys. 60
Figure 4-6: SEM micrographs of AC a) - b) Ti-10Mo AC alloy and c) –d) Ti-15Mo alloy. .. 61
Figure 4-7 : EDX Spectra of AC a) Ti-10Mo and b) Ti-15Mo alloy specimens. 63
Figure 4-8: SEM micrographs of ST a) Ti-10Mo and b) Ti-15Mo alloys. 65
Figure 4-9. EBSD IPF maps and phase maps of AC Ti-8Mo, Ti-10Mo and Ti-15Mo binary alloys 66
Figure 4-10. EBSD IPF maps of ST Ti-10Mo and Ti-15Mo binary alloys. 67

Figure 4-11: Microhardness of the AC Ti-Mo binary alloys and the conventional orthopaedic implant materials considered for comparison [54,104]. 71
Figure 4-12: Microhardness of the ST Ti-Mo binary alloys and the conventional orthopaedic implant materials considered for comparison [54,104]. 72
Figure 4-13. Fracture surfaces of AC a) Ti-8Mo, b) Ti-10Mo and c) Ti-15Mo binary alloys. 75
Figure 4-14: Fracture surfaces of ST a)- b) Ti-8Mo, c)- d) Ti-10Mo, and e) and f) Ti-15Mo binary alloys. 76
Figure 4-15: Elastic moduli of AC Ti-Mo alloys and the conventional orthopaedic implant materials considered for comparison [6,26] 78
Figure 4-16. Elastic moduli of ST Ti-Mo alloys and the conventional orthopaedic implant materials considered for comparison [6,26] 79
Figure 4-17: Variation of the elastic moduli of the AC/ ST Ti-Mo binary alloys with their *Moeq*. 80
Figure 4-18. Variation of the elastic moduli of the AC/ ST Ti-Mo binary alloys with their e/a ratio. 81
Figure 4-19: Elastic admissible strain of the AC Ti-Mo alloys and the conventional orthopaedic implant materials [20] considered for comparison. 83
Figure 4-20: Elastic admissible strain of the ST Ti-Mo alloys and the conventional orthopaedic implant materials [20] considered for comparison. 83
Figure 4-21: Bending stress-deflection of AC Ti-8Mo, Ti-10Mo and Ti-15Mo alloy specimens. 84
Figure 4-22: Bending stress-deflection of ST Ti-8Mo, Ti-10Mo and Ti-15Mo alloy specimens. 85
Figure 4-23: Bending strengths of as-cast and solution treated Ti-8Mo, Ti-10Mo and Ti-15Mo alloys. 86
Figure 4-24: Bending modulus of the Ti-Mo binary alloy specimens. 87
Figure 4-25: Fracture surfaces of the AC a) Ti-8Mo, b) Ti-10Mo and c) Ti-15Mo binary alloys after bend test. 89
Figure 4-26: Compression stress-strain curves of ST Ti-Mo binary alloys. 90
Figure 4-27. XRD patterns of AC a) TMT, b) TMN1, c) TMN2, d) TMN3 and e) TMNZ alloy specimens. 92

Figure 4-28: XRD patterns of ST a) TMT, b) TMN1, c) TMN2, d) TMN3 and e) TMNZ alloy specimens. 95
Figure 4-29. Comparison of XRD patterns of AC and ST a) TMT, b) TMN1, c) TMN2, d) TMN3 and e) TMNZ alloys. 97
Figure 4-30: Optical micrographs of AC a) TMT, b) TMN1, c) TMN2, d) TMN3 and e) TMNZ alloys. 99
Figure 4-31: Optical micrographs of a) TMT, b) TMN1, c) TMN2, d) TMN3 and e) TMNZ ST alloys. 101
Figure 4-32: SEM images of AC a) TMT, b) TMN1, c) TMN2, d) TMN3 and e) TMNZ alloys. 103
Figure 4-33. SEM micrographs of ST a) TMT, b) TMN1, c) TMN2, d) TMN3 and e) TMNZ alloys. 104
Figure 4-34: EBSD IPF maps of a) TMT, b) TMN1, c) TMN2, d) TMN3 and e) TMNZ AC alloys. 106
Figure 4-35: EBSD phase maps of AC a) TMT, b) TMN1, c) TMN2, d) TMN3 and e) TMNZ alloys 108
Figure 4-36: EBSD IPF maps of a) TMT, b) TMN1, c) TMN2, d) TMN3 and e) TMNZ ST alloys 110
Figure 4-37: EBSD phase maps of ST a) TMT, b) TMN1, c) TMN2, d) TMN3 and e) TMNZ alloys 112
Figure 4-38: Microhardness of AC alloy specimens and the conventional orthopaedic implant materials considered for comparison [54,104]. 117
Figure 4-39: Microhardness of ST alloy specimens and the conventional orthopaedic implant materials considered for comparison [54,104]. 119
Figure 4-40: Comparison of the microhardness of the AC and ST alloy specimens. 120
Figure 4-41: Elastic modulus of the AC alloy specimens with the common orthopaedic materials considered for comparison 125
Figure 4-42: Elastic modulus of the ST alloy specimens with the common orthopaedic materials considered for comparison. 127
Figure 4-43: Comparison between the elastic moduli of the AC and ST alloy specimens. 128
Figure 4-44: Variations of the elastic modulus of the AC alloy specimens with the molybdenum equivalence. 129

Figure 4-45: Variations of the elastic modulus of the ST alloy specimens with the molybdenum equivalence. 130
Figure 4-46: Variations of the elastic modulus of the AC alloy specimens with e/a ratio. ... 131
Figure 4-47: Variations of the elastic modulus of the ST alloy specimens with e/a ratio. 132
Figure 4-48: Elastic admissible strains of the AC alloy specimens and conventional orthopaedic implant materials considered for comparison [20]. 133
Figure 4-49: Elastic admissible strain of the ST alloy specimens and the conventional orthopaedic implant materials [20]. 134
Figure 4-50: Bending stress-deflection curves of the AC alloy specimens. 136
Figure 4-51: Bending stress-deflection curves of the ST alloy specimens. 137
Figure 4-52: Bending strength of the AC alloy specimens. 138
Figure 4-53: Bending strength of the ST alloy specimens. 139
Figure 4-54: Bending modulus of the AC alloy specimens. 141
Figure 4-55: Bending modulus of ST alloy specimens. 142
Figure 4-56. Comparison of the bending moduli of the AC and ST alloy specimens. 143
Figure 4-57: Compressive stress-strain curves of the AC alloy specimens. 144
Figure 4-58: Compressive stress-strain curves of the ST alloy specimens. 146

List of Tables

Table 2-1: Mechanical properties of bone. (adapted from [19])....10
Table 2-2: Comparison of tensile strength, yield strength and elastic modulus of the conventional orthopaedic materials. Sources: Compiled from [6,26] 11
Table 2-3. Critical concentrations (wt. %) of β phase stabilizing elements in binary Ti alloys required to retain 100% of the BCC β-phase after quenching to room temperature [28,30]...16
Table 2-4: Bo and Md values for various elements in β Ti. 25
Table 2-5: Metastable β-type Ti alloys, design approaches, predicted phases, fabrication methods, experimental observations and elastic modulus. 35
Table 3-1. *Moeq*, e/a ratio and Bo and Md values of the Ti-Mo binary alloys 39
Table 3-2. Cluster formula, composition, *Moeq* and e/a ratio values of the designed alloys. .41
Table 3-3: Bo and Md values and the predicted phases of the designed alloys....42
Table 3-4: Particle sizes of the starting materials. 44
Table 3-5: Solution Treatment Temperature....46
Table 4-1: EDX Spectra of AC Ti-10Mo binary alloy. 62
Table 4-2. EDX Spectra of AC Ti-15Mo binary alloy. 64
Table 4-3. Summary of the experimental observations and the theoretical predictions. 68
Table 4-4: Tensile properties of the AC Ti-Mo binary alloys. 73
Table 4-5: Tensile properties of the ST Ti-Mo binary alloys. 74
Table 4-6: Compressive properties of the ST Ti-Mo binary alloys 91
Table 4-7: Summary of the experimental observations and the theoretical predictions. 114
Table 4-8.Microhardness of the designed alloys and the alloys considered for comparison. 116
Table 4-9: Tensile properties of the AC, ST and similar alloys considered for comparison. 121
Table 4-10. Comparison of the elastic admissible strains of the AC and ST alloys investigated in this study. 134
Table 4-11. Bending strengths of AC alloys. 138
Table 4-12. Bending strengths of ST alloys. 139
Table 4-13. Bending moduli of AC alloys. 140
Table 4-14. Bending moduli of ST alloys. 141
Table 4-15: Compressive properties of the ST Ti-Mo binary alloys 144

UNIVERSITY
OF
JOHANNESBURG

1.0 Introduction

1.1 Background of Research

Metallic materials for orthopaedic applications are preferable in orthopaedic applications as they can withstand high load applied on human bones. They are primarily employed in the human body as replacing materials that substitute or repair damaged bones. They are in high demands due to the rapid increase in the average age of the human population [1]. An ideal orthopaedic implant material is characterized by excellent biocompatibility, superior corrosion resistance, the exceptional combination of high strength and low modulus, high fatigue and wear resistance, high ductility [2]-[3]. Among the stated mechanical characteristics, elastic modulus plays a significant role because, at a higher value than that of the human bone, it can cause stress-shielding effect, which can result in resorption of the bone and failure of the implant [4].

Over the past decades, there has been a remarkable impact of metallic biomaterials such as 316L stainless steel (SS), cobalt-chromium (Co-Cr) based alloys and titanium (Ti) and its alloys for orthopaedic applications. However, the release of nickel (Ni), cobalt and chromium from 316L SS and Co-Cr materials is associated with long term health problems, whereas the elastic moduli of the materials are higher than that of the human bone (10-40 GPa), which can result in stress-shielding effect [5][6]. In Ti alloys, Ti6AL4V alloy (110 GPa) is the most widely used in orthopaedic applications. Although its elastic modulus is higher than those of 316L SS and CoCr material, it is higher than that of the human bone and the dissociation of vanadium and aluminium form the parent material can cause long term health problems including Alzheimer disease, neuropathy and osteomalacia [4,5,7].

As alternatives of the Ti6AL4V material, Ti6Al7Nb and Ti5Al2.5Fe were developed. Although they offered mechanical properties similar to those of Ti6Al4V alloy, concerns about the ability of aluminium to induce neurological disorders, as well as Alzheimer's disease, were also reported. Moreover, they also have higher elastic moduli (105 GPa and 110 GPa for Ti6Al7Nb and Ti5Al2.5Fe, respectively) than that of the human bone (10-30 GPa). These drawbacks suffered by these alloys have motivated for the development of non-cytotoxic orthopaedic Ti implant materials with the elastic modulus comparable to that of the human [4,5]. As a result,

metastable β-type Ti alloys with low elastic modulus are considered promising candidates as orthopaedic implant materials.

1.2 Problem Statement

Extensive efforts have been undertaken to develop non-toxic metastable β-type Ti alloys with the elastic modulus that is comparable to that of the human bone. Up to date, the lowest elastic modulus that has been reported is about 36 GPa in metastable β-type Ti-33Nb-4Sn alloy series [4] and Ti-Mo-Nb-Zr alloy series [8], but the alloys have not been commercialized yet. Development of metastable β-type Ti alloys presents the following short-comings:

- Proper selection of β-stabilizing elements to prevent segregation during fabrication.
- An effective approach for designing the metastable β-type Ti alloys with high β stability and low elastic modulus to avoid the time-consuming and uneconomical trial-and-error experiments.
- Accurate theoretical prediction of the undesirable martensitic (α' and/ α") and omega (ω) precipitates in the β matrix.
- Control of the concentration of β-stabilizing elements to suppress the precipitation of the martensitic phases and the ω phase while increasing the stability of the β phase.
- Control of microstructural evolution during fabrication e.g. casting and/ or heat treatment, e.g. solution treatment.

Thus, the development of metastable β-type Ti alloy with modulus comparable to that of human bone has become an ever more pressing subject in the area of advanced orthopaedic materials [4,5].

1.3 Research Questions

The following are questions posed:

- How does the microstructure of Ti-Mo binary alloys correlate with their mechanical properties and deformation mechanisms?
- Can the cluster-plus-glue-atom model be successfully employed to design the metastable β-type T-Mo-Nb(-Zr) alloys for orthopaedic applications.
- How accurate are the β stability predicting approaches when compared with the experimental observations?
- Which non-toxic elements are suitable for increasing the β phase stability of Ti-alloys?
- What are the design strategies available for alloy design?

- How do Nb and Zr alloying elements affect the microstructure and mechanical properties of as-cast Ti-Mo-based alloys?
- What are the effects of Nb and Zr additions to Ti-Mo on the mechanical properties of the overall alloy series?
- How accurate are the β stability predicting approaches when compared with the experimental observations?

1.4 Research Motivation

This study is aimed at developing a metastable β-type Ti alloy containing non-toxic β-stabilizing elements, which can resolve the adverse effects of Ti6Al4V alloy on the bone (stress-shielding effect and the release of toxic Al and V metallic ions). The β-stabilizing elements selected in this study are molybdenum (Mo), niobium (Nb) and zirconium (Zr) [9]. Mo is the most effective β-Ti stabilizer, but it has a high elastic modulus, whereas Nb is a fairly good β stabilizer with low elastic modulus. Zr is a weak β stabilizer and possesses low elastic modulus. However, Zr acts as strong β stabilizer in multicomponent alloy systems. Furthermore, Mo, Nb and Zr elements exhibit good biocompatibility. Thus, the combination of these different elements is simultaneously expected to reduce the elastic modulus through the enhancement of the β stability of metastable β-type Ti alloys [10].

1.5 Research Objectives

The aim of this research is to design a series of Ti-Mo-Nb(-Zr) alloys with low elastic modulus for orthopaedic applications using a combination of cluster-plus-glue-atom model and β stability predicting approaches including molybdenum equivalence, average electron concentration ratio and d-electron theory. The feasibility of using the combined approaches will be assessed by studying the microstructural and mechanical characteristics of fabricated alloys.

To achieve the aim, the objectives of this study are as follows:

- Investigate the correlation between alloy composition, microstructure, and mechanical properties of binary Ti-Mo alloys also to generate useful data for developing new Ti-Mo based alloys.

- Formulate multicomponent alloy compositions using cluster-plus glue-atom model and determination of their β phase stability using the Mo equivalence, d-electron method and the e/a ratio approaches.
- Assess the influence of Nb and/or Zr β stabilizers on the microstructural evolution of and mechanical properties of as-cast designed Ti-Mo-Nb-Zr alloys.
- Investigate the effect of solution treatment with subsequent quenching on phase transformation and mechanical properties of the as-cast designed alloys.
- Evaluate the accuracy of the theoretical prediction tools with reference to the experimentally obtained results in the alloys designed using the cluster-plus-glue atom model.

1.6 Significance of the study

This study will provide useful guidelines on the design of a new generation metastable β-type Ti alloys as alternatives of the conventional Ti6Al4V orthopaedic material for application under load-bearing conditions. These metastable β-type Ti alloys, containing non-toxic β-stabilizing elements, would offer superior biocompatibility and mechanical properties suitable for long-term implantation. The design of the alloys will be conducted through a synergic combination of approaches (cluster-plus-glue-atom model and β stability predicting theories) instead of using trial-and-error method with no fundamental basis, which is time-consuming and costly during manufacturing. The cluster-plus-glue atom model will be useful in the formulation of alloy compositions, while the β predicting tools will provide with the theoretical prediction of phases during quenching. The combinatorial use of the approaches will resolve the complexity of predicting phase constituents by minimizing the number of trials for alloy development, which will also simplify the optimization process. The findings of this study will contribute to the knowledge of researchers about alloy design, phase and microstructural evolution as well as mechanical behaviour of metastable β-type alloys for orthopaedic applications.

1.7 Research Methodology

β-type Ti alloys suitable for orthopaedic applications are generally developed using non-toxic β-stabilizing elements including Mo, Nb, Zr, etc. [9,11]. These alloys have high β phase stability which results in the low elastic modulus [4]. A summary of the methodology is exhibited in Figure 1-1. In this study, the selection of alloying elements was based on the

cytotoxicity level (biocompatibility) and their ability to stabilize the β phase of Ti. The alloy compositions of the binary Ti-Mo alloys were formulated using the conventional trial-and-error method, whereby the Mo content was 8, 10 and 15 wt%. On the contrary, the compositions of the multicomponent alloys (one binary Ti-Mo alloy as a control material, three ternaries and one quaternary) were designed using the cluster-plus-glue-atom model followed by the prediction of the β phase stability by the molybdenum equivalence, d-electron method and the average electron concentration (e/a) ratio approaches. Fabrication of the alloys was performed in a vacuum arc remelting furnace using elemental powders of Ti, Mo, Nb and Zr. The developed alloy ingots were then solution treated above the β-transus for 1 hr in a muffle furnace followed by quenching in ice water. Both the as-cast and solution treated specimen were then cut and prepared using the metallographic standard procedure for phase identification using the X-ray-diffraction and microstructural analysis using the optical microscopy, scanning electron microscopy and electron backscatter diffraction technique. Mechanical testing of the alloy specimens included microhardness measurements, tensile testing, compression testing and bending testing at room temperature. This PH.D.study was conducted within these limits as also depicted in Figure 1-1 below.

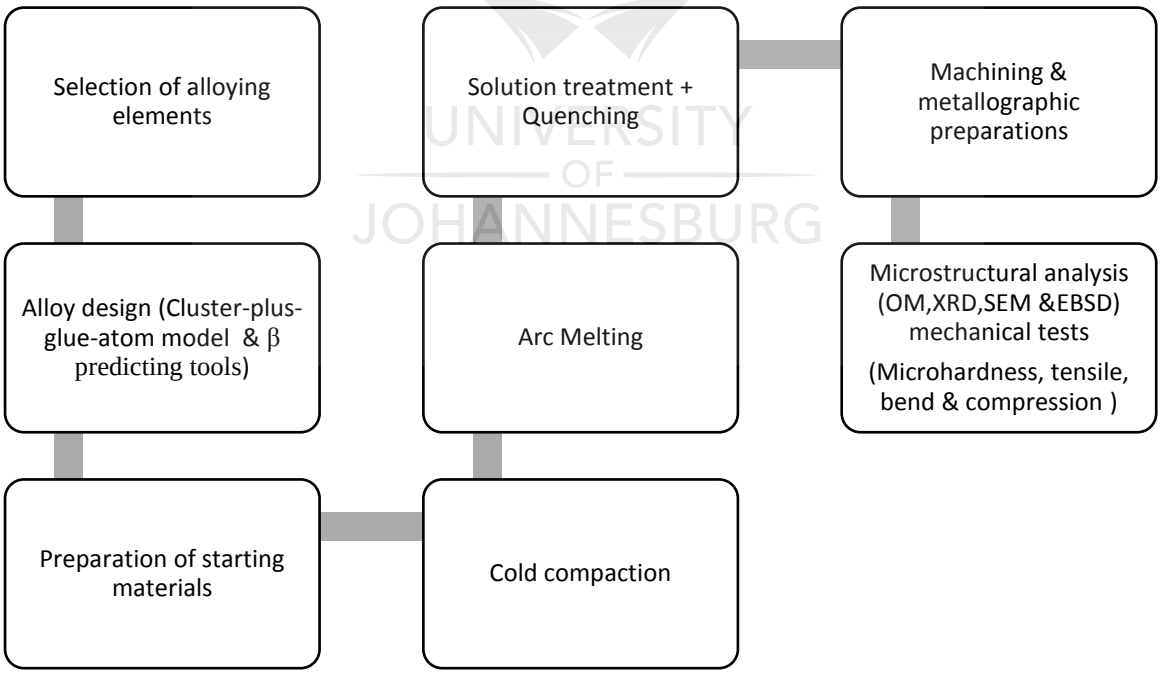

Figure 1-1. Flow diagram (methodology).

1.8 Delimitation

β-type Ti-based alloys particularly those containing Mo, Nb and/ or Zr were investigated because these β-stabilizing elements have low cytotoxicity levels and can enhance the stability of the β phase, which can induce low elastic modulus. The processing technique selected in this study is the conventional casting, considering the difficulty in accessing the advanced processing techniques, e.g. powder metallurgy techniques, and the lack of knowledge or reports on the microstructural and mechanical characterization of as-cast β-type Ti alloys. The content of alloying elements was varied according to their positions in the cluster formula. No clinical trials were conducted after the development of these alloys due to essential optimisation stage. The alloys were only developed and characterized to understand the microstructural evolution and mechanical behaviour of these alloys in the as-cast condition.

1.9 Ethical statement

There were no ethical issues associated with this research study.

1.10 Conclusion

The use of Ti6Al4V alloy as a permanent implant material for orthopaedic applications is limited due to the higher elastic modulus than that of the bone which induces stress-shielding effects as well as the release of Al and V metallic ions from the Ti6Al4V material into the human body causing long-term health issues. Metastable β-type Ti alloys have been developed using the trial-and-error method and the β prediction tools, and the lowest elastic modulus obtained is about 3 GPa in Ti-33Nb-4Sn alloy series [4]. Although the elastic modulus of this alloy is comparable to that of the human bone (10-40 GPa), it has not been commercialized yet. Therefore, the design and development of low elastic β-type Ti-based alloys consisting of non-toxic β-stabilizing elements is still a pressing issue in orthopaedic applications. To avoid using the conventional trial-and-error method, which is time-consuming and uneconomical, the design of alloys in this study was undertaken using the cluster-plus-glue-atom model with the aid of the β phase stability prediction tools. The non-toxic β-stabilizing elements selected were Mo, Nb and Zr.

1.11 Structure of the thesis

This thesis is structured as follows:

In this Chapter, the study was introduced. In addition, the problem statement, research questions, objectives, motivation and significance of the study were highlighted. In Chapter 2 a background on orthopaedic materials and the drawbacks, they present during the application, are detailed. Recent literature on the metastable β-type Ti alloys currently developed, design approaches and their limitations are reviewed. Chapter 3 focuses on the development of the metastable β-type Ti alloys, details on alloy design as well as the fabrication of the alloy specimens; preparation of the alloy specimens for microstructural characterization as well as mechanical testing are presented. Chapter 4 is divided into two sections, with the first section focusing on the design and development as well as the structure and properties of Ti-Mo binary alloys designed using the conventional trial-and-error method. The second section discusses the microstructural evolution, mechanical properties and deformation behaviour of the designed metastable β-type Ti-Mo based multi-component alloys. It specifically explains, in details, the limitations experienced when designing multi-component systems using the cluster-plus-glue-atom model with the aid of the β-phase stability prediction tools. Conclusions drawn based on the findings observed in this study and arising thereof are summarised in Chapter 5. Chapter 6 outlined the recommendations and proposals for future work.

2 Chapter 2: Literature Review

2.1 Metallic biomaterials

Metallic biomaterials have been primary implant materials in orthopaedic applications owing to their superior mechanical properties in comparison with ceramics, polymers and composites [2,3]. They are used extensively around the world to treat a spectrum of orthopaedic-related disorders. Their primary function is to substitute or repair different tissues such as bone, cartilage or ligaments and tendons, and even by guiding repair if it is essential. The most critical cases in orthopaedic applications are the dysfunctional knee and hip joints [12]. Hip and knee joints are complex and delicate structures primarily functioning to bear the load and provide structural integrity to the human body [13].

Biomaterials are used for the production of implants to compensate or replace diseased damaged living tissues or organs. Metallic biomaterials make a significant group of biomaterials mostly used for orthopaedic and dental applications due to a superior combination of high mechanical strength and fracture toughness.

Figure 2-1 exhibits the prosthesis for total knee joint replacement (TKR) and hip joint replacement. The prosthesis of the total knee joint replacement is composed of femoral, tibial, and/or patellar components. The knee joint exhibits a more complicated geometry and movement mechanics, and it is not intrinsically stable in comparison with the hip joint. Therefore, the design of an implant for joint replacement should be based on the kinematics and dynamic load transfer characteristics of the joint. The optimized combination of the articular cartilage, a load-bearing connective tissue covering the bones involved in the joints and synovial fluid, a nutrient fluid secreted within the joint ensures the performance.

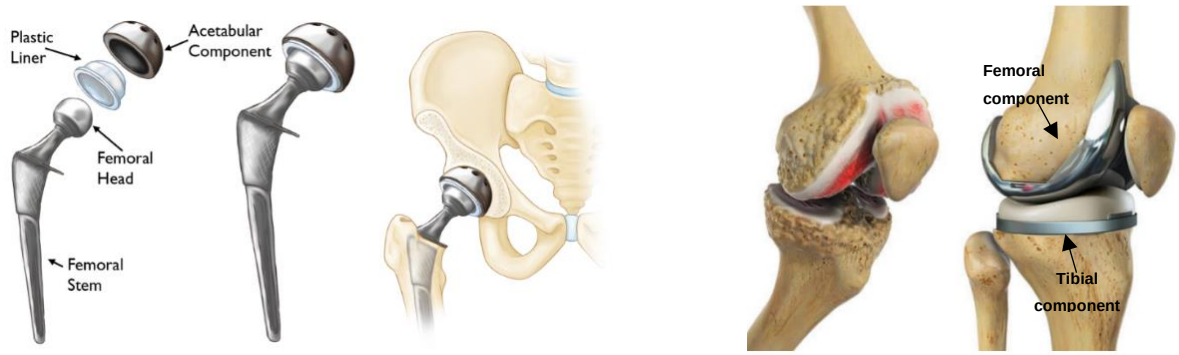

a) **b)**

Figure 2-1: a) Hip and b) Knee joint replacements. (Source: *https://www.sharanhospital.com/index.html?v=139*)

Hip and knee joints are susceptible to degenerative and inflammatory diseases that can cause pain and joint stiffness [14]. The most common degenerative diseases affecting them include primary or secondary osteoarthritis (osteoarthrosis) and to a lesser extent rheumatoid arthritis (inflammation of the synovial membrane) and chondromalacia (softening of the cartilage). These diseases have affected millions of people around the world and they account for half of all the chronic diseases e.g. mobility disturbance, cancer, circulatory diseases (cardiovascular diseases). They often cause the surgery to relieve pain and increase mobility, including total joint replacement in cases of deterioration of the natural joint [2,14].

In the last few years, knee and hip joint surgery has advanced tremendously due to the development of new and improved techniques for bone repair. This has led to the predictions that by the end of 2030, the number of total hip replacement surgery will rise by 174% (572 000 procedures) whereas the total knee arthroplasties are estimated to increase by 873% from the present rate (3.48 million procedures). Not only the replacement surgeries have increased, but also the revision surgeries of hip and knee implants. Revision surgeries are carried out as a result of failed hip and knee joint implants during permanent implantation caused by stress-shielding effect, low corrosion resistance, etc.. as shown in Figure 2-2. Revision surgeries are associated with pains experienced by patients and are costly and at times unsuccessful. The total number of hip and knee revision surgeries is projected to grow by 137% and 607%, respectively, between 2005 and 2030. This indicates that implant manufacturing is expected to increase in the next coming years [6,15,16].

Design of orthopaedic implant material is focused on the ability of the material to sustain the load-bearing function of human bones and reconstruction. They are required to possess excellent biocompatibility i.e. should not cause any adverse effects such as allergy, cytotoxicity and inflammation during implantation, superior corrosion resistance in body environment, an excellent combination of high strength and low modulus, high fatigue and wear resistance, high ductility to sustain forces they are subjected to and thus prevent fracture and no cytotoxicity [2,17,18]. Therefore, to ensure the stability of orthopaedic implant materials, their elastic modulus, tensile and compressive strength are generally optimized with reference to the mechanical properties of bone shown in Table 2-1. Their manufacturing and processing techniques should be also economically be viable.

Table 2-1: Mechanical properties of bone. (adapted from [19])

Tissue	**Compressive Strength (MPa)**	**Tensile Strength (MPa)**	**Elastic Modulus (GPa)**
Tibia	159	140	18.1
Femur	167	121	17.2
Radius	114	149	18.6
Humerus	132	130	17.2
Cervical	10	3.1	0.23
Lumbar	5	3.7	0.16

Amongst all issues displayed in Figure 2-2, the mismatch between the elastic moduli of the human bone and implant has been identified as one of the major issues associated with the current orthopaedic implant materials. Under normal circumstances (without the implant) bone carries the load itself. However, bone shares the load with an implant as soon as it is introduced into the bone. As a result, the reduced stress experienced by bone will induce stress-shielding. When a load is applied, the bone tries to oppose it and according develop the most suitable structure. This results in the increased bone mass in areas of the bone that are under high load. The areas with less load will have reduced bone mass, which is called bone resorption and can cause the failure of the implant [6].

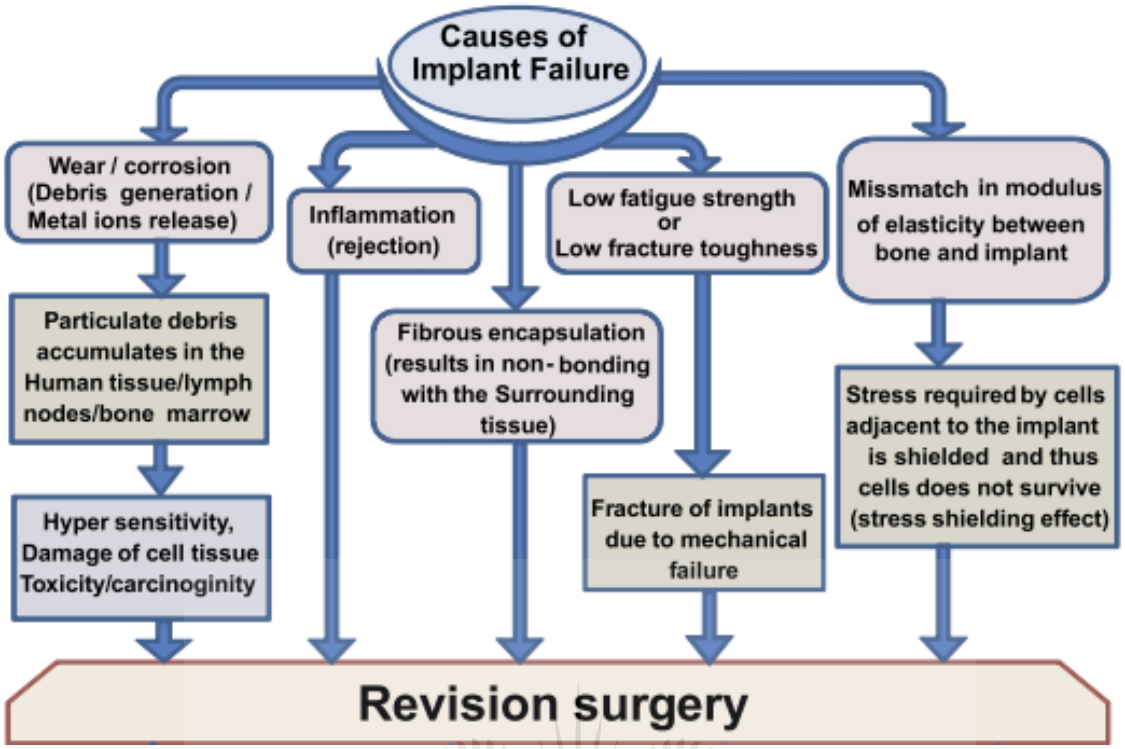

Figure 2-2: – Various causes for failure of implants that lead to revision surgery [20].

2.2 Conventional orthopaedic biomaterials and their limitations

316L stainless steel, cobalt-chromium alloys, and titanium-based alloys are the frontrunners amongst the available biomaterials in various orthopaedic applications particularly joint replacement [6]. The mechanical properties of common metallic biomaterials for joint replacement are exhibited in Table 2-2.

Table 2-2: Comparison of tensile strength, yield strength and elastic modulus of the conventional orthopaedic materials. Sources: Compiled from [6,26]

Material	Compressive Strength (MPa)	Tensile Strength (MPa)	Yield Strength (MPa)	Elastic Modulus (GPa)
316L Stainless steel	170-310	465- 950	170-750	205- 210
CoCrMo	450-1896	600- 1785	275- 1585	220- 230
CP Ti	590-1117	785	692	105
Ti6Al4V	-	960- 970	850- 900	110

The use of stainless steel materials is based on its relatively low cost, availability, processability and acceptable biocompatibility, whereas cobalt-chromium materials possess better wear resistance, corrosion resistance and fatigue strength. However, the use of 316L stainless steel and Co-Cr based alloys is restricted because they have potential hazards during orthopaedic

application due to the release of Ni, Co and Cr caused by corrosion and wear. Reports indicate that Ni can cause some skin related disease such as dermatitis, while Co is associated with neurological symptoms in some patients after some years of implantation. The presence of Cr in the human body can lead to damage of kidney, liver and blood cells via oxidation reactions. Moreover, the elastic modulus of both materials (240 GPa for Co-Cr based alloys and 210 GPa for 316L stainless steel) is much higher than that of the bone in the human body (10-30 GPa), thereby causing stress-shielding effect [2,6,21,22].

In light of the adverse effects of the 316L stainless steel and Co-Cr based alloys in orthopaedic applications, titanium and its alloys have emerged as the alloys of choice owing to their excellent properties that include lower elastic modulus, higher specific strength (e.g. ratio of strength to density), better corrosion resistance and biocompatibility than stainless steel and cobalt-chromium alloys [15,23,24,25].

2.3 Ti and its alloys

2.3.1 Effects of alloying elements on Ti

Titanium undergoes an allotropic transformation, i.e. it changes from one crystallographic form to another. It possesses a hexagonal close-packed crystal structure (HCP) commonly known as alpha (α) below 883°C. Above this temperature, it has a body centreed cubic structure (BCC referred to as beta (β). The α to β phase transformation of pure Ti is dependent on the alloying elements, which are classified as the alpha (α) stabilizing elements, β-stabilizing elements and neutral elements as illustrated in Figure 2-3. The α-stabilizing elements such as aluminium (Al) and small quantities of the interstitials elements such as oxygen (O), nitrogen (N) and carbon (C) extend the hcp α phase-field to elevated temperatures, i.e. increase the β-transus temperature. They provide Ti with low strength and good corrosion resistance, e.g. CP Ti. The β-stabilizing elements such as V, Mo, Nb, tantalum (Ta), iron (Fe), etc., move the β phase-field to lower temperatures, i.e. decrease the β-transus temperature. Neutral elements exhibit minor effect on the stability of any of the phases, i.e. do not show any marked effect on the β-transus temperature.

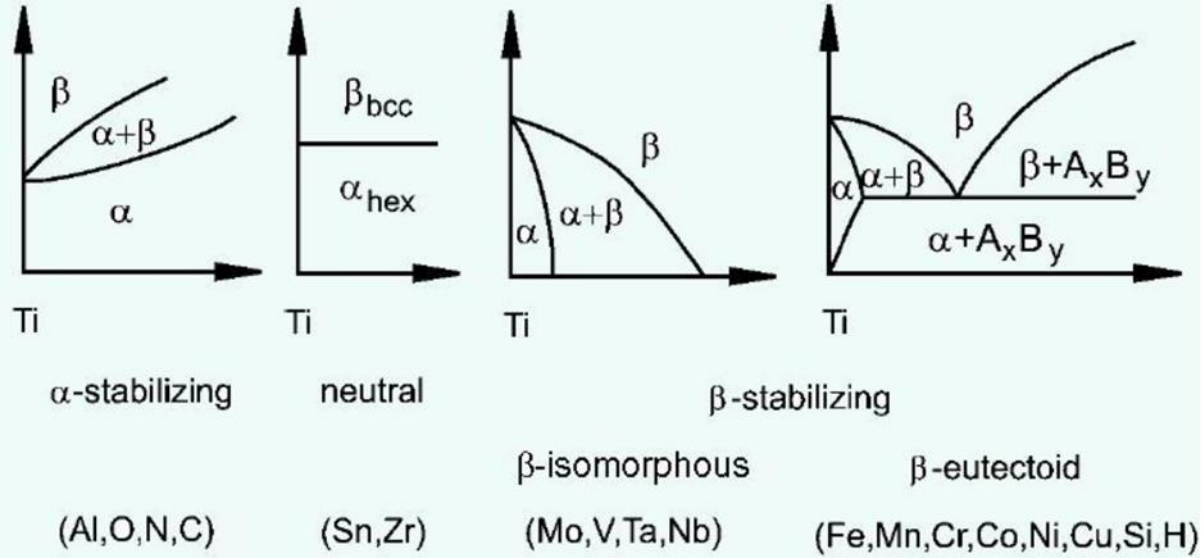

Figure 2-3. Effects of alloying elements on Ti. (Source: http://www.dierk-raabe.com/titanium-alloys/)

2.3.2 Classification of Ti and its alloys

Ti and its alloys are classified as α, near α, the dual alpha-beta (α+β), metastable β and stable β depending on the microstructure at room temperature. The α phase Ti alloys are comprised entirely of the hcp α phase. The near α Ti alloys are made up of 1-2% of β-stabilizing elements and about 5-10% of β phase and their strength is normally enhanced through the addition of large amount of oxygen, however, in the expense of their ductility. The dual-phase α+β Ti alloys contain higher concentrations of β-stabilizing elements which results in 10-30% of β phase in the microstructure. They possess higher strength, good toughness, good fatigue behaviour and excellent corrosion strength, e.g. Ti6Al4V alloy. The metastable β Ti alloys are composed of higher concentrations of β-stabilizing elements, in which the β phase can be retained upon fast cooling but decompose to α + β upon ageing. The stable β phase Ti alloys also contain higher concentrations of the β stabilizers, but theoretically, they do not precipitate secondary phases upon ageing and are not hardenable [15,27,28].

2.3.3 Limitations of Ti and its alloys in orthopaedic applications

The most widely used titanium alloy in orthopaedic applications is (α + β) Ti6Al4V ELI material. However, some studies have indicated that vanadium is a potential cytotoxic element, as it can cause adverse reactions with human tissues. To mitigate this problem, vanadium-free Ti alloys such as Ti6Al-7Nb and Ti-5Al-2.5Fe alloys were developed, which offered mechanical properties similar to those of Ti6Al4V alloy. Furthermore, concerns about the ability aluminium to induce neurological disorders, as well as Alzheimer's disease, were also

reported in other studies. Additionally, the marked difference between the elastic moduli of these Ti alloys (110 GPa, 105 GPa and 110 GPa for Ti6Al4V, Ti6Al7Nb and Ti5Al2.5Fe, respectively,) and that of the human body (10-30 GPa) can cause stress-shielding effect. This high elastic modulus is induced more by the α phase than the β phase present in the microstructure of Ti6Al4V alloy [5,6,7]. For instance, when the any of these alloys is used as a knee implant material, the implant takes over a considerable part of the body loading, thus shielding the bone from necessary stressing required to maintain its strength, density and health structure. This is defined as 'stress-shielding effect" and it can cause implant loosening, bone resorption and premature failure of the knee implant [3,29]. These drawbacks suffered by these alloys have motivated for the development of non-cytotoxic orthopaedic Ti implant materials with the elastic modulus comparable to that of the human [4,5]. As a result, metastable β-type Ti alloys with low elastic modulus are considered promising candidates as orthopaedic implant material.

2.3.4 Metastable beta (β) titanium alloys

Metastable beta (β) alloys are defined as any alloy that contain sufficient β-stabilizing element(s) to retain 100% β phase upon rapid cooling from the β phase region. β-stabilizing elements are classified into isormophous and eutectoid. The isomorphous β-stabilizing elements such as Mo, V, W, Cr and Ta possess high β_c values, decompose to form alpha plus beta (i.e no compound formation), have high melting points and densities and are relatives uneconomical. They tend to have narrow freezing ranges and therefore segregate in the bulk material [1,30,31].

Eutectoid beta stabilizers including Fe, Cr, Cu, Ni, Co, Mn and Si are characterized by low β_c values, are more effective in suppressing the β-transus and economical. They are not miscible in Ti, thereby showing limited solubility and form a eutectoid reaction $\beta \rightarrow \alpha + Ti_xA_y$ upon decomposition, where Ti_xA_y is an intermetallic compound of the Ti a eutectoid alloying element. They tend to have wide freezing ranges and therefore segregate strongly. In addition to the fact that they are effective in suppressing the β-transus temperature, segregation can be observed in areas with significantly lower β-transus values than the bulk [1, 28,30].

Both the isomorphous and eutectoid β-stabilizing elements lower the β-transus temperature, thereby increasing the size of the single β-phase-field, while decreasing the size of the hcp α

phase-field. Table 2-3 exhibits the critical concentrations of beta phase stabilizing elements (β_c) in binary Ti alloys required to retain 100% of the BCC β-phase after quenching to room temperature. It is evident that out of all the isomorphous β-stabilizing elements listed, Mo is the most effective β stabilizer in Ti. Tin (Sn) and Zr are effective in stabilizing the β phase in multicomponent system only, hence they are classified as neutral elements [30].

The concentration of the β-stabilizing element(s) strongly affects phase transformation in metastable β-type Ti alloys [4]. Figure 2-4 exhibits the phase diagram of titanium alloys with the decomposition products of the β-phase upon cooling from the β phase region (above the β-transus). The concentration of the β-stabilizing elements should be sufficiently high to avoid intercepting the martensitic transformation start temperature (M_s) upon quenching, thereby precipitating martensitic phases. β_c denotes the critical minimum composition of the β stabilizer(s) amount needed to retain 100% β phase upon rapid cooling from the β phase-field. β_s refers to the minimum amount of β-stabilizing elements needed to form stable β-Ti alloys. If the concentration of the β-stabilizing elements in metastable β–type Ti alloy is limited to below the critical concentrations given in Table 2-3, then the alloy will precipitate the martensitic phases upon quenching.

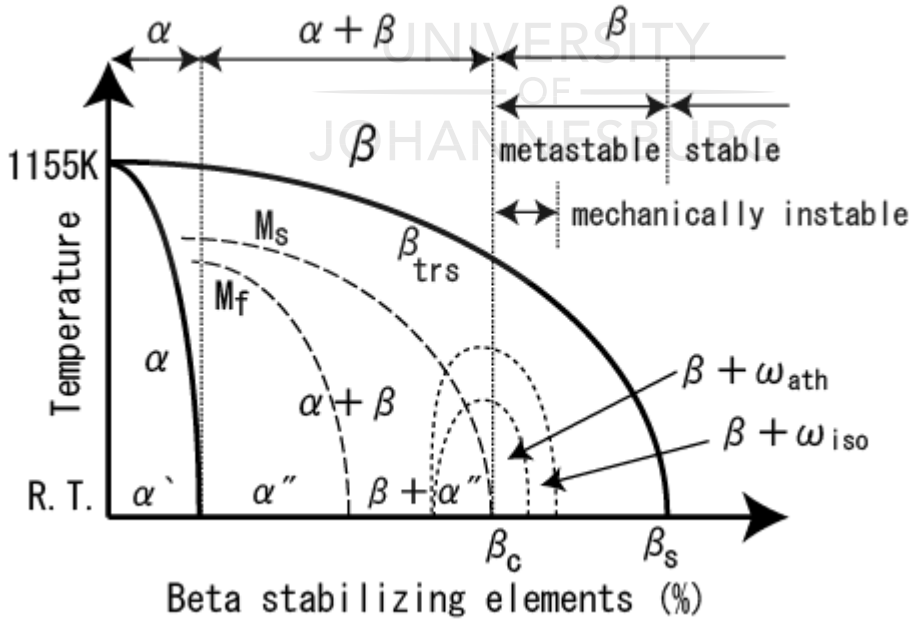

Figure 2-4: Schematic phase diagram of titanium alloys with the decomposition products of the β-phase [32].

Furthermore, alloys categorized between β_c and β_s boundaries are considered metastable β-Ti alloys because they fall within the two-phase-field (α+β). This can be ascribed to the

precipitation of a second phase (alpha or omega phase) from the β phase upon ageing. However, an alloy will comprise a single β phase upon quenching from the β phase-field when the concentration of the β-stabilizing element is greater than the critical concentration listed in Table 2-3 and schematically depicted in Figure 2-4 [30]. The omega (ω) phase is precipitated in metastable β-type Ti alloys either upon rapid cooling from the β phase region (ω_{ath}), deformation at room temperature or during ageing of a quenched material (ω_{iso}) [4]. It has negative effects on the mechanical properties of metastable β-type Ti alloys as it decreases the ductility due to their brittle nature, which is ascribed to its ability to restrict slip and thus increasing the strength of the β phase above the value for brittle fracture in β phase. It also increases the elastic modulus of metastable β-type Ti alloys significantly. Alloys beyond the β_s boundary are theoretically classified as stable β alloys. The values of β_c and β_s are dependent on the chemistry of an alloy. β_{trs}, Ms and Mf refer to β-transus, martensite transformation start and finish temperatures, respectively [4,5,32].

Table 2-3. Critical concentrations (wt. %) of β phase stabilizing elements in binary Ti alloys required to retain 100% of the BCC β-phase after quenching to room temperature [28,30]

Element	Type	β_c (wt%)
Molybdenum	Isomorphous	10.0
Niobium	Isomorphous	36.0
Tantalum	Isomorphous	45.0
Vanadium	Isomorphous	15.0
Tungsten	Isomorphous	22.5
Cobalt	Eutectoid	7.0
Copper	Eutectoid	13.0
Chromium	Eutectoid	6.5
Iron	Eutectoid	3.5
Manganese	Eutectoid	6.5
Nickel	Eutectoid	9.0
Silicon	Eutectoid	-

2.3.4.1 *Ti-X binary alloys*

Previous studies have reported on the development of Ti-X binary alloys containing a non-cytotoxic β-stabilizing element (X) to reduce their elastic moduli so that it [the elastic modulus] matches that of the human bone. For instance, Ho *et al.* [33] studied the microstructural evolution and modulus of elasticity of as-cast Ti-Mo binary alloy series with Mo concentration ranging between 6 and 20 wt% by three-point bend tests. Microstructural results indicated the transformation of β phase to a single martensitic α' phase between 3 and 5 wt% Mo, the

coexistence of the α' and α" martensitic phases at 6 wt%, α" phase in at 7.5 wt%, and β phase between 10wt % ad 20 wt%. Bending modulus of elasticity of this alloy series ranged between 55 GPa (7.5 wt%) to 95 GPa (10 wt%). The α" martensitic phase in Ti-7.5Mo binary alloy exhibited the lowest bending modulus, whereas the highest bending modulus was measured on the Ti-10Mo alloy among the Ti-Mo alloys. The highest elastic modulus in Ti-10Mo alloy was later confirmed by Ho [34] to be the result of the presence of a large amount of the ω phase. This conclusion was in good agreement with Sung *et al*. [35] s experimental observations, who obtained the lowest elastic modulus in α" phase (7 wt%) and the highest elastic modulus in β phase (15 wt%).

These observations were not in accordance with the findings revealed in other studies. Cardoso *et al.* [36] observed the transformation of β phase to a single martensitic α' phase at between 3 and 5 wt% Mo, martensitic α" phase, athermal ω phase and β phase in at 7.5- 10 wt%,, and single β phases at 15 wt%. Bending modulus of elasticity of this alloy series ranged between 55 GPa (7.5 wt%) to 95 GPa (10 wt%). However, no ω phase could be detected by the conventional x-ray diffraction (XRD) due to its formation in small volume fractions and its diffraction peaks which overlap with the β phase ones. Its diffraction peaks have low intensities, therefore it is unlikely to detect it if its volume fraction is less [37]. The elastic modulus was found to range between 75 GPa (15wt %) and 91 GPa (3 wt%). The β phase exhibited the lowest elastic modulus among all the investigated Ti-Mo alloys.

Alemida *et al*. [1] observed martensitic α" phase and retained β-phase between 4 and 8 wt% Mo, single β phase at 10 wt% or more. The elastic modulus ranged between 75 GPa (13 wt% with a single β phase) and 120 GPa (5 wt% with α" and β-phases). Lee *et al*. [38] reported that Nb concentration of 15 wt% or less to resulted in the precipitation of a single martensitic α' phase. At an Nb content range of 17.5 and 25 wt%, the alloys were primarily composed of the martensitic α" phase, whereas the β coexisted with the α" phase at Nb content between 27.5 and 30 wt%. The elastic modulus ranged between 68 GPa (35 wt% with a single β phase) and 85 GPa (5 wt% Nb with α' phase). At Nb concentration above 30 wt%, a single β phase was formed, which is comparable to the critical concentration of Nb given in Table 2-3.

Aleixo *et al.* [39] also studied the elastic modulus of swaged Ti-Nb alloys as a function of composition and cooling rate. As per their experimental findings, the Ti-Nb alloys containing

up to 10 wt%Nb possessed the elastic modulus of about 100 GPa. In comparison with the water-quenched and air-cooled specimen, the furnace cooled specimen showed the highest values of elastic modulus. Upon increasing the Nb content to 15 wt%, the elastic modulus of 65 GPa was observed in the water-quenched specimen. This was attributed to the high volume fraction of β phase. Increasing the Nb content up to 30 wt % resulted in the increase in the elastic modulus values of 90 GPa upon water-quenching, 85 GPa upon air cooling and 95 GPa upon furnace cooling. This was ascribed to the precipitation of the ω phase as well as the tentative variations in the dimensions of crystalline structure resulting from the alloying of Ti with large amounts of Nb. The precipitation of the ω phase predominated in the furnace cooled specimen. At 35 wt% Nb, the elastic modulus decreased to about 70 GPa as a result of the presence of a high volume fraction of the β phase in the alloy. Generally, the lowest elastic modulus was observed in alloys containing the β phase, medium values in alloys containing α, α' and α" phases and the highest value in ω phase containing Ti-Nb alloy compositions.

In a study of Zhou *et al*. [40] on the effect of Ta content on the microstructural and mechanical properties of Ti-Ta alloys, the formation of the phase constituents changed from hexagonal α' martensitic phase in Ta less than 20 wt%, orthorhombic α" martensitic phase in Ta ranging between 30 and 50 wt%, coexistence of the metastable BCC β phase and the martensitic α" phase at Ta of 60 wt% and a single β phase at Ta content above 60 wt%. This finding indicate that the critical concentration of Ta to form a single β phase was greater than 60 wt%, which are inconsistent with the critical concentration of Ta listed in Table 2-4. The elastic modulus ranged between 67 GPa (at 70 wt% with a single β phase) and 100 GPa (at 10 wt% with α' phase). No investigation of the presence of the ω phase was conducted [40].

Ho *et al.* [41] observed α+ β + ω phases at 5 wt%Cr, β+ ω phases at 10 wt%Cr, β phase between 20 and 30 wt%. The bending modulus of elasticity of the Ti-Cr alloy series ranged between 95 GPa (5 wt% Cr) and 163 GPa (10 wt% Cr). The highest elastic modulus in Ti-10Cr binary alloy was attributable to the precipitation of the largest volume fraction of the ω phase during quenching. Hsu *et al*. [42] reported that the microstructures of Ti-Sn alloy series (Sn ranged between 1 and 30 wt%) exhibited no β phase, but the predominance of the α phase. The bending modulus of elasticity ranged between 110 (5wta5 Sn) and 150 GPa (30 wt% Sn), which was ascribed to the resulted slight change in the crystal structure. It is noteworthy that Sn is categorized as a neutral element, i.e. does not show any effect on the β-transus

temperature. Guo *et al.* 2015 [43] reported an elastic modulus of 56 GPa in a cold-rolled plus annealed Ti-38Nb alloy.

The lowest elastic modulus obtained in the binary Ti-X alloys still did not match that of the human bone. This motivated for the design and development of multi-component metastable β-type Ti alloys containing two or more β-stabilizing elements.

2.3.4.2 *Multicomponent β Ti alloys*

Recent advances have been made to obtain low elastic modulus comparable to that of the bone through the development of metastable β-type Ti alloys containing two or more β-stabilizing elements. Most of the metastable β-type Ti alloy series developed for orthopaedic applications are ternary Ti-Mo-Nb [9,44], Ti-Nb-Zr [45,46], Ti-Nb-Mo [47], Ti-Nb-Sn [48,49], Ti-Zr-Mo [50,51], quaternary, Ti-Nb-Zr-Sn [52,53], Ti-Ta-Hf-Zr [54], Ti-Nb-Ta-Zr [55] and quinary Ti-Nb-Mo-Zr-2 [56], Ti-Mo-Sn-Nb-Zr [57], Ti-Zr-Mo-Sn-Nb [58], Ti-Nb-Zr-Ta-Si-Fe [25] alloys, which make it difficult to obtain uniform distribution of the chemical composition.

In the last two decades, design of the metastable β-type Ti alloys has been carried out using either the trial-and-error method with no fundamental basis, which is time-consuming and uneconomical during manufacturing [20,59,60]. In the past decade, in addition to the trial-and-error method, the molybdenum equivalence, d-electron method and average electron concentration (e/a) ratio approaches have been employed as tools that determine the stability of the β phase in the designed β-type alloys [28,61,62]. Recently, a new alloy design approach that focuses on the formulation of alloy compositions has been developed by Wang *et al.* [63,64]. The design approaches are discussed in details as follows:

- **Molybdenum Equivalence**

The molybdenum equivalence (*Moeq*), proposed by Bania, reflects on the capability of each alloying element (Mo, Ta, Nb, Sn and Zr) to stabilize the β phase by comparing the elemental contribution to that of the major β stabilizer (Mo) experimentally. The Mo equivalence formula is expressed as follows:

$$Moeq = 1.00\text{Mo} + 0.67\text{V} + 0.44\text{W} + 0.28\,\text{Nb} + 0.22\,\text{Ta} + 2.90\text{Fe} + 1.60\text{Cr} + 0.77\,\text{Cu} + 1.11\,\text{Ni} + 1.43\,\text{Co} + 1.54\,\text{Mn} + 0\,\text{Sn} + 0\,\text{Zr} - 1.00\text{Al}\ (\text{wt\%})$$

Equation 1

The prefix coefficient of each alloying element indicates the β-stabilization capability [of that element] with respect to that of Mo. Qualitatively, this coefficient value is equal to the ratio of the β_c value of Mo (i.e., 10 wt%) to that of the respective β stabilizer. Most of the alloying elements contribute positively to the stability of the β phase. Al is also included as an α stabilizer to demonstrate its opposing effect when it is added to a metastable β-type Ti alloy. Sn and Zr are considered nearly neutral with coefficients of zero because the β phase could not be retained at room temperature in the Ti-Sn, Ti-Zr, Ti-Si and Ti-Al binary alloy systems. They contribute weakly or negatively to the stability of the β phase. Bania empirically set the critical lower limit of β stability (β_c) as 10 wt% Mo. The stability of the β phase increase generally with increasing molybdenum equivalence value. However, this Mo Equivalence is empirically based on the binary alloy systems, and there are no reports on their mechanism. Therefore, the characterization of metastable β-type Ti alloys with low β stabilities using the molybdenum equivalence has been a challenge as a result of the complex interactions between multi-elements. This has been observed in Ti-5.51Mo-6.50Sn-9.98Zr-10.17Nb alloy with Mo_{eq} of 8.1 wt% (below β_c of 10 wt%), but it could form a single β phase upon quenching [28,46,61].

As a result, Qing *et al*. [61] proposed a new molybdenum equivalence approach for complex metastable β-type Ti alloys using the relative slopes of the [β/(α+β)] boundary lines in the Ti-X phase diagrams exhibited in Figure 2-5 a) and b). They explored the contributions of alloying elements on the β stabilities through the use of phase diagrams characteristics in the Ti-rich Ti-M binary phase diagrams. The Ti-Mo binary phase diagram is illustrated in Figure 2-5 b), which shows a monotectoid point at a Mo content of 12 at.% or 21.46 wt% at 695°C. Since well Bania determined the critical concentration of Mo as 10 wt%, the Mo concentration at the monotectoid point demonstrates that it has the highest β stability in the whole phase diagram. It can be clearly seen that Mo extends the β phase-field in the phase diagram, exhibiting a favourable β stabilization.

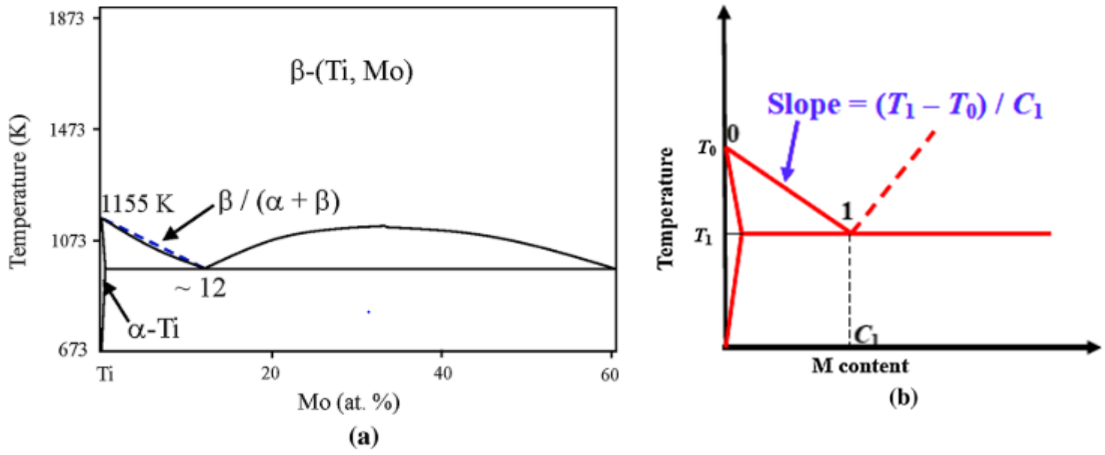

Figure 2-5. a) Ti-rich corner of the Ti-Mo binary phase diagram. The [β/(α+β)] boundary line shows a fairly rapid drop, the slope of which (the dotted line) is taken as a measure of the b-stabilization capability of Mo. b) The Schematic plot for the slope calculation, i.e., slope = (T1 T0)/C1 [61].

The relative stability of β phase against that of α phase in a Ti-X binary alloy system could then be demonstrated by the slope of the [β/(α+β)] phase-boundary line from the pure Ti to the monotectoid point. Thus, the slope of the [β/(α+β)] phase-boundary line in the binary Ti-X phase diagram indicates the β-stabilization capability of that solute element, X. Then the Mo equivalent (Mo_{eq})Q formula would be established from the molybdenum equivalence coefficient of this solute element if the slope is normalized by that of Ti-Mo. The schematic plot for the slope calculation is illustrated in Figure 2-5 b). The slope is calculated as slope = $(T_1\text{-}T_0)/C_1$, where T_1 and C_1 are the temperature and solute content of the special point 1, respectively, and T_0 is the temperature of the pure β being 1155 K (882 °C). The formula is expressed as follows:

$$Moeq = 1.00\text{Mo} + 1.25\text{V} + 0.59\text{W} + 0.28\text{Nb} + 0.22\text{Ta} + 1.93\,\text{Fe} + 1.84\,\text{Cr} + 1.50\,\text{Cu} + 2.46\,\text{Ni} + 2.67\,\text{Co} + 2.26\text{Mn} + 0.30\,\text{Sn} + 0.47\,\text{Zr} + 3.01\,\text{Si} + 1.47\text{Al}\ (\text{wt\%}). \quad \text{Equation 2}$$

- **Average electron concentration ratio**

The average electron concentration (e/a) approach is defined as the average number of valence electrons in each atom of an alloy. It is calculated using the following equation:

$$\frac{e}{a}\ ratio = (v_1\, m_{1+}\, v_2\, m_2 + v_3\, m_3 + \cdots + v_n\, m_n)/100 \quad \text{Equation 3}$$

where v_n is the total number of valence electrons in the valence shell of the n^{th} element and m_n is the atomic percentage of the n^{th} element. The e/a ratio is presented in Figure 2-6 (a) as a function of microstructure. It is evident that the stability of the β phase is guaranteed at e/a ratio of 4.20 or more [54]. Conversely, Buzatu *et al.* reported that the β phase is stable at e/a ratio

above 4.30, whereas the precipitation of the metastable omega (ω) phase occurs between the range 4.13 and 4.30 [65].

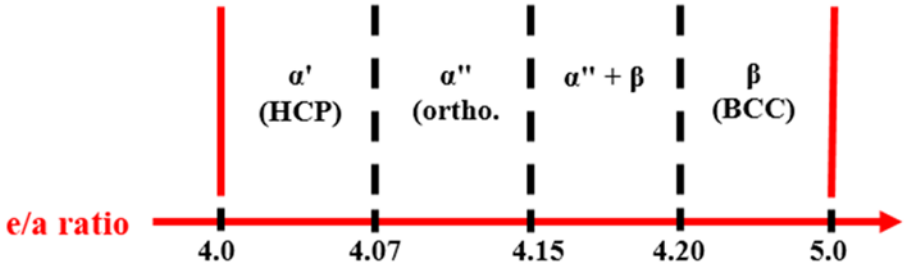

Figure 2-6. Microstructural evolution of Ti alloys after quenching with respect to the e/a ratio scale [60].

The variation of the elastic modulus with the e/a ratio for most Ti alloys is schematically shown in Figure 2-7. At low values of e/a ratio, the stability of the β phase is low. This results in the formation of the α or α' martensitic phase, which have a high modulus. As the e/a ratio increase, the β phase stability increases with increasing alloying elements, resulting in an increase in elastic modulus. The e/a ratio reaches a limited range where the β phase stability is high, but the undesirable ω phase is precipitated, which causes an increase in the elastic modulus. The broken line shows the true minimum of elastic modulus of the β phase when the formation of the metastable phases is suppressed through proper alloying.

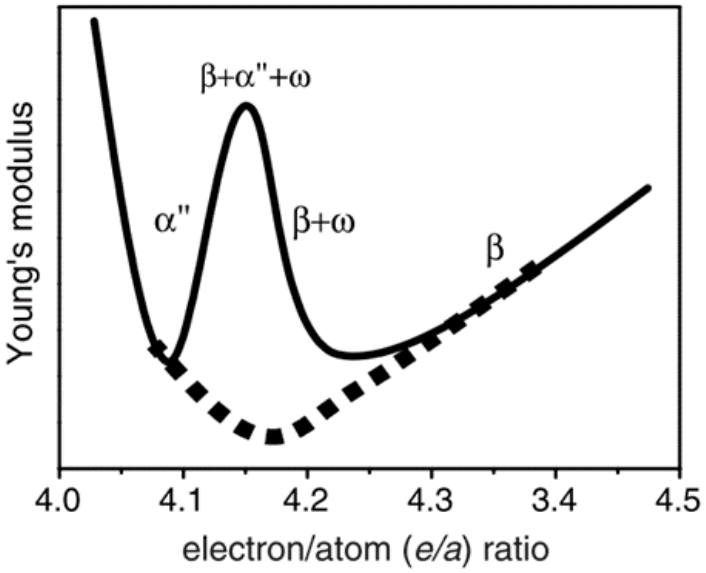

Figure 2-7: Schematic variation of elastic modulus with electron/atom (e/a) ratio in binary Ti alloys [53].

- **D-electron theory**

The molecular orbital theory uses two alloying parameters, the bond order (*Bo*) and the *d* orbital energy level (*Md*), to provide a physical background to the phase stability and phase transformations by connecting *Bo* and *Md* to the stability of the β phase. The *Bo* parameter demonstrates how the electron clouds overlap between alloying element M and parent metal X as illustrated in Figure 2-8 (a). It measures the strength of the covalent bond between M and X atoms. The Bo parameter increases with increasing chemical bond between M and X atoms. On the hand, *Md* correlates with the electronegativity and atomic radius of elements. A larger average radius of the d-orbital is observed in any atom with a larger atomic radius. As a result, an increase in the average distance between the d electrons and the nucleus at a centre weakens the attractive Coulomb force existing between them. This result in the increase in Md with increasing atomic radius. In a case where the isolated M atom has a d level that is higher than that of the isolated X atom, the electrons are transferred from M atom to X atom to lower the energy. This charge transfer causes the effective charge to become positive for M and negative for X. Thus, the direction for charge transfer is controlled by the energy level, which makes it related to the electronegativity as exhibited in Figure 2-8 b). A lower *Md* is observed in an element with a higher electronegativity. The two parameters change periodically in the order of the elements in the periodic table [62,66,67].

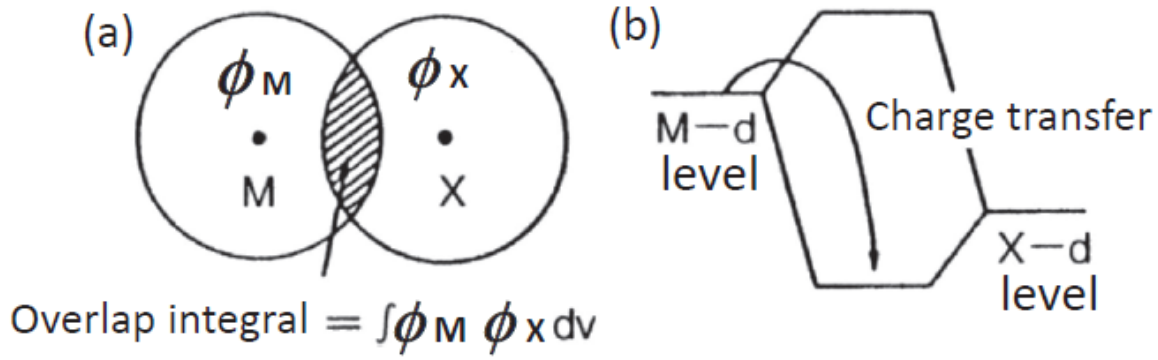

Figure 2-8. Alloying parameters, (a) bond order, Bo and (b) d-orbital energy level, Md. In (a), ϕM and ϕX are the atomic orbitals of M and X, and Bo is proportional to the overlap population between them.

The *Bo* and *Md* values are calculated using both the BCC Ti cluster and the HCP Ti cluster shown in Figure 2-9. The determination of the alloying parameters for Ti is performed by substituting Ti atom with an alloying element (M) at the central site, followed by a series of calculations with a variety of alloying elements. Table 2-4 lists the *Bo* and *Md* parameters for various alloying elements in BCC Ti (β-Ti). The average values of *Md* and *Bo* of an alloy are defined by taking their compositional average, and $\overline{Md}$ and $\overline{Bo}$ are denoted as follows:

$$\overline{Md} = \sum_{i=i}^{n} X_i \,.\, (Md_i) \qquad \text{Equation (4a)}$$

$$\overline{Bo} = \sum_{i=i}^{n} X_i \,.\, (Bo_i) \qquad \text{Equation (4b)}$$

whereby, *Xi* is the atomic fraction of component *i* in the alloy, $(Md)_i$ and $(Bo)_i$ are the respective values for component *i*. The summation of extends over the components, *i*= 1,2,3,…, *n*.

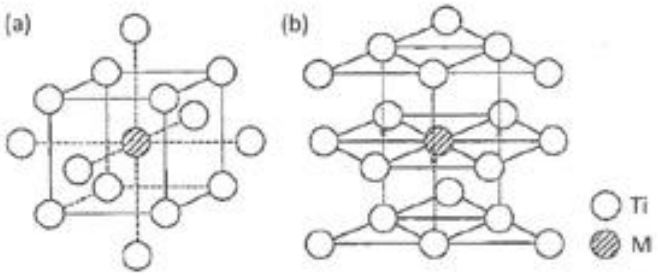

Figure 2-9: Cluster models used for calculations a) BCC cluster and b) HCP cluster.

Table 2-4: Bo and Md values for various elements in β Ti.

3d	***Bo***	***Md (eV)***	***4d***	***Bo***	***Md (eV)***	***5d***	***Bo***	***Md (eV)***	***other***	***Bo***	***Md (eV)***
Ti	2.790	2.447	**Zr**	3.086	2.934	**Hf**	3.110	2.975	**Al**	2.426	2.200
V	2.805	1.872	**Nb**	3.099	2.424	**Ta**	3.144	2.531	**Si**	2.561	2.200
Cr	2.779	1.478	**Mo**	3.063	1.961	**W**	3.125	2.072	**Sn**	2.283	2.100
Mn	2.723	1.194	**Tc**	3.026	1.294	**Re**	3.061	1.490			
Fe	2.651	0.969	**Ru**	2.704	0.859	**Os**	2.980	1.018			
Co	2.529	0.807	**Rh**	2.736	0.561	**Ir**	3.168	0.677			
Ni	2.412	0.724	**Pd**	2.208	0.347	**Pt**	2.252	0.146			
Cu	2.114	0.567	**Ag**	2.094	0.196	**Au**	1.953	0.258			

The characteristics of each alloying element are represented by alloying vectors presented in Figure 2-10. The alloying vector is constructed from the position of pure Ti to the position of Ti-10mass%M alloy in the *Bo-Md* diagram. As an example, the Ti-Al vector is directed towards the α-phase region, demonstrating that Al is an α-stabilizing element. Contrarily, the direction of the vectors of Ti-Ta, Ti-Nb, Ti-W and Ti-Mo is towards the β- phase-field, indicating that Ta, Mo, Nb and W are β-stabilizing elements [62].

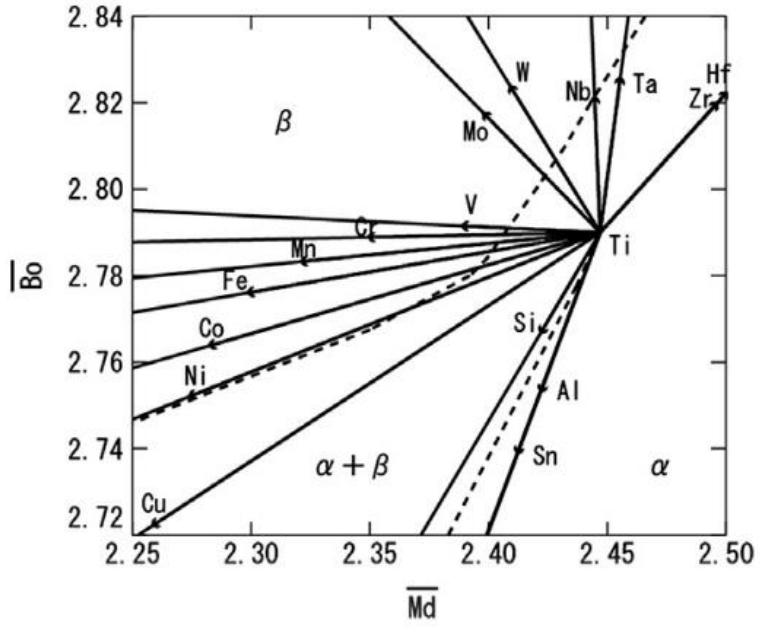

Figure 2-10: Phase stability change with alloying elements [62].

Depending on the composition, some β-type Ti alloys precipitate the martensitic phase (α") and ω phase. Figure 2-11 shows positions of Ti and its alloys by the numbers surrounded by open circles. The β/ β+ω boundary separates the β phase region from the β+ω phase regions. Along this β/ β+ω boundary, exists a region of the least stable single β phase. The dotted line represents the martensitic start temperature, while the martensitic finish temperature is presented by a solid lie. The martensitic transformation begins at the martensitic starts temperature (M_s) and ends at the martensitic finish temperature (M_f). In between the M_s and the M_f boundaries, the α" phase co-exists with the β phase and/ or ω phase in the alloy at room temperature. The elastic modulus decreases with increasing Bo parameter, following an arrow direction next to the β/ β+ω boundary [68].

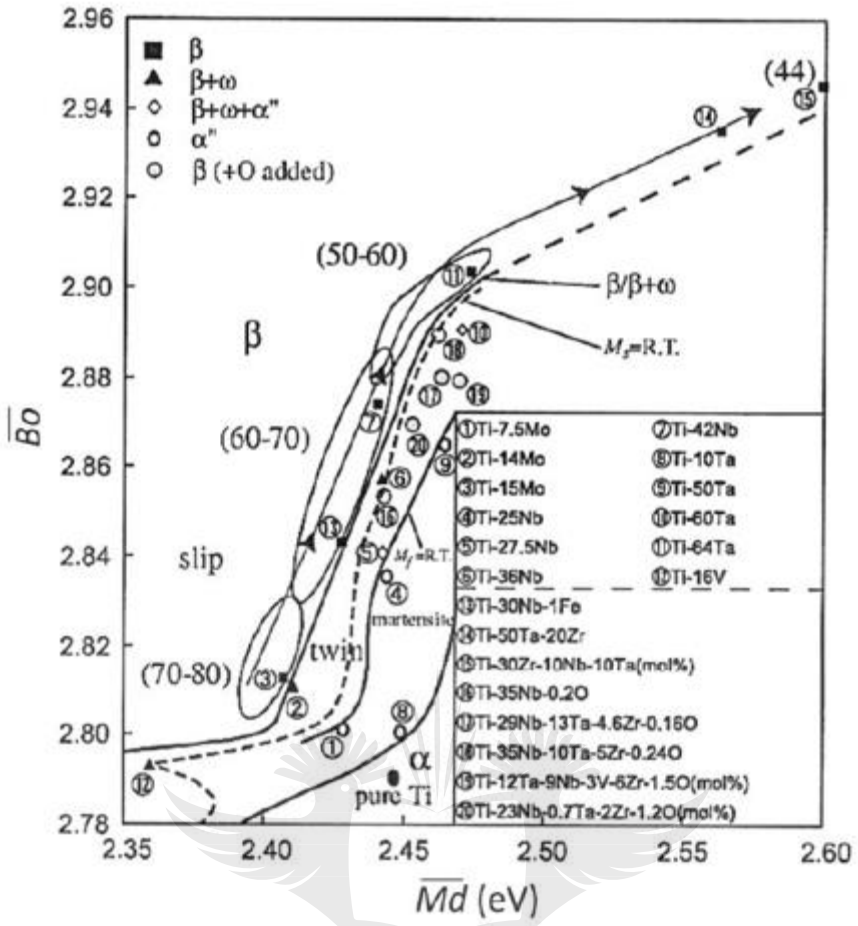

Figure 2-11: Extended Bo-Md diagram of different Ti alloys [62].

The least stable β phase alloys, which are reported to contain the least amount of β stabilizers, lie along the narrow region of the left or upper side of the β/β+ω phase boundary drawn as a dashed line. The values of moduli of elasticity are also illustrated in parentheses. The values of moduli of elasticity for these alloys decrease with increasing $\overline{Bo}$ and $\overline{Md}$ values in β-type alloys region on the Bo–Md map [62]. Once an alloy has been designed and located in the Bo-Md map, the corresponding alloy composition is simply determined using the rule of the vector sum.

- **Cluster-Plus-Glue-Atom Model**

The cluster-plus-glue-atom model describes the atomic structure of complex multi-component alloy systems using appropriate polyhedral units. It describes the 1st- and 2nd neighbour short-range-order structures of β-Ti alloys. Few reports are available that explores this model to design metastable β-type Ti alloys for orthopaedic applications. This model provides a

material's basic compositional and structural information in its cluster formula, which is expressed as [cluster](glue atoms)$_x$. This formula indicates that the atomic structure of any material is made up of the cluster part and the glue atom part. As shown in the image in Figure 2-12, all atoms in a given structure belong to their kinds of central atom (orange sphere), shell atoms (blue spheres) and glue atoms (green spheres) [61,69,70]. Generally, the interactions between two elements are characterized by their enthalpy of mixing ΔH: a large negative ΔH corresponds to strong interaction and favours clustering.

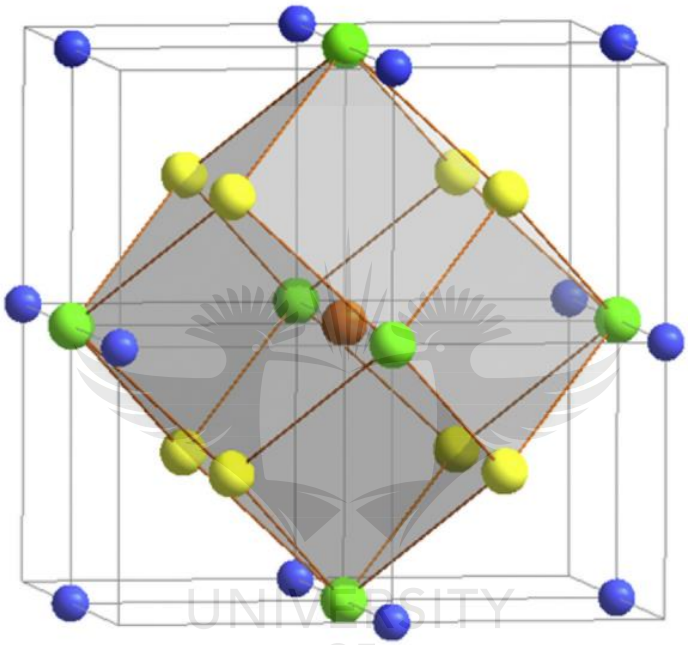

Figure 2-12: 1st-neighbour rhombic-dodecahedral cluster consisting of two sub-shells covering the eight nearest neighbours (yellow balls) and the six nearest neighbours (green balls). The orange ball represents the cluster centre atom. The outer shell, consisting of twelve atoms (blue balls), are locations of the glue atoms [71].

In BCC solid solution alloys, the maximum displacements between the solute atoms and the solvent atoms due to strong chemical actions occur at the 1st- and 2nd-neighbour shells around the solute atoms [16,70]. A BCC lattice is composed of eight atoms, positioned at cube vertices as the first nearest neighbour shell and centred by an atom, and the six atoms capping above the cubic facets as the second-neighbour shell [72]. Moreover, research has emphasized on the extension of the local structure information in BCC solid solutions to the second sub-shell [72]. Therefore, the 1st neighbour short-range order in BCC solid solutions should be made up of two sub-shells of the eight nearest neighbouring atoms and the six nearest neighbouring atoms, thereby forming a rhombic dodecahedron CN14 (CN: coordination number) illustrated in

Figure 2-12 [72]. This method reduces the need for trial-and-error methods experiments, thus saving time, expenses and other resources.

In a metastable β-Ti alloy, solute elements interacting strongly with the parent Ti such as Mo and Sn have a negative ΔH should be nearest-neighboured with Ti to form the solute-centred coordination polyhedral in the BCC lattice. Solute elements such as Nb with positive ΔH should be positioned in the second neighbour, acting as glue atoms in between the clusters. Solute elements with ΔH of zero such as Zr can be placed either in the glue atoms site or replace Ti in the cluster [61]. As a result, the use of a trial-and-error method is no longer essential for optimization of the alloy composition [73].

Extensive research on the development of metastable β-type Ti alloys containing two or more β stabilizers with the aim of reducing the elastic modulus so that it matches that of the human bone is still on-going. Gabriel *et al.* [64] designed a metastable β-type Ti-12Mo-3Nb alloy using the conventional trial-and-error method and found that the alloy contained a single β phase and the elastic modulus of 105 GPa after swageing [74]. Kuroda *et al*. [64] designed a metastable Ti-Zr-Mo alloy series by trial-and-error method with the elastic modulus ranging between 92 and 101 GPa. Li *et al*. [45] explored the microstructural and mechanical properties of β-type Ti-Mo-Si alloy series during compression tests. It was shown that all the as-cast samples primarily contained equiaxed β-Ti phase and minor α" phase particles. They also exhibited low elastic modulus in the range of 20.7–26.6 GPa.

You & Song [45] designed a series of Ti-Nb-Zr alloys with the d-electron theory approach with $\overline{Bo}$ and $\overline{Md}$ values of single β phase and non-single β phase in Ti–Nb–Zr ternary alloys. The elastic modulus ranged between 38.8 GPa and 74.7 GPa. It was reported that the elastic modulus of the Ti-Nb-Zr alloys comprising a single β phase decreased with increasing $\overline{Bo}$ and $\overline{Md}$ values. Contrarily, when the martensitic α' phase co-existed with the β phase in some of the alloys, their elastic modulus increased with increasing $\overline{Bo}$ and $\overline{Md}$ values.

Li *et al.* [75] designed Ti-Nb-Zr-Ta-Si alloy series also using the d-electron theory, in which the alloys were located in the β phase region with varying $\overline{Bo}$ and $\overline{Md}$ values. The obtained compressive elastic modulus was in the range 37 to 48 GPa, with the lowest value comparable to that of the human bone. The lowest value of 37 GPa was observed in the alloy with the

highest values of the average Bo and Md and vice versa. The theoretical predictions were consistent with the experimental observations.

Although the β phase stability predicting approaches have been considered useful in the design of metastable β-type Ti alloys, contradictions have been observed between theoretical predictions and experimental findings. The results showed either an overestimation or underestimation of the β-stabilizing effect of the alloying elements in the alloys. Ozan *et al.* [59] theoretically predicted the formation of a single β phase in Ti-Ta-Zr-Nb alloy series with *Moeq* in the range between 9.4 and 10.7 wt% ($\beta_c \geq 8$), e/a ratio in the range 4.21 and 4.25 as well as the location of the alloy in the β phase region in the Bo-Md phase stability map. However, the experimental results revealed the existence of the ω phase with the β phase matrix as exhibited in Figure 2-13 a) and b). This indicates that the β-stabilizing effect of the Ta, Nb and Zr alloying elements was overestimated in Ti-Ta-Nb-Zr alloy series.

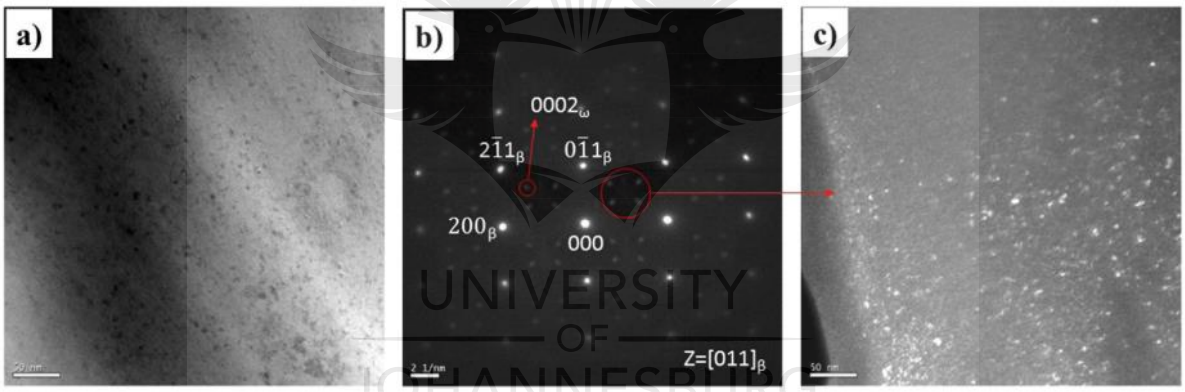

Figure 2-13. TEM images of Ti-39.5Ta-28Zr-2.5Nb a) bright-field image, b) selected area electron diffraction pattern and c) dark field image derived from the ω spots circled in (b) [59].

Similar observations were reported by Lin *et al.* [54] in Ti-Ta-Hf-Zr alloy series with *Moeq* of 8.1- 9.9, e/a ratio of 4.21-4.24 and they were located in the β phase region in the Bo-Md phase stability map. However, precipitates of the ω phase were detected as shown in the TEM images in Figure 2-14 a)- b).

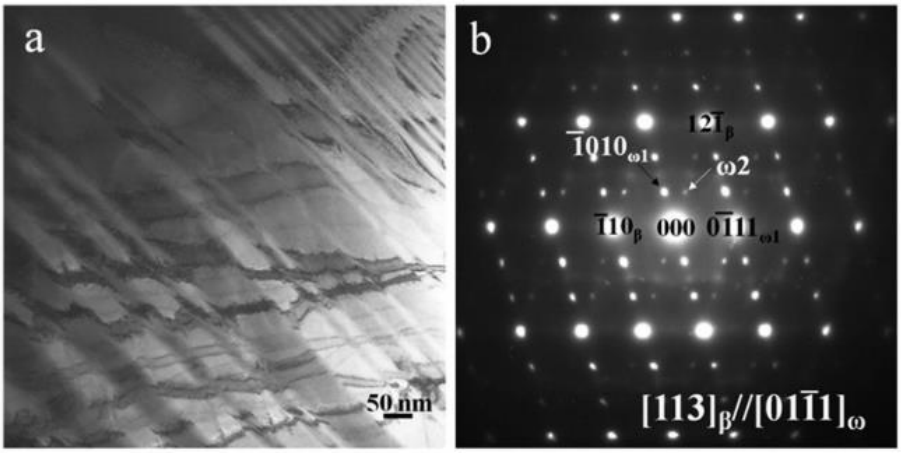

Figure 2-14. TEM images of Ti-45Ta-18.4Hf-10Zr: a) bright-field image, b) the corresponding selected area electron diffraction of a).

Wang *et al.* [63] developed (Ti,Zr)-(Mo,Sn)-Nb alloys with high β stabilities using the cluster-plus-glue atom model and obtained elastic modulus values as low as 48 GPa inthe as-cast condition. In a study conducted by Tulugan *et al.* [64], it was observed that the presence of one Mo atom in the cluster centre in as-cast Ti-Mo-Nb-Zr favoured the formation of a single β phase. Their elastic modulus values ranged between 69 and 92 GPa inthe as-cast condition [64]. Although this model showed the ability to design metastable β-type Ti-Mo based alloys with low elastic modulus values inthe as-cast condition, it was not intensively explored. Furthermore, it would also be interesting to evaluate the accuracy of the β phase stability predicting tools on the alloys designed using this model by comparing the theoretical predictions with the experimental observations.

Ozaki *et al.* [76] evaluated the composition dependence of the elastic modulus in relation to β phase stability and the feasibility of the d-electron theory approach on the development of metastable β Ti-V-(Sn) and Ti-Nb-(Sn) alloys with low elastic modulus. At low alloying contents in Ti-V and Ti-Nb binary alloys, very fine ω particles with a high density were observed, which increased in the elastic modulus. Increasing the alloying content led to the increase in β phase stability and weakening of the intensities of the ω reflections, which resulted in a minimum value of the elastic modulus. Micro-alloying the binary alloys with Sn suppressed the precipitation of the ω phase, thus reducing the elastic modulus to 50.7 GPa.

Xu *et al.* [43] investigated the effect of Nb on microstructural and bending properties Ti-15Mo-xNb ternary alloy inthe as-cast condition. Their experimental results indicated that the stability

of the β phase increased with increasing Nb content. Moreover, the micro-hardness, compression yield strength, compression strength and elastic modulus decreased with increasing Nb content. Lin *et al*. [43] studied the effect of Fe on the microstructural and bending properties ofthe as-cast Ti-7.5MoxFe alloy series (0- 7 wt% Fe). Results suggested that the Ti-7.5Mo-0Fe binary alloy was primarily composed of the martensitic α" phase, whereas all the ternaries alloys containing from as little as 0.1 wt% Fe consisted of a single β phase. Furthermore, the binary alloy possessed a lower bending strength (1749 MPa) and modulus (65 GPa) in comparison with the ternary alloys containing Fe, whose bending strength and modulus were in the range 1851- 2453 MPa and 72 – 111 GPa, respectively.

The problems associated with stress-shielding effect in metastable β-type Ti alloys have resulted in the proposal of solutions for controlling the elastic modulus. The control of the elastic modulus of metastable β-type Ti alloys has been carried out by controlling the phase transformation, formation of single crystals and introducing pores.

Alloying of Ti with a different combination of the β-stabilizing elements, necessary heat treatments and processing can result in the formation of equilibrium phases such as hcp α and BCC β as well as the non-equilibrium phases such as the hexagonal ω phase and the martensitic phases (hcp α' and orthorhombic α") even at room temperature. However, the formation of α, ω and the martensitic phases should be suppressed as they have higher elastic moduli. The formation of these phases is dependent on the concentration of the solute atoms. The higher the stability of the β phase, the lower elastic modulus. However, some published studies indicate that minimum values in elastic modulus are obtained in Ti alloys comprising the least amount of β-stabilizing elements (low β stability) to form a single β phase [12,30,56,77,78].

In their study, Zhao et *al*. [79] reported that Ti-(15;16)Mo alloys subjected to solution treatment were comprised of the β phase and a certain amount of the athermal ω phase, whereas Ti-(17;18)Mo alloys contained the β phase only. Contrarily, all the alloys were made up of the β phase and deformation-induced ω phase upon cold rolling. The elastic modulus values of all the alloys subjected to solution treatment were below 80 GPa, while those of the cold-rolled specimen increased due to the precipitation of the deformation-induced ω phase [5].

Guo *et al.* [4] reported that the elastic modulus in metastable β-type Ti alloys increased due to the precipitation of the ω phase, which can be substantially suppressed by micro-alloying Ti-based alloys containing (Mo, Nb, and Ta) as major β stabilizers with Zr and/or Sn. They further reported an ultra-low elastic modulus of 36 GPa of a metastable β-type Ti-33Nb-4Sn alloy produced through cold rolling and annealing treatment. This ultra-low elastic modulus was attributed to the β phase and α" phase with low content of β stabilizers retained at room temperature by high density of dislocations and grain boundaries introduced by the cold rolling and annealing treatment [4]. Figure 2-15 a) and b) show the Bright-field TEM image of solution-treated Ti-33Nb-4Sn specimen and the corresponding electron diffraction pattern, respectively.

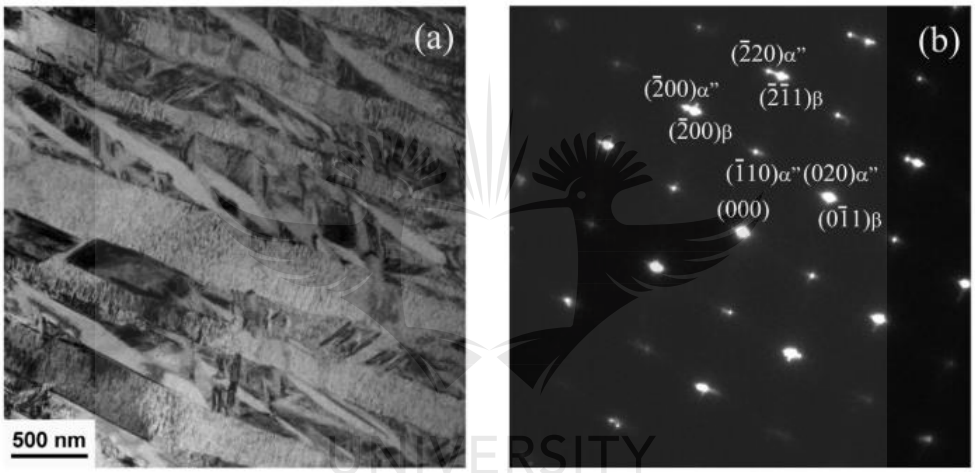

Figure 2-15. Bright-field TEM image of solution-treated (ST) Ti-33Nb-4Sn specimen (a) and the corresponding electron diffraction pattern (b). The bright-field image displays typical martensite structure.

Lin *et al.* [80] studied the microstructural evolution of Ti-Ta-Hf-Zr alloy series during casting, solution treatment and ageing. The experimental results indicated that thethe as-cast alloy consisted of β + ω phases, which transformed into a single β phase after solution treatment. The β phase further transformed into β+ α", β + α"+ α, and β + α + ω (isothermal) after ageing for 15 min, 1. 5 h, 12 h and 24 h, respectively.

Hanada *et al*. [81] investigated the effect of swageing of hot forged plus quenched Ti-33.6Nb-4Sn alloy on the microstructural evolution and the elastic modulus. Experimental observations revealed that the hot forged/ quenched specimen was comprised of predominant β phase with the elastic modulus of 56 GPa. After swageing, the α" martensitic phase was stabilized in addition to the β phase and the elastic modulus was reduced to 44 GPa. Gabriel *et al*. [82]

investigated the processing conditions (swageing + ageing treatments) on the hardness and elastic modulus of Ti-10Mo-20Nb alloy. They pointed out that the elastic modulus ranged between 100.12 -101.36 GPa, due to the precipitation of the ω phase. Moreover, microstructural features induced by thermo-mechanical treatment, such as dislocation and grain boundary, can lead to the suppression of the ω formation, which is known to increase the elastic modulus of metastable β-type Ti alloys [83].

Hagihara *et al.* [83] used a single crystal to reduce the elastic modulus, which is dependent on the orientation of crystals. Highest elastic modulus of about 80 GPa was observed along the <111> orientation and the lowest elastic modulus 35 GPa along the < 001> orientation, which is close to that of the human bone (10-30 GPa). Similar elastic modulus anisotropy was reported by Tane *et al.* [84], who revealed the elastic anisotropy of $E_{100} < E_{110} < E_{111}$ in β Ti–Nb–Ta–Zr, where E_{100}, E_{110} and E_{111} were elastic moduli in the ⟨1 0 0⟩, ⟨1 1 0⟩ and ⟨1 1 1⟩ directions, respectively.

The elastic modulus of an alloy can also be reduced by controlling the implant´s inner structure including the introduction of a porous structure. However, the use of porous implants in applications where load is applied (e.g. artificial hip joints) is still questionable regarding the reliability of their mechanical properties [85].

Wan *et al.* [86] used first-principles calculations to investigate the effect phase stability and the elastic properties of Ti-Nb and Ti-Mo binary alloys with BCC crystal structure. The β phase stability and the elastic modulus of the Ti-Mo and Ti-Nb binary alloy systems were found to increase with increasing Mo and Nb concentrations. However, no experimental study was carried out to verify the theoretical obtained findings. Cao *et al*. [87]studied the effect of Mo on phase stability and elastic modulus of Ti-Mo random alloys from *ab initio* calculations. Theoretical observations indicated that the stability of the β phase increased with increasing Mo content and the β_c for the formation of a single β phase was estimated to be about 11.2 at%. The transformation of the ω phase was realised at 4at% Mo. Furthermore, theoretical results indicated that the elastic modulus of the β phase increased with increasing Mo content, whereas the elastic moduli of both α and ω phases decrease with increasing Mo content. It was also observed that the elastic modulus of the ω phase was higher than those of β and α phases. The theoretical predictions were consistent with the experimental observations.

More metastable β-type Ti alloys containing non-toxic β-stabilizing elements with low elastic modulus developed using these approaches as alternatives to conventional orthopaedic implant materials are given in Table 2-5.

Table 2-5: Metastable β-type Ti alloys, design approaches, predicted phases, fabrication methods, experimental observations and elastic modulus.

Alloy	Design approach(es)	Predicted Phases	Fabrication method	Experimentally obtained Phases	E (GPa)
Ti-Nb-Ta-Zr [60]	d-electron	$\beta + \alpha''$	Thermo (rolling/STQ)	β	40-63
Ti-Ta-Hf-Zr [54]	d-electron, *e/a* & *Moeq*	β	casting	β	71.7 79.1
Ti−25Nb−11Sn [49]	Trial & Error	-	STQ + ageing	β	53
Ti-Nb-Zr [45]	d-electron	β + (α')	Suction casting	β + α'	38,8- 74,7
Ti–25Nb–2Mo–4Sn [88]	Trial & Error	-	STQ + ageing	β + ω	78-82
Ti-33Nb-4Sn [4]	Trial & Error	-	Thermo	β + α	36
Ti-Ta-Zr-Nb [59]	d-electron, *e/a, Moeq*	β	Cold-crucible levitation melting	β + ω	73.12 - 76.62
Ti-12Mo-5Ta [89]	Trial & error	-		β	74

- **Selection of alloying elements for designing β-type Ti alloys**

Kuroda *et al.* [73] have reported on the cytotoxicity of pure metals and the relationship between biocompatibility and polarization resistance of typical pure metals and surgical implant materials illustrated in Figure 2-16 a) and b). Vanadium, nickel, copper and cobalt exhibit high toxicity, whereas CoCr alloy, 316 L stainless steel, 304 L stainless steel, Al, etc. demonstrate tissue response of capsule (scar tissue). Elements like Ti, Nb, Ta, etc., illustrate excellent biocompatibility and belong to the loose connective vascularized (vital) category in the type of tissue reaction. Zhang *et al*. [90] reported that Mo is an effective β stabilizer in Ti alloys. Niobium is non-toxic and non-allergic and can also stabilize the β phase demonstrating low elastic modulus and great strength. Furthermore, Mo and Nb have the ability to form a homogeneous solid solution with Ti in all kinds of Ti alloys when they are added within certain content. Mo has excellent mechanical compatibility and good biocompatibility in Ti. When Zr is added to Ti individually, it acts as a weak β stabilizer, however, it exhibits strong β-stabilizing effects when added into multicomponent alloys.

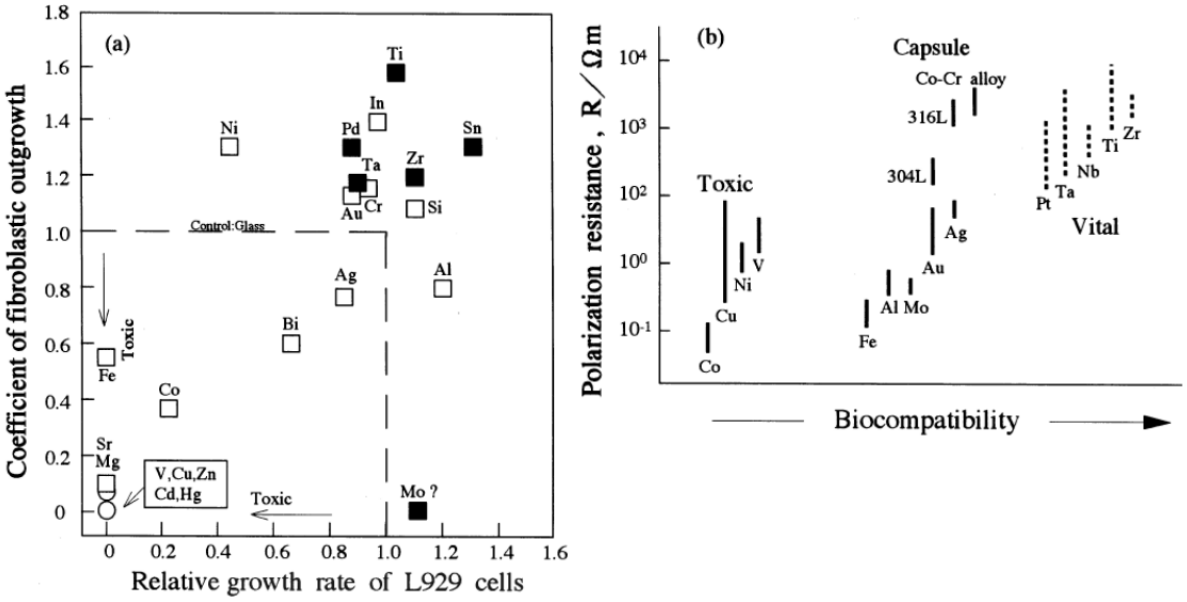

Figure 2-16: Biological safety of metals (a): cytotoxicity of pure metals, and (b): the relationship between polarization resistance and biocompatibility of pure metals, Co–Cr alloy and stainless steels [73].

Extensive efforts have been undertaken to develop non-toxic metastable β-type Ti alloys with the elastic modulus that is comparable to that of the human bone. Up to date, the lowest elastic moduli that have been reported in metastable β-type alloys are ≈36 GPa in Ti-33Nb-4Sn [4] and Ti-8Mo-4Nb-2Zr [8], and 38.8 GPa in Ti-11Nb-38Zr [45]. These values only match the maximum elastic modulus values of the human bone and the alloys have not been commercialized yet. These identified gaps have motivated for the design and development of metastable β-type Ti-Mo-based alloys with the elastic modulus that is comparable to that of the human bone.

3 Methodology

3.1 Introduction

This chapter introduces the experimental procedure followed in this study. It provides detailed information on the materials, processing techniques as well as analytical techniques used to carry out this work in this project. The first section of the experimental procedure outlines the alloy design approaches and manufacturing procedure employed, while the second section of the procedure describes the analytical and testing techniques used to characterize the samples.

3.2 Alloy Design

3.2.1 Selection of alloying elements

In this study, the selection of non-toxic β-stabilizing elements suitable for reducing the elastic modulus of Ti was based on the biological safety of metals presented in Figure 2-16 a) and b). In Figure 2-16 a), the cytotoxicity of pure metals is shown, whereas Figure 2-16 b) exhibits the relationship between polarization resistance and biocompatibility of pure metals, Co–Cr alloy and stainless steels. Nb and Zr exhibit good biocompatibility and are categorized as the loose connective vascularized (vital) group in the type of tissue reaction. Mo has been reported to be non-toxic and non-allergic that can be used as a β-stabilizing element [91]. Therefore, Mo, Nb and Zr were selected as non-toxic alloying elements for designing β- type Ti alloys with high β structural stability and low elastic modulus. Mo, Nb, and Zr have high *Bo* values, which promotes low elastic values [68]. In this study, Ti-Mo alloys are used as base alloy systems to develop multicomponent alloys upon further alloying with Nb and Zr [70].

3.3 Design Model

3.3.1 Ti-Mo binary alloys

The Ti-Mo binary alloys were designed following the trial-and-error method. The stability of the β phase was predicted using the molybdenum equivalence, e/a ratio and d-electron theory approaches.

- **Molybdenum equivalence**

The molybdenum equivalence, which quantifies the stability contribution of each alloying element in comparison to that of the major β-Ti stabilizer (Mo), was calculated using the molybdenum formula proposed by Bania [28]. As listed in Table 3-1, the *Moeq* value of the

Ti-8Mo binary alloy is 8 wt%, which indicate that the alloy would precipitate the martensitic phase(s). The Mo equivalence of Ti-10Mo is 10 wt%, which is the same as the critical limit for the retention of 100% β phase. Ti-15Mo binary alloy would also form a single β phase because its Mo equivalence is a critical limit. This suggests that all the designed alloys will form the metastable β phase and the precipitation of martensitic and/ or the ω phase will be suppressed upon rapid cooling.

- **Average electron concentration (e/a) ratio**

In this study, the e/a ratio of the Ti-Mo binary alloys are displayed in Table 3-1. Ti-8Mo and Ti-10Mo binary alloys wit e/a ratio of 4.16 and 4.20 would precipitate the martensitic α" in addition to the β phase. Ti-15Mo binary alloy would form a single β phase [60] or precipitate the ω phase in addition to the β phase [65]. All the values are greater than the critical e/a ratio (4.20), thus categorizing the alloys as β-type Ti alloys.

- **D-electron method**

The d-electron molecular orbital theory exploits the relationship between the phase stability and elastic properties of Ti alloys by theoretically determining the two alloying parameters, the bond order (*Bo*) and the metal d-orbital energy level (*Md*). The $\overline{Bo}$ and $\overline{Md}$ values are given in Table 3-1. The Bo-Md phase stability map in Figure 3-1 shows the location of the binary alloys. The Bo-Md phase stability map predicts that Ti-8Mo alloy would form β+ω +α" phases. At 10 wt%Mo, the precipitation of the martensitic α" phase would be suppressed and the alloy will only consist of β+ω phases. When the Mo content increases to 15 wt%, the precipitation of the secondary ω phase would also be suppressed and the β phase would be predominant.

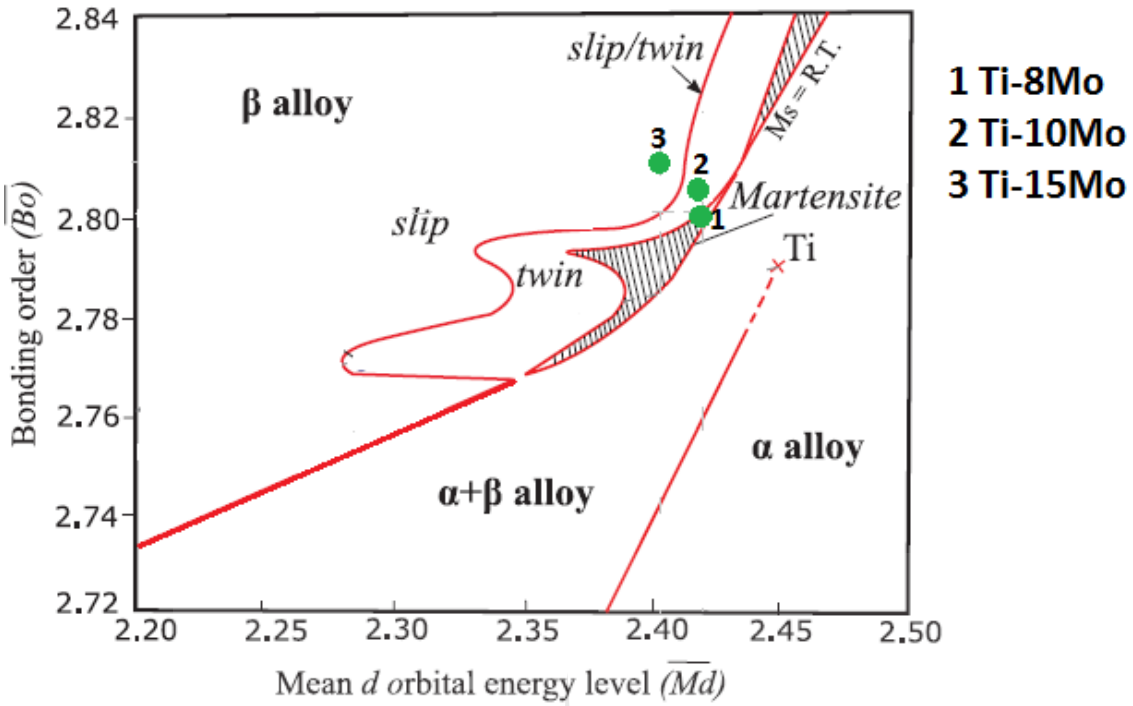

Figure 3-1: Bo-Md phase stability map [92]

Table 3-1. *Moeq*, e/a ratio and $\overline{Bo}$ and $\overline{Md}$ values of the Ti-Mo binary alloys

Alloy	***Moeq*$_{\text{Bania}}$ (wt.%)**	***e/a* ratio**	**$\overline{\text{Bo}}$**	**$\overline{\text{Md}}$**
Ti-8Mo	8	4.16	2.426	2.802
Ti-10Mo	10	4.20	2.421	2.804
Ti-15Mo	15	4.30	2.408	2.812

3.3.2 Ti-Mo-Nb(-Zr) multicomponent alloy system

- *Cluster-plus-glue-atom model*

The cluster-plus-glue-atom model was used to formulate the alloy compositions. The cluster model for the BCC structure used for the formulation of the alloy compositions was the rhombic dodecahedron with coordination number 14 (CN14) exhibited in Figure 3-2. Mo, Nb and Zr alloying elements were assigned in the cluster formula [(centre atom)-(shell atoms)$_{14}$](glue atoms)$_x$ according to their enthalpies of mixing with Ti. The square brackets of the cluster formula consist of the eight red solvent atoms in the 1st nearest-neighbour shell and the six solvent atoms in the 2nd six blue nearest-neighbours centreed by a solute atom in the BCC structure. The glue atoms (green) are located only at the twelve next outer shell. Although

Mo is a β-Ti stabilizer, it has a high elastic modulus, whereas Nb is a fairly good β stabilizer with low elastic modulus. Zr is a weak β stabilizer and possesses low elastic modulus. The combination of these different elements is simultaneously expected to reduce the elastic modulus and enhance the β stability of β-Ti alloys.

Since Mo has a negative enthalpy with Ti ($\Delta H_{Ti\text{-}Mo}$= -4 kJ/mol), it occupies preferentially the cluster centre, while Nb with a positive enthalpy of mixing with Ti ($\Delta H_{Ti\text{-}Nb}$= 2 kJ/mol) is assigned to the glue site. Zr and Ti can be placed in any site due to their $\Delta H_{Ti\text{-}Zr}$ and $\Delta H_{Ti\text{-}Ti}$ of 0 kJ/mol. Therefore, the common cluster formula for this study was expressed as $[(Mo)(Ti_{14-x}Zr_x)]Ti_yNb_z$ (x=0-1, y=0-1, and z= 0-3). A Ti-Mo binary alloy cluster formula was expressed by fixing $[(Mo)(Ti_{14},Zr_0)]$ and placing one Ti atom in the glue site. Ternary alloys were designed by fixing the $[Mo(Ti_{14},Zr_0)_{14}]$ and replacing the Ti in the glue site with Nb atom(s) with atom variations of 1 to 3. The quaternary alloy was designed by substituting one Ti atom in the shell cluster with one Zr atom. Ti was placed in the shell cluster and in the glue site, while Zr substituted one Ti atom in the shell cluster. The cluster formula and the designed compositions in wt% are shown in Table 3-2.

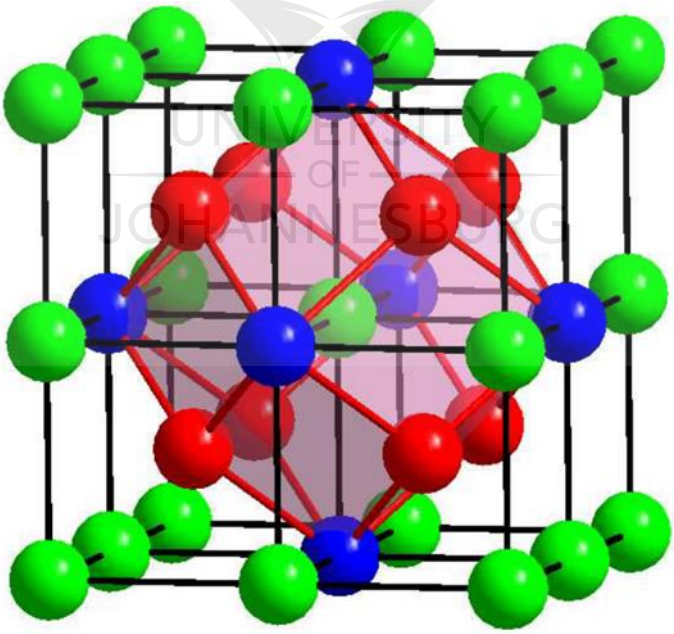

Figure 3-2. CN14 rhombic dodecahedron as the cluster in BCC structure [70].

Table 3-2. Cluster formula, composition, *Moeq* and e/a ratio values of the designed alloys.

Cluster Formula	**Alloy Composition (wt%)**	***Moeq*$_{Qing}$**	**e/a ratio**
$[Mo(Ti_{14})]Ti_1$	Ti-11.78Mo	11.78	4.24
$[Mo(Ti_{14})]\ Nb_1$	Ti-11.1Mo-10.8Nb	13.65	4.37
$[Mo(Ti_{14})]Nb_2$	Ti-10.2Mo-19.5Nb	14.57	4.40
$[Mo(Ti_{14})]Nb_3$	Ti-9.2Mo-26.7Nb	15.32	4.45
$[Mo(Ti_{13}Zr_1)]Nb_1$	Ti-10.6Mo-10.3Nb-10.1Zr	16.43	4.32

- **Molybdenum equivalence approach**

The molybdenum equivalence, which quantifies the stability contribution of each alloying element (Nb or Zr) in comparison to that of the major β-Ti stabilizer (Mo), of the designed alloys was calculated using the formula proposed by Qing discussed in details in section 2.3.4.2, page 19 [93]. Qing's formula was employed over Bania's formula because it is empirically based on binary alloys and there are no reports on their mechanism. Therefore, the characterization of metastable β-type Ti alloys with low β stabilities using the molybdenum equivalence has been a challenge as a result of the complex interactions between multi-elements.

According to this Wang *et al*. [93], a multicomponent alloy requires a Mo equivalence of 11.78 or more to stabilize the β phase. As listed in Table 3-2, the *Moeq* value of the binary alloy is 11.78 wt%, which is the same as the critical limit for the β-Ti formation, while the other alloys have values that are above the critical limit. This suggests that all the designed alloys will form the metastable β phase and the precipitation of martensitic and/ or the ω phase will be suppressed upon rapid cooling.

- **e/a Ratio**

The e/a ratio values of the designed alloys are displayed in Table 3-2. All the values are greater than the critical e/a ratio (4.20), thus categorizing the alloys as β-type Ti alloys.

- **Bo-Md Diagram**

The Bo-Md phase stability map in Table 3-3. Figure 3-3 shows the location of the designed alloys. The β stability in these alloys increased in the order TMT→ TMN1→ TMN2→ TMN3. TMNZ alloy was located in the martensitic phase region.

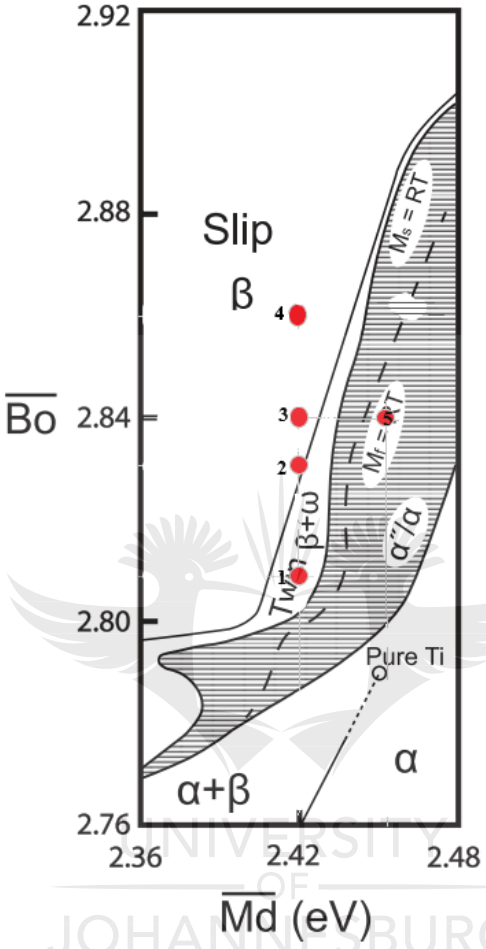

Figure 3-3: Bo-Md phase stability map [94].

Table 3-3: Bo and Md values and the predicted phases of the designed alloys

Cluster Formula	Alloy Composition (wt.%)	$\overline{Bo}$	$\overline{Md}$	Predicted Phase(s)
$[Mo(Ti_{14})]Ti_1$	Ti-11.78Mo	2.81	2.42	β/ ω
$[Mo(Ti_{14})]$ Nb_1	Ti-11.1Mo-10.8Nb	2.83	2.42	β
$[Mo(Ti_{14})]Nb_2$	Ti-10.2Mo-19.5Nb	2.84	2.42	β
$[Mo(Ti_{14})]Nb_3$	Ti-9.2Mo-26.7Nb	2.86	2.42	β

$[Mo(Ti_{13}Zr_1)]Nb_1$	Ti-10.6Mo-10.3Nb-10.1Zr	2.84	2.45	α''

3.4 Starting Materials

In this study, the starting materials were spherical Ti powder, purity of 99.9% and average particle size of 45µm supplied by CSIR, Mo powder with an irregular morphology, purity of 99.5% and average grain size of 100µm provided by Alfa Aesar, Nb powder with irregular morphology, purity of 99.8% and average grain size of 100µm provided by Alfa Aesar and Zr powder with irregular morphology, purity of 99.9% and average grain size of 2 -3 µm from Alfa Aesar. Safety precautions were considered as indicated on the datasheets from suppliers due to the flammable nature of the particles.

The morphology of the powder particles Ti, Mo, Nb and Zr was characterized using a scanning electron microscope (SEM, JEOL: JSM-6510) exhibited in Figure 3-4 a) and the images are presented in Figure 3-5 (a), (b), (c) and (d), respectively. The particle size was analyzed using the particle size analyzer (Microtrac S3500) shown in Figure 3-4 b) and the results are given in Table 3-4.

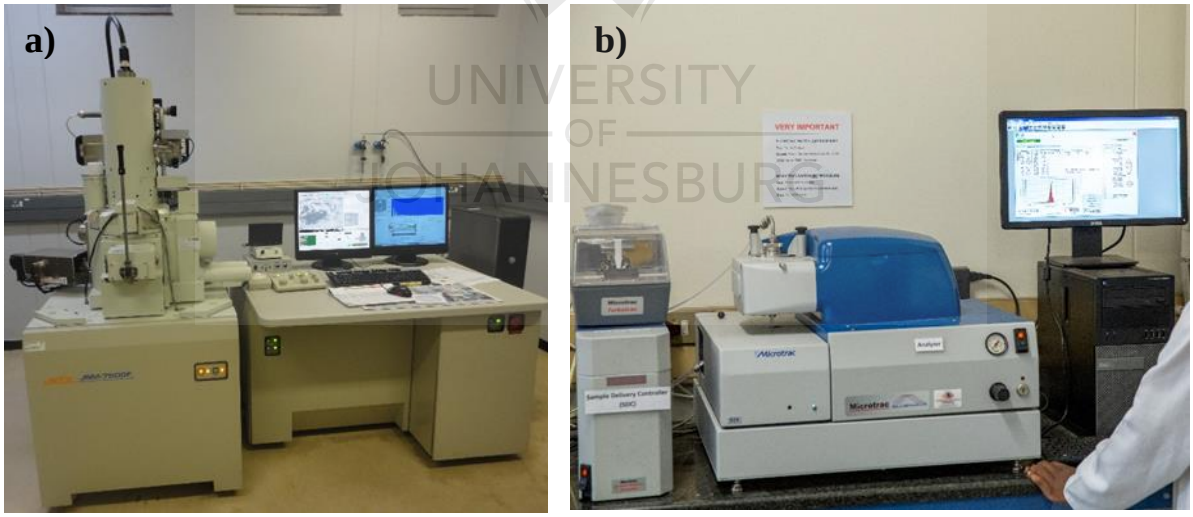

Figure 3-4: a) Scanning electron microscopy and b) particle size distribution analytical apparatus

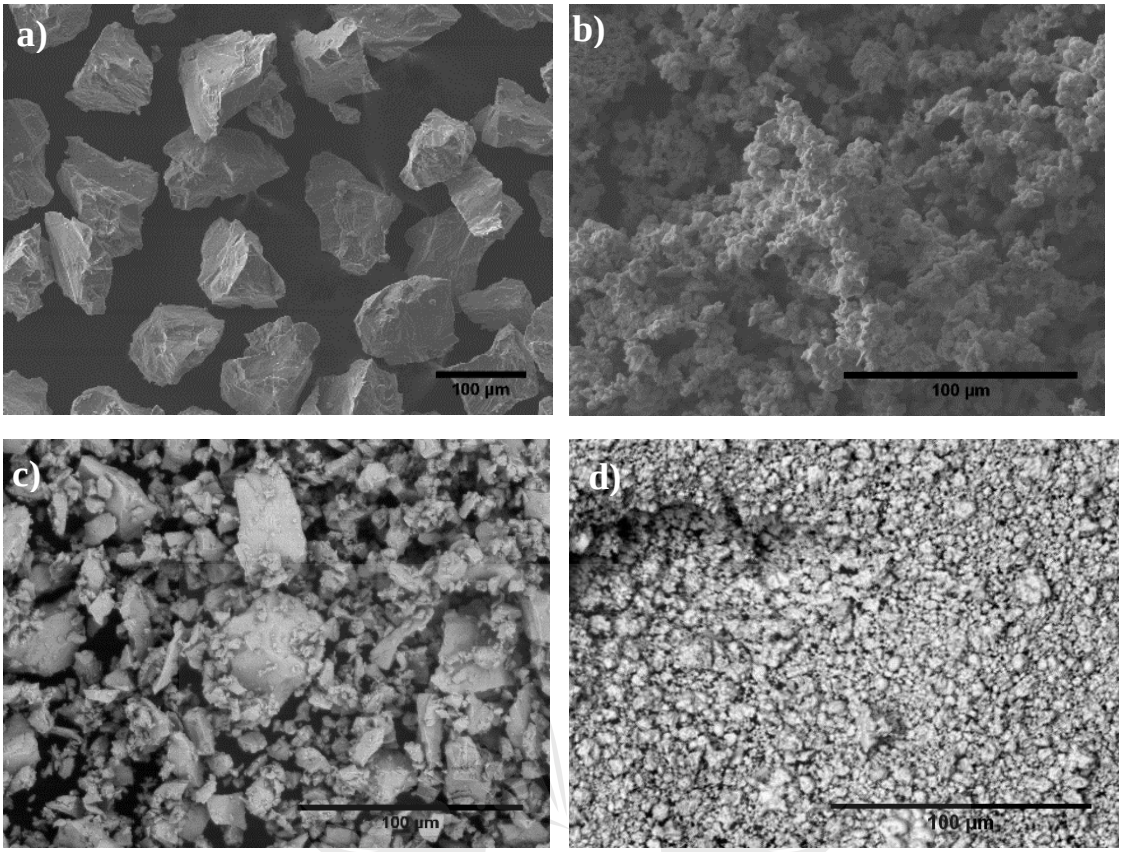

Figure 3-5: SEM micrographs of as-received powders (a) CP Ti. (b) Mo, (c) Nb and (d) Zr.

Table 3-4: Particle sizes of the starting materials.

Diameters (µm)	d_{10}	d_{50}	d_{90}
Ti	15.18	28.07	45.76
Mo	6.34	16.84	50.11
Nb	6.05	18.61	50.37

3.5 Fabrication of Specimen

3.5.1 Casting

The Ti-based alloys of 100 g each were prepared from elemental powders of CP Ti (99.9%), molybdenum (99.5%) and niobium (99.8%). The starting powders were hand-mixed and subsequently compacted into a button-shaped green compact at 250 bar in a die with the diameter of 45mm with a cold uniaxial compacting machine. The green bodies were subsequently melted in a water-cooled copper crucible with a tungsten electrode using a commercial arc melting vacuum-pressure casting system. Melting was conducted in an argon atmosphere using Ti getters to minimise oxidation. The evacuation and purging of the melting chamber with argon was carried out before melting. The ingots were each turned over and

remelted three-times to promote chemical homogeneity. Figure 3-6 illustrates the arc melting furnace, which exhibits the ingot in the form of a button. This casting method is similar to water quenching because it cools the alloy rapidly and is conducive to obtaining a single β phase in the alloy [45].

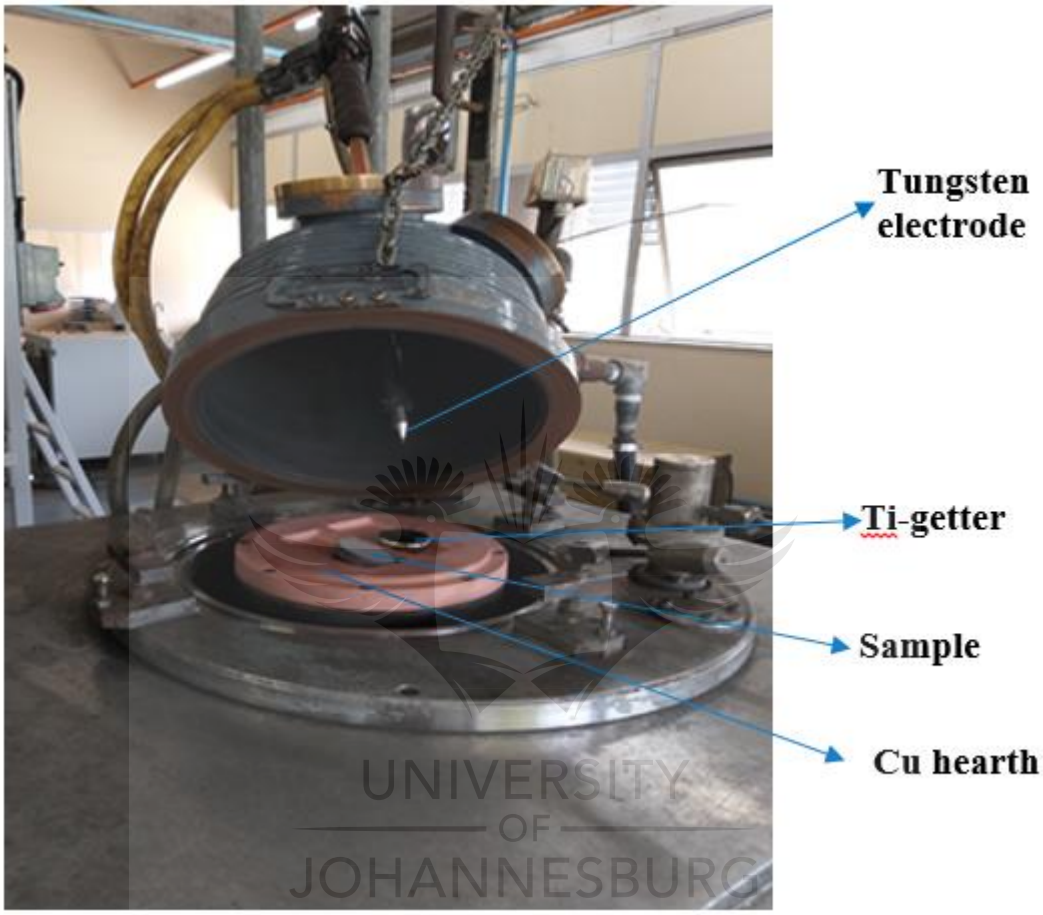

Figure 3-6: Arc remelting furnace.

3.5.2 Solution Treatment followed by Quenching

The alloys ingots were solution treated at temperatures shown in Table 3-5. The β-transus was calculated using the following formula [80]:

$$T_\beta = 10^2(40.65 - 1.052\overline{M_d} - 9.79\overline{B_o} - 273) \quad \text{Equation (5)}$$

Table 3-5: Solution Treatment Temperature

Cluster Formula	Alloy Composition (wt%)	β-transus °C	Solution treatment temperature (°C)
Binary 1	Ti-8Mo	794	894
Binary 2	Ti-10Mo	791	891
Binary 3	Ti-15Mo	786	886
$[Mo(Ti_{14})]Ti_1$	Ti-11.78Mo	790	890
$[Mo(Ti_{14})]\ Nb_1$	Ti-11.1Mo-10.8Nb	770	870
$[Mo(Ti_{14})]Nb_2$	Ti-10.2Mo-19.5Nb	755	855
$[Mo(Ti_{14})]Nb_3$	Ti-9.2Mo-26.7Nb	741	841
$[Mo(Ti_{13}Zr_1)]Nb_1$	Ti-10.6Mo-10.3Nb-10.1Zr	750	850

Solution treatment was carried out in a muffle furnace for 1 hr at a heating rate of 20 °C/min under no controlled atmosphere. To minimise oxidation, Ti getters were used during solution treatment. The solution treated specimen were then quenched in ice water as shown in the schematic diagram in Figure 3-7.

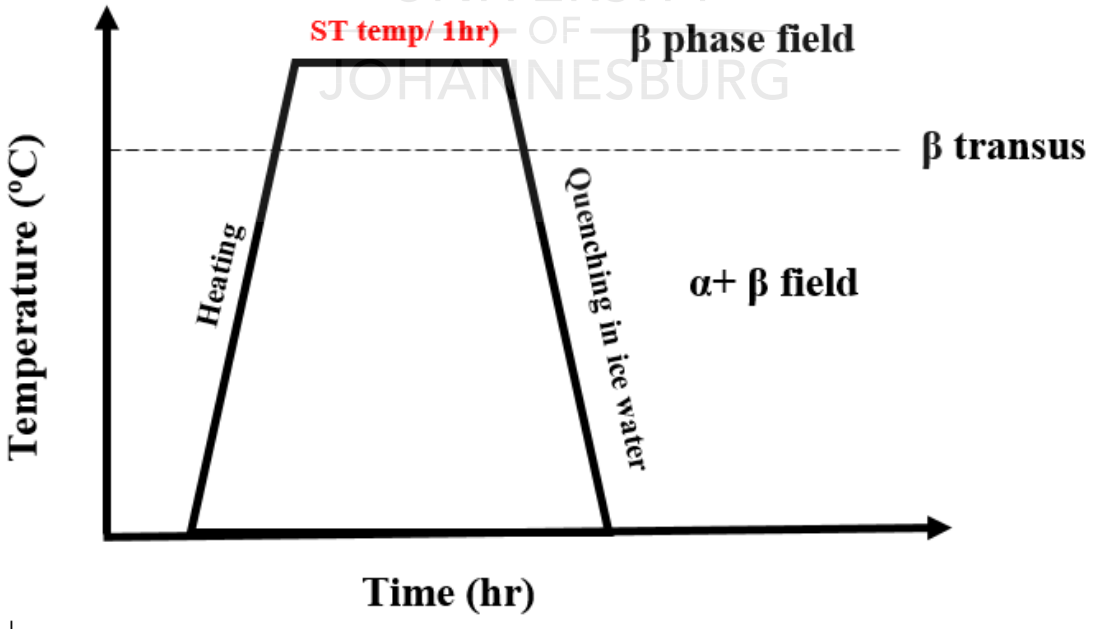

Figure 3-7: Schematic diagram displaying the solution treatment procedure.

3.6 Microstructural Characterization methods

3.6.1 Preparation of specimen

For microstructural analysis, samples were sectioned from the vacuum arc-meltthe as-cast ingots using a Precision cut-off cutting machine (Brilliant 250x and 221x) to obtain specimens for various purposes followed by mounting conductive phenolic hot mounting resin using a Beuhler apparatus 1000 mounting machine. The samples were ground on silicon carbide papers of 800, 1000, 12000 and 2400 mesh at a speed of 150 rpm, load of 15N for 4 minutes. Grinding of the specimen was followed by polishing using 3 μm diamond suspension and colloidal silica (final polishing) at the speed of 300 rpm, force of 20N for 2 minutes. Etching of the polished specimens was carried out in Kroll's reagent with the compositions 85 ml of distilled water, 15 ml of Nitric acid and 5 ml of hydrofluoric acid.

For EBSD analysis, specimens were electro-polished in perchloric acid from Struers using a Struers polishing machine (LectroPol-5) at 30 voltage for 80 seconds after the final polishing step. Figure 3-8 a) shows the electropolishing apparatus used in this study.

Figure 3-8. a) Electropolishing apparatus and b) optical microscope.

3.6.2 Optical Microscopy

An optical microscope (Leica CTR4000) exhibited in Figure 3-8 b) was used to observe the microstructural constituents of the designed alloy specimens.

3.6.3 X-ray diffraction

Phase determination of the ST and CT alloys was conducted using a PANalytical X'Pert Pro powder x-ray diffractometer (XRD 6000, Shimadzu, Japan)exhibited in Figure 3-9 with Fe filtered Co K_α radiation (λ= 1.789Å and graphite monochromator operating at an accelerating voltage of 40 kV and a current of 40 mA. The various Ti phases were identified by matching

the observed XRD profile peaks with the Joint Committee on Powder Diffraction Standards files or in prior published work. XRD patterns were recorded at 2θ ranging between 30° and 80°, a step size of 0.02° and a scan speed of 4°/ min.

Figure 3-9: XRD equipment.

3.6.4 Scanning electron microscopy

A scanning Electron Microscope employs a focussed beam of electrons to obtain topographical, morphological and compositional information. The analysis is based on the detection of the characteristic X-rays produced by the electron beam-specimen interaction. The information can be collected in very specific local points or on the whole sample.

In this study, a Scanning electron microscope (SEM) (JEOL: JSM-6510) equipped with Energy Dispersive Spectroscopy. Energy-Dispersive X-ray spectroscopy (EDXS) is the technique that allows obtaining information concerning the elemental chemical composition using the EDX spectrometer.

3.6.5 Electron Back-Scatter Diffraction (EBSD)

Electron Backscatter Diffraction (EBSD) is a technique that analyses the Kikuchi pattern by the excitation of the electron beam on the surface of the sample. It can provide detailed information on the crystal structure, orientation, and correlative information. Its advantage over

the conventional analytical techniques is its ability to determine the crystal orientation and microstructure, i.e. it can observe the grain boundary types (high angle and low angle grain boundaries), disorientations and their distribution. It can also perform statistical measurement and quantitative analysis. EBSD analysis was carried out using Oxford integrated Aztec HKL advanced EBSD system exhibited in Figure 3-10. EBSD scans were performed using a field emission gun Zeiss Sigma scanning electron microscope operating at 15 kV with a step size ranging from 0.5 to 0.05 mm.

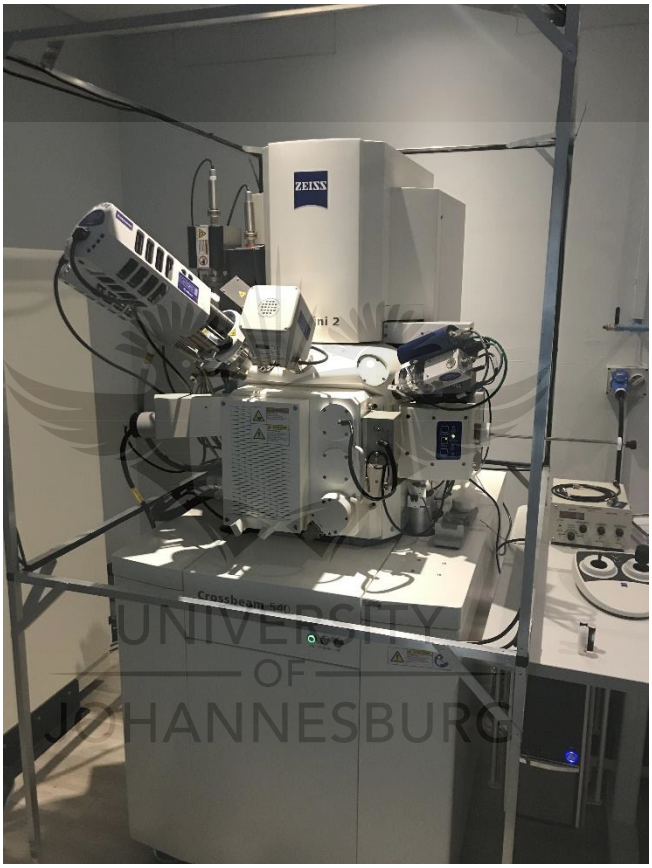

Figure 3-10: EBSD equipment

3.7 Mechanical testing

3.7.1 Micro-Vickers Hardness Testing

Vickers micro-hardness measurements were conducted on the test specimens using Vickers micro-hardness tester (FM-700, micro-indenter with a square base pyramid tip) with a load of 500 g over a 15 s dwell exhibited in Figure 3-11. For each specimen, ten separate areas were

indented across the sample surface. The indents were separated by at least five times the diagonal to prevent one indent from affecting the neighbouring indent.

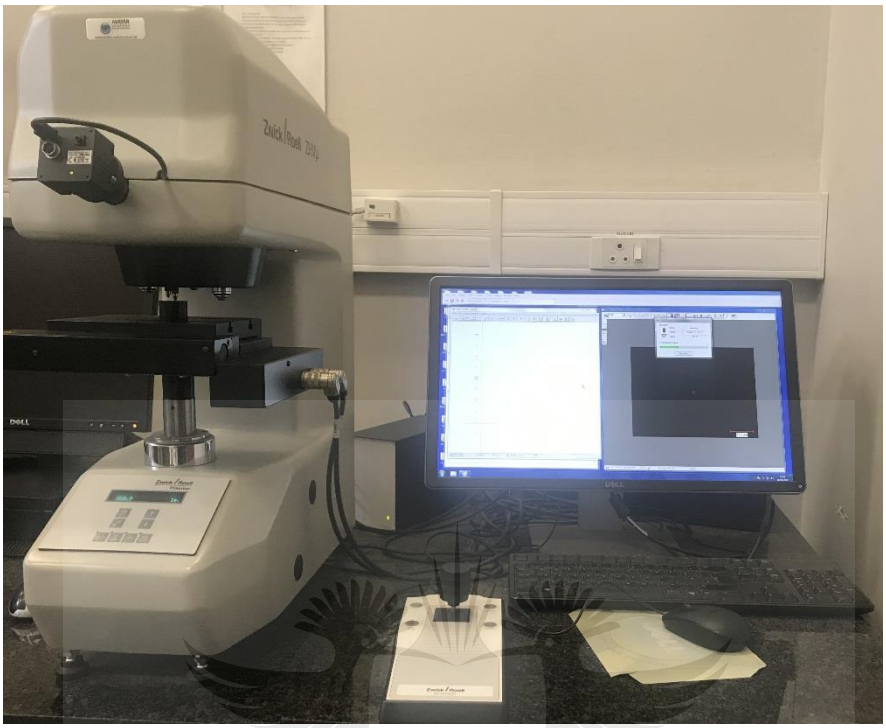

Figure 3-11: Vickers microhardness tester

3.7.2 Tensile Testing

Figure 3-12 exhibits the tensile test specimen with a schematic drawing of the tensile test specimen with the dimensions. Uniaxial tensile tests were performed on the specimen prepared from the vacuum arc-melt as-cast ingots and the solution treated specimens via electrical discharge machining (EDM) using Instron test machine (TM 1342, Freiberg, Germany) shown in Figure 3-13 at room temperature. At least three samples of each alloy were measured, and the average was calculated. Young's modulus, yield strength and ultimate tensile strength were determined from the stress-strain curves. An extensometer was used for accurate strain measurement; however, it was removed just after the yield strength was measured to avoid breakage of the device.

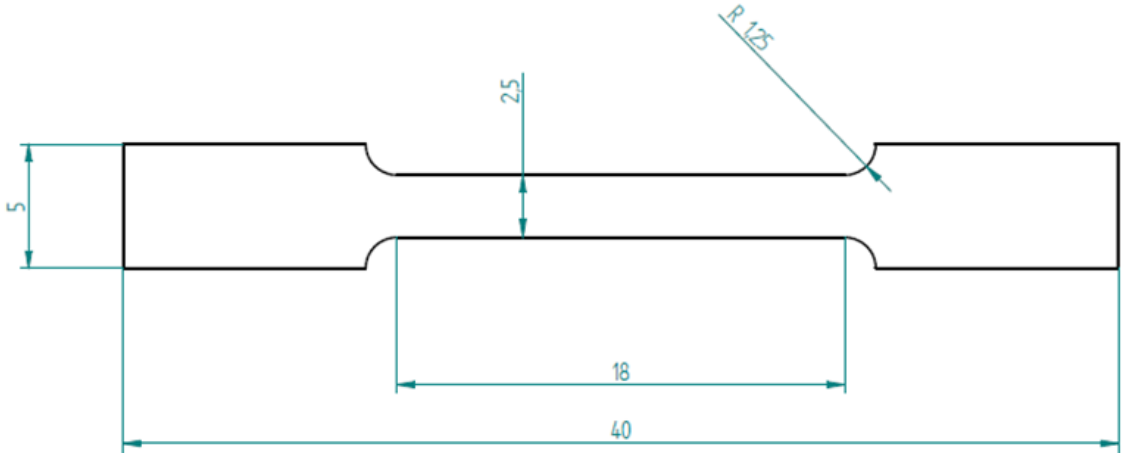

Figure 3-12. Schematic dimensions of the tensile specimen.

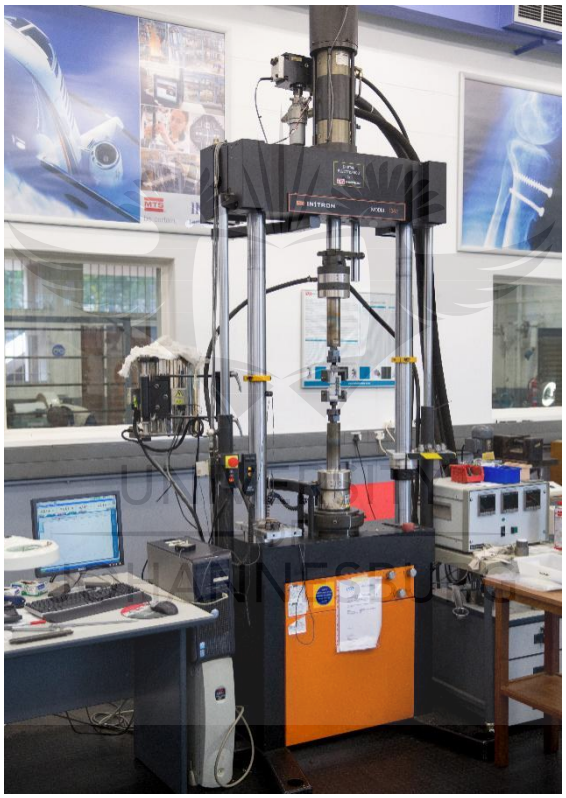

Figure 3-13: Instron™ 1342 model apparatus

3.7.3 Compression Testing

Compression tests were also performed on rectangular specimens with the dimensions 4 mm x 4 mm x 8 mm. The tests were implemented by the uniaxial test machine (Instron TM 1342) shown Figure 3-13 at room temperature. The machine was equipped with a 100 kN load cell and strain rate was 0.50000 mm/min.

3.7.4 Bending Testing

Three-point bending tests were carried out at room temperature using the Instron™ 1342 model apparatus shown in Figure 3-13. The determination of the bending strength was performed using the following equation:

$$\sigma = \frac{3PL}{2bh^2} \qquad \text{Equation 6}$$

Where σ is the bending strength (MPa), P is the load (N), L is the span length (mm), b is the specimen width (mm), and h is the specimen thickness (mm). The dimensions of the specimens were l = 30 mm, b = 4 mm and h = 3 mm. The bending modulus was calculated from the load increment and the corresponding deflection increment between the two points on the straight line as far apart as possible using the following equation:

$$E = \frac{L^3 \Delta P}{4bh^3 \Delta} \qquad \text{Equation 7}$$

where E is the bending modulus of elasticity (GPa), ΔP is the load increment as measured from preload (N) and $\Delta\delta$ is the deflection increment at mid-span as measured from preload. The average bending strength and modulus of elasticity were calculated from three test specimens.

4 Results and discussion

Introduction

This chapter compiles the microstructural and mechanical test results obtained in this study on the designed Ti-Mo-Nb-Zr alloy series.

4.1 Structure and Properties of the Binary Alloys

Emphasis of the research study on the as-cast (designated as AC henceforth) and solution treated (designated as ST henceforth) Ti-Mo binary alloy series was on the evaluation of the correlation between Mo content in Ti-Mo alloys, the microstructural evolution and the mechanical properties of the Ti-Mo alloys. This study was carried out to generate useful experimental data for designing and developing new metastable β-type Ti-Mo based alloys with low elastic modulus for orthopaedic applications. It should be noted that the binary alloys were designed using the conventional method.

4.1.1 Phase analysis of AC and ST Ti-Mo binary alloys

The X-ray diffraction patterns of the AC Ti-Mo binary alloys are presented in Figure 4-1. The XRD pattern of AC Ti-8Mo alloy specimen was composed of the primary BCC β phase peaks, the orthorhombic α" martensitic phase peaks and an ω phase peak, which was detected at 2θ≈34°. When the Mo content was increased to 10 wt%, the proportion of orthorhombic α" martensitic phase was reduced while the β phase stability was significantly enhanced. The existence of the orthorhombic α" martensitic phase in AC Ti-8Mo and Ti-10Mo alloy specimens is confirmed by the splitting of the XRD peaks, and has also been observed in the experimental findings of Oliveira *et al.* and Almeida *et al.* [1,95]. With further increase in Mo to 15 wt%, the precipitation of α" in the alloy was significantly retarded while the β phase stability was further enhanced. The ω phase peak disappeared. The increase in β phase stability in Ti-10Mo and Ti-15Mo alloy specimens is indicated by their strong intensities of the β phase peaks at 2θ≈45° in comparison with the Ti-8Mo alloy specimen. These observations indicate the dependence of phase transformation on the Mo content, as shown by the diffractograms.

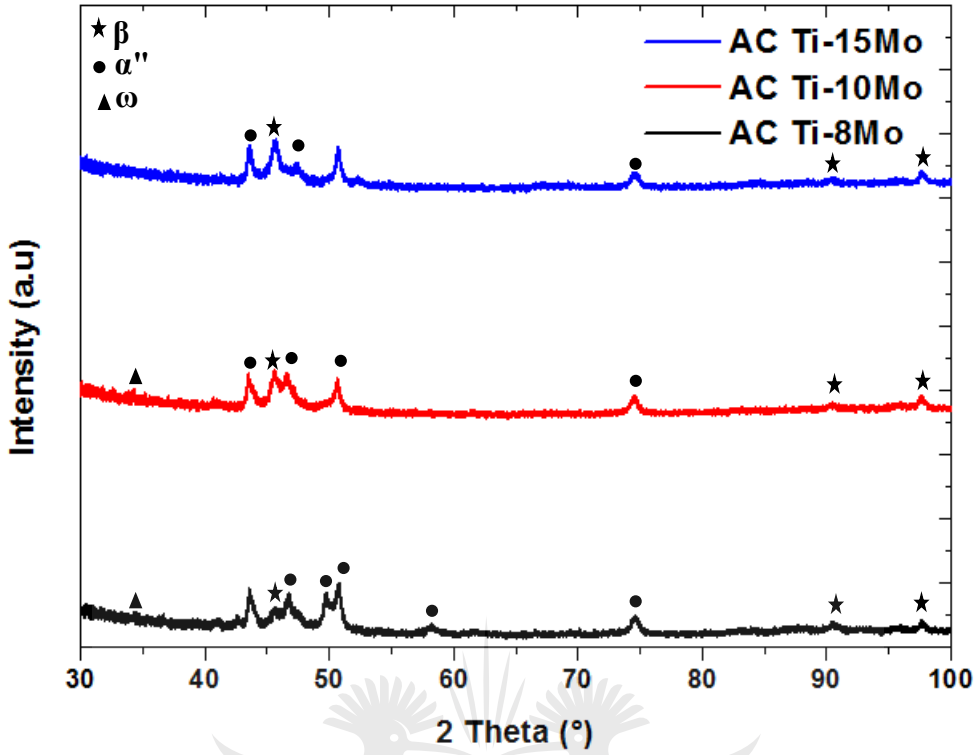

Figure 4-1: XRD patterns of the AC Ti-Mo binary alloys.

Figure 4-2 presents the X-ray diffraction profiles of the Ti-Mo alloys subjected to solution treatment and subsequently quenched in ice water. The XRD pattern of the ST Ti-8Mo alloy exhibited primary BCC β peaks and orthorhombic α" martensitic phase. When the Mo concentration was increased to 10 wt%, the intensities of the β phase peaks were slightly increased, suggesting an increased β phase stability. A small ω phase peak could also be distinguished. When the Mo content was increased to 15 wt%, the XRD could detect the primary β phase peaks, a single ω and α" phase peaks. It is evident that the intensity of the β phase peak at 2θ≈45° was significantly increased, indicating an increase in the β phase stability, whereas the intensity of the ω phase was slightly reduced compared to that of ST Ti-10Mo alloy.

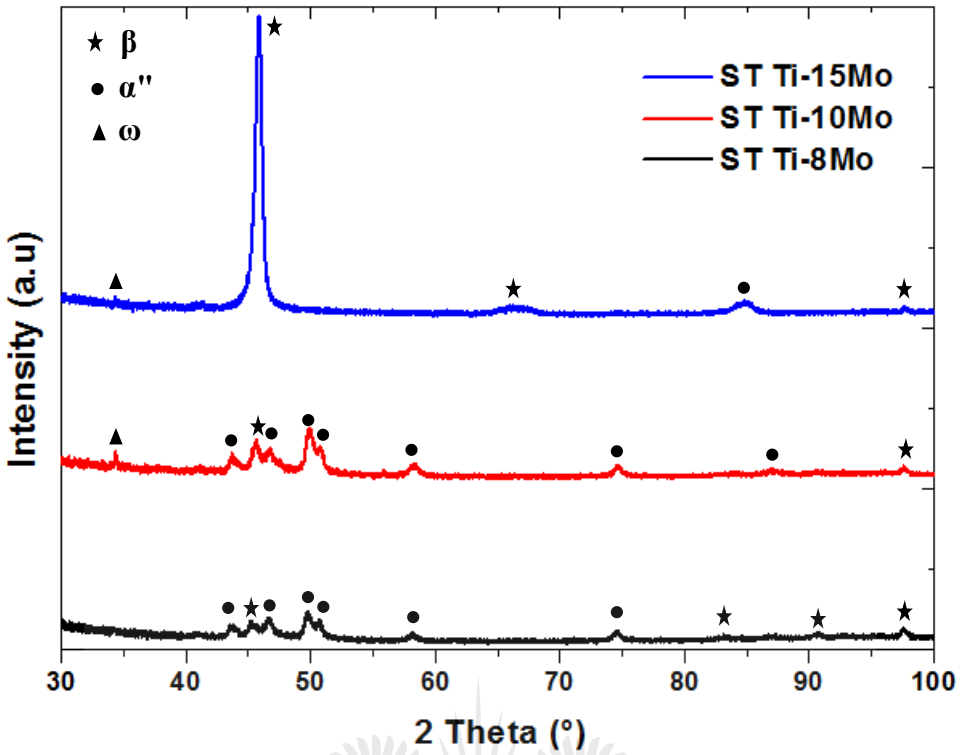

Figure 4-2. XRD patterns of the ST Ti-Mo binary alloys.

The precipitation of the orthorhombic α" martensitic phase is sensitive to the composition and cooling rate from the β phase-field. The martensite start temperature and finish temperatures depend on the composition of an alloy, and they both decrease with increasing concentration of the solute (β-stabilizing elements) [40]. When the Mo content increases, both the martensite transformation start temperature and the critical cooling rate decrease [96]. When the martensite start temperature is above room temperature and the martensite finish temperature is below room temperature, the β phase is partly transformed. When the martensite start transformation temperature is below room temperature, the martensite transformation is completely suppressed and the high-temperature β phase is fully retained upon rapid cooling [40].

In this study, the XRD results also exhibited the increase in the stability of the β phase with increasing Mo concentration, whereas the volume fraction of the orthorhombic α" martensitic phase decreased with increasing Mo content in the alloys. The incomplete retention of the β phase in all the AC Ti-Mo alloys, the ST Ti-8Mo and the ST Ti-10Mo alloys upon cooling indicated that the martensite start transformation temperature of the alloys was slightly higher

than room temperature, while the martensite transformation finish temperature fell below room temperature. The retention of 100% β phase (no traces of the orthorhombic α" martensitic phase) in the ST Ti-15Mo alloy at room temperature is in agreement with the observations of Ho *et al.* [97], Oliveira *et al.* [95] and Davis *et.al* [96]. At this composition, the martensite start transformation temperature was below room temperature, and the precipitation of the α" martensitic phase was suppressed [38]. It is clear that the crystal structure of the as-cast binary alloys is dependent on the Mo composition of the alloys.

Bania reported that a binary Ti-Mo alloy requires a Mo content of 10 wt% or more to fully stabilize the β phase upon rapid cooling to room temperature [28]. In a study conducted by Davies *et al.*, no β phase could be detected in ST Ti-8Mo alloy [96]. For Ti-10Mo alloy, the β phase became the dominant constituent as reported by Bania and Almeida *et al.* [1]. Contrarily, Cardoso *et al*. observed the precipitation of the athermal ω phase and the orthorhombic α" martensitic phase in the β matrix of Ti-10Mo alloy specimen [36]. Zhao *et al.* observed the athermal ω phase in the solution treated Ti-15Mo and also found its quantity in the Ti-Mo alloys to be dependent on the stability of the β phase [79]. They further reported that the precipitation of the ω phase at Mo content higher than 15 wt% was significantly reduced due to the increased β phase stability in the alloys.

Figure 4-3 gives a comparison of the XRD diffractograms of the AC and ST binary alloy. It can be seen that all the binary alloys precipitated the secondary martensitic α" and ω phases in the β matrix in both AC and ST conditions. The XRD patterns of Ti-8Mo alloy in Figure 4-3 a) show no considerable difference in the peaks of the detected phases. In Figure 4-3 b), the intensity ω phase peak in the ST XRD pattern is stronger than in the AC pattern, suggesting that more ω phase was precipitated during ST than during AC. It is worth noting that the intensity of the ω phase peak was slightly stronger after solution treatment. The XRD pattern of the AC Ti-15Mo alloy in Figure 4-3 c) exhibits BCC β and the martensitic α" phase peaks. Solution treatment resulted in the appearance of a single ω phase peak and the disappearance of some the martensitic α" phase peaks. Additionally, the ω phase peak was also evident in the XRD pattern of the ST alloy, while the β phase peak was substantially increased.

Generally, more ω phase was precipitated during ST, whereas the peaks corresponding to the martensitic α" phase and the β phase were slightly changed (with the exception of the Ti-15Mo alloy).

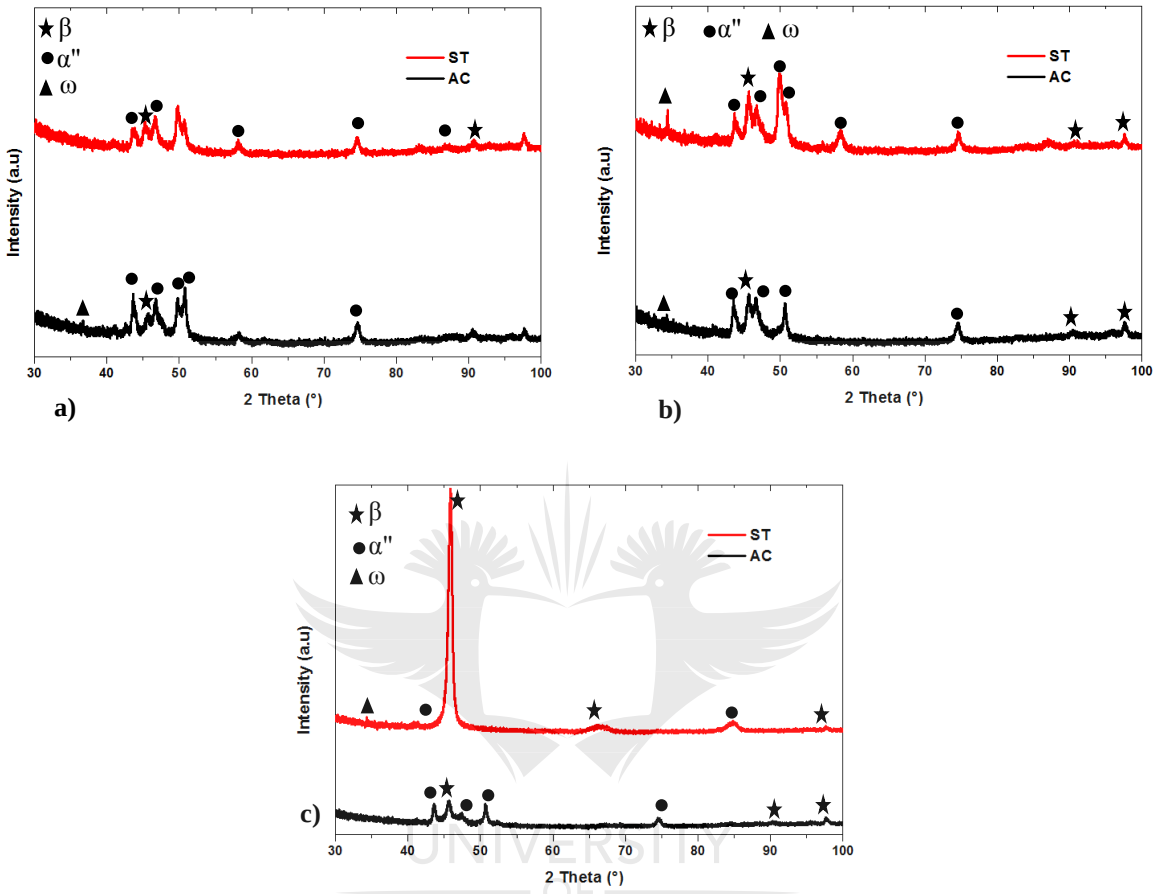

Figure 4-3: Comparison of the XRD patterns of AC and ST a) Ti-8Mo, b) Ti-10Mo and c) Ti-15Mo binary alloys.

The effect of Mo on the formation of phase constituents/ crystal structure of the as-cast and solution treated Ti-Mo alloy specimens was investigated. The OM, SEM and EBSD were used to characterize the microstructures of the alloys and the results will follow.

4.1.2 Optical Microscopy analysis

The microstructural evolution in the AC Ti-Mo binary alloys with varying Mo contents is depicted in Figure 4-4. The microstructures of the investigated AC Ti-Mo alloy specimens exhibited large equiaxed BCC β grains and visible grain boundaries, which appeared first during etching. However, as the degree of etching increased, sub-grain structures throughout the primary grains were observed. Dendritic structures from cooling are minimal and no

precipitation of the martensitic α" and/or the ω phase was evident. Fine black marks distributed across the grains could be seen, which were attributed to etch pits. Pores were also visible in the microstructures throughout the material, typically coinciding with grain boundaries, which were attributed primarily to dissolved gases in the melt. It can be clearly seen that the degree of the sub-grain structures decreases with increasing Mo content. The development of sub-grain structures could be attributed to chemical inhomogeneity, i.e. segregation of the β stabilizers which occurred during casting due to differences in melting point. However, it should be noted that the sub-grain structures observed in the optical micrographs of these alloys were not present in Ti-15Mo binary alloy. Thus, the sub-grain structures could be the orthorhombic α" martensite phase features. The phase constituent (single β phase) detected by the XRD in AC Ti-15Mo alloy specimen was in good agreement with the OM results. The retention of the β phase with an equiaxed morphology in AC Ti-15Mo alloy specimen was consistent with the results of Ho [98].

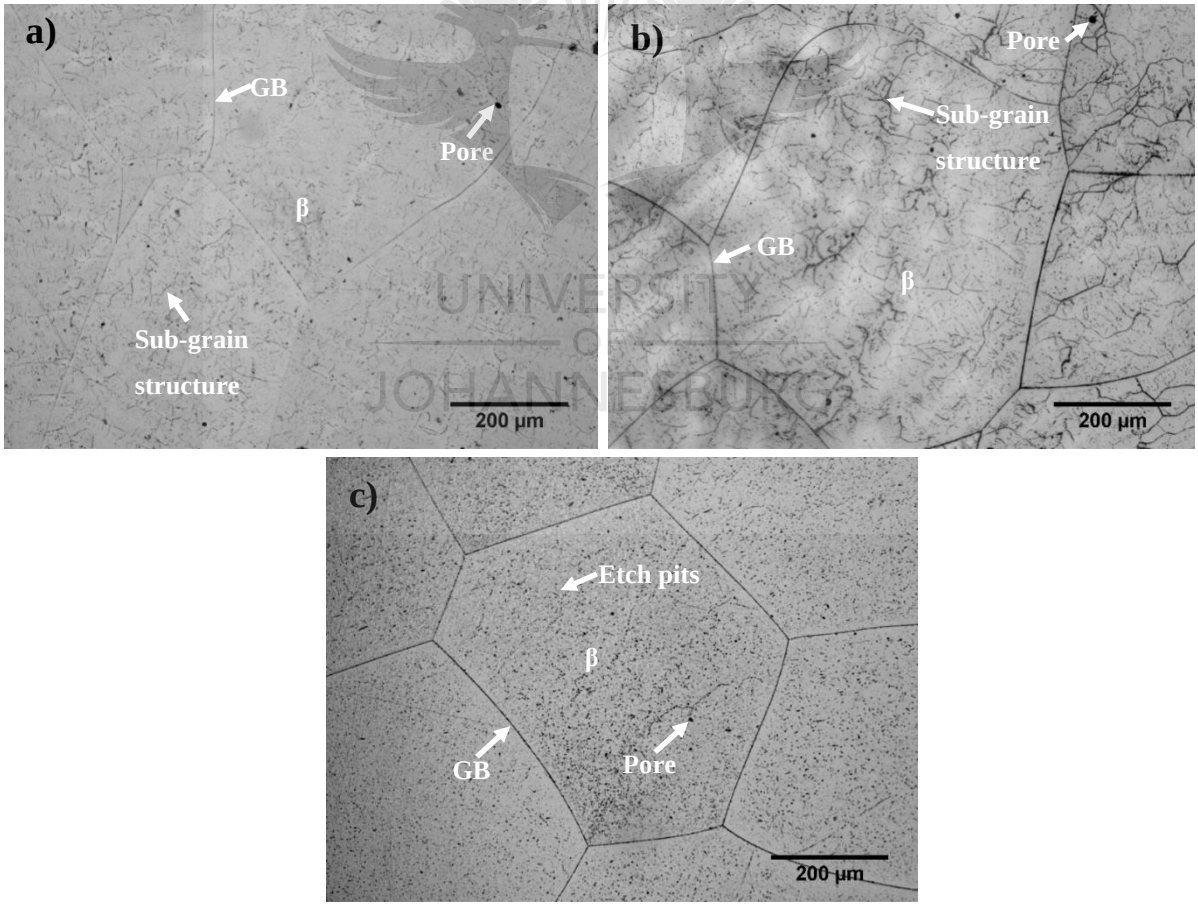

Figure 4-4: Optical micrographs of AC a) Ti-8Mo, b) Ti-10Mo and Ti-15Mo alloy specimens.

The optical micrographs of the Ti-Mo alloy specimen subjected to solution treatment and subsequently quenched in ice water are presented in Figure 4-5. The optical micrograph of ST Ti-8Mo alloy specimen in Figure 4-5 (a) reveals numerous acicular structures corresponding to the orthorhombic α" martensitic phase precipitated preferentially in the BCC β phase grains. Grain boundaries are clear and visible. Davis et al. [96] reported that the orthorhombic martensitic α" phase in Ti-Mo binary alloy series was characterized by acicular structures while the hexagonal α' phase was made up of lamellar structures. When the Mo content was increased to 10 wt%, precipitation of the acicular α" martensitic phase was substantially suppressed, and β phase was significantly retained as shown in Figure 4-5 (b). These observations are not in agreement with Davies *et al.* [96] findings, in which the ST Ti-10Mo alloy consisted of untransformed equiaxed β phase grains, with no traces of the martensitic phase(s). They indicated that the martensite start transformation temperature was reduced to below room temperature, thus hindering the transformation of the high-temperature β phase to martensitic α" phase. With further increase in the Mo content to 15 wt%, the microstructure in Figure 4-5 (c) was composed entirely of the equiaxed β grains. This indicates that the martensitic start temperature was dropped below room temperature and the formation of acicular α" martensitic phase was completely suppressed. These observations are consistent with the XRD results of the ST Ti-15Mo alloy. It is noteworthy that the sub-grain structures observed in AC Ti-8Mo and Ti-10Mo alloy specimens were not evident in the ST Ti-Mo alloy specimens.

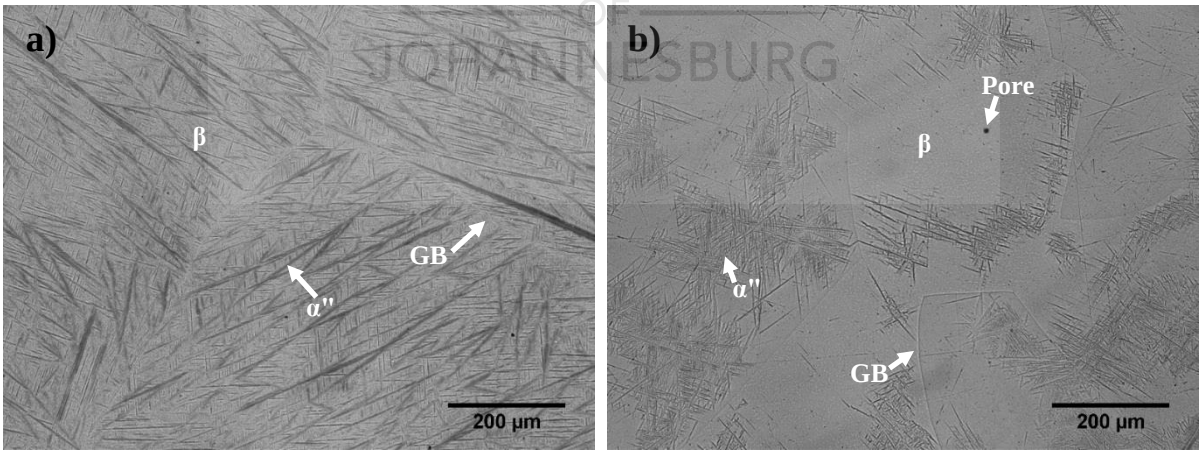

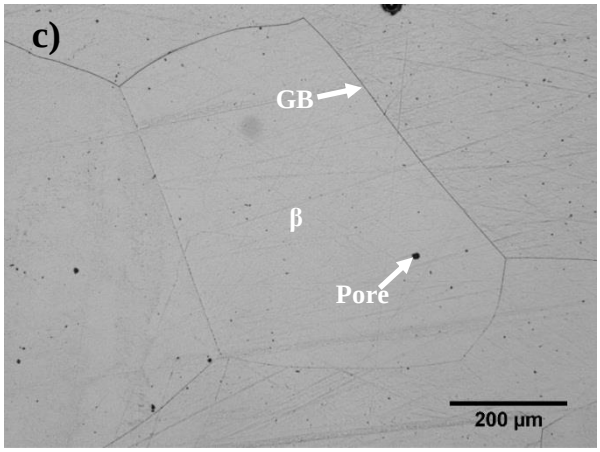

Figure 4-5: Optical micrographs of ST a) Ti-8Mo, b) Ti-10 and Ti-15Mo binary alloys.

Generally, the AC Ti-10Mo constituted β grains and sub-grain structures, whereas the optical micrographs of the ST alloys showed the acicular structures of the martensitic α" phase. However, the formation of these acicular structures was suppressed upon increasing the Mo content to 15 wt%, due to increased β stability.

4.1.3 Scanning electron microscopy (SEM) characteristics

Figure 4-6 shows the SEM microstructures of the AC Ti-10Mo and Ti-15Mo alloy specimens obtained at both high and low magnifications[1]. In Figure 4-6 a), the microstructure of Ti-10Mo alloy specimen is composed of retained BCC β phase grains with visible grain and sub-grain structures. Figure 4-6 b) exhibits the SEM micrograph of the Ti-10Mo alloy specimen at a higher magnification, which clearly illustrates the acicular structures of the orthorhombic α" phase nucleating preferentially from the grain and sub-grain boundaries into the interior of the β phase grains. The microstructure of Ti-15Mo alloy specimen shown in Figure 4-6 c) exhibits β phase grains, and grain and sub-grain boundaries. At a higher magnification as displayed by Figure 4-6 d), the sub-grain structures appeared in the form of small pores. Similar pores were observed by Li *et al.* [99], which were deduced to be original places of the tiny α" martensitic particles which detached from the continuous β matrix during the polishing process. It can be seen that the stability of the β phase in Ti-15Mo alloy was significantly enhanced compared to Ti-10Mo alloy. At 15 wt% Mo, the melting point of the alloy was lower than the melting points at 8 and 10 wt%. This low melting point caused by the increased Mo content (15 wt%), allowed

[1] Based on the XRD & OM findings, the phase evolution in the Ti-8Mo is not significant – therefore in this section, the discussion is focused only on the Ti-10Mo and Ti-15Mo.

for the formation of large amounts of the β phase, i.e. increased β phase stability, while suppressing the formation of α" phase. The α" martensitic structures precipitated in the β phase matrix observed in the AC Ti-10Mo alloy are consistent with the SEM observations by Li *et al.* [99], but did not corroborate the findings of Sung *et al.* [35].

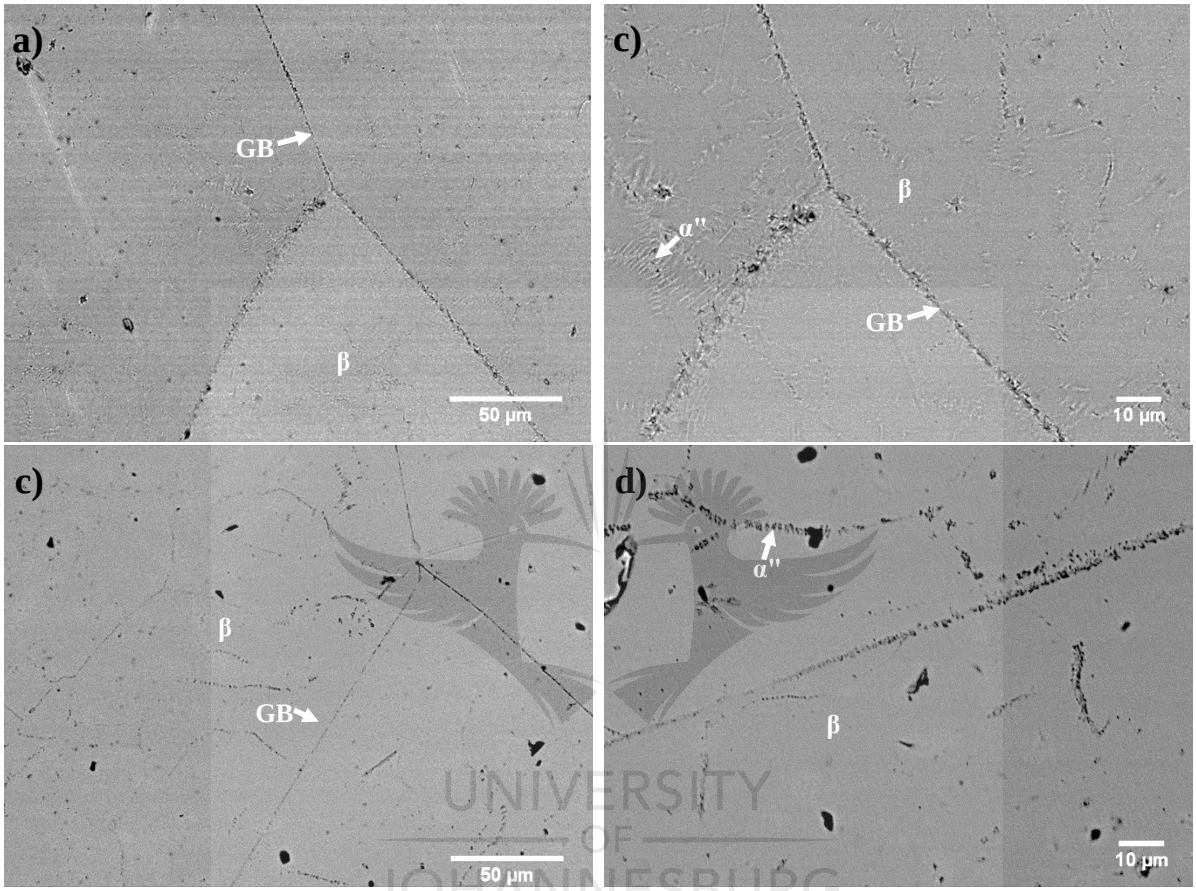

Figure 4-6: SEM micrographs of AC a) - b) Ti-10Mo AC alloy and c) –d) Ti-15Mo alloy.

The variation in Mo concentration in different regions of the AC Ti-10Mo and Ti-15Mo alloy specimens was also determined. In

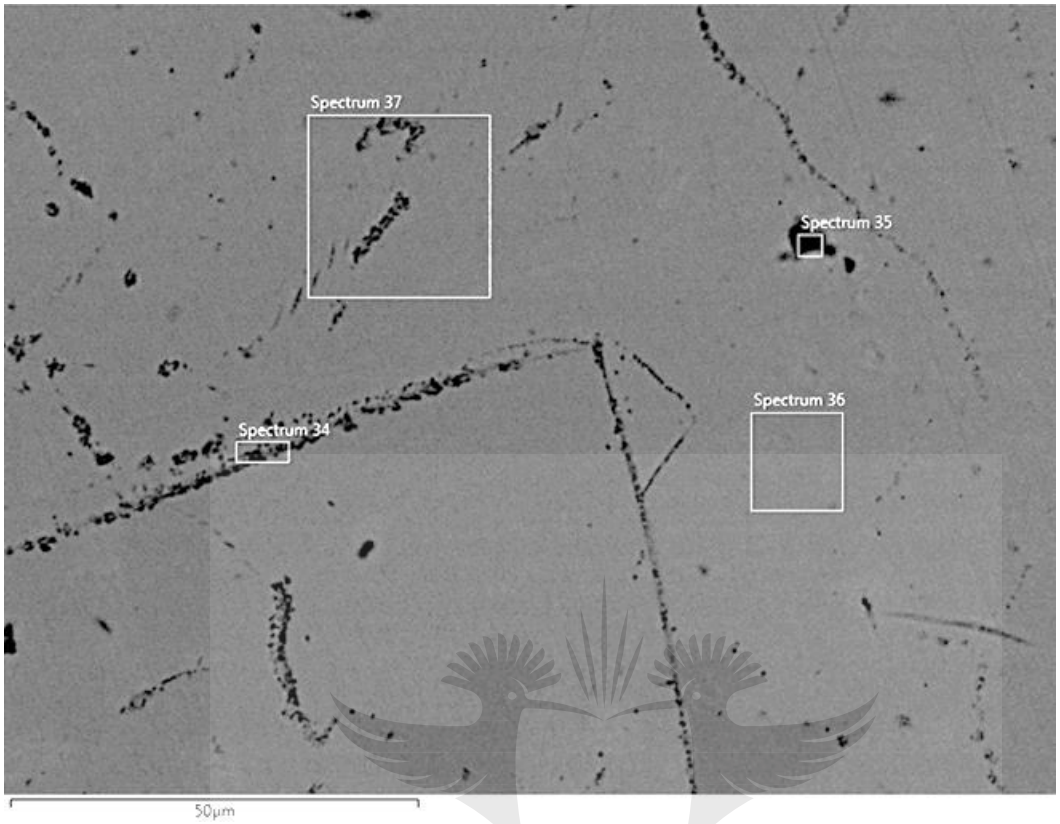

Figure 4-7 (a) and Table 4-1, spectra 51, 53 and 55 indicated regions were the α" acicular structures was significantly precipitated with about 10 wt% Mo content. In spectrum 54, where the amount of the precipitated α" was less, the Mo content was about 10.8 wt%. Spectrum 52 represents the region that is enriched with the β phase, where almost no precipitates of the α" acicular structures were observed. This region contained about 11 wt% Mo. This indicates that the acicular structures of the orthorhombic α" phase were precipitated preferentially in Mo-lean regions, i.e. regions containing about 10 wt% Mo. Conversely, a single β phase (with no precipitates of the α" acicular structures) was preferentially retained in Mo-rich regions (regions constituting about 11 wt% Mo).

Table 4-1: EDX Spectra of AC Ti-10Mo binary alloy.

Element	**Spectrum**				
	51	**52**	**53**	**54**	**55**
Ti (wt%)	89.8 ± 0.5	88.8 ± 0.5	90.0 ± 0.5	89.3 ± 0.5	89.9 ± 0.5
Mo (wt%)	10.2 ± 0.3	11.2 ± 0.3	10 ± 0.3	10.7 ± 0.3	10.1 ± 0.3

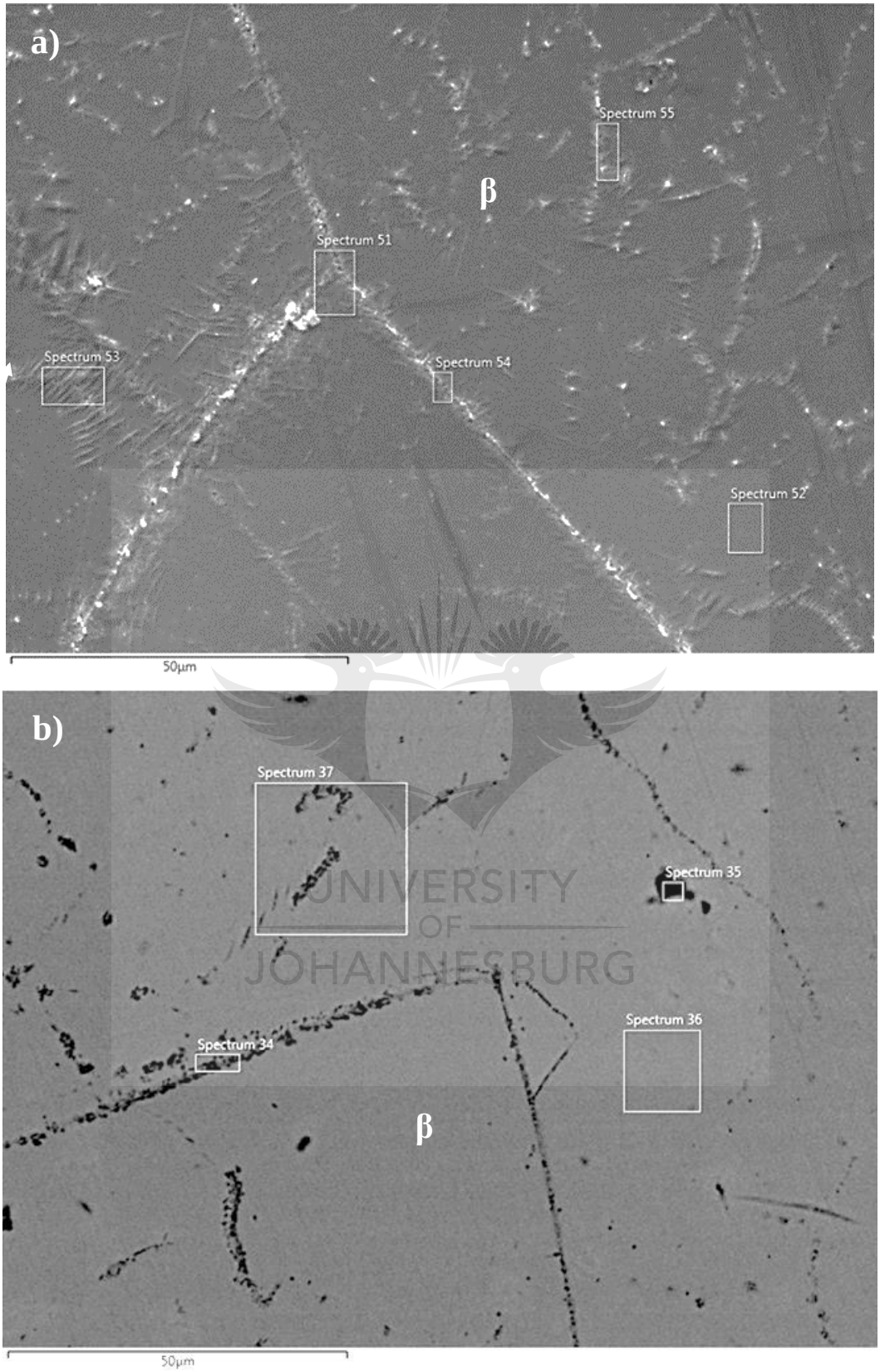

Figure 4-7 : EDX Spectra of AC a) Ti-10Mo and b) Ti-15Mo alloy specimens.

Spectrum 34 in

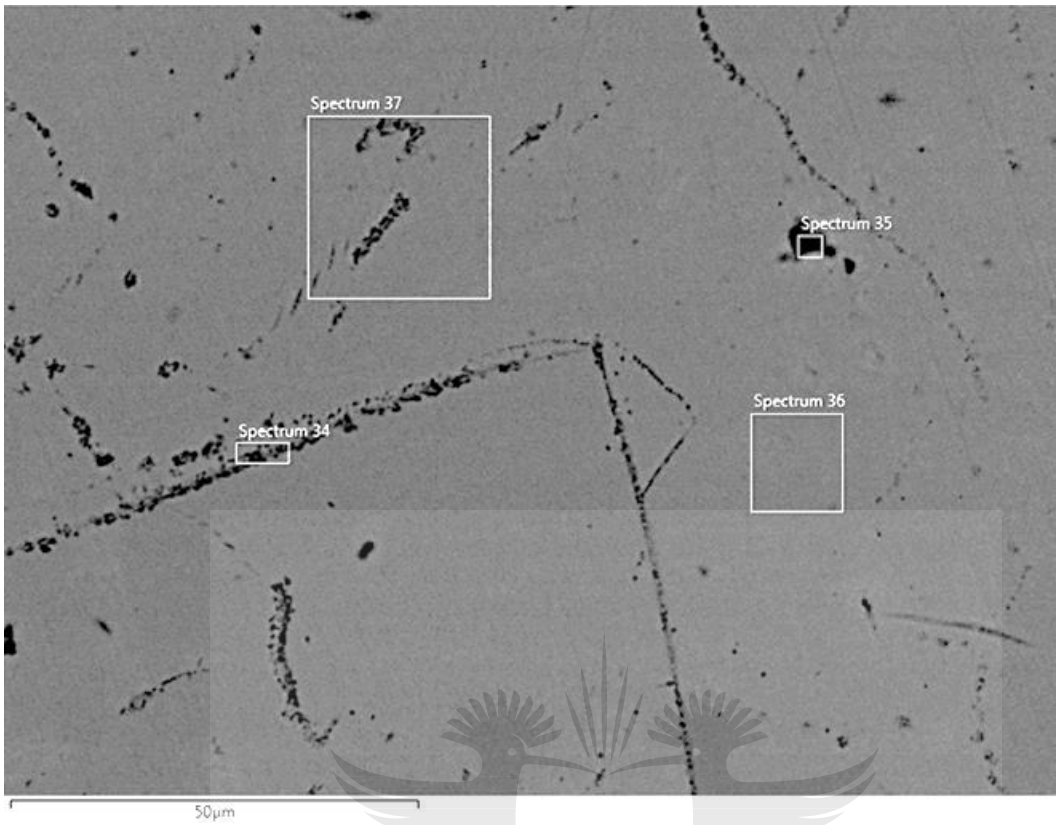

Figure 4-7 (b) and Table 4-2, which covers mainly the grain boundary, was enriched with molybdenum. Similar to that, spectrum 37 also contained more molybdenum than spectra 34 and 35, in which the molybdenum content was below the nominal composition. This suggests that these areas were Mo-lean. This could have resulted from compositional differences or segregation in the alloys. Generally, it can be seen that the molybdenum was segregated from the interior of the grain into the grain and sub-grain boundaries.

Table 4-2. EDX Spectra of AC Ti-15Mo binary alloy.

Element	**Spectrum**			
	34	**35**	**36**	**37**
Ti (wt%)	84.3 ± 0.3	85.4 ± 0.3	86.1 ± 0.3	85.0 ± 0.3
Mo (wt%)	15.7 ± 0.2	14.6 ± 0.2	13.9 ± 0.2	15.0 ± 0.2

The SEM micrographs of ST Ti-10Mo and Ti-15Mo alloy specimens are presented in Figure 4-8. In Figure 4-8 a), the microstructure of Ti-10Mo alloy specimen exhibits retained BCC β phase matrix and the acicular structures corresponding to the α" martensitic phase. Contrary to that, Figure 4-8 b) shows the microstructure of Ti-15Mo alloy specimen, which consists of β grains and visible grain boundaries. The acicular-features of the orthorhombic α" phase in the

β phase matrix could not be observed. These observations confirm that the martensite start transformation temperature in Ti-15Mo alloy was reduced to below room temperature during quenching, thus retarding the transformation of the high-temperature β phase to the martensitic α" phase. Zhou *et al*. [100] and Sung *et al*. [35] also observed fine acicular patterns in the β phase matrix in Ti-10Mo alloy. Contrarily, no acicular structures of the α" martensitic phase were observed in the microstructure of ST Ti-10Mo alloy investigated by Lu *et al.* [101]. In this study, the α" phase was precipitated because the martensite transformation start temperature was reached before the β phase was fully retained.

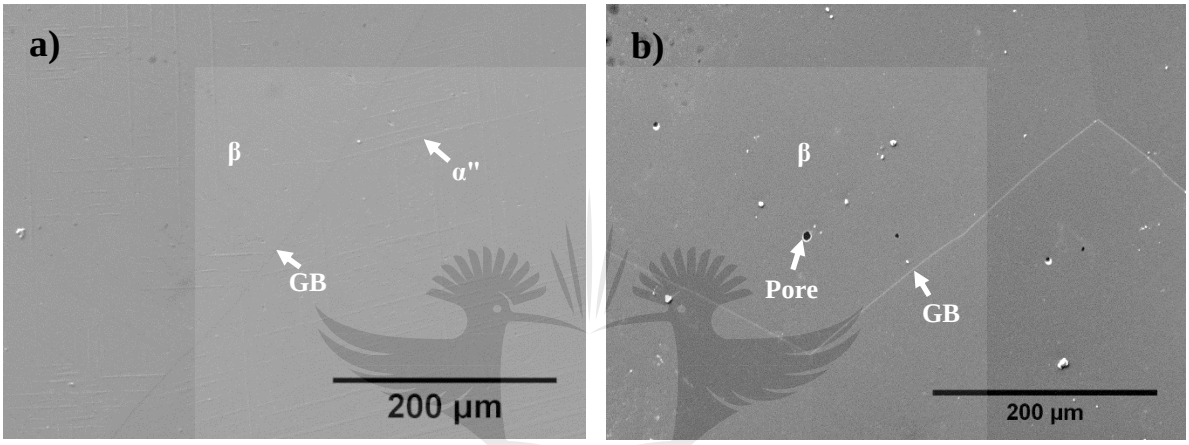

Figure 4-8: SEM micrographs of ST a) Ti-10Mo and b) Ti-15Mo alloys.

Generally, the Ti-10Mo alloy in both AC and ST conditions consisted of acicular structures of the martensitic α" phase, which disappeared in Ti-15Mo alloy due to increased β stability.

4.1.4 EBSD results

Figure 4-9 shows the EBSD inverse pole figure (IPF) maps and phase maps of AC binary alloys of the AC Ti-Mo binary alloys. It should be noted that the artifacts revealed in the IPF map of AC Ti-15Mo alloy were introduced during preparation of the specimen for analysis. The EBSD IPF maps of the Ti-8Mo, Ti-10Mo and Ti-15Mo binary alloys reveal coarse, equiaxed β phase grains. Nano-sized particulates precipitated in the β phase matrix and along the grain boundaries could also be distinguished but could not be identified. To identify these nano-sized particulates and verify the phase constituents revealed by the X-ray diffraction, optical microscopy and scanning electron microscopy analysis, electron backscatter diffraction analysis was conducted.

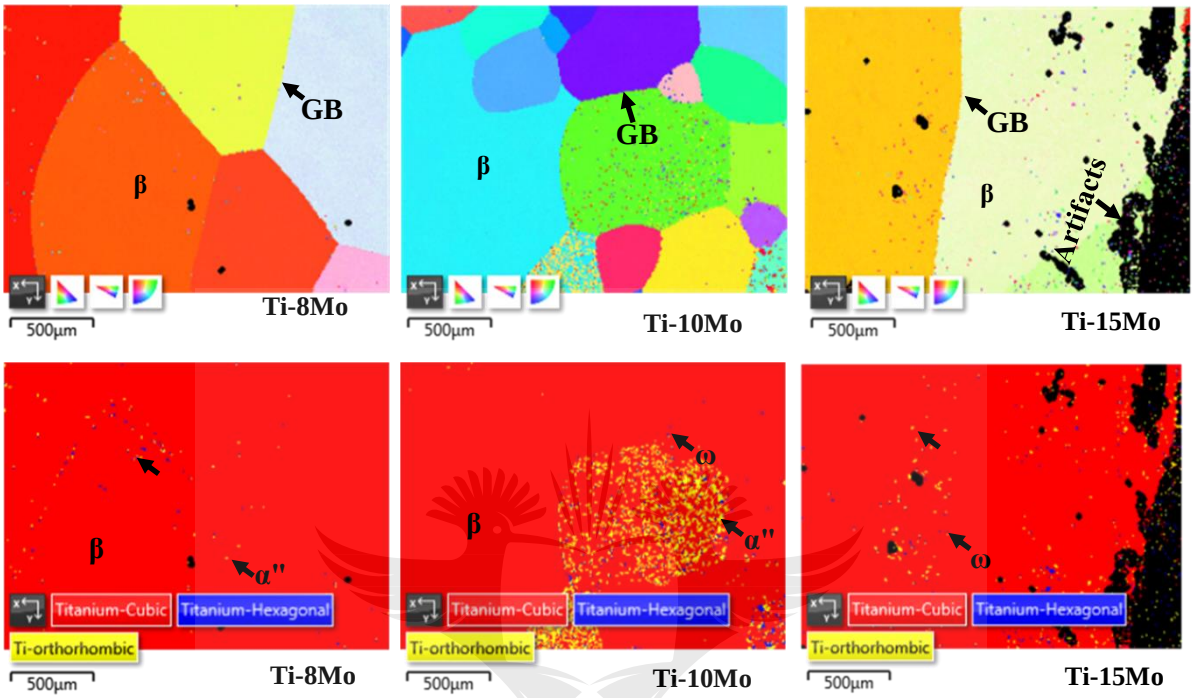

Figure 4-9. EBSD IPF maps and phase maps of AC Ti-8Mo, Ti-10Mo and Ti-15Mo binary alloys

EBSD phase maps of the AC Ti-8Mo, Ti-10Mo and Ti-15Mo binary alloys were generated. It could be seen that the nano-sized particulates observed in the inverse pole figure maps of the AC Ti-Mo alloys were identified in the phase maps as the orthorhombic α" martensitic phase (yellow particulates) and the hexagonal ω phase (blue particulates). In the phase map of AC Ti-8Mo binary alloy, the nano-sized particulates of the orthorhombic α" martensitic phase (yellow particulates) and the hexagonal ω phase (blue particulates) are precipitated preferentially along the grain boundaries and in the interior of the β phase matrix (red phase). Contrarily, large amounts of the nano-sized particulates of the orthorhombic α" martensitic phase (yellow particulates) and the hexagonal ω phase (blue particulates) were formed preferentially in the β phase grains in AC Ti-10Mo alloy. In the phase map of AC Ti-15Mo alloy, nano-sized particulates of the orthorhombic α" martensitic phase and the hexagonal ω phase were observed in all the grains, however, their volume fraction was substantially smaller in AC Ti-8Mo and Ti-10Mo alloys. The observation of the hexagonal ω phase in EBSD phase

maps was also reported by Dyakonov *et al.* in their study of CP Ti produced via equal channel analyser pressing [102].

Figure 4-10. shows the EBSD inverse pole figure (IPF) maps and phase maps of ST alloy specimens[2]. The artifacts appearing in both IPF maps also originate from the preparation of the specimen for analysis. As in the IPF maps of the AC alloys, the IPF maps of the ST alloy specimens exhibited coarse, equiaxed β phase grains with nano-sized particulates precipitated in the matrix. The phase maps of the ST Ti-Mo binary alloys revealed the existence of the orthorhombic α" martensitic phase (blue) and the hexagonal ω phase (yellow). The precipitation of a large amount of the secondary ω phase occurred preferentially in a single grain in the Ti-10Mo alloy as seen in the phase map, while the secondary martensitic α" phase was formed all throughout the specimen. The phase map of the Ti-15Mo alloy exhibited a large amount of the α" martensitic phase throughout the specimen compared to the ω phase.

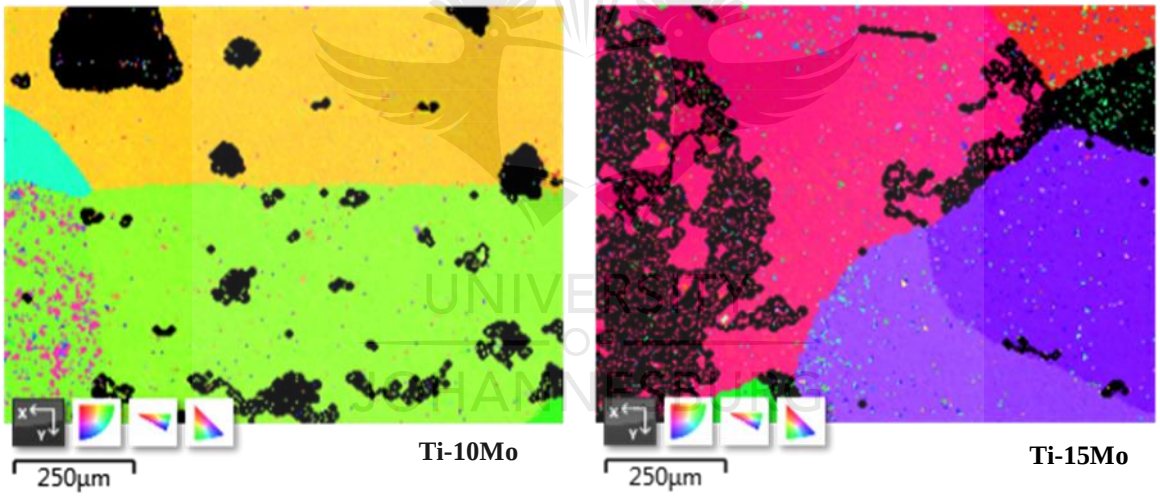

[2] The author observed that no significant microstructural differences exist in the maps of ST Ti-8Mo and Ti-10Mo alloys. Therefore, the ST Ti-8Mo images were not included

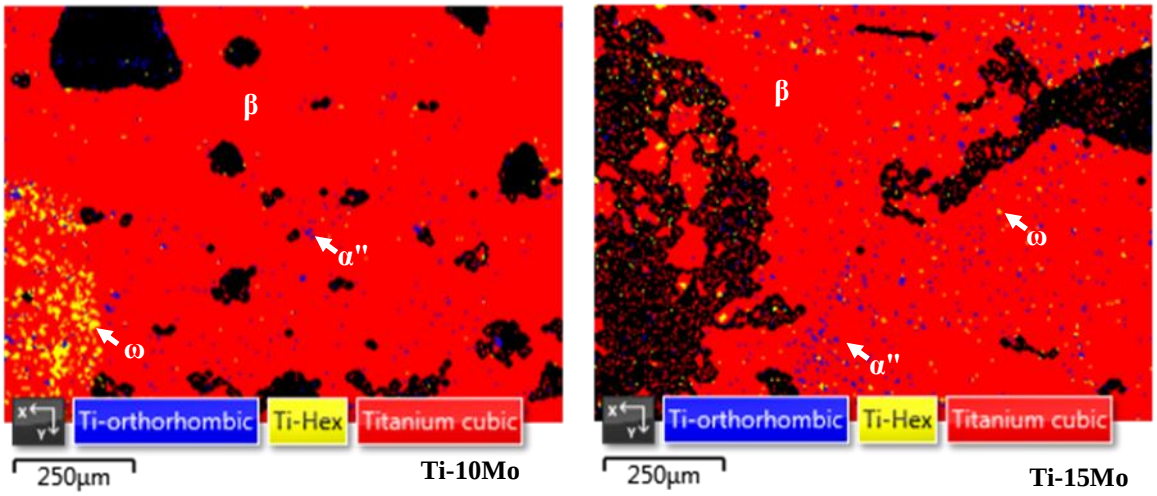

Figure 4-10. EBSD IPF maps of ST Ti-10Mo and Ti-15Mo binary alloys.

Generally, by visual examination of the EBSD maps, considerable amount of secondary ω and martensitic α" nano-particles in AC Ti-10Mo alloy precipitated preferentially in individual grains. Contrarily, the secondary phases were formed throughout the microstructure in Ti-15Mo alloy. In the case of the ST alloy, the ST Ti-10Mo alloy comprised more ω nano-particles in preferential areas (grains) than the Ti-15Mo alloy, which constituted more α" nano-particles.

In both AC and ST conditions, the OM and SEM microstructures could exhibit martensitic α" and β phase, whereas the XRD and EBSD further revealed the existence of the ω phase. The OM and SEM could not show the ω phase, due to its existence in the alloys as nano-particles or small volume fraction, which could have been below the detection limit of the two analytical techniques.

4.1.5 Comparison of Experimental Phase Observations with the theoretical Predictions

The stability of the β phase was determined using the molybdenum equivalence *(Moeq)*, d-electron theory and the average electron concentration *(e/a)* ratio approaches, and the predictions are listed in Table 4-3.

Table 4-3. Summary of the experimental observations and theoretical predictions.

Alloy		Theoretical predictions			Experimental observations			
		Moeq	*e/a* ratio	d-electron	OM	SEM	XRD	EBSD
Ti-8Mo	AC	β+ α"	β+ α"	β+ω +α"	β	-	β + α" + ω	β + α" + ω
	ST				β + α"		β + α"	

Ti-10Mo	AC ST	β	β+ α"	β+ω	β	β + α"	β+ α"+ ω	β + α" + ω
Ti-15Mo	AC ST	β	β	β	β	β	β+ α" β+ α"+ ω	β + α" + ω

4.1.5.1 *Molybdenum equivalence*

Careful analysis of the phase constituents using EBSD technique revealed subtle differences in the actual phases identified compared to the phases predicted by the molybdenum equivalence (*Moeq)* formula according to Bania [103]. It was proposed that a binary alloy requires a *Moeq* of 10.0 wt% or more to form a single BCC β phase upon rapid cooling [103]. This suggests that the *Moeq* of 10.0 wt% would be sufficient to suppress the formation of the martensitic phases (α' and α"). According to the *Moeq* values calculated in this study, AC/ST Ti-8Mo binary alloys were expected to precipitate the martensitic α" phase in the β phase matrix, whereas Ti-10Mo and AC/ ST Ti-15Mo binary alloys were expected to retain 100% β phase upon rapid cooling. However, experimental results indicated that these alloys precipitated the martensitic α" phase and the ω phase in the β matrix. This indicates that the *Moeq* approach overestimated the stabilization effect of molybdenum in Ti-10 and Ti-15Mo alloys. This discrepancy could be ascribed to chemical inhomogeneity in the alloy specimens, which could have led to Mo-lean and Mo-rich areas in the specimens, thus resulting in the precipitation of the secondary phases. Furthermore, this prediction approach does not take into consideration the precipitation of the ω phase, but the stability of the β phase and the precipitation of martensitic phases in the alloy.

4.1.5.2 *D-electron Method*

The Bo-Md phase stability map has a direct connection with the relative chemical stability of the high-temperature BCC β phase and predicts the microstructure of as-quenched materials theoretically [60]. By directly reading from the Bo-Md phase stability map, it was observed that the binary Ti-8Mo binary alloy would form β + α"+ ω phases, whereas Ti-10Mo and Ti-15Mo would form β + ω phases and β phase, respectively. However, the results showed that the theoretical predictions of Ti-8Mo alloy were consistent with its experimental findings. In the case of Ti-10Mo and Ti-15Mo binary alloys, the d-electron method overestimated the effect of stabilization of molybdenum because it precipitated martensitic α" phase.

4.1.5.3 *E/a Ratio*

The *e/a* ratio scale developed for Ti alloys by Laheurte *et al*. [60] indicates that the stability of the β phase increases with increasing *e/a* ratio. The scale also highlights that a single β phase can be formed at *e/a* ratio of 4.20 or more [60]. Furthermore, Buzatu *et al.* [65] reported that the β phase is stable at *e/a* ratio above 4.30, whereas the precipitation of the metastable omega (ω) phase occurs between the range 4.13 and 4.30. In this work, the *e/a* ratio of the AC/ ST Ti-Mo binary alloys at 8, 10 and 15 wt% Mo were 4.16, 4.20 and 4.30, respectively. According to Lauherte *et al*. [60]'s prediction, Ti-8Mo alloy would precipitate the α" martensitic phase, whereas AC/ ST Ti-10Mo and Ti-15Mo binary alloys would retain 100% β phase upon rapid cooling. Conversely, Buzatu [65] predicted that all the AC/ ST Ti-Mo binary alloys would form the ω phase in the β phase matrix. However, in this study, all the AC/ ST Ti-Mo binary alloys precipitated both the martensitic α" phase and the ω phase in the β phase matrix. Similar to the *Moeq*, this approach overestimated the stabilization effect of molybdenum in the Ti-10Mo and Ti-15Mo alloys.

4.1.6 Summary of findings

Table 4-3 gives a summary of the phases revealed by the XRD, OM, SEM and EBSD analytical techniques. In both AC and ST conditions, the OM and SEM microstructures could exhibit martensitic α" and β phase, whereas the XRD and EBSD further revealed the existence of the ω phase. The OM and SEM could not show the ω phase, due to its existence in the alloys as nano-particles or small volume fraction, which could have been below the detection limit of the two analytical techniques. The predictions by the d-electron theory were generally consistent with the theoretical findings, whereas the predictions by the *Moeq* and *e/a* ratio approaches contradicted considerably with the experimental observations. Generally, the stability of the β phase increased with increasing molybdenum content, while the precipitation of the secondary phases (martensitic α" and ω phases) was suppressed. Generally, solution treatment did not considerably influence the microstructure of the AC alloys, because by visual observation in both conditions, the formation, variation and distribution of the phases in the alloys was similar.

4.2 Effect of microstructure on the mechanical properties of Ti-Mo alloys

4.2.1 Microhardness Results

Figure 4-11 exhibits the micro-hardness of the AC Ti-Mo binary alloy specimens. The average microhardness values were 310±21.1 $HV_{0.5}$, 474±34.6 $HV_{0.5}$ and 350±16.1 $HV_{0.5}$ for AC Ti-

8Mo, Ti-10Mo and Ti-15Mo alloy specimens, respectively, compared to 135 $HV_{0.5}$ for CP-Ti, 220 $HV_{0.5}$ for 316 stainless steel, 250 $HV_{0.5}$ for CoCr and 350 $HV_{0.5}$ for Ti6Al4V materials. The microhardness values of AC Ti-8Mo alloy is greater than that of CP-Ti, 316 stainless steel and CoCr, but lower than that of Ti6Al4V materials. The microhardness values AC Ti-10Mo binary alloy was substantially greater than those of the commonly used orthopaedic implant materials. The microhardness value of AC Ti-15Mo binary alloy was substantially higher than those of CP Ti, 316 stainless steel and CoCr materials, but it was similar to that of Ti6Al4V alloy. When comparing the microhardness of the AC Ti-Mo binary alloys among themselves, n the microhardness of AC Ti-8Mo alloy was significantly lower than those of the AC Ti-10Mo and AC Ti-15Mo alloys. Meanwhile, Ti-10Mo alloy exhibited microhardness that was significantly higher than that of the ST Ti-15Mo alloy. It is evident that the microhardness increased with increasing β phase stability and then decreased.

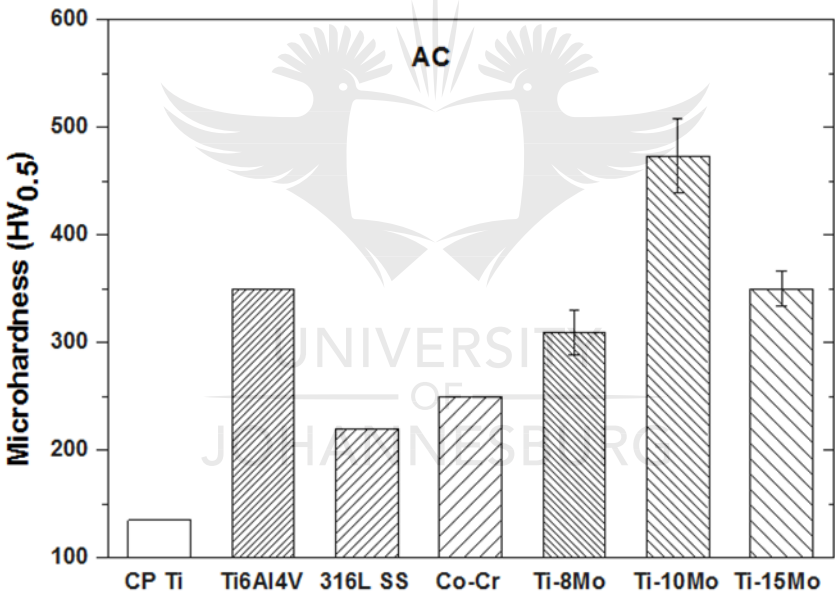

Figure 4-11: Microhardness of the AC Ti-Mo binary alloys and the conventional orthopaedic implant materials considered for comparison [54,104].

The microhardness of the ST Ti-8Mo, Ti-10Mo and Ti-15Mo alloys exhibited in Figure 4-12 were 293±11.5 $HV_{0.5}$, 334±35.9 $HV_{0.5}$ and 355±18.1 $HV_{0.5}$, respectively. It is evident that the microhardness of all the ST Ti-Mo alloys was greater than those of CP-Ti, 316 stainless steel and CoCr materials. On the other hand, the microhardness of the ST Ti-10Mo and Ti-15Mo alloy was similar to that of Ti6AlV alloy, which was higher than that of the ST Ti-8Mo alloy. When comparing the microhardness of the ST alloy amongst themselves, the Ti-8Mo alloy had

the microhardness that was significantly lower than those of the ST Ti-10Mo and Ti-15Moalloy, which had comparable microhardness values. When compared with the microhardness of the AC Ti-Mo alloy specimens, the microhardness of the ST alloy specimens increased with increasing Mo content, i.e. they did not show a similar trend.

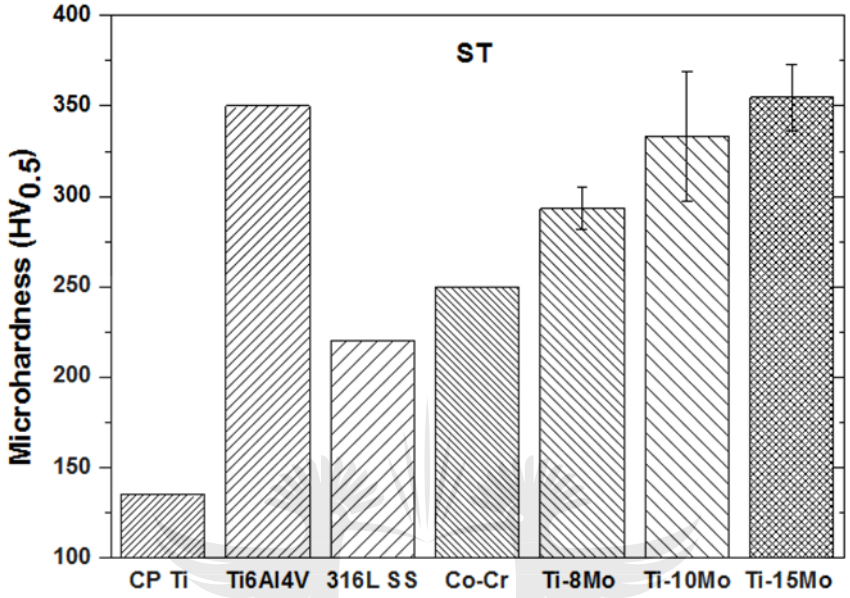

Figure 4-12: Microhardness of the ST Ti-Mo binary alloys and the conventional orthopaedic implant materials considered for comparison [54,104].

Ho *et al.* [33] reported the microhardness value of about 340 HV in AC Ti-10Mo alloy, which is substantially lower than the value obtained on the AC Ti-10Mo alloy in this study, but similar to the microhardness of the ST Ti-10Mo alloy. In a study conducted by Cardoso *et al*. [36], the ST Ti-10Mo alloy obtained was about 330 HV, which was comparable to the value measured on the ST Ti-10Mo alloy in this study. The microhardness values reported in Refs. [33] and [36] were attributed to the dispersion hardening of the β phase matrix by the precipitated athermal ω phase, which precipitate over a limited composition range of Ti-Mo alloys. As observed in this study, the Ti-10Mo alloy in both the as-cast and solution treated condition comprised the highest volume fraction of the athermal ω phase compared to the Ti-8Mo and Ti-15Mo alloys.

Ho *et al.* [33] also obtained the microhardness of about 320 HV in AC Ti-15Mo binary alloy, which was substantially lower than the microhardness values obtained in AC/ST Ti-15Mo binary alloys. The low microhardness in Ti-15Mo binary alloy observed by Ho *et al.* [33]

occurred due to presence of 100 % retained β phase in the alloy. Davis *et al.* [96] reported a low hardness in Ti-8Mo binary alloy (≈260 HV) in comparison with Ti-10Mo binary alloy (≈300 HV), which was ascribed to the smaller strains involved during the transition of the orthorhombic martensitic α" phase from the bcc β phase, which results in less work hardening of the α" phase. The transformation from a dislocated to a twinned substructure could also have contributed to the drop in hardness [2]. Additionally, Lee *et al*. [38] investigated the effect of phase constituents on the microhardness and tentatively summarized it in the order ω > α' > α" > β > α.

4.2.2 Tensile properties

Table 4-4 shows the tensile properties including tensile strength, yield strength and elongation at rupture of the AC Ti-Mo binary alloys measured at room temperature. The tensile yield strength of AC Ti-8Mo alloy specimen (715 ± 18.2 MPa) increased to (741 ± 4.3 MPa) in AC Ti-10Mo alloy specimen and then decreased to (543 ± 6.7 MPa) in AC Ti-15Mo alloy specimen. This clearly indicates that AC Ti-10Mo alloy specimen had the yield strength that was significantly higher than those of Ti-8Mo and Ti-15Mo alloys, while the yield strength of the AC Ti-15Mo binary alloy was significantly lower than that of the AC Ti-8Mo alloy. The tensile strength of the Ti-8Mo alloy was significantly higher than those of the Ti-10Mo and Ti-15Mo alloys, while the Ti-10Mo alloys exhibited tensile strength that was significantly higher than that of the Ti-15Mo alloy. The decrease in tensile strength in AC Ti-10Mo alloy specimen could be attributed to the premature, brittle fracture, which occurred as a result of the nano-particles precipitated in the β matrix. The lowest tensile strength in AC Ti-15Mo alloy specimen resulted from the high stability of the β phase, whereas the highest tensile strength in AC Ti-8Mo alloy specimen was attributable to a large amount of the secondary α" phase, and the existence of the ω phase nano-particles, which induced strengthening effect on the β phase matrix. The elongation at rupture of the AC alloys indicates that they all failed in a brittle manner.

Table 4-4: Tensile properties of the AC Ti-Mo binary alloys.

Alloy	**Yield strength (MPa)**	**Ultimate tensile strength (MPa)**	**Elongation (%)**
Ti-8Mo AC	715 ± 18.2	870 ± 38.9	1.43± 0.7
Ti-10Mo AC	741 ± 4.3	764 ± 14.6	0.71± 0.2

Ti-15Mo AC	543 ± 6.7	593 ± 22.5	0.35± 0.1

The tensile properties of the ST Ti-Mo binary alloys were also investigated and they are listed in Table 4-5. The yield strength of ST Ti-8Mo alloy was comparable to the yield strength of Ti-15Mo alloy. However, it was significantly lower than the yield strength of Ti-15Mo alloy. The yield strength of Ti-15Mo alloy was comparable to that of Ti-10Mo alloy. The tensile strength of the ST Ti-8Mo alloy was significantly higher than those of the ST Ti-10Mo and Ti-15Mo alloys, which possessed tensile strengths that were comparable. The ST Ti-15Mo alloy exhibited elongation at rupture that was significantly lower than those of the ST Ti-8Mo and Ti-10Mo alloys, which had elongation that was comparable.

Table 4-5: Tensile properties of the ST Ti-Mo binary alloys.

Alloy	**Yield strength (MPa)**	**Ultimate tensile strength (MPa)**	**Elongation (%)**
ST Ti-8Mo	481.65± 27.8	923.82 ± 5.4	12.48± 0.9
ST Ti-10Mo	594.31± 25.4	684.65± 28.5	20.71± 13.2
ST Ti-15Mo	546.34± 49.3	705.91± 102.5	6.95± 3.7

It is noticeable that the yield strengths of the AC Ti-8Mo and Ti-10Mo alloy specimens were substantially higher than those of ST Ti-8Mo and Ti-10Mo alloy specimens; whereas the yield strengths of both AC and ST Ti-15Mo alloy specimens were comparable. However, the tensile strengths of ST Ti-8Mo and Ti-15Mo alloy specimens were higher than those of AC Ti-8Mo and Ti-15Mo alloy specimens. AC Ti-10Mo binary alloy showed higher tensile strength than ST Ti-10Mo alloy specimens as a result of the localized precipitation of the athermal ω phase observed in the EBSD images of the AC alloy. The elongation values of ST Ti-Mo alloy specimens were far greater than those of AC Ti-Mo alloy specimens. This suggests that solution treatment generally enhanced the tensile strengths and improved the ductility of the Ti-Mo alloy specimens. The high tensile strength in Ti-8Mo alloy could be attributed to the presence of a high proportion of α" phase. Meanwhile, the small amount of ω_{ath} phase precipitated during quenching in Ti-15Mo alloy increased the tensile strength. Ductility in both alloys was improved by the large amount of β phase retained upon quenching.

The yield and tensile strengths of the AC and ST Ti-Mo binary alloys are comparable or substantially lower than those of the annealed biomedical Ti-Mo based alloys currently in use,

such as Ti-11.5Mo-6Zr-4.5Sn, Ti-15Mo-5Zr-3AL and Ti-15Mo-3Nb-0.3O with yield and tensile strengths of 620 and 690 MPa, 900 and 930 MPa, and 1020 and 1020 MPa, respectively [20]. Wang *et al*. 2016 [44] reported yield strengths of 420 ±31 and 302±18 MPa in AC Ti-10Mo and Ti-15Mo binary alloys, respectively, which are substantially lower than the yield strengths of Ti-10Mo and Ti-15Mo in both AC and ST conditions. This demonstrates that the Ti-10Mo and Ti-15Mo alloys in this study have the potential to withstand large applied forces without failure during orthopaedic applications.

4.2.2.1 *Fracture surfaces*

Fracture surfaces of the AC Ti-Mo binary alloys were examined after tensile tests and the SEM images are exhibited in Figure 4-13. It can be seen that all the AC Ti-Mo binary alloys are generally brittle as indicated by their bright plane fracture surfaces. Furthermore, cleavage facets are evident in all the SEM images of the AC Ti-Mo binary alloys, which are a characteristic of brittle fracture. These results are consistent with the fracture behaviour observed in the stress-strain curves of the AC Ti-Mo binary alloys in Figure 4-13.

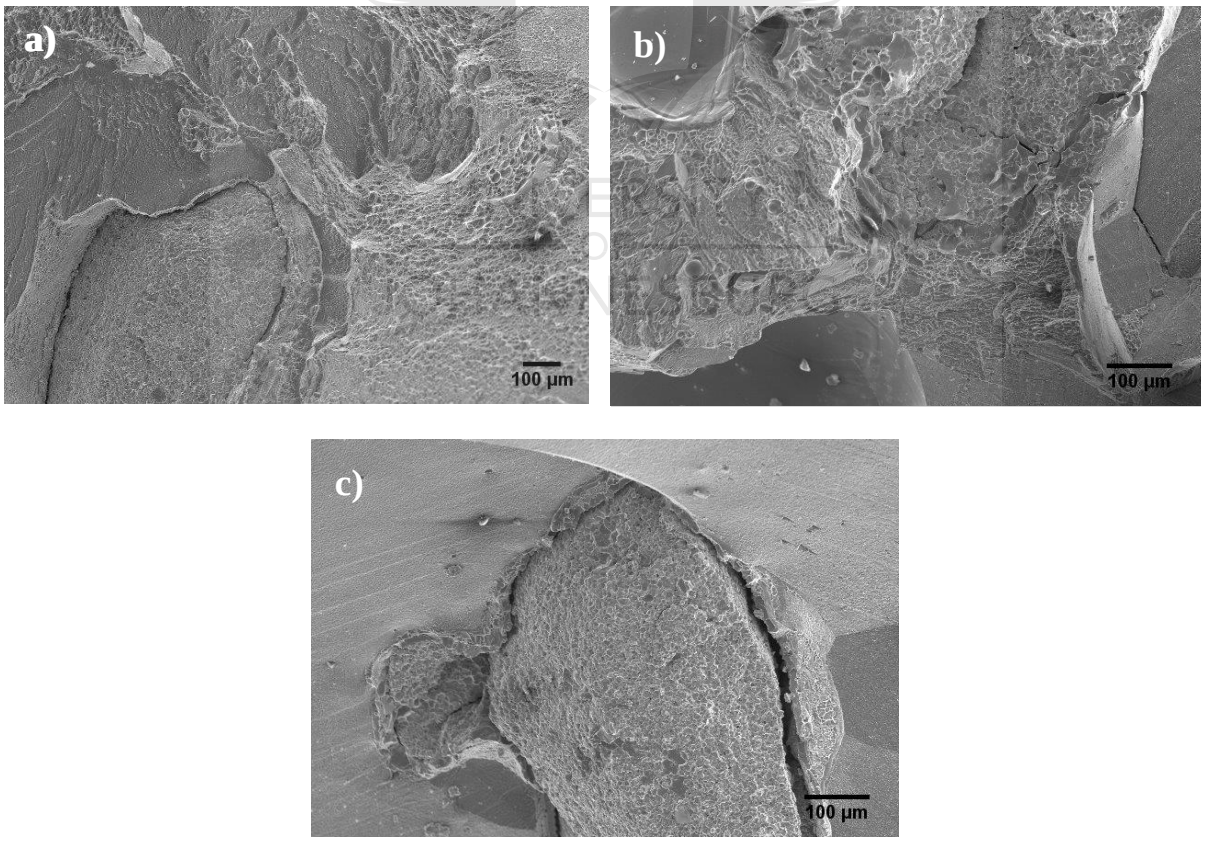

Figure 4-13. Fracture surfaces of AC a) Ti-8Mo, b) Ti-10Mo and c) Ti-15Mo binary alloys.

Fracture surfaces of the ST Ti-Mo binary alloys were examined after tensile tests and the SEM images are exhibited in Figure 4-14., cleavage facets and small dimples are visible in fracture surfaces of ST Ti-8Mo binary alloy shown in Figure 4-14 a) and b), although its fracture surface is almost flat. The fracture surface of ST Ti-10Mo binary alloy exhibits small dimples, indicating that ductile fracture characteristics were present. However, the fracture surface of ST Ti-15Mo alloy shows a combination of dimples and cleavage features. The existence of dimples resulted from the β phase present in the alloy, while the cleavage features were caused by the secondary α" and ω_{ath} phases. Dimples are a characteristic of ductile fracture, while cleavage features represent brittle fracture. These observations are in agreement with the elongation values listed in Table 4-5. Similar observations were reported by Wang *et al*. [105].

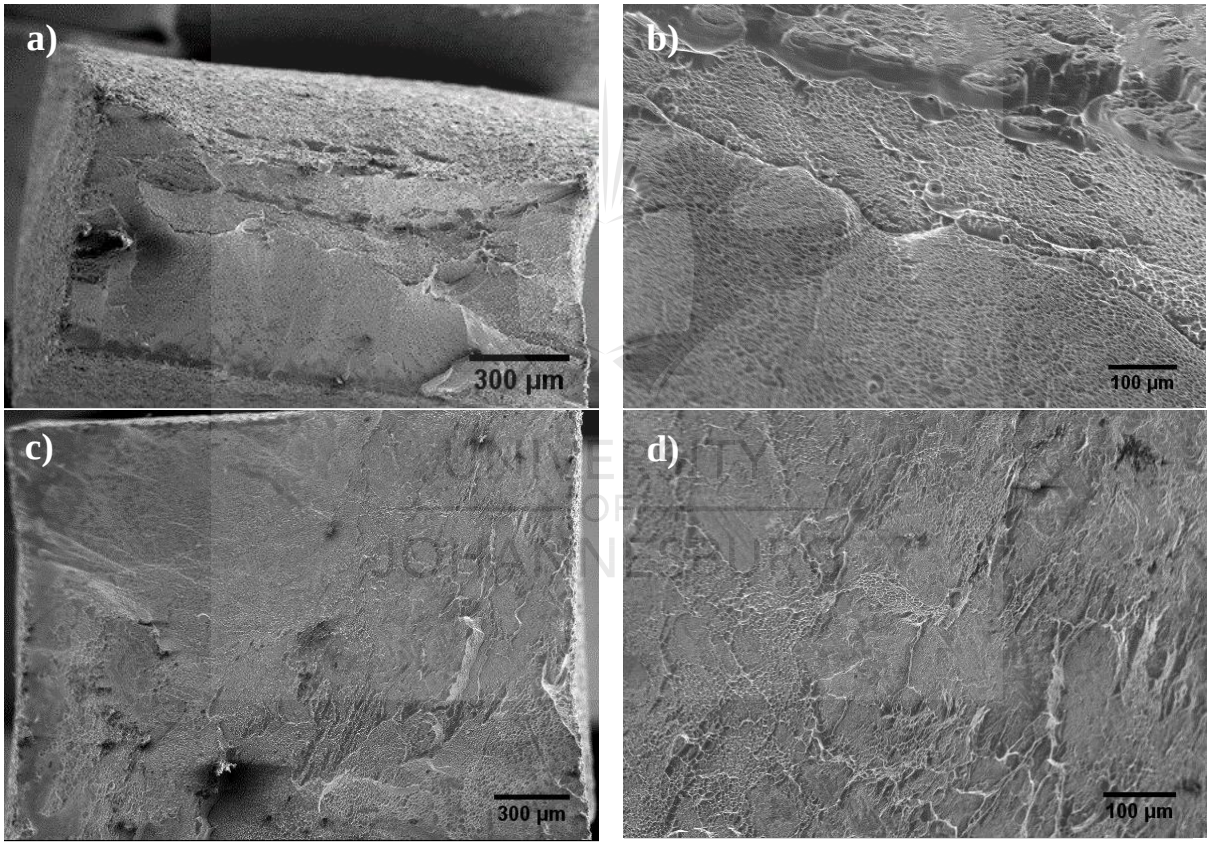

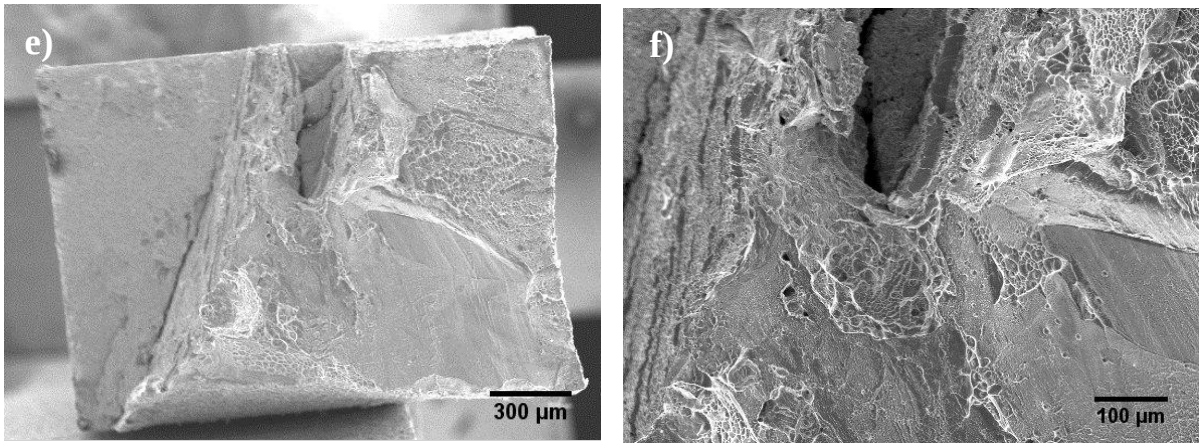

Figure 4-14: Fracture surfaces of ST a)- b) Ti-8Mo, c)- d) Ti-10Mo, and e) and f) Ti-15Mo binary alloys.

4.2.2.2 Elastic Modulus

It is noteworthy that the elastic modulus of biomaterial must match that of the human bone to prevent stress-shielding effect during implantation. It has also been established that the elastic modulus is sensitive to the crystal structure, which is dependent on the Mo content in the Ti-Mo alloy. The effect of Mo content on the elastic modulus of Ti-Mo alloys was studied and the elastic modulus of the studied alloys and the alloys considered for comparison is presented in Figure 4-15. The elastic moduli of AC Ti-8Mo, Ti-10Mo and Ti-15Mo alloy specimens are 100 ± 4.4 GPa, 111 ± 0.3 GPa and 70 ± 13.5 GPa, respectively. The elastic moduli of AC Ti-8Mo and Ti-10Mo alloys are comparable to those of the commonly used CP Ti and Ti6Al4V (110 GPa) orthopaedic implant material, but substantially lower than those of CoCr and 316L Stainless steel materials. Conversely, the elastic modulus of AC Ti-15Mo alloy specimen was substantially lower than those of the common orthopaedic implant materials. The elastic moduli of ST Ti-8Mo, Ti-10Mo and Ti-15Mo alloy specimens were 78 ± 8.4 GPa, 95 ± 1.7 GPa and 72 ± 12.2 GPa, respectively. All these elastic modulus values were substantially lower those of the conventional orthopaedic implant materials. In comparison with the commercial biomedical Ti-Mo based materials such as Ti-11.5Mo-6Zr-4.5Sn, Ti-15Mo-5Zr-3AL and Ti-15Mo-3Nb-0.3O with elastic moduli of 79, 80 and 82 GPa, respectively, [20] the elastic moduli of the Ti-Mo binary alloys were comparable (AC Ti-15Mo and all the ST Ti-Mo binary alloys) or substantially high (AC Ti-8Mo and Ti-10Mo).

When comparing the elastic moduli of the AC Ti-Mo alloy specimens, AC Ti-10Mo alloy specimen had the elastic modulus that was significantly higher than those of AC Ti-8Mo and AC Ti-15Mo alloy specimens. Contrarily, the elastic modulus of AC Ti-15Mo alloy specimen

was significantly lower than those of AC Ti-8Mo and Ti-10Mo alloy specimens. The highest elastic modulus in AC Ti-10Mo alloy specimen was ascribed to the large amount of the ω phase. A similar trend was observed in the elastic moduli of the ST Ti-Mo alloy specimen. However, the elastic moduli of ST Ti-8Mo and Ti-10Mo alloy specimens were substantially decreased in comparison with AC Ti-8Mo and Ti-10Mo alloy specimens. The elastic modulus of ST Ti-15Mo alloy specimens increased slightly compared to AC Ti-15Mo alloy. It is evident that the AC Ti-15Mo and ST Ti-15Mo alloys had the lowest elastic moduli among the investigated Ti-Mo alloys. Cardoso *et al.* [20] observed elastic moduli of about 89, 100 and 75 GPa for ST Ti-8Mo, Ti-10Mo and Ti-15Mo alloys, which are comparable to the elastic moduli of the ST Ti-Mo alloys investigated in this study. Their variation of elastic modulus exhibited a trend similar to the variation of elastic modulus of the AC/ST Ti-Mo alloy specimens in this study. The highest elastic modulus of ST Ti-10Mo alloy specimens was ascribed to the high volume fraction of the ω phase, whereas the lowest elastic modulus of ST Ti-15Mo alloy was due to the high β phase stability and reduced ω phase proportion. Almeida *et al.* [20] obtained elastic moduli of about 100 and 80 GPa in laser clad Ti-10Mo and Ti-15Mo binary alloys, respectively, which were also comparable the observed elastic modulus values in this study.

The elastic modulus trend is not consistent with the microhardness. Mo tends to segregate during casting, resulting in the formation of regions that are Mo-lean and Mo-rich. Regions that are Mo lean have low stability of the β phase, while regions that are Mo-rich possess high stability of the β phase. Therefore, the inconsistency in properties during mechanical tests resulted from the inhomogeneous chemical distribution (presence of both regions in the alloys) during melting.

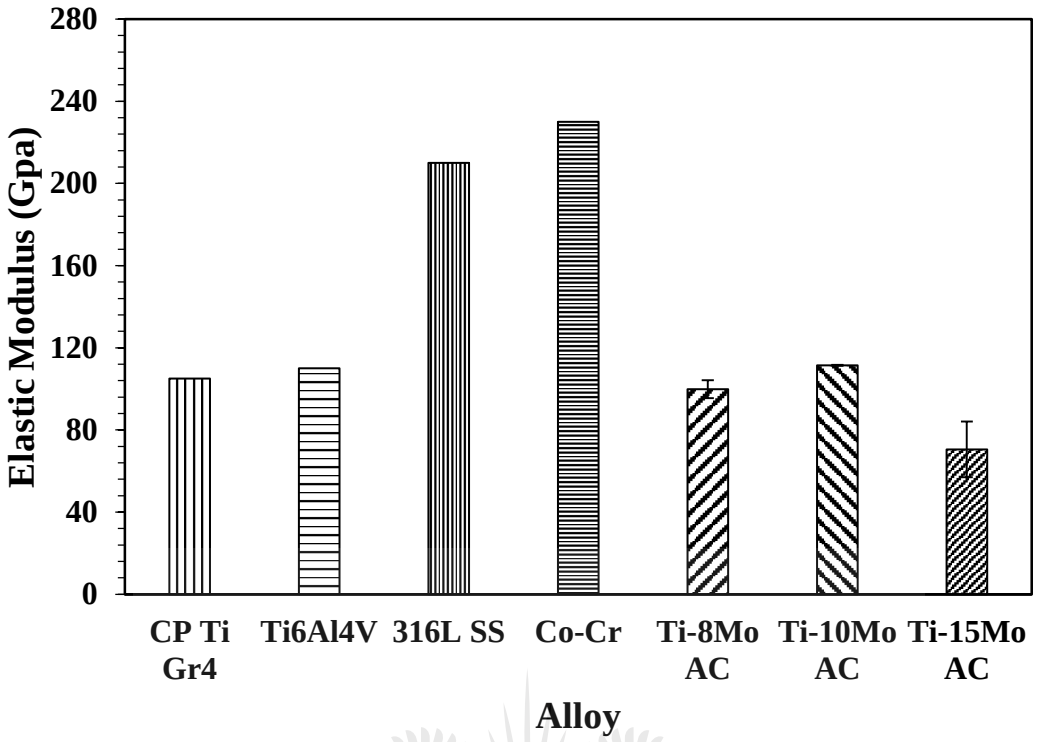

Figure 4-15: Elastic moduli of AC Ti-Mo alloys and the conventional orthopaedic implant materials considered for comparison [6,26].

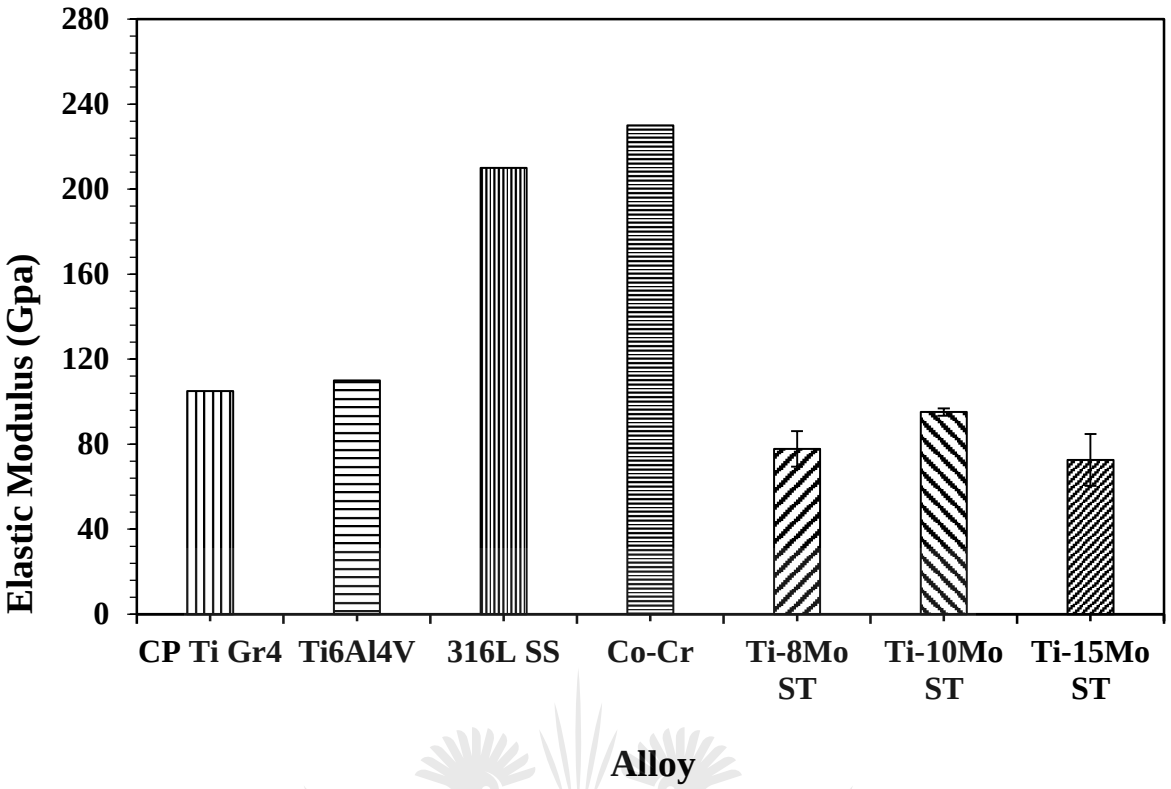

Figure 4-16. Elastic moduli of ST Ti-Mo alloys and the conventional orthopaedic implant materials considered for comparison [6,26].

4.2.2.2.1 Variation of the elastic moduli of the alloy series with *Moeq*

The Mo equivalence was used to determine the contribution of the alloying elements on the stability of the β phase in the alloys, whereby the critical lowest limit of β stabilization was experimentally determined as 10 wt% in Ti-Mo binary alloys. It is noteworthy that the contribution of other alloying elements can is observed when they are added to the alloy. In the Ti-Mo binary alloys, Mo was only alloying element added, indicating that is the only element contributing to the stability of the β phase. Figure 4-17 shows the variation tendency of the elastic modulus with the molybdenum equivalence of the AC/ ST Ti-Mo alloy specimens.

Generally, the stability of the β phase increases with increasing molybdenum equivalence. In view of the molybdenum equivalence, the elastic modulus of β-type Ti alloys increases with increasing molybdenum Equivalence [57,93]. However, in this study, the elastic modulus increased at molybdenum equivalence of 10 wt% and subsequently decreased at Mo equivalence of 15 wt%. This could be attributed to the variations in the proportion of the ω phase nano-particles precipitated in the β matrix, which was the highest in AC/ST Ti-10Mo binary alloy specimens. Moreover, the precipitation of the α" martensitic phase precipitates in the β matrix was also observed, which might also have contributed towards the variation in

elastic modulus values in the AC/ ST Ti-Mo alloy specimens. Therefore, it can be concluded that the prediction of the elastic modulus of metastable β-type Ti binary alloys using the molybdenum equivalence is questionable, due to the discrepancy that was observed in this study.

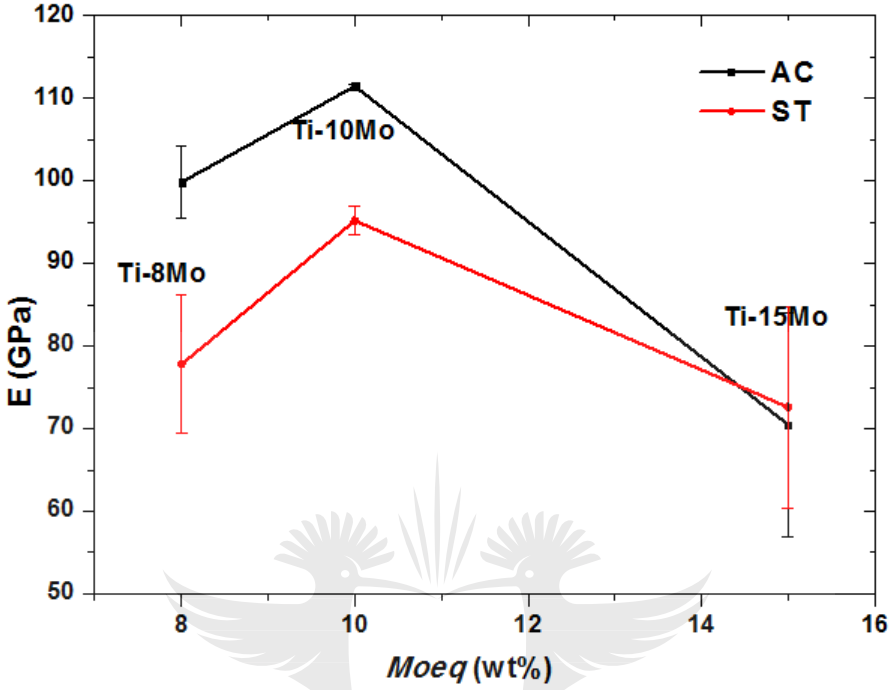

Figure 4-17: Variation of the elastic moduli of the AC/ ST Ti-Mo binary alloys with their *Moeq*.

4.2.2.2.2 Variation of the elastic moduli of the alloy series with e/a ratio

Figure 4-18 illustrates the variation of elastic moduli of AC/ ST Ti-Mo alloy specimens with their e/a ratio. The variation in elastic modulus with e/a ratio exhibit a similar trend as in the variation of elastic modulus with molybdenum equivalence. The elastic modulus increases with increasing e/a ratio from 100 GPa /4.16 in AC Ti-8Mo alloy specimens to 111 GPa/ 4.20 in AC Ti-10Mo alloy specimens and then decrease to 70 GPa/4.30 in Ti-15Mo binary alloy. In the case of the ST Ti-Mo alloy specimens, a similar trend in the variation of the elastic moduli with the e/a ratio of Ti-Mo AC binary alloys was observed. The trend is consistent with the variation presented by Lauherte *et al.* [60] in Figure 2-7. As shown in Figure 4-18, at the e/a ratio of 4.16 in AC/ST Ti-8Mo alloy specimens, the precipitation of the secondary phase particles (α" and ω nano-particles) in the β matrix which resulted in the high elastic modulus was consistent with the observations reported by Lauherte *et al.* [60]. The e/a ratio of AC/ ST Ti-10Mo alloy specimens (4.20) fell within the region where the ω phase would precipitate in the β matrix, which would result in a decrease in the elastic modulus. However, in addition to

the ω precipitates, the α" precipitates was also observed and the effect of both secondary phases resulted in the highest elastic modulus. The secondary precipitates were also revealed in AC/ ST Ti-15Mo alloy specimens with the e/a ratio of 4.30, were a single β phase was expected to form. However, the presence of the secondary phase particles in the alloys could not exert a significant influence on their elastic modulus.

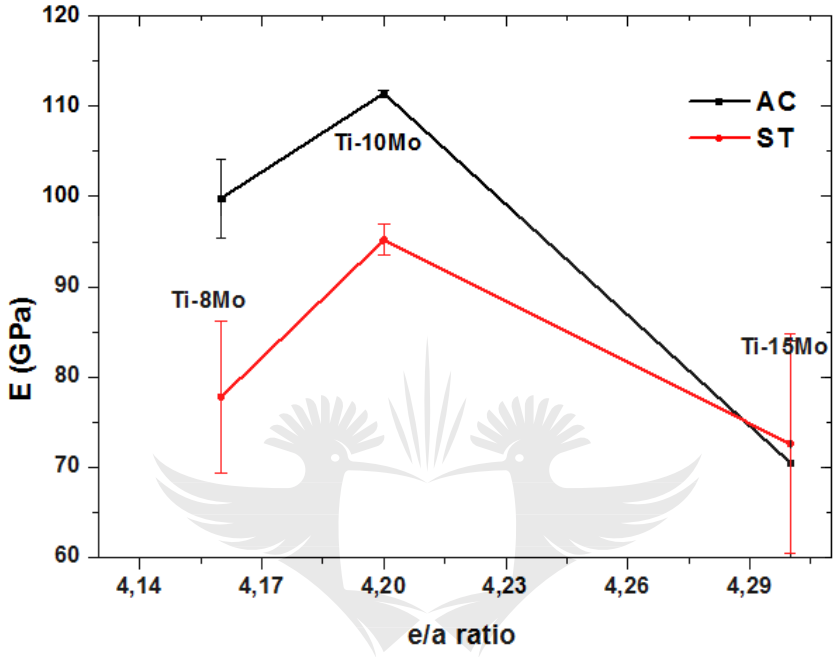

Figure 4-18. Variation of the elastic moduli of the AC/ ST Ti-Mo binary alloys with their e/a ratio.

4.2.2.3 D-electron theory

The elastic modulus is correlated with the Bo and Md parameters of the d-electron design theory. The elastic modulus generally decreases with increasing $\overline{Bo}$ and $\overline{Md}$ values in the β-Ti region in the Bo-Md phase stability map. The $\overline{Bo}$ and $\overline{Md}$ values of the Ti-Mo alloy series are given in Figure 3-3: Bo-Md phase stability map [94].. The values of moduli of elasticity for these alloys decrease with increasing $\overline{Bo}$ and $\overline{Md}$ values in β-type alloys region on the Bo–Md map [62]. In the case of the AC/ST Ti-Mo binary alloys, as the Mo content increases, the $\overline{Bo}$ value decreases, while the $\overline{Md}$ value increases. The elastic modulus increases at 10 wt% and then decreases at 15 wt%.

4.2.3 Elastic admissible strain

In orthopaedic applications, it is a requirement for ideal biomedical implant materials to have greater elastic admissible strain. The elastic admissible strain is defined as the ratio of the yield strength over the elastic modulus of a material and it is a useful parameter in orthopaedic applications. The greater the elastic admissible strain, the more desirable the material is for such applications [17,38,55,65]. Thus, a good biomaterial should have a higher permissible strain than human cortical bone (0.67). Figure 4-19 displays the elastic admissible strain of the AC Ti-8Mo, Ti-10Mo and Ti-15Mo alloy specimens in comparison with CP Ti, Ti6Al4V, Co-Cr and 316L Stainless steel (SS) [9]. The elastic admissible strain of the AC Ti-Mo binary alloy specimens are comparable to those of the human bone, CP Ti and CoCr material. On the contrary, the admissible strains are lower than that of Ti6Al4V alloy, but substantially higher than that of 316 L stainless steel. When comparing the admissible strains of the AC Ti-Mo alloy specimens among themselves, it is evident that AC Ti-10Mo alloy specimens possessed the lowest admissible strain, whereas AC Ti-15Mo alloy specimens had the highest admissible strain. In the case of the ST Ti-Mo alloy specimens, ST Ti-15Mo alloy specimens had the admissible strain that was comparable to those of the bone, CP Ti, Ti6Al4V and CoCr conventional orthopaedic implant materials, but substantially higher than that of 316L stainless steel. ST Ti-8Mo and ST Ti-10Mo alloy specimens exhibited lower admissible strains than the bone, CP Ti, Ti6Al4V, and CoCr materials, but higher than that of 316L stainless steel. When comparing the ST Ti-Mo alloy specimens among themselves, ST Ti-15Mo alloy specimen showed the highest admissible strain than ST Ti-8Mo and ST Ti-10Mo alloy specimens, which had comparable elastic admissible strains. Generally, it can be seen that the AC Ti-Mo binary alloy specimens had better elastic admissible strains than ST Ti-Mo alloy specimens. Based on the observations presented in Figure 4-19 and Figure 4-20, it can be concluded that AC Ti-8Mo, AC Ti-15Mo and ST Ti-15Mo alloy specimens would offer promising performance in practical applications in terms of mechanical compatibility.

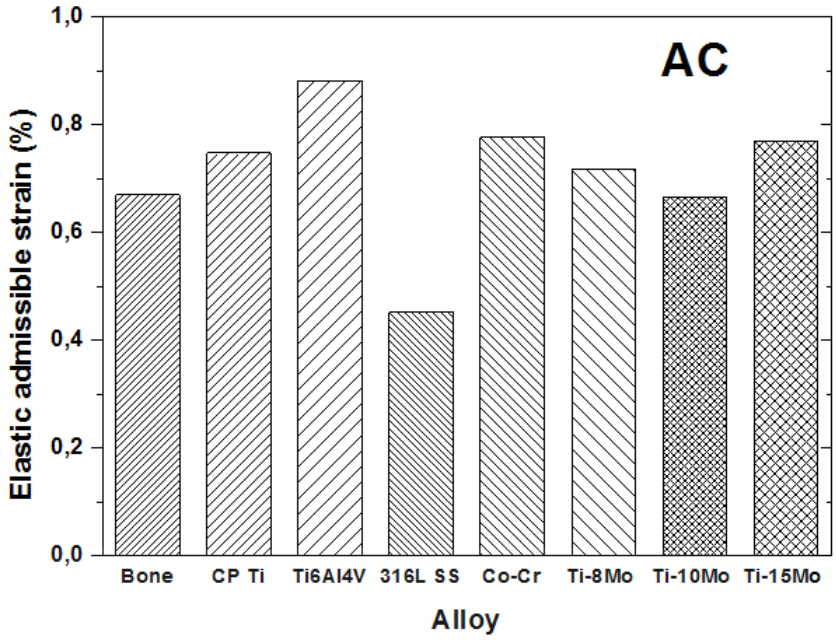

Figure 4-19: Elastic admissible strain of the AC Ti-Mo alloys and the conventional orthopaedic implant materials [20] considered for comparison.

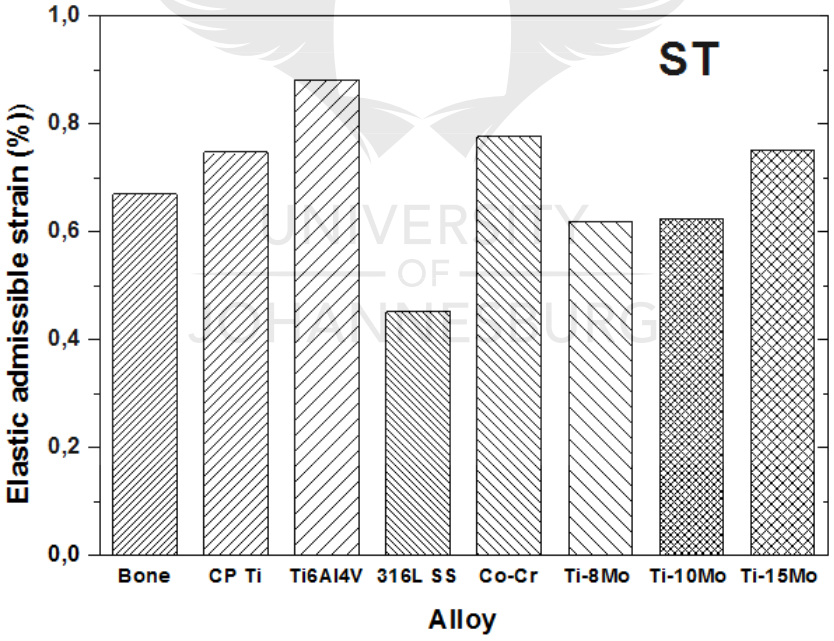

Figure 4-20: Elastic admissible strain of the ST Ti-Mo alloys and the conventional orthopaedic implant materials [20] considered for comparison.

4.2.4 Bending Properties

Figure 4-21 displays typical bending stress-deflection profiles of the AC Ti-Mo alloys condition. Ti-8Mo alloy specimen with the average fracture deflection of 2.5mm, exhibited a combination of brittle fracture behaviour and little ductile fracture behaviour. Contrary to that, Ti-10Mo and Ti-15Mo alloy specimens failed in a brittle manner at average fracture deflections of about 1 and 2mm, respectively. It is noteworthy that fracture in Ti-10Mo alloy was observed at the maximum load, where the fracture strength, maximum strength and yield strength were the same. The brittleness observed in all the Ti-Mo alloy specimens was attributable to the presence of the ω phase nano-particles, which is reported to induce embrittlement under applied stress [59,106,107]**.** The ω-induced embrittlement was also reported by Ho *et al.* in Ti-10Mo [98] and Ti-Cr [41] binary alloy and Lee *et al.* [38] in Ti-Nb binary alloys.

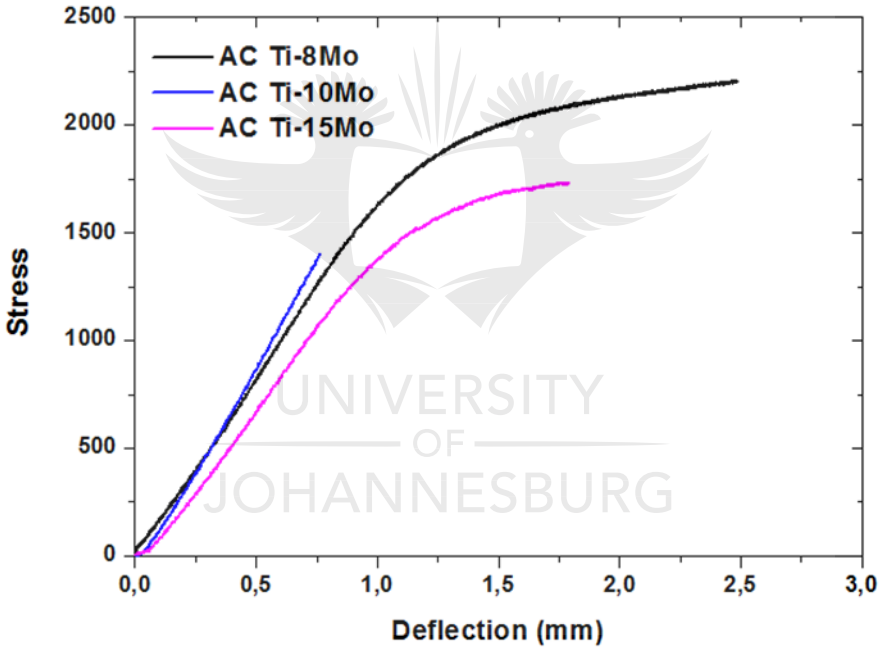

Figure 4-21: Bending stress-deflection of AC Ti-8Mo, Ti-10Mo and Ti-15Mo alloy specimens.

The bending stress-deflection profiles of the ST alloy specimen were also plotted and they are presented in **Fehler! Verweisquelle konnte nicht gefunden werden.**. The average bending deflections of the Ti-8Mo, Ti-10Mo and Ti-15Mo alloys were ≈ 7 mm, 4.5 mm and 9 mm, respectively. Ti-8Mo and Ti-15Mo alloys showed ductile fracture properties after solution treatment. However, Ti-10Mo alloy exhibited a combination of brittle and ductile fracture behaviour with an average fracture deflection of about 4.5mm. The brittleness originated from the ω_{ath} precipitates due to its brittle nature.

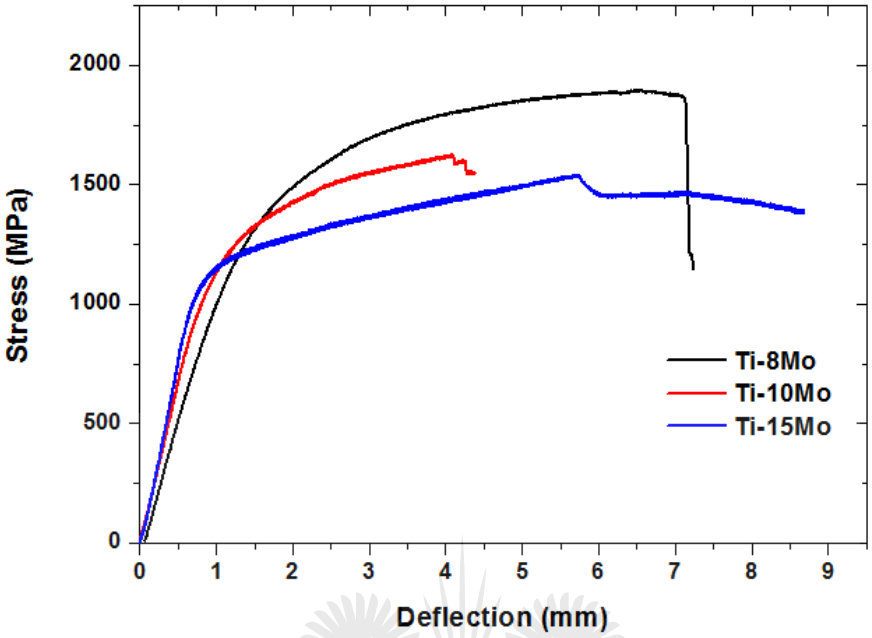

Figure 4-22: Bending stress-deflection of ST Ti-8Mo, Ti-10Mo, and Ti-15Mo alloy specimens.

When comparing the fracture behaviour of the ST with the AC alloy specimens, it is evident that solution treatment-induced considerable plasticity in all the alloys.

The effect of Mo content, i.e. β phase stability on the bending strength of Ti-Mo alloys was investigated and the bending strength variations are presented in Figure 4-23. The bending strengths of AC Ti-8Mo, AC Ti-10Mo and AC Ti-15Mo alloy specimens are 2070 ± 150.9 MPa, 1341 ± 233.3 and 1664 ± 173.1 MPa, respectively. The bending strength of AC Ti-8Mo alloy specimen was significantly higher than the bending strengths of AC Ti-10Mo and AC Ti-15Mo alloy specimens. Although the bending strength of AC Ti-15Mo alloy was generally higher than that of AC Ti-10Mo alloy, the increase in bending strength was not significant.

The effect of solution treatment on the bending strength of the Ti-Mo alloys was also evaluated and the bending strengths of ST Ti-8Mo, Ti-10Mo and Ti-15Mo alloy specimens are 1731 ± 14.5 MPa, 1529 ± 15.8 and 1627 ± 12.1 MPa, respectively. It can be seen that the bending strength of the ST Ti-8Mo alloy specimen was significantly higher than those of the Ti-10Mo and Ti-15Mo alloys. Meanwhile, the bending strength of the Ti-15Mo alloy was significantly

increased compared to that of the Ti-10Mo alloy. The bending strengths of the ST Ti-Mo alloy specimens exhibited a similar trend to that shown by the AC Ti-Mo alloy specimens.

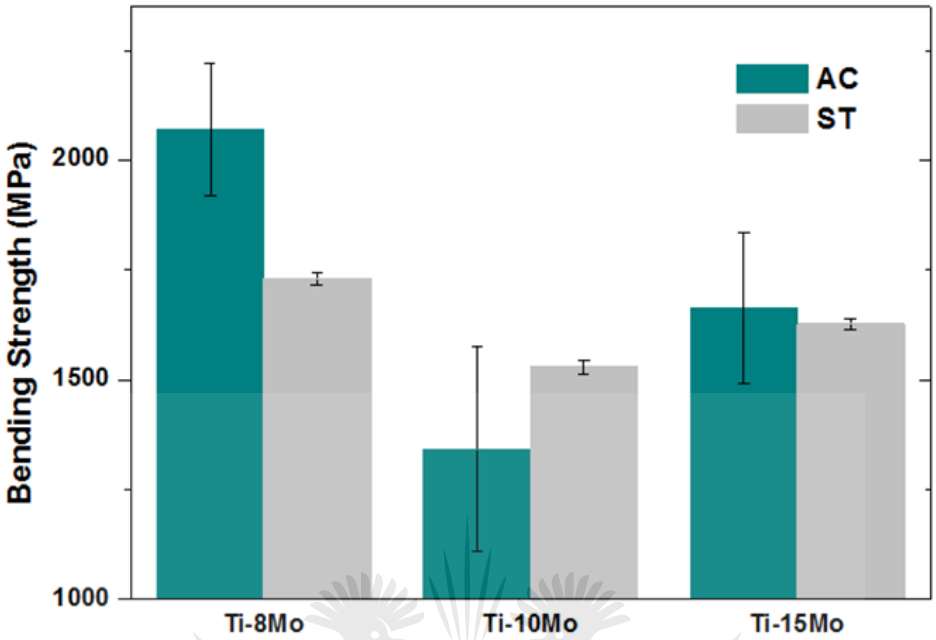

Figure 4-23: Bending strengths of the as-cast and solution treated Ti-8Mo, Ti-10Mo and Ti-15Mo alloys.

Ho *et al.* [33] reported bending strengths of 1750 MPa and 1440 MPa for AC Ti-10Mo and AC Ti-15Mo alloy specimens, respectively, which are considerably higher than the bending strength of the AC and ST Ti-10Mo alloy specimens in this study. The lower bending strengths could be ascribed to the premature, brittle fracture induced by the high proportion of the ω phase in alloys. The brittle nature of the ω phase causes embrittlement in metastable β-type alloys, which causes brittle fracture in the alloys which occurs prematurely, resulting in low strength. Bending strengths of the AC and ST Ti-15Mo alloy specimens investigated in this study were substantially higher than those reported by Ho *et al.* [33]. This could be due to the existence of the ω nanoparticles. Lee *et al.* [38] evaluated the effect of phase transformation on the bending strength and tentatively summarized in the sequence $\omega_{bending\ strength} > \alpha'_{bending\ strength} > \alpha''_{bending\ strength} > \beta_{bending\ strength} > \alpha_{bending\ strength}$. This suggests that the highest bending strength in AC/ST Ti-8Mo alloy specimens could be ascribed to the high volume fraction of the secondary α" phase and the ω nano-particles precipitated in the β phase matrix, while the lower bending strength in AC/ST Ti-15Mo alloy specimens was attributable to the increased stability of the β phase.

The variation of bending modulus of elasticity with Mo content i.e. β phase stability is illustrated in Figure 4-24. The bending moduli of AC Ti-8Mo, Ti-10Mo and Ti-15Mo alloy specimens are 80 ± 3.5 GPa, 92 ± 2.5 GPa and 57 ± 18.0 GPa, respectively. The bending modulus of the AC Ti-10Mo alloy was significantly increased relative to that of the AC Ti-8Mo alloy. Despite the high β stability in the AC Ti-10Mo alloy than in the AC Ti-8Mo alloy, the large volume fraction of the ω phase in the AC Ti-10Mo alloy specimen contributed to the high bending modulus. The AC Ti-15Mo alloy specimen exhibited the bending modulus of elasticity, which was significantly lower than those of the AC Ti-8Mo and Ti-10Mo alloy specimens. This was attributed to the high stability of the β phase and the significant suppression of the orthorhombic α" martensitic phase and hexagonal ω phase particles in the AC Ti-15Mo alloy. In general, the bending moduli of the AC Ti-Mo alloys exhibited a similar trend to that of the microhardness of the AC Ti-Mo alloy.

After solution treatment, ST Ti-8Mo, ST Ti-10Mo and ST Ti-15Mo alloy specimens had bending moduli of 60 ± 1.2 GPa, 79 ± 0.7 GPa and 67 ± 8.1 GPa, respectively. As in the AC condition, the bending modulus of the ST Ti-10Mo alloy was significantly higher than those of the ST Ti-8Mo and Ti-15Mo alloys. However, the bending modulus of the ST Ti-8Mo alloy was comparable to that of the ST Ti-15Mo alloy. The bending moduli of the ST Ti-Mo alloys exhibited a similar trend to that of the AC Ti-Mo alloy.

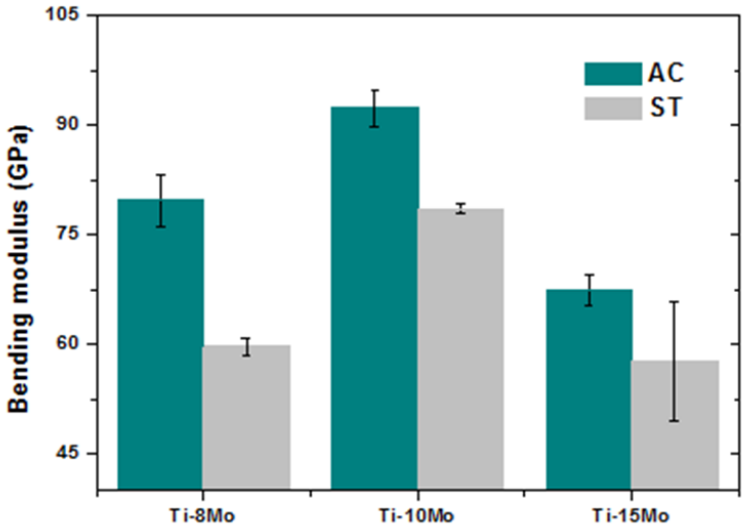

Figure 4-24: Bending modulus of the Ti-Mo binary alloy specimens.

The work of Ho *et al.* [33] indicated that the orthorhombic phase (with Mo concentration of 7.5 wt%) possessed a significantly lower bending modulus than all the β-phase Ti-Mo alloys. Moreover, among the β-phase containing Ti-Mo alloys Ho *et al.* [33] investigated, Ti-10Mo alloy specimen had the highest bending modulus, whereas Ti-15Mo alloy specimen possessed the lowest bending modulus. Ho *et al.* [98] further confirmed the highest bending modulus of elasticity in Ti-10Mo alloy to be induced by the high proportion of the ω phase. Similar to Ho *et al.* [33,98] observations, the bending moduli of Ti-10Mo alloy in both the as-cast and solution treated condition in this study were the highest among all the investigated Ti-Mo binary alloys, due to the large amount of the ω nanoparticles in the β matrix. A low elastic modulus results in large deflection even if the material possesses higher yield strength 108]. The results indicated that the β-dominated Ti-15Mo alloys had lower bending moduli than the other Ti-Mo alloys. Lee *et al.* [38] studied the effect of phase constituents on the bending modulus and tentatively summarized it in the order ω > α > α' > α" > β > α.

Figure 4-25 a) – c) illustrates the SEM micrographs of the fractured surfaces of the AC Ti-8Mo, AC Ti-10Mo and AC Ti-15Mo alloy specimens after bend tests, respectively. The micrograph of AC Ti-8Mo alloy specimen in Figure 4-25 a) shows cleavage facets, small region of dimples and some terrace-like morphology. These characteristics are consistent with the quasi-fracture behaviour indicated by the stress-deflection curve of the AC Ti-8Mo binary alloy observed in Figure 4-21. The fractograph of the AC Ti-10Mo alloy specimen Figure 4-25

b) is characterized by cleavage facets, which indicate that the alloy specimen had undergone brittle fracture. This observation is in agreement with the brittle fracture behaviour exhibited by the stress-deflection curve of this alloy Figure 4-21. In the fractured surface of the AC Ti-15Mo alloy specimen in Figure 4-25 c), intergranular cracks were observed. The brittle behaviour observed in all the AC Ti-Mo binary alloy specimens could be attributed to the presence of the ω phase, which is known to induce embrittlement in metastable β-type Ti alloy systems such as Ti-Nb-Fe and Ti-Mo-Fe [109].

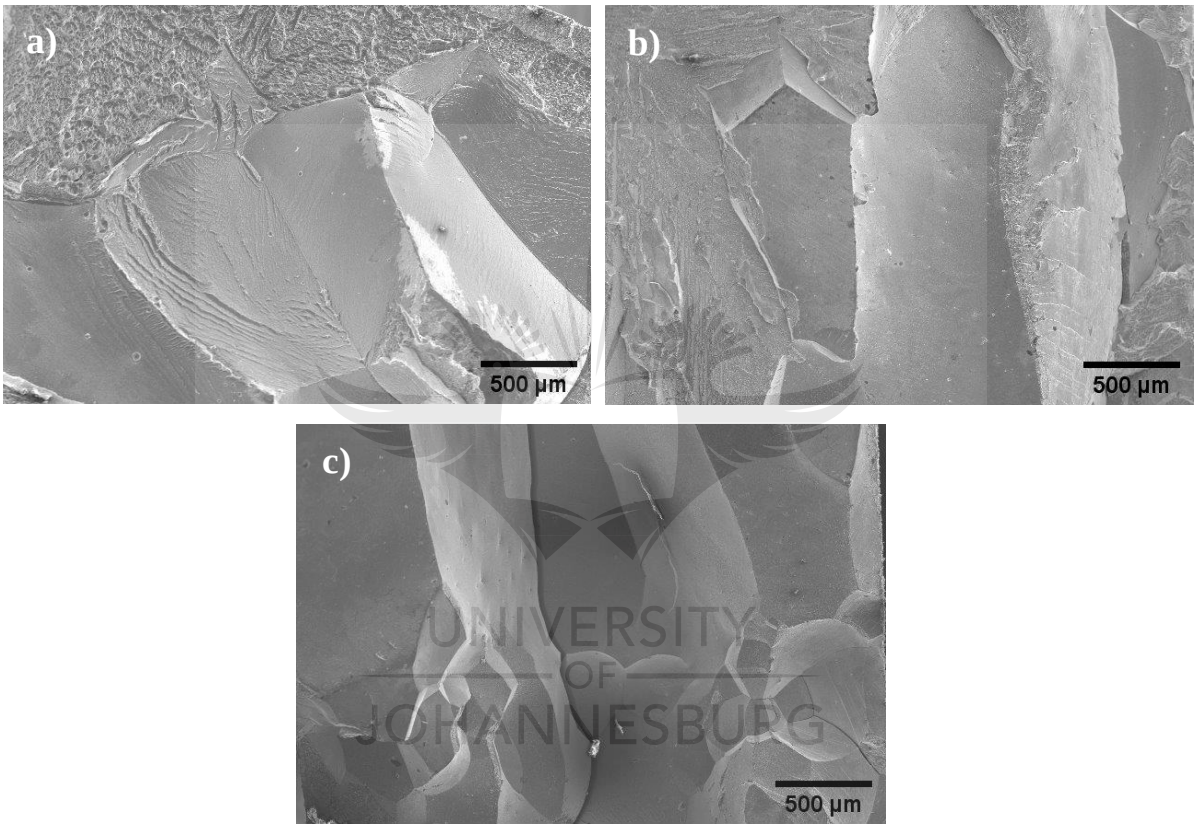

Figure 4-25: Fracture surfaces of the AC a) Ti-8Mo, b) Ti-10Mo and c) Ti-15Mo binary alloys after bend test.

4.2.5 Compressive properties of the alloy series

Typical room temperature compressive stress-strain curves of the ST Ti-Mo alloy specimens are displayed in Figure 4-27. It is evident that under compression, the alloys showed considerable plastic deformation. It can be clearly seen that no cracking or fracturing occurred during compression tests. It is noteworthy that the compression tests were stopped after the

strain of about 12 % [3]. The average compressive properties of the ST Ti-Mo alloy specimens are listed in Table 4-6. ST Ti-8Mo alloy specimens exhibited the highest compressive strength and compressive yield strength, while ST Ti-10Mo alloy specimen showed the lowest compressive strength and compressive yield strength. The compressive elastic modulus of ST Ti-10Mo alloy specimen was the highest, while the compressive elastic modulus of ST Ti-15Mo binary alloy was the lowest. The compressive elastic modulus trend was similar to the one in tensile elastic modulus. Zang *et al.* [44] reported a compression elastic modulus, yield strength and compressive strength of 18.388 GPa, 617.89 MPa and 2084. 57 MPa in AC Ti-15Mo alloy, respectively. This alloy possessed lower compressive yield strength, higher compressive strength and lower elastic modulus than the Ti-15Mo alloy in this study. A previous study by Li et al. [99] indicated that the compressive elastic modulus, compressive strength and yield strength of AC Ti-10Mo alloy were 25,082 GPa, 1092,026 MPa and 507,919 MPa, respectively. This alloy exhibited lower compressive strength and compressive yield strength than the CT Ti-10Mo alloy specimen in this study, while the compressive elastic moduli were comparable. In a study conducted by Lu *et al*. [110], the compression yield strength and elastic modulus of Ti-(6-14)Mo binary alloys ranged between 1800–2182 MPa and 71–85 GPa, respectively, which were larger those obtained the ST Ti-15Mo alloy specimen in this study. The higher strength and elastic modulus values were attributed to the presence of a small amount of fine α lath precipitated from the β phase.

[3] According to the technician, the laboratory stops compression tests at strains of about 12 % as a condition under which the equipment can be operated safely.

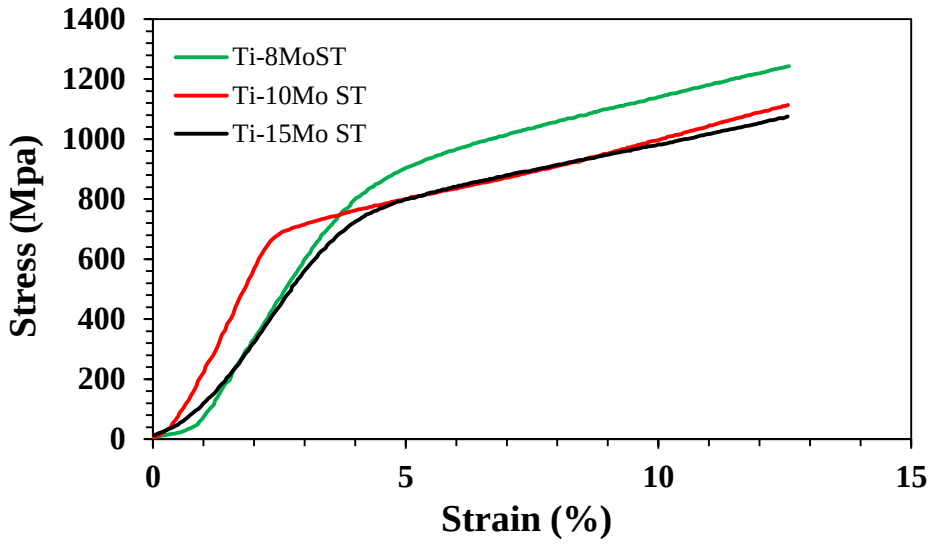

Figure 4-26. Figure 4-27: Compression stress-strain curves of ST Ti-Mo binary alloys.

Table 4-6: Compressive properties of the ST Ti-Mo binary alloys

Alloy	**Compressive strength (MPa)**	**Compressive yield strength (MPa)**	**Elastic modulus (GPa)**	**Reference**
Ti-8Mo	1262	831	20	This study
Ti-10Mo	1103	657	26	This study
Ti-15Mo	1193	709	13	This study
AC Ti-10Mo	1092,026	507,919	25,082	[98]
AC Ti-15Mo	2084. 57	617.89	18.388	[44]

4.3 Effect of Nb and Zr on the microstructural evolution of [Mo($Ti_{14-x}Zr_x$)]Nb_yTi_z alloy series.

Solid-state phase transformation is a function of the cooling rate after the solidification of alloys from the high-temperature liquid. Depending on the cooling rate, solid-state phase transformation reported in Ti alloys mainly include β → α, β → α′, β → α", β → ω, etc.. In this study, all the designed alloys were fabricated in a water-cooled copper crucible through arc melting. Therefore, the cooling rate was expected to be sufficiently high for the microstructures of the alloy specimens to undergo a complete solid-state phase transformation. Furthermore, Ti, Mo and Nb have the same structure type, space group and similar crystal lattice. Therefore, they can dissolve in each other and form the metastable β phase at high-temperatures [77,100,111].

The microstructural observations of the AC/ST Ti-Mo binary alloys demonstrated that phase evolution is strongly dependent on the concentration of the Mo β-stabilizing element. The transformation of the high-temperature β phase to martensitic α" phase decreased with increasing Mo concentration, while the β phase stability increased. Furthermore, the precipitation of the ω phase was also evident, however, its volume fraction was substantially reduced in Ti-15Mo binary alloy specimens.

4.3.1 Phase analysis of AC and ST designed alloys.

Phase constituents of the AC/ST Mo($Ti_{14-x}Zr_x$)]Nb_yTi_z alloy series were determined using the conventional X-ray diffraction analysis. The XRD patterns of the AC TMT, TMN1, TMN2, TMN3 and TMNZ alloys with identified phases are exhibited in Figure 4-28. As illustrated, the expected BCC β phase diffraction peaks were detected in the XRD patterns of all the alloys. Furthermore, diffraction peaks corresponding to the martensitic α" phase were also identified, indicating that the martensitic transformation start temperature was above room temperature, thus allowing for the transformation of the high-temperature β phase to α" phase. In all the XRD patterns, small peaks at 2θ≈34° could also be distinguished and were identified as the ω phase. The weak intensity of the ω phase peak could be attributed to its quite small size or volume fraction. A similar ω peak was reported by Sadeghpour in the ST Ti-Al-Mo-V-Cr alloy system [112]. The presence of the ω phase was also observed in metastable β-type Ti alloys from previous studies by the conventional XRD at a low scanning rate [113,114].

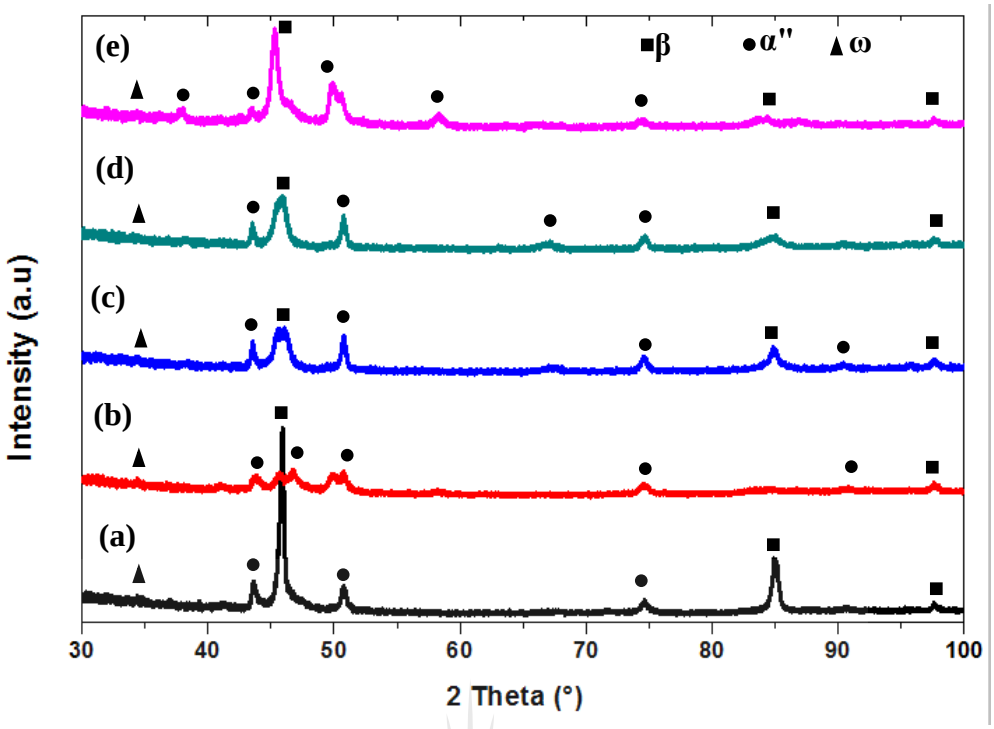

Figure 4-28. XRD patterns of AC a) TMT, b) TMN1, c) TMN2, d) TMN3 and e) TMNZ alloy specimens.

In the XRD pattern of AC TMN1 ternary alloy specimen, the intensity of the β phase peak at 2θ≈45° was increased significantly in comparison with that of the AC TMT binary alloy specimen. This increase in the intensity of the β phase peak indicates that the substitution of the Ti glue atom with the third element Nb (one atom) increased the stability of the β phase in the alloy. Substitution of the Ti glue atom with two Nb atoms improved the stability of the β phase as indicated by the slightly increased intensities of the β phase peaks at 2θ≈45° and 83° in the XRD pattern of TMN2 alloy specimen. The intensities of the β phase peaks at 2θ≈45° and 83° in the TMN3 ternary alloy specimen were substantially reduced, whereas the peak at 2θ≈65° was slightly increased in comparison with TMN2 ternary alloy specimen. This suggests a decrease in the volume fraction of the β phase when the Ti glue atom was substituted with three Nb atoms. In the XRD pattern of TMNZ alloy specimen, the intensity of the β phase peak at 2θ≈45° was stronger than the one in the XRD patterns of all the TMN alloys, suggesting that the addition of Zr contributed to the increase instability of the β phase. In comparison with XRD results from previous studies, the XRD pattern of both TMN and TMNZ alloy specimens consisted of diffraction peaks corresponding to a single β phase, which suggested that the precipitation of martensitic α" phase and the athermal ω phases was suppressed [58,63,64].

It is known that the stability of the β phase in metastable β-type Ti alloys is dependent on their composition. Microalloying of Ti with low concentrations of the β-stabilizing elements results in Ti alloys containing the martensitic phases (α'and/ or α"). The transformation of the β phase to the martensitic phases is suppressed during quenching when the concentration of the β-stabilizing elements is sufficiently high [109]. The formation of the ω nano-particles is reported to occur over a limited composition range in metastable β-type Ti alloys [34]. Therefore, the formulated compositions in this study fall within the limited range in metastable β-type Ti alloys that precipitate the β phase upon rapid cooling. Additionally, the concentration of the β-stabilizing elements could have not been ideal to reduce the martensitic transformation start temperature to below room temperature, as a result, the transformation of the β phase to the α" martensitic phase occurred.

In comparison with the XRD results obtained from literature, the XRD patterns of AC TMT, TMN1, TMN2, TMN3 and TMNZ alloy specimens consisted of diffraction peaks corresponding to a single β phase, which suggested that the martensitic transformation start temperature was reduced to below room temperature [58, 63,64]. In this study, the precipitation of the martensitic α" phase and the athermal ω phase could be attributed to the cooling mode undertaken.

By careful comparison, it can be seen that the diffraction peak of the β phase at 2θ≈45° in the XRD patterns of AC TMN1, TMN2, TMN3 and TMNZ alloy specimens slightly shifted to the left relative to the AC TMT binary alloy specimen. It was reported that Zr and Nb have atomic radii that are larger than that of Ti, which may cause the substitution of Ti atoms with Zr atoms, and thus shifting the β phase peaks toward the left [99,115,116]. Therefore, the substitution of Ti with Nb in the glue site and/or with Zr in the cluster shell led to the slight shifting of the β phase peak towards the left. These XRD results are similar to previous studies conducted on Ti-Mo-Si [99] and Ti-Nb-Fe [109] alloy systems.

The XRD patterns of ST TMT binary, TMN1, TMN2, TMN3 ternary and TMNZ quaternary alloys are exhibited in Figure 4-29. The XRD patterns of all the solution treated alloy specimens also revealed the martensitic α" phase peaks and the BCC β phase peaks. Moreover, the small peak at 2θ≈34° that corresponds to the ω phase was observed only in the XRD patterns of the TMN1 alloy specimen. In the XRD patterns of TMN2 and TMN3 ternary alloy

specimens, the intensities of the β phase peak at 2θ≈45° were significantly increased in comparison with the TMN1 ternary alloy specimen, whereas the intensity of the split martensitic α" peak at 2θ≈49/51° in TMN3 ternary alloy specimen was reduced in compared to TMN1/2 ternary alloy specimens. The substitution of the Ti atom in the cluster shell with one Zr atom in TMNZ quaternary alloy specimen resulted in a significant decrease in intensity of the β phase peak β at 2θ≈45° and further combined the split peaks of the martensitic α" at 2θ≈49/51° into one peak at 2θ≈50°.

It can be seen that the XRD patterns of the solution treated alloys exhibited more martensitic α" martensitic phase peaks than the XRD patterns of the as-cast alloys. This suggests that the martensitic transformation start temperature was reached while only a small amount of the β phase was retained during solution treatment compared to casting [81]. Hence the more α" phase was predicated during solution treatment. Hence higher volume fraction of the martensitic α" phase was precipitated in the solution treated alloy specimens than in the as-cast alloy specimens. Furthermore, the peak corresponding to the ω phase in the TMN2, TMN3 and TMNZ alloy specimens disappeared after solution treatment, suggesting that solution treatment contributed to the suppression of the formation of the ω phase. This strongly indicates the dependence of phase transformation on cooling mode.

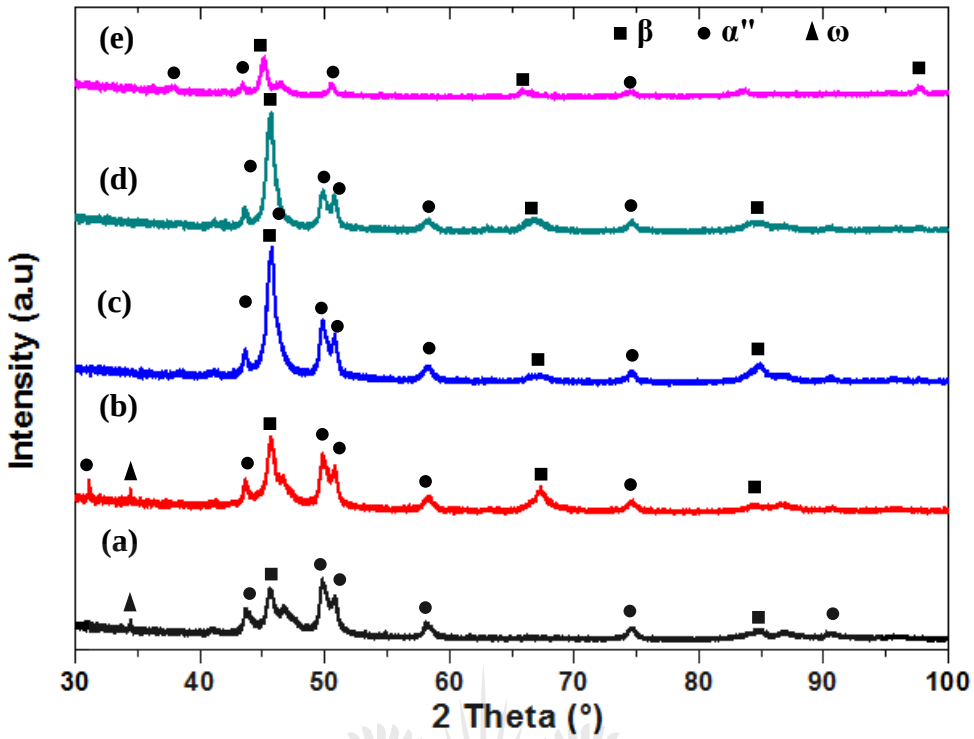

Figure 4-29: XRD patterns of ST a) TMT, b) TMN1, c) TMN2, d) TMN3 and e) TMNZ alloy specimens.

The XRD patterns of the AC and ST TMT binary alloy specimen with identified phases are exhibited in Figure 4-30 a). It can be seen that after solution treatment, more martensitic α" phase was precipitated as indicated by the additional peaks at 2θ≈ 47˚, 50˚, 58˚, 87˚ and 91˚. This suggests that the martensite start transformation temperature of the TMT alloy during quenching following solution treatment was substantially higher. Moreover, the ω phase was detected after solution treatment as shown by the peak at 2θ≈34°. Meanwhile, the intensities of the β phase peaks 2θ≈43°, 83°and 98° were substantially reduced. Generally, the XRD findings of the TMT alloy showed that precipitation of the secondary martensitic α" phase and the ω phase was increased, while the less β phase was retained upon quenching.

Similar to the TMT alloy, the precipitation of the secondary α" and ω phases in the TMN1 alloy specimen shown in Figure 4-30 b) was enhanced after solution treatment. The β phase peak at 2θ≈ 98° in TMN1 alloy disappeared, while an additional peak at 2θ≈65° emerged. Moreover, the intensity of the existing β phase peak at 2θ≈43° increased substantially. A slight increase in the intensity of the ω phase peak was also observed, while the intensity of the martensitic α" phase peaks became stronger and an additional peak appeared at 2θ≈32°. Generally, the precipitation of the secondary phases in the TMN1 alloy was slightly increased.

In Figure 4-30 c), the XRD patterns of the TMN2 alloy exhibited strong intensities of the β phase peaks after solution treatment. An additional α" phase peak was also detected at 2θ≈ 50°. Generally, solution treatment of the TMN2 alloy led to a slight enhancement of precipitation of the secondary phases. Similar observations were evident in the XRD patterns of the TMN3 alloys shown in Figure 4-30 d). The intensity of the β phase peak at 2θ≈43° was stronger than in the AC condition. In Figure 4-30 e), the XRD patterns of the TMNZ alloy showed that the β phase peak at 2θ≈43° was substantially reduced after solution treatment. Generally, no significant change in the peaks of the α" and ω phases was evident.

For all the designed alloy, the diffraction patterns exhibit strong β phase peak intensities corresponding to the large volume fraction of the BCC β phase and weak α" martensitic phase peak intensities corresponding to the small volume fraction of the α" phase. The peak corresponding to the athermal ω phase was also evident in some of the designed alloys.

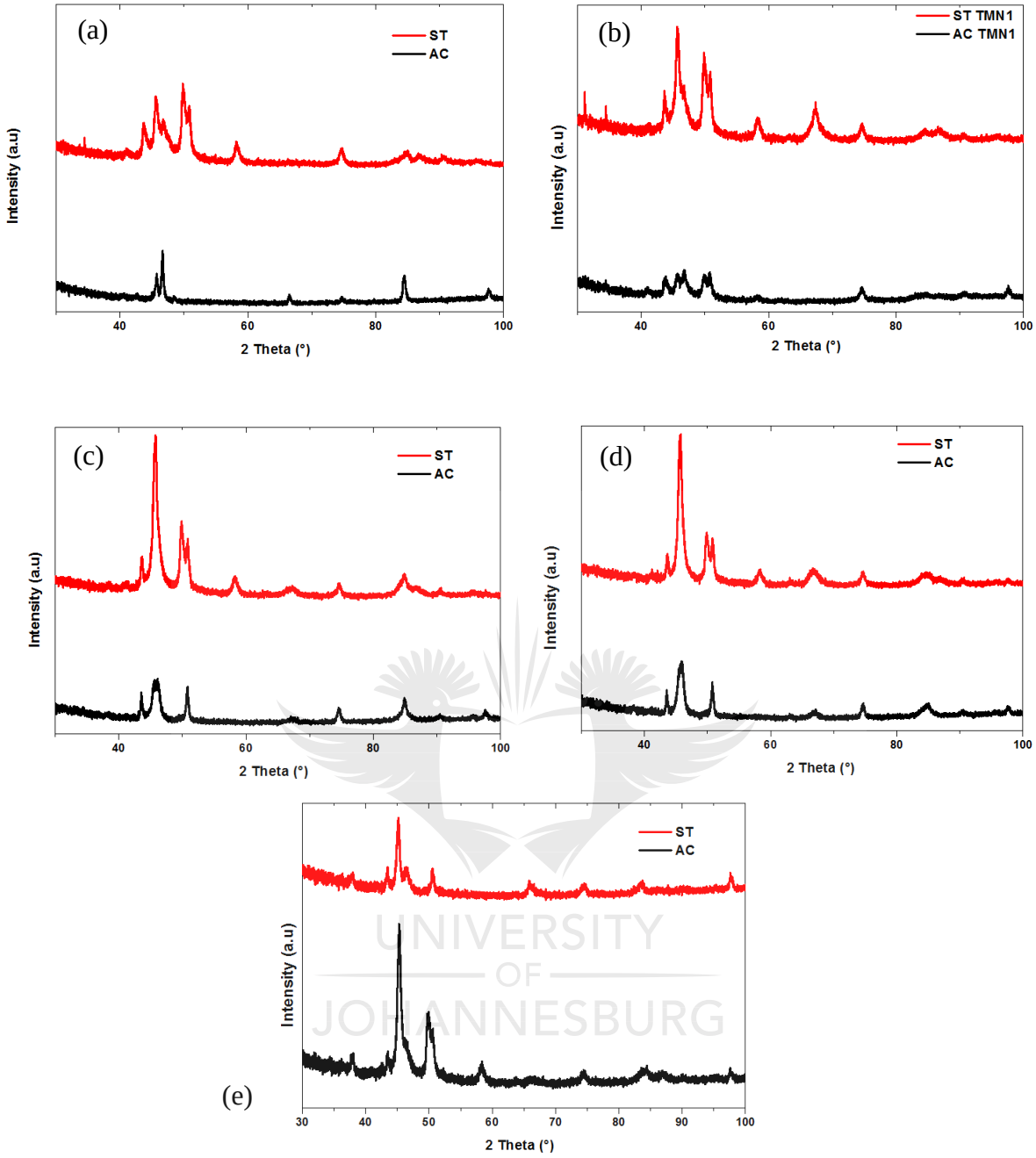

Figure 4-30. Comparison of XRD patterns of AC and ST a) TMT, b) TMN1, c) TMN2, d) TMN3 and e) TMNZ alloys.

4.3.2 Microstructural Characteristics

4.3.2.1 *Optical Microscopy Observations*

Typically etched microstructures under optical microscope of AC TMT binary, TMN1, TMN2 and TMN3 ternary, and TMNZ quaternary alloys are displayed in Figure 4-31 a) - e). These microstructures exhibited the predominant large equiaxed β phase grains. The grain boundaries of the original high-temperature β phase could also be distinguished in all the micrographs. Further etching resulted in the appearance of the sub-grain structures throughout the primary grains. Similar microstructural observations were reported by Ozan *et al.* [59] in their study on an as-cast Ti-Ta-Zr-Nb alloy series which showed sub-grains with peaks corresponding to a single β phase in their XRD patterns. The appearance of sub-grain structures in the microstructures was ascribed to compositional differences. The formation of sub-grain structures in as-cast metastable β-type Ti alloys has also been reported in other previous research studies [80].

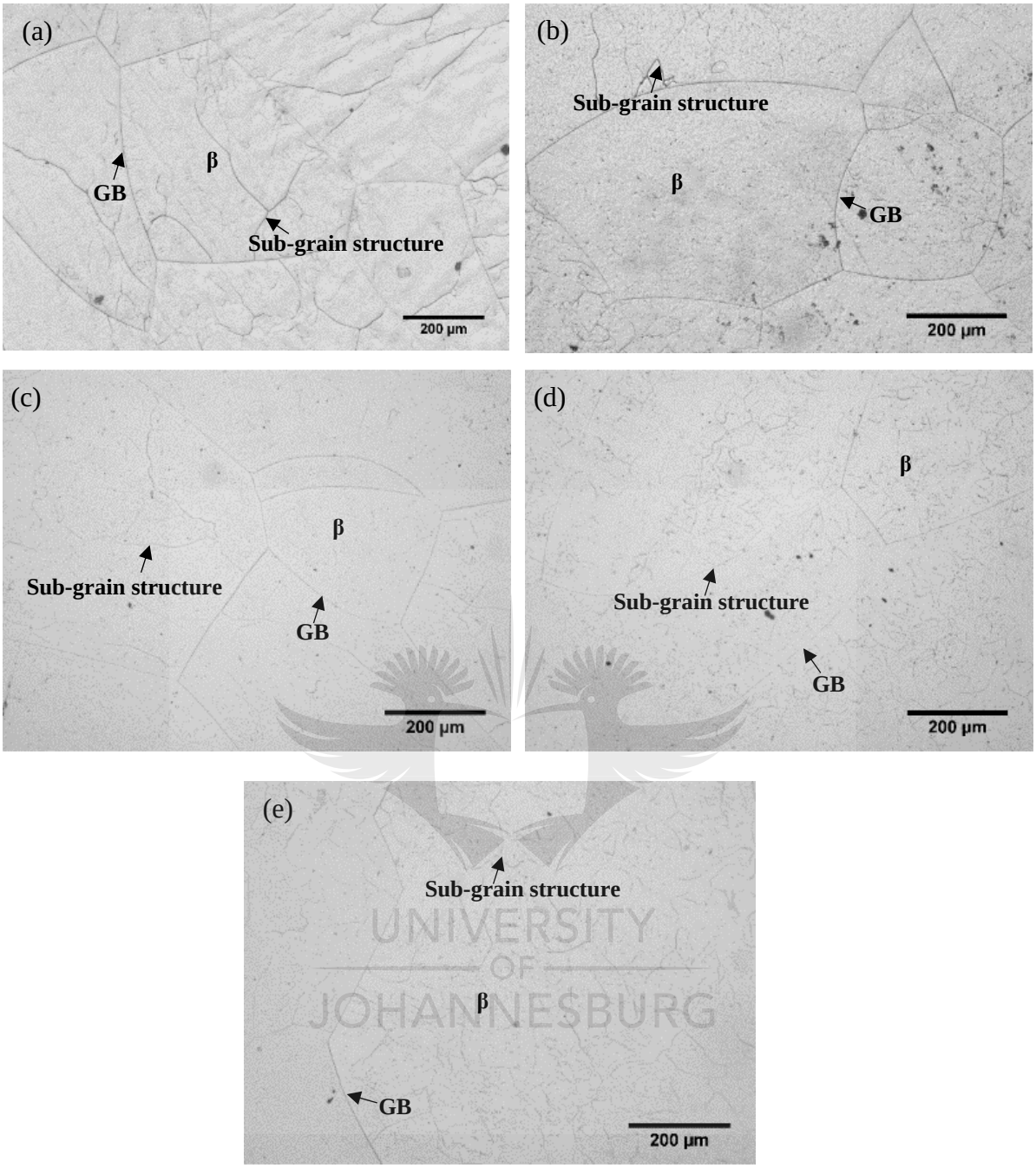

Figure 4-31: Optical micrographs of AC a) TMT, b) TMN1, c) TMN2, d) TMN3 and e) TMNZ alloys.

Dendritic structures from cooling are minimal and no precipitation of the martensitic α" and/or the ω phase observed. The dark regions and pots resemble pitting corrosion, which occurred during to etching of polished surfaces, being favoured by internal tensions on the surface, creating regions where chemical kinetics of the reaction is accelerated [117]. These observations are not consistent with the results from previous studies. In a study performed by Wang *et al.* [63] and Tulugan *et al.* [64], the microstructure of AC TMT binary alloy, which

was made up of Ti and Mo, comprised columnar crystals. The microstructure of AC TMN (which was made up of Ti, Mo and Nb) ternary and the TMNZ quaternary alloys (which was made up of Ti,Mo, Nb and Zr) was constituted of fine dendrites, which were induced by the presence of Nb and Zr. Similar optical micrographs were reported in the as-cast Ti-Ta-Hf-Zr [54], Ti-Nb-Sn-Cr [118], Ti-Nb-Zr [115], Ti-Ta-Zr-Nb [59] alloy systems.

Figure 4-32 a) – e) exhibits the optical microscopy images ST TMT, TMN1, TMN2, TMN3 and TMNZ alloys. Although traces of the martensitic α" phase were clearly visible in the XRD patterns of all the solution treated designed alloy specimens, this phase could not be observed in the optical micrographs. As a result, all the alloys were dominated by the coarse equiaxed grains of the single β phase microstructures retained upon quenching in ice water from the β phase region above the β-transus to room temperature and primary grain boundaries, which appeared first during etching. The sub-grain structures observed in the β grains of the as-cast alloy specimens were not present in the microstructures of solution treated alloy specimens, which suggested that the compositional differences were minimal in the solution treated alloys. The black spots represent etch pits that developed during extended etching time and could be seen in all specimens. These microstructural observations are similar to those of solution treated titanium alloy systems containing β-stabilizing elements such Ti-6Mo-6V-5Cr-3Sn-2.5Zr alloy [119].

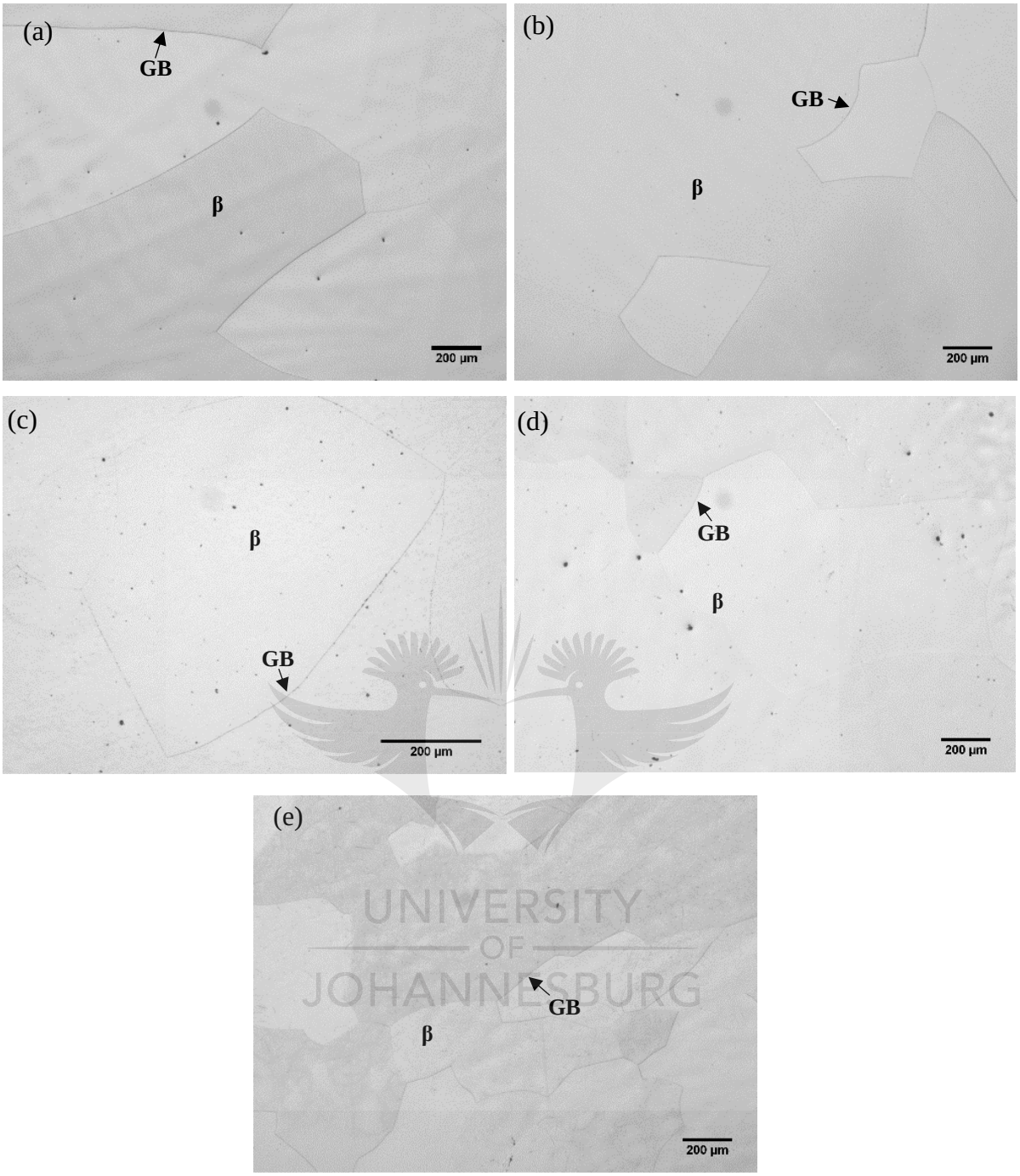

Figure 4-32: Optical micrographs of a) TMT, b) TMN1, c) TMN2, d) TMN3 and e) TMNZ ST alloys.

The microstructures of the designed alloys in both AC and ST conditions generally comprised predominant β phase and sub-structures. No features corresponding to the martensitic α" phase were observed.

4.3.2.2 *Scanning electron microscopy observations*

Figure 4-33 presents the scanning electron micrographs of the AC [Mo($Ti_{14-x}Zr_x$)]Nb_y Ti_z alloy series. The microstructures of all the alloys show coarse equiaxed grains of the BCC β phase with visible primary grain boundaries and sub-grain structures in the equiaxed β phase grains. Although no precipitation of the martensitic α" and/or the ω phase observed, etch pits were visible. These microstructures are consistent with the optical microscopy results but do not corroborate the XRD results, which detected small peaks corresponding to the martensitic α" phase.

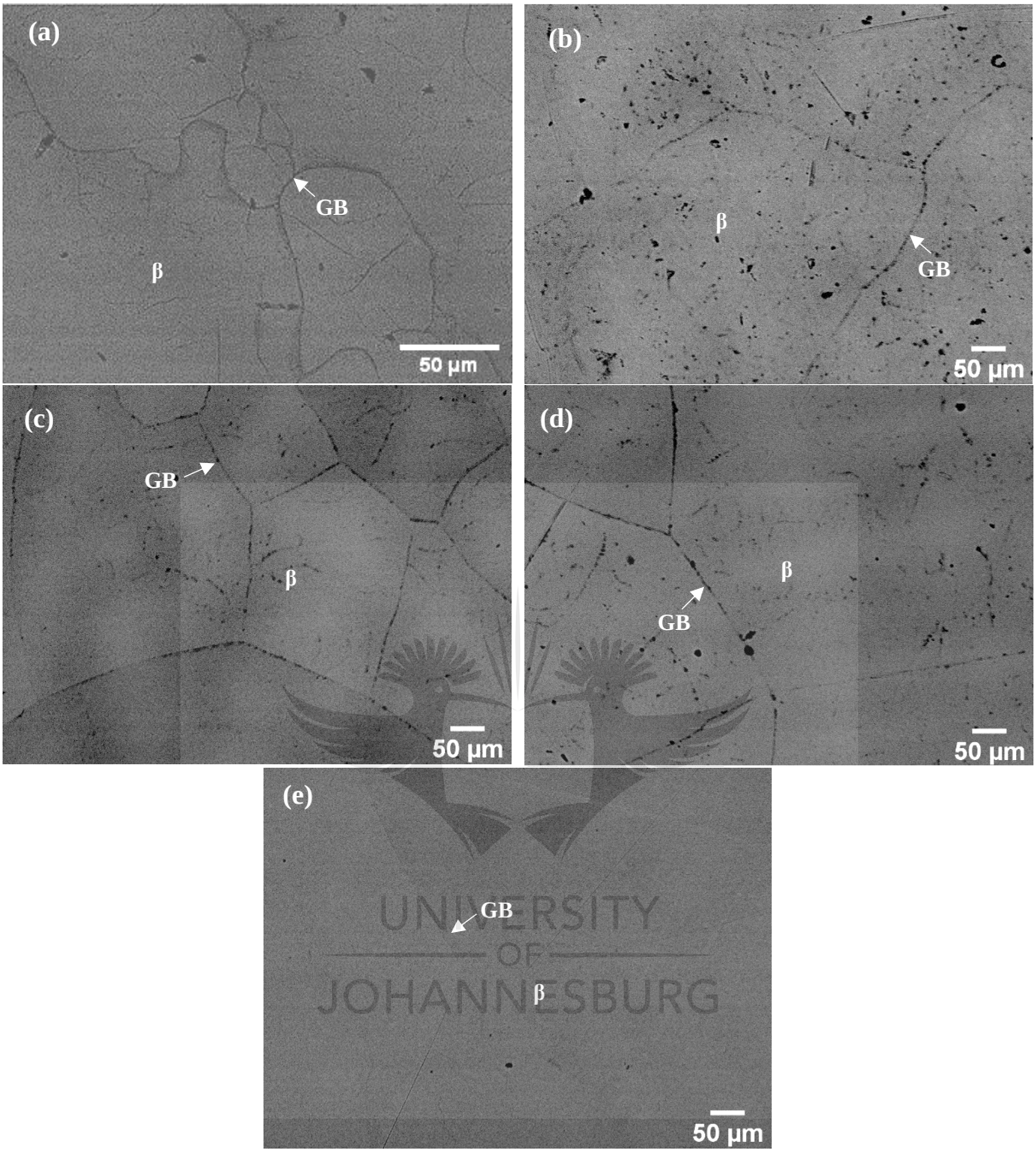

Figure 4-33: SEM images of AC a) TMT, b) TMN1, c) TMN2, d) TMN3 and e) TMNZ alloys.

Figure 4-34. a) - e) presents the scanning electron micrographs of ST TMT, TMN1, TMN2, TMN3 and TMNZ alloy specimens. It can be seen that the microstructures of all the alloy specimens consist of large β phase grains with visible grain boundaries. No microstructural features corresponding to the martensitic phases and the athermal ω phase were revealed. These SEM observations are similar to the optical microscopy findings. Similar SEM results have also been reported in a study by Bahl *et al.* [12], who observed a single β phase after quenching from a temperature above the β-transus in Ti-Nb-Sn ternary alloy series. The ω and α″

secondary phases could not be observed, due to the presence of the high amount of Sn, which is known to suppress their formation upon quenching or ageing, thereby retaining the single β phase.

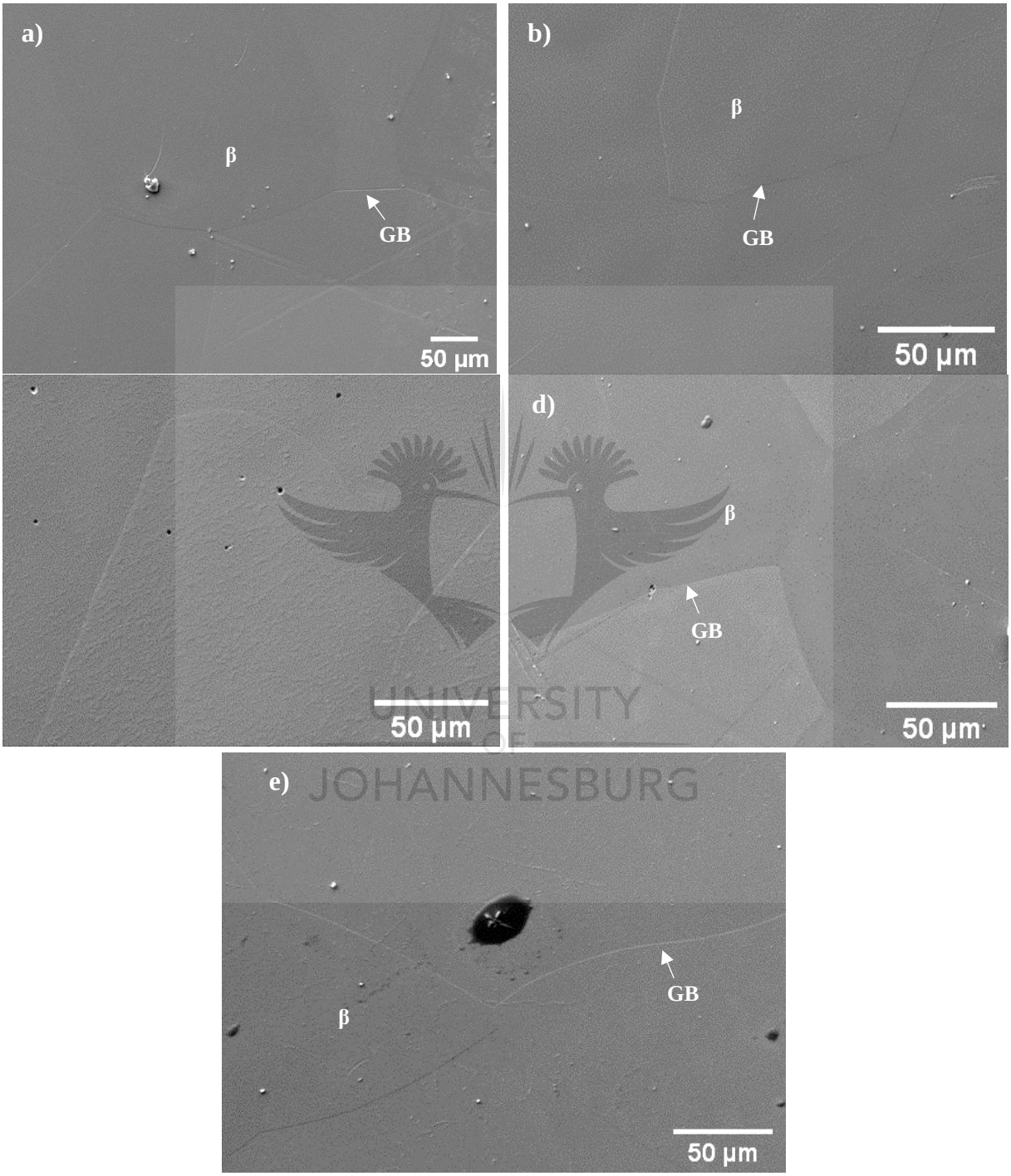

Figure 4-34. SEM micrographs of ST a) TMT, b) TMN1, c) TMN2, d) TMN3 and e) TMNZ alloys.

The microstructures of the designed alloys in both AC and ST conditions under the SEM generally consisted predominantly of β phase, with no traces of the acicular structures of the martensitic α" phase.

4.3.2.3 *EBSD results*

Figure 4-35 a) – e) exhibits the inverse pole figure maps (IPF) of AC TMT, TMN1, TMN2, TMN3 and TMNZ alloy specimens. It should be noted that the scale bars in the IPF maps of TMN3 and TMNZ alloys are different from the ones in the IPF maps of TMT, TMN1 and TMN2 alloys. The experimentally observed microstructures of AC TMT, TMN1, TMN2 and TMNZ alloys are composed of coarse, equiaxed β phase grains with average grain sizes. The grain boundaries of the high-temperature β phase and some nano-sized particles precipitated in the β phase matrix and along the grain boundaries could also be distinguished. On the other hand, the microstructure of AC TMN3 alloy specimen exhibited elongated, equiaxed β grains. The development of elongated grains is reported in deformed materials [120]. These alloys were still in the as-cast condition, and therefore the mechanism behind the development of the elongated grains needs to be investigated. The investigation will form part of the future work.

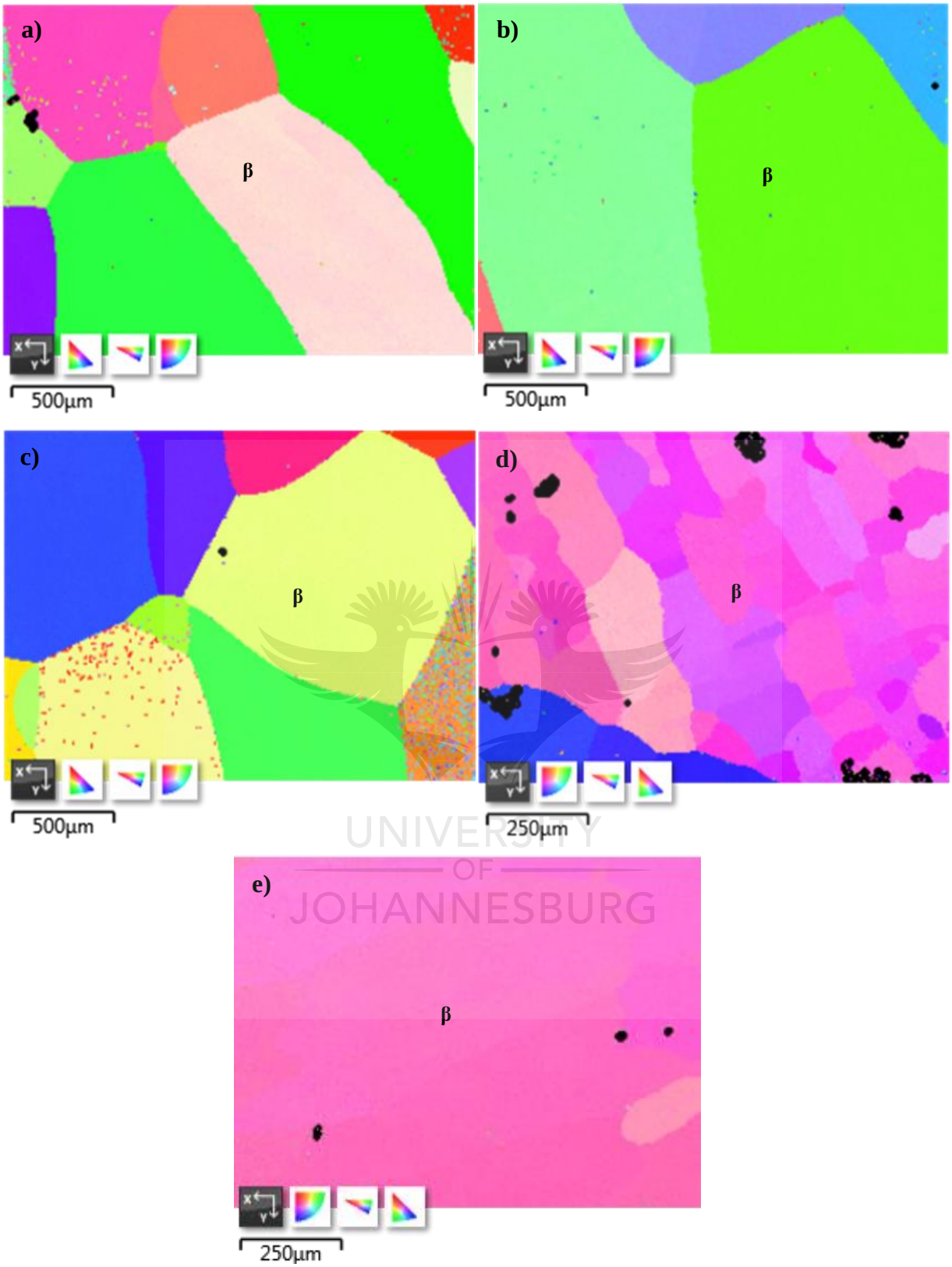

Figure 4-35: EBSD IPF maps of a) TMT, b) TMN1, c) TMN2, d) TMN3 and e) TMNZ AC alloys.

To identify these nano-sized particulates and verify the phase constituents observed in the x-ray diffraction, optical microscopy and scanning electron microscopy analysis, electron

backscatter diffraction analysis was performed. The generated phase maps are clearly illustrated in Figure 4-36 a) - e). The nano-sized particulates observed in the inverse pole figure maps of the AC TMT, TMN1, TMN2, TMN3 and TMNZ alloy specimens were identified in the phase maps as the orthorhombic α" martensitic phase and the hexagonal ω phase. It is noteworthy that the α" phase and the hexagonal ω phase in the phase maps of TMT, TMN1 and TMN2 alloys are represented by the colour yellow and blue, respectively. Conversely, the α" phase and the hexagonal ω phase in the phase maps of TMN3 and TMNZ alloys appear as blue and yellow, respectively. It can be seen that precipitates of the hexagonal ω phase and the orthorhombic α" phase coexisted in the β matrix of the binary TMT alloy. However, the volume fraction of the hexagonal ω phase precipitates decreased after the substitution of the Ti atom in the glue site with the one Nb atom.

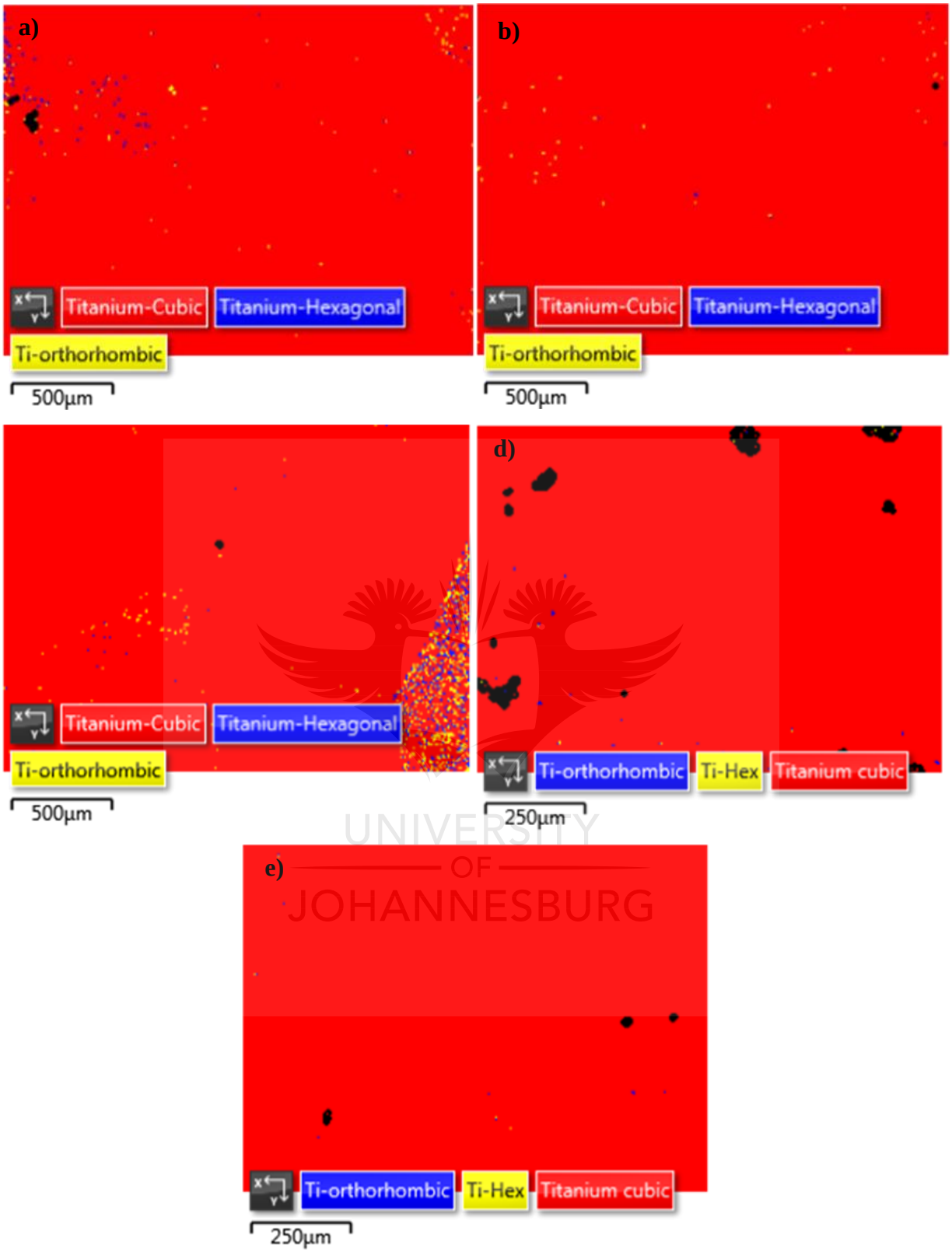

Figure 4-36: EBSD phase maps of AC a) TMT, b) TMN1, c) TMN2, d) TMN3 and e) TMNZ alloys

The existence of the ω phase has been observed in microstructures of other metastable β-type Ti alloys such as the as-cast Ti-Ta-Hf-Zr [54] and Ti-Ta-Zr-Nb[59] alloy series. In previous

studies, microstructural analysis of Ti-11.8Mo alloy revealed the presence of β and ω_{ath} phases, while Ti-11.1Mo-10.8Nb alloy was made up of β, ω_{ath} and α" phases [58]. Zr suppresses the transformation of the β phase to athermal ω phase in metastable β-type Ti alloys upon quenching from above the β-transus [59,120,121]. This observation from the literature is consistent with the findings in this study, in which the precipitation of the ω phase in the TMNZ alloy was suppressed.

Generally, retention of a single β phase occurs when the β-transus temperature, is lower than that of pure titanium (882.5°C) [54]. The calculated β-transus temperatures of the alloys given in Table 3-5 were also lower than that of pure titanium. Therefore, the formation of the secondary phases could be attributed to the occurrence of segregation of Mo and Nb during solidification, resulting in enrichment or depletion of both β stabilizers in the alloys [123]. Due to the inhomogeneous distribution of Mo and Nb in this study, ω_{ath} and α" nano-particles were precipitated within some grains and along some grain boundaries as seen in the EBSD maps. This indicates that segregation occurred in the alloys which led to the formation of regions with high- and low-stability of the β phase. Therefore, it can be concluded that the ω_{ath} and α" nano-particles precipitated preferentially in low β stability regions, while in the high β stability regions the transformation of the nano-particles was significantly hindered.

Figure 4-37 a) – e) displays the inverse pole figure maps (IPF) of TMT, TMN1, TMN2, TMN3 and ST TMNZ alloys. The IPF maps reveal artifacts (black areas/spots) introduced during the preparation of the alloy specimens. These artifacts can affect the phase constituents, thereby enhancing or deteriorating the pattern quality, thus affecting the indexing process. The IPF maps of ST TMN1, TMN2, TMN3 and TMNZ alloys revealed coarse β phase grains and high angle grain boundaries. However, the grain boundary could not be seen in the IPF map of AC TMT alloy. As in the IPF maps of the AC alloys, nano-sized particles could also be distinguished in the β grains of the ST alloys.

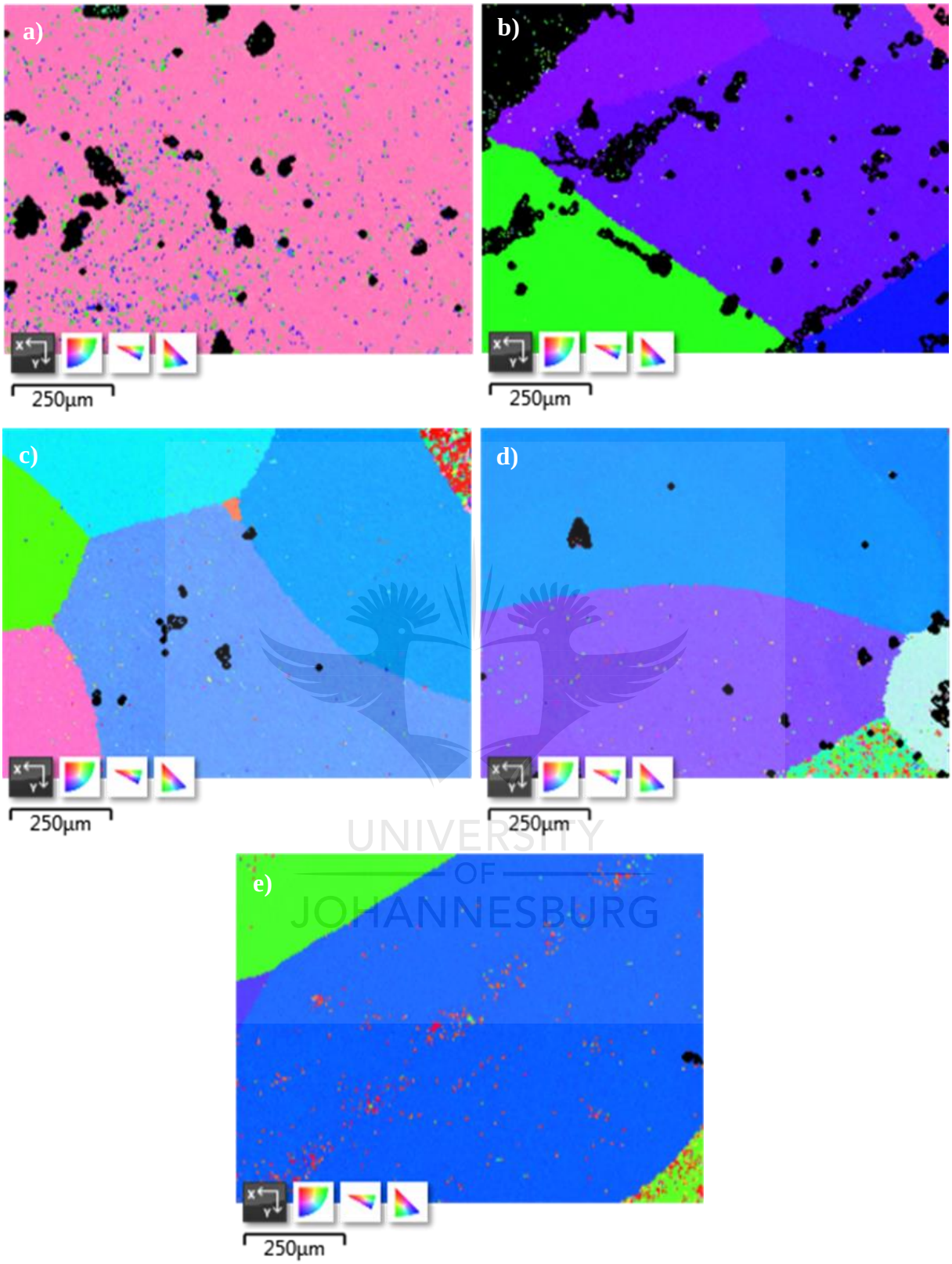

Figure 4-37: EBSD IPF maps of a) TMT, b) TMN1, c) TMN2, d) TMN3 and e) TMNZ ST alloys

To identify these nano-sized particulates and verify the phase constituents observed in the x-ray diffraction, optical microscopy and scanning electron microscopy analysis, electron

backscatter diffraction analysis was also carried out. The generated phase maps are clearly illustrated in Figure 4-38 a) - e). The nano-sized precipitates revealed in the IPF maps of ST TMT, TMN1, TMN2, TMN3 and TMNZ alloys were orthorhombic α" martensitic phase (blue phase) and the hexagonal ω phase (yellow phase). It can be seen that the martensitic α" nano-particles appeared more than the ω nano-particles.

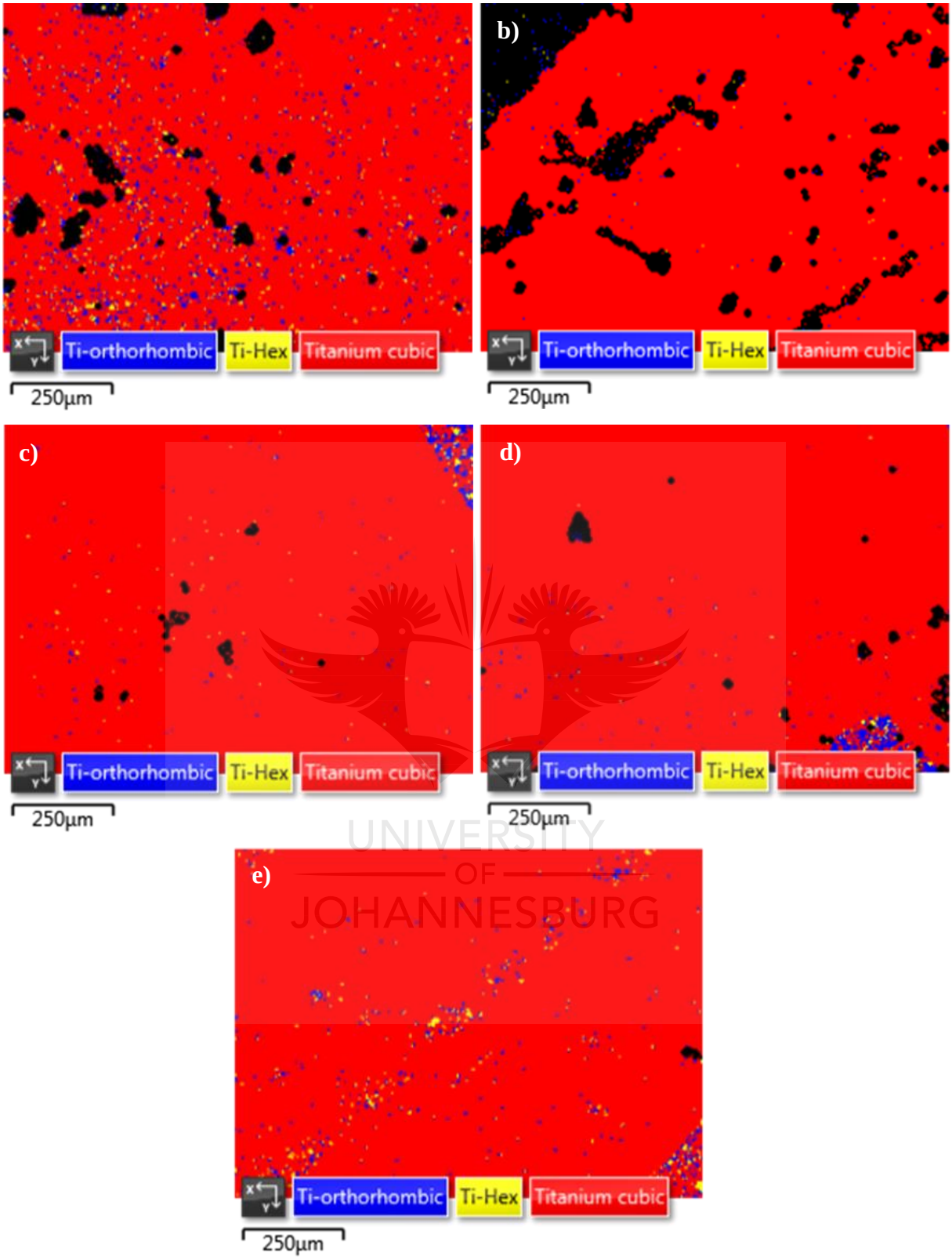

Figure 4-38: EBSD phase maps of ST a) TMT, b) TMN1, c) TMN2, d) TMN3 and e) TMNZ alloys

It is evident that the amount of the martensitic α" phase was substantially increased in the solution-treated alloys than in the-cast alloys. This observation is consistent with the XRD results, which showed more martensitic α" phase peaks in the XRD patterns of the solution treated alloys than the as-cast alloys. It can also be seen that the volume fraction of the ω phase precipitated in the TMNZ alloys was significantly increased in comparison with the as-cast TMNZ alloy.

Generally, by visual observation of the EBSD maps, the large amount of the secondary martensitic α" and ω nano-particles were observed in the designed alloys after solution treatment.

4.3.3 Summary of findings

Table 4-7 summarizes the constituent phases observed during analysis with the x-ray diffraction, optical microscopy, scanning electron microscopy and electron backscatter diffraction techniques. It is noteworthy that careful examination of the microstructure using the optical microscopy and the scanning electron microscopy techniques did not reveal the presence of the secondary orthorhombic martensitic α" phase and hexagonal ω phase in the microstructures of the designed alloy series investigated in this study. This alone does not prove that these secondary phases were absent in the alloys, but it could be due to the size of the precipitates being below the detection limit of the microscopes. Contrary to that, the XRD and EBSD revealed the primary β phase and precipitates of the secondary martensitic α" and ω phases. Generally, the substitution of the Ti glue atom with the Nb atom(s) and/or the substitution of the Ti atom in the cluster shell with a Zr atom suppressed the formation of the martensitic α" and ω phases considerably. Furthermore, the ST alloys comprised larger volume fractions of the secondary martensitic α" and ω phases than the AC alloys.

Table 4-7: Summary of the experimental observations and the theoretical predictions.

Alloy		Theoretical predictions			Experimental observations			
		Moeq	*e/a* ratio	d-electron	OM	SEM	XRD	EBSD
TMT	AC	β	β	β	β	β	β + α" + ω	β + α" + ω
	ST							
TMN1	AC	β	β	β	β	β	β+ α"+ ω	β + α" + ω
	ST							
TMN2	AC	β	β	β	β	β	β+ α"+ ω	β + α" + ω
	ST						β+ α"	
TMN3	AC	β	β	β	β	β	β+ α"+ ω	β + α" + ω
	ST						β+ α"	
TMNZ	AC	β	β	α"	β	β	β+ α"+ ω	β + α" + ω
	ST						β+ α"	

Comparison of microstructural observations with the theoretical predictions

Careful analysis of the phase constituents using EBSD and XRD techniques revealed subtle differences in the actual phases identified compared to the theoretical predictions. The experimental phase analysis confirmed microstructures consisting of β phase matrix with ω phase and α'' phase precipitates.

Wang *et al*. [61] indicated that a multicomponent alloy requires a molybdenum equivalence of 11.8 wt% or more to fully retain the BCC β phase upon rapid cooling. This suggests that the molybdenum equivalence of 11.8 wt% would be sufficient to suppress the formation of the martensitic phases. According to the Mo equivalence values calculated in this study which were all above 11.8 wt%, all the designed alloys would be expected to form a single β phase. However, the molybdenum equivalence approach could not predict the precipitation of the orthorhombic α'' martensitic phase and the hexagonal ω phase as revealed by the experimental microstructural results. These results are not in good agreement with Wang *et al*. [93] observations, in which the same alloys (all the TMN and TMNZ alloys) formed a single β phase. This discrepancy could be attributed to the inaccuracy of the equivalent coefficients of Nb (0.28) and Zr (0.47), which could not be verified experimentally [61]. Furthermore, this prediction approach does not take into consideration the precipitation of the ω phase, but the stability of the β phase in the alloy.

The e/a ratio scale developed for Ti alloys by Lauherte *et al.* [60] indicates that the stability of the β phase increases with increasing e/a ratio. The scale also highlights that a single β phase can be formed at e/a ratio above 4.20. On the contrary, Buzatu *et al.* [65] reported that the β phase is stable at e/a ratio above 4.30, whereas the precipitation of the metastable omega (ω) phase occurs between the range 4.13 and 4.30. In this work, the e/a ratio of the designed alloys ranged between 4.24 and 4.45, which suggested that all the alloys would form a single β phase. Thus, the calculated e/a ratio values of the designed alloys demonstrated that no secondary phases (martensitic phases and the ω phase) would be precipitated upon rapid cooling. However, all the alloys precipitated the orthorhombic α" martensitic and hexagonal *ω* phase as secondary phases in the β matrix. Both the Mo equivalence and e/a ratio approaches overestimated the β-stabilizing effect of the Mo, Nb and Zr alloying elements in the designed alloys.

The Bo-Md phase stability map has a direct connection with the relative chemical stability of the high-temperature BCC β phase and predicts the microstructure of as-quenched materials theoretically [60]. By directly reading from the $\overline{Bo}$ and $\overline{Md}$ phase stability map, it was observed that all the TMN alloys would theoretically retain a single β phase, whereas the TMNZ alloy would form a single orthorhombic α" martensitic phase upon quenching. These theoretical findings are not consistent with the experimental observations. This suggests that the martensitic start transformation temperature was slightly above room temperature, thus allowing for the precipitation of the α" phase in the TMN alloys experimentally. This indicates that the d-electron theory approach overestimated the β-stabilizing effect of the Mo and Nb alloying elements in the TMN alloys, whereas the β-stabilizing effect of Zr alloying element in multicomponent alloys was underestimated. This suggests that there could be a discrepancy between the positions of the martensitic start transformation temperature theoretical and experimental lines of both alloys on the $\overline{Bo}$ and $\overline{Md}$ phase stability map because the orthorhombic α "martensitic phase was already precipitated at room temperature. Similar discrepancies in microstructural investigations have been reported by Laheurte *et al.* [60] in which no α" martensitic phase was observed in Ti-Nb-Ta-Zr alloys upon quenching.
Based on the results observed, the theoretical predictions were partly consistent with the experimental observations.

4.4 Effect of microstructure on the mechanical properties

4.4.1 Micro-hardness Test Results

The microhardness results of the Ti-Mo binary alloy specimens demonstrated that the microhardness was strongly dependent on the microstructural characteristics, specifically the phase constituents. It was observed that the Ti-Mo alloy specimens consisting of large volume fractions of the ω phase possessed the highest microhardness, whereas the alloys comprising large volume fractions of the β phase showed the lowest microhardness values. Ruzic *et al*. [5] summarized the effect of phase constituents on the micro-hardness in the sequence Hω>Hα'>Hα">Hβ>Hα, which shows that the ω phase possesses the highest microhardness among the phases formed in metastable β-type Ti alloy. Figure 4-39 and Table 4-8 exhibit the microhardness of the AC alloy specimens in comparison with the commonly used orthopaedic implant materials. It can be seen that the microhardness values of the TMT binary, the TMN1 ternary and the TMNZ quaternary alloy specimens are comparable to that of Ti6AL4V materials, whereas they substantially higher than those of CP Ti, CoCr and 316L stainless steel materials. The microhardness of the TMN2 and TMN3 alloy specimens were far lower than that of Ti6Al4V, but greater than those of CP Ti, CoCr and 316L stainless steel materials.

Table 4-8.Microhardness of the designed alloys and the alloys considered for comparison.

Alloy	Microhardness ($HV_{0.5}$)	Reference
TMT	367.90 ± 20.18	This study
TMN1	377.50 ± 5.25	This study
TMN2	275.40 ± 18.07	This study
TMN3	282.50 ± 8.36	This study
TMNZ	351.20 ± 11.89	This study
CP Ti,	135	[54]
CoCr	250	[54]
316L stainless steel	220	[54]

When comparing the microhardness of the AC alloy specimens among themselves, it is evident that TMT, TMN1 and TMNZ alloy specimens possessed microhardness values that were significantly higher than those of TMN2 and TMN3 alloy specimens, which showed no significant difference between their microhardness values. The microhardness of the TMT

alloy specimen was comparable to that of TMN1 and TMNZ alloy specimens. However, the TMN1 alloy specimen exhibited microhardness significantly higher than the TMNZ alloy specimen.

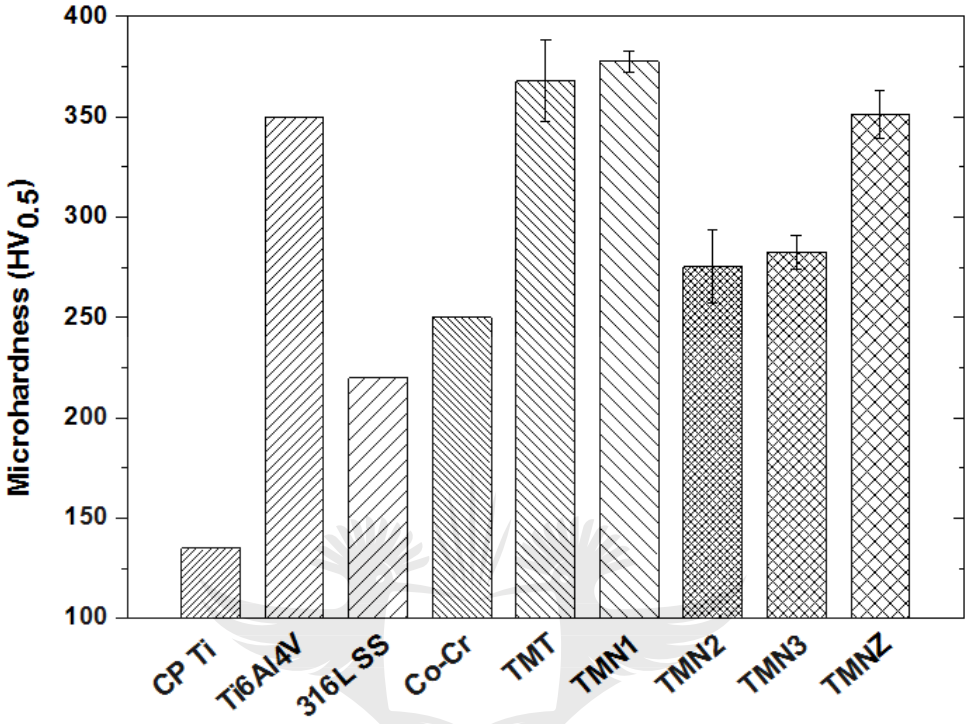

Figure 4-39: Microhardness of AC alloy specimens and the conventional orthopaedic implant materials considered for comparison [54,104].

Segregation of the β stabilizers, which affects the distribution of the phase constituents in the alloy, has a strong influence on the microhardness. An alloy containing regions rich and lean in β stabilizers due to segregation of the β stabilizers causes variations in the microhardness values, resulting in a high average microhadness. High microhardness values can be observed in specimens with local regions lean in the β stabilizers, where the large amount of the ω_{ath} phase is precipitated. Therefore, the insignificant change in the microhardness after the substitution of the Ti glue atom with the Nb_1 atom occurred due to the existence of segregation in the specimen, which caused inhomogeneous distributions and/ or clustering of the ω_{ath} phase in the alloy. The significant reduction of microhardness in both TMN2 and TMN3 alloy specimens resulted from the high β phase stability compared to the other designed alloys. The high microhardness in the TMNZ alloy was attributed to the combined solid solution hardening effect of Mo, Nb and Zr elements, and the existence of the exceptionally hard nanoparticles of

the ω phase [51,123]. These microhardness values are substantially lower than the microhardness values of Ti-Mo-Nb-(Zr) alloy series from the literature [44,64,124].

The microhardness of the ST alloy specimens and the conventional orthopaedic materials considered for comparison are exhibited in Figure 4-40. TMT, TMN1, TMN2, TMN3 and TMNZ alloy specimens exhibited microhardness values of 285.30 ± 11.29 $HV_{0.5}$, 283.20 ± 10.60 $HV_{0.5}$, 280.10± 14.58 $HV_{0.5}$, 266.60 ± 14.46 $HV_{0.5}$ and 356.10 ± 13.22 $HV_{0.5}$, respectively. The microhardness of the TMNZ quaternary alloy specimen was far greater than those of CP Ti, CoCr and 316L stainless steel orthopaedic implant materials, however comparable to that of Ti6Al4V material. However, TMT, TMN1, TMN2 and TMN3 specimens exhibited microhardness values that were substantially lower than that of Ti6Al4V materials, but higher than those of CP Ti, CoCr and 316L stainless steel orthopaedic implant materials. When comparing the ST alloys among themselves, it can be seen that the microhardness of ST TMNZ alloy specimens was significantly greater than those of the other alloy specimens. This could be attributed to the combined solid solution hardening effect of the Mo, Nb and Zr β-stabilizing elements and the ω nano-particles present in the alloy. Conversely, no significant difference among the microhardness of TMT, TMN1, TMN2 and TMN3 alloy specimens was observed. This could be attributed to the segregation of the β stabilizers, which resulted in the precipitation of ω_{ath} nanoparticles in the alloys. The ω_{ath} nanoparticles present in the alloys did not cause a significant change in the microhardness of the alloys.

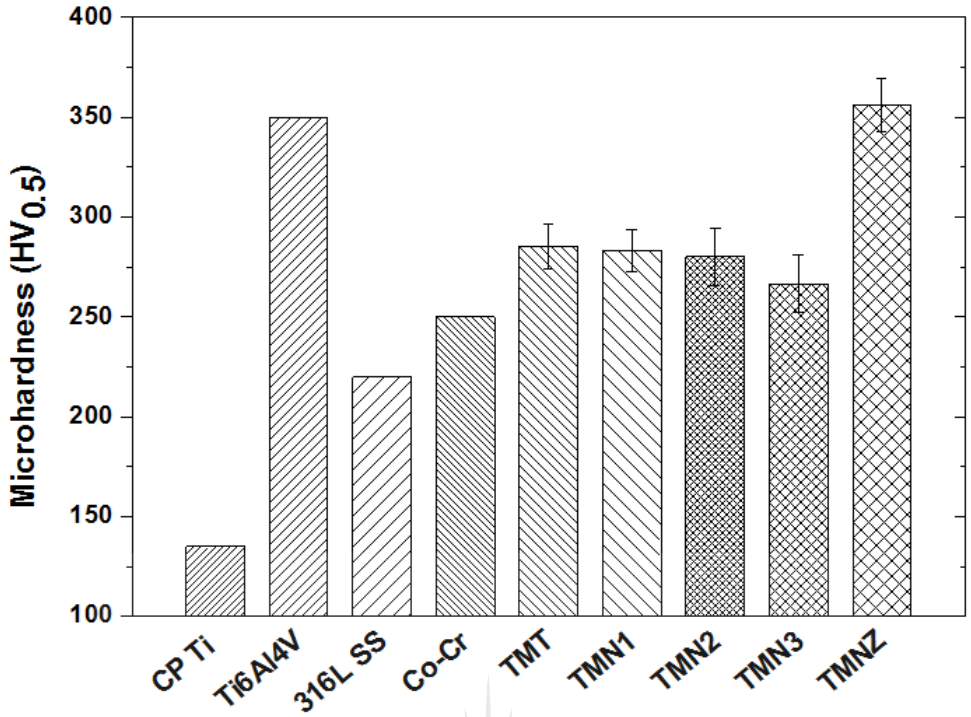

Figure 4-40: Microhardness of ST alloy specimens and the conventional orthopaedic implant materials considered for comparison [54,104].

Figure 4-41 compares the microhardness of the AC and ST alloy specimens. The microhardness of the AC TMT and TMN1 alloy specimens showed a significant increase in the microhardness after solution treatment. Contrarily, the microhardness of the TMN2, TMN3 and TMNZ alloys were not significantly different. Generally, the microhardness of the AC alloys decreased after solution treatment, suggesting that the precipitation of the ω phase during solution treatment could have been suppressed.

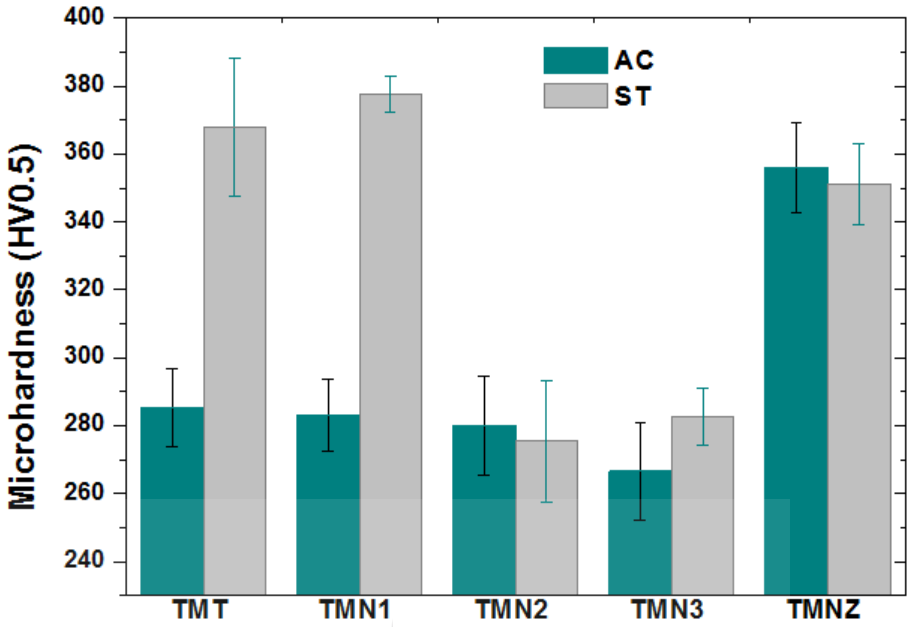

Figure 4-41: Comparison of the microhardness of the AC and ST alloy specimens.

4.4.2 Tensile tests results

The mechanical properties, including the yield strength, ultimate tensile strength and elongation after tensile tests, are listed in Table 4-9. The tensile strength of the AC TMT alloy specimen was significantly higher than that of the AC TMN1 alloy specimen, which was comparable to that of TMN2 alloy specimen. The significant difference between the tensile strengths of TMT and TMN1 alloy specimens could be attributed to the difference in the volume fraction of the ω nano-particles, which induces solid solution strengthening effect in the β matrix. The tensile strength of TMN3 alloy specimen was significantly increased in comparison with that of TMN2 alloy specimen. Although TMNZ alloy specimen exhibited significantly lower tensile strength than TMN3 alloy specimen, its tensile strength value was significantly higher than those of TMT, TMN1 and TMN2 alloy specimens. The high tensile strength in TMNZ alloy specimen could be attributed to the solid solution strengthening effect of Mo, Nb and Zr, which have a higher solubility in the β phase as well as the ω phase precipitates in the β matrix of the alloy.

Table 4-9: Tensile properties of the AC, ST and similar alloys considered for comparison.

Alloy		Yield Strength (MPa)	UTS (MPa)	Elongation (%)
TMT	AC	639 ± 326.6	752 ± 286.3	0.52 ± 0.2
	ST	483 ± 37.9	668 ± 34.8	27.5 ± 1.7
	[63]	696	784	29
TMN1	AC	654 ± 47.1	671 ± 42.5	0.61 ± 0.3
	ST	614 ± 15.3	870 ± 30.8	15.4 ± 2.6
	[63]	499	685	31.3
TMN2	AC	873 ± 8.2	685 ± 68.2	0.44 ± 0.3
	ST	-	875± 12.6	8.5 ± 1.1
	[63]	424	617	29.3
TMN3	AC	845 ± 32.2	1669± 23.8	3.1 ± 2.6
	ST	651 ± 33.7	688 ± 56.9	7.3 ± 2.9
	[63]	394	496	19.4
TMNZ	AC	-	1111 ± 3.8	3.6 ± 1.5
	ST	-	1024 ± 78.2	3.7 ± 2.8
	[63]	737	793	13.4

NB. The yield strengths of AC TMN2, AC & ST TMNZ alloys could not be measured due to the removal of the extensometer to avoid breakage.

Large elongation is desirable in orthopaedic applications to prevent breakage in case an alloy is accidentally stressed beyond its proportional limit [41]. The elongation at fracture of the AC TMT, TMN1 and TMN2 alloy specimens was comparable. Contrarily, they were significantly lower than those of TMN3 and TMNZ alloy specimens. Nonetheless, all the alloy specimens failed in a brittle fracture behaviour, which could be attributed to the ω_{ath} nanoparticles which were clustered considerably along the grain boundaries and within the grains, causing stress concentration. Similar brittle fracture behaviour was reported in Ti-Ta-Zr-Nb [59] and Ti-Mo-Nb [126] alloy series. The combination of large elongation and high tensile strength results in good fracture resistance [41]. Therefore, the alloys in this study would have poor fracture resistance, due to their brittleness.

No significant difference in the yield strengths of TMT and TMN1 alloy, and TMN2 and TMN3 specimens was observed. The yield strengths of TMN2 and TMN3 were significantly higher than those of TMT and TMN1 alloy specimens. It is noteworthy that the extensometer was removed before the TMNZ alloy specimen could yield. This suggests that the yield strength of the TMNZ alloy specimen was above its recorded tensile strength of 1111 ± 3.8 MPa. The yield strength values obtained in this study were greater than those found in the literature [63].

Table 4-9 also lists the yield strength, tensile strength and elongation values of the TMT, TMN1, TMN2, TMN3 and TMNZ alloys in the as-cast condition investigated by Wang *et al.* [63]. It can be seen that the tensile strengths of the TMNT, TMN1 and TMN2 alloy specimens were comparable to those investigated by Ref. [63], whereas TMN3 and TMNZ alloy specimens showed tensile strengths that were far greater than those obtained by Ref. [63]. The yield strength of the TMT alloy specimens were comparable, whereas those of TMN1, TMN2, TMN3 and TMNZ were substantially higher than those studied in Ref [63]. The elongation values obtained in this study are substantially low, indicating that the alloy specimens were brittle in comparison to those studied by Ref. [63].

Jiang *et al.* [57] observed the elongation in the range of 7.6 and 14.2% in as-cast Ti-Mo-Sn-Nb-Zr alloys. In comparison with the conventional orthopaedic biomaterials listed in Table 2-2, the tensile strengths of the AC alloys at Ti_1, Nb_1 and Nb_2 glue atoms generally fell within the tensile strength range of the conventional orthopaedic 316 L SS, CoCrMo and CP Ti materials, but lower than that Ti6Al4V material. Conversely, the tensile strengths of TMNZ and TMN3 were substantially higher than those of 316 L SS, CP Ti and Ti6Al4V materials, but within the range of the tensile strength range of CoCrMo material. The yield strengths at Ti_1 and Nb_1 were within the yield strength range of the 316L SS, CP Ti and CoCrMo materials, but out of the yield strength range of the Ti6AL4V material. Meanwhile, the yield strength at Nb2 and Nb_3 glue atoms were greater than those of the 316L SS and CP Ti, but within the range of Ti6Al4V and CoCrMo materials.

In the case of ST alloy specimens, the tensile strength of the TMT alloy specimen was significantly low in comparison with that of TMN1 alloy specimen, which was comparable to that of the TMN2 alloy specimen. The tensile strength of the TMN3 alloy specimen was

significantly reduced compared to the TMN2 alloy specimen, whereas the tensile strength of the TMNZ alloy specimen was significantly increased. This significant increase in tensile strength obtailed on the TMNZ specimen could be attributed to the combined solid solution strengthening effect of Mo, Nb and Zr as well as the precipitation hardening of the secondary phases.

It should be noted that the yield strengths of TMN2 and TMNZ alloy specimens could not be measured due to the removal of the extensometer. The yield strengths of both alloy specimens would have been higher than those of TMT, TMN1 and TMN3 alloy specimens as indicated by their tensile strength values. Although the yield strengths of both TMN1 and TMN3 alloy specimens were comparable, they were significantly higher than that of TMT alloy specimens. The low yield strength in TMT alloy specimen was not expected because the alloy comprised the largest volume fraction of the ω phase.

The stress-strain curves indicate that all the alloys, except for TMN2 alloy specimens, showed a single stage yielding behaviour. The TMN2 alloy specimen exhibited a double yielding behaviour, which is observed in alloys with β stability that is not sufficiently high to impede the martensitic α" transformation. [57]. The first yielding behaviour occurred at around 200 MPa, which was attributed to the stress-induced α" martensitic transformation and the reorientation of martensite variants. However, the second yielding behaviour resulting from the initiation of permanent plastic deformation could not be observed because the extensometer was removed before it could occur. A double yielding phenomenon was also reported by Guo *et al*. [88] in the solution treated Ti-30Nb-1Mo-4Sn , Matsumoto *et al.* [77] in solution treated Ti–35Nb–4Sn alloy.

The elongation at fracture of TMN1 alloy specimen was significantly reduced compared to TMT alloy specimen. TMN2 alloy specimen had elongation that was significantly lower than that of TMN1 alloy specimen, which was comparable to that of TMN3 alloy specimen. No significant difference was observed in the elongation of TMNZ and TMN3 alloy specimens. These observations indicate that the TMT alloy specimen showed the largest ductility, which then decreased with increasing Nb atoms in the glue site. It is also evident that the Zr atom in the cluster shell induced some brittleness during solution treatment of the TMNZ alloy specimen. Generally, solution treatment has significantly enhanced the ductility of the alloy

specimens compared casting. The structure of the β phase is reported to have high plasticity [126]. Therefore, the large elongation in the ST alloy specimens suggests that the β phase stability was enhanced after solution treatment.

Nnamchi *et al*. [8] reported the elongation at fracture of thermo-mechanically processed Ti-Mo-Nb-Zr alloys ranging from 15 to 26%, which were similar to the elongation obtained in the ST alloy specimens. Gabriel *et al.* [74] obtained elongation of 41.2% in a thermos-mechanically processed Ti–12Mo–3Nb alloy. In comparison with the conventional orthopaedic biomaterials given in Table 2-2, the tensile strengths of the ST alloys at Ti_1 and Nb_3 glue atoms were generally, within the tensile strength range of the conventional 316 L SS and CoCrMo materials, but lower than the minimum yield strengths of CP Ti and Ti6Al4V materials. The yield strengths at Nb_1 and Nb_2 were lower than that of Ti6Al4V material but within the range of 316L SS and CoCrMo. The yield strength at Zr_1 cluster shell atom was far greater than those of 316L SS, Ti6AL4V, and CP Ti materials, but within the range of CoCrMo. The yield strengths at Ti_1 and Nb_1 were within the yield strength range of the 316L SS and CoCrMo materials, but out of the yield strength range of the CP Ti and Ti6AL4V materials. Meanwhile, the yield strength at Nb_2 and Nb_3 glue atoms were greater than those of the 316L SS and CP Ti, but within the range of Ti6Al4V and CoCrMo materials. The yield strength at Nb_3 fell within the yield strength range of 316L SS, CoCrMo and Ti6Al4V, but lower than that of CP Ti.

- **Elastic modulus**

The elastic modulus of a biomaterial has to match that of the human bone (10 – 30 GPa) to mitigate the stress-shielding effect. The elastic modulus findings of the Ti-Mo binary alloy specimens showed the strong dependence of the elastic modulus values on the phase constituents present. It was observed that the lowest elastic modulus values were obtained in Ti-Mo alloy specimens consisting of large volume fractions of the β phase (high β phase stability) and the highest in alloy specimens with large volume fractions of the ω phase precipitates. Furthermore, the alloy specimen consisting of larger volume fractions of the martensitic α" phase than the ω phase resulted in lower elastic modulus values.

The elastic moduli of the AC $[(Mo)Ti_{14-x}Zr_x]Ti_yNb_z$ alloy series and the alloys considered for comparison are shown in Figure 4-42. The elastic moduli of the AC TMT, TMN1, TMN2,

TMN3 and TMNZ alloy specimens are 133 ± 12.9 GPa, 57 ± 6.2 GPa, 62 ± 4.1 GPa , 71 ± 1.2 GPa and 68 ± 2.5 GPa respectively. Among the designed alloys in this study, TMT alloy with the modulus of 133 ± 12.9 GPa was noticeably higher than the moduli of conventional CP Ti and Ti6Al4V implant materials. However, the modulus of TMT alloy was substantially lower than the moduli of the conventional CoCr and 316L stainless steel implant materials. Meanwhile, the elastic moduli of the designed TMN1, TMN2, TMN3 and TMNZ alloys were far lower than those of the conventional orthopaedic implant materials as shown in Figure 4-42.

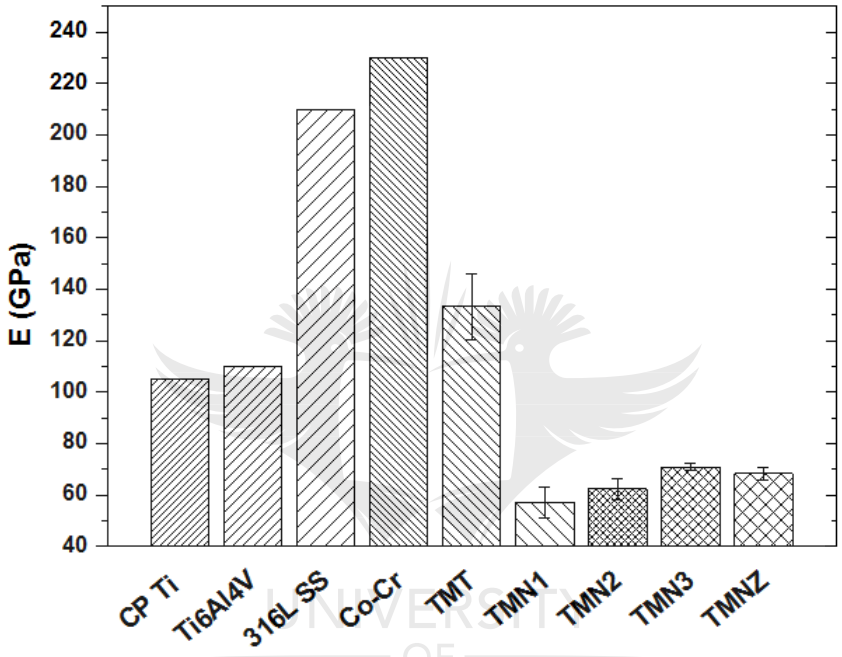

Figure 4-42: Elastic modulus of the AC alloy specimens with the common orthopaedic materials considered for comparison

When comparing the AC alloy specimen amongst themselves, it is evident that the elastic moduli of the TMT binary alloy specimen were significantly higher than those of the TMN ternary alloy specimens and TMNZ quaternary alloy specimen due to the high volume fraction of the ω phase it comprised, which is reported to increase the elastic modulus of metastable β-type Ti alloys [87]. There was no significant difference between the elastic moduli of TMN1 and TMN2 ternary alloy specimens, but both of them were significantly lower than those of TMN3 and TMNZ alloy specimens. An elastic modulus comparable to that of TMT binary alloy specimen was expected in TMN1, because of its high proportion of the ω phase. The low elastic modulus in the TMN1 alloy specimen could be attributed to the multiple micro-pores

formed during casting. Furthermore, no significant difference between the elastic moduli of TMN3 and TMNZ alloy specimens was observed.

In the case of ST TMT, TMN1, TMN2, TMN3 and TMNZ alloy specimens, the obtained elastic moduli were 98 ± 8.1 GPa, 84 ± 2.6 GPa, 67 ± 4.5 GPa, 68 ± 8.4 GPa and 73 ± 3.0 GPa, respectively. It is evident that the elastic modulus of TMT binary alloy specimen is similar to those of CP Ti and Ti6Al4V implant materials, but substantially lower than those of CoCr and 316L stainless steel. Contrarily, the elastic moduli of the rest of the ST alloy specimens were substantially lower than those of the conventional orthopaedic implant materials. Comparison of the ST alloy specimens among themselves showed that the elastic modulus of The TMT binary alloy specimen was significantly higher than those of the other alloys. This could be ascribed to the existence of the ω phase in high volume fractions as indicated by the XRD and EBSD analytical results. Conversely, no significant difference was evident among the elastic moduli of TMN2, TMN3 and TMNZ alloy specimens. These observations show that substitution of Ti atom with the Nb atom(s) (Nb_1, Nb_2 or Nb_3) in the glue site and/or Zr atom in the cluster shell significantly decreased elastic modulus. The significant difference in the elastic moduli of TMN1 (without Zr) and TMNZ (with Zr) suggests that Zr played a major role as a β stabilizer in the multicomponent alloy [63].

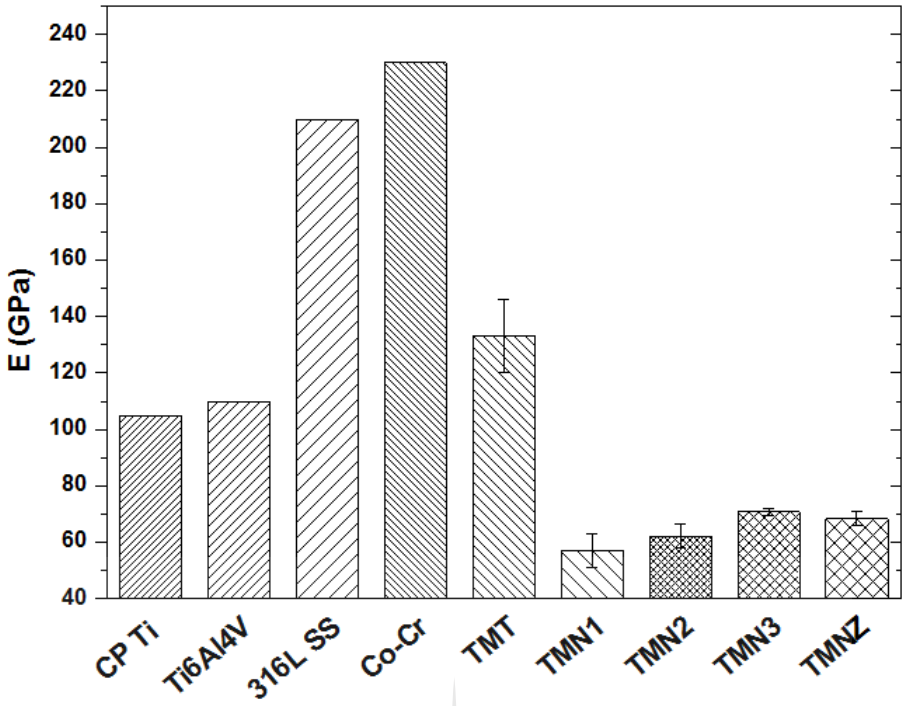

Figure 4-43: Elastic modulus of the ST alloy specimens with the common orthopaedic materials considered for comparison.

Figure 4-44 gives a comparison between the elastic moduli of the AC and ST alloy specimens. Although the elastic moduli of the TMT binary alloy specimen in both AC and ST conditions were significantly higher than those of the other alloy specimens, the elastic modulus of the ST alloy specimen was significantly lower than that of the AC alloy specimen. This suggests that the amount of ω phase precipitated during solution treatment was significantly reduced. The transformation of the high-temperature β phase to ω phase in ST TMN1 alloy specimen was significantly enhanced, hence the elastic modulus was significantly increased compared to that of the AC alloy specimen. The elastic moduli of the AC and ST TMN2, TMN3 and TMNZ alloy specimens were not significantly changed, because the amount of the ω phase present in the alloys low in both conditions.

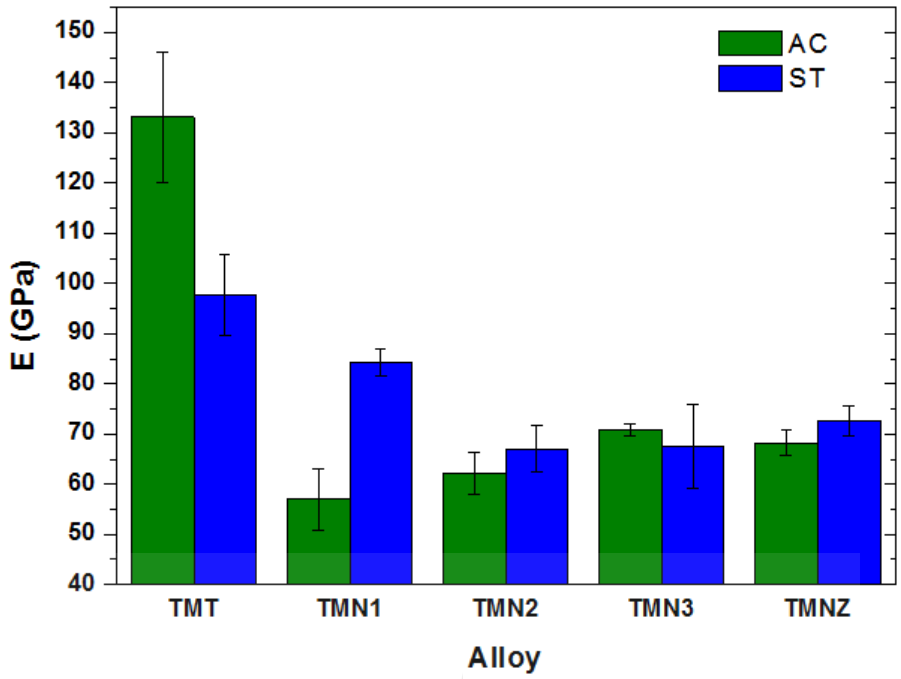

Figure 4-44: Comparison between the elastic moduli of the AC and ST alloy specimens.

Nnamchi *et al*. [8] reported a low elastic modulus of 35.4 GPa in thermos-mechanically processed Ti–8Mo–4Nb–2Zr alloy, which was attributable to the existence of α" phase, which presents a modulus about half that of the β phase.

- **Variation of the elastic modulus of the alloy specimens with the molybdenum equivalence**

The molybdenum equivalence was used to determine the contribution of the alloying elements on the stability of the β phase in the alloys, whereby the critical lowest limit of β stabilization was experimentally found to be 11.8 wt% in Ti-Mo binary alloys. Figure 4-45 shows the variation tendency of molybdenum equivalence vs. the elastic modulus (E) of the AC alloy specimens, where all the molybdenum equivalence values exceed β_c (11.78 wt%). With increasing molybdenum equivalence, the elastic modulus of the alloys first decreased noticeably in TMN1, then became comparable at TMN2, followed by a considerable increase at TMN3 and no significant difference at TMNZ. This can be summarized as $E_{TMT} > E_{TMN1} \approx E_{TMN2} < E_{TMN3} \approx E_{TMNZ}$ alloy specimens with increasing molybdenum equivalence. When the TMT binary alloy is excluded, it can be seen that the elastic moduli of the AC alloys generally increased with increasing molybdenum equivalence. In view of the molybdenum equivalence from literature, the elastic modulus of β-type Ti alloys increases with increasing molybdenum

equivalence [93,57], which is consistent with the observations in this study. The molybdenum equivalence formula according to Qing suggests that Mo and Nb are good β stabilizers, whereas Zr is considered neutral. However, in this work, Zr played a positive role as a β-stabilizing element, thus contributing to the low elastic modulus in TMNZ alloy. The Ti-Mo binary alloy results indicated that the elastic modulus of β-type Ti alloys is not only sensitive to the stability of the β phase, but also to the secondary phases (α" and ω) precipitated in the β matrix. From the XRD, OM and SEM results, it can be concluded that sufficient β stability can be achieved with one Mo atom in the cluster centre of the cluster formula. However, the variations in the number of glue atoms/ cluster shell atoms and/ or the substitution of the atoms can result in significant variations in the elastic modulus values.

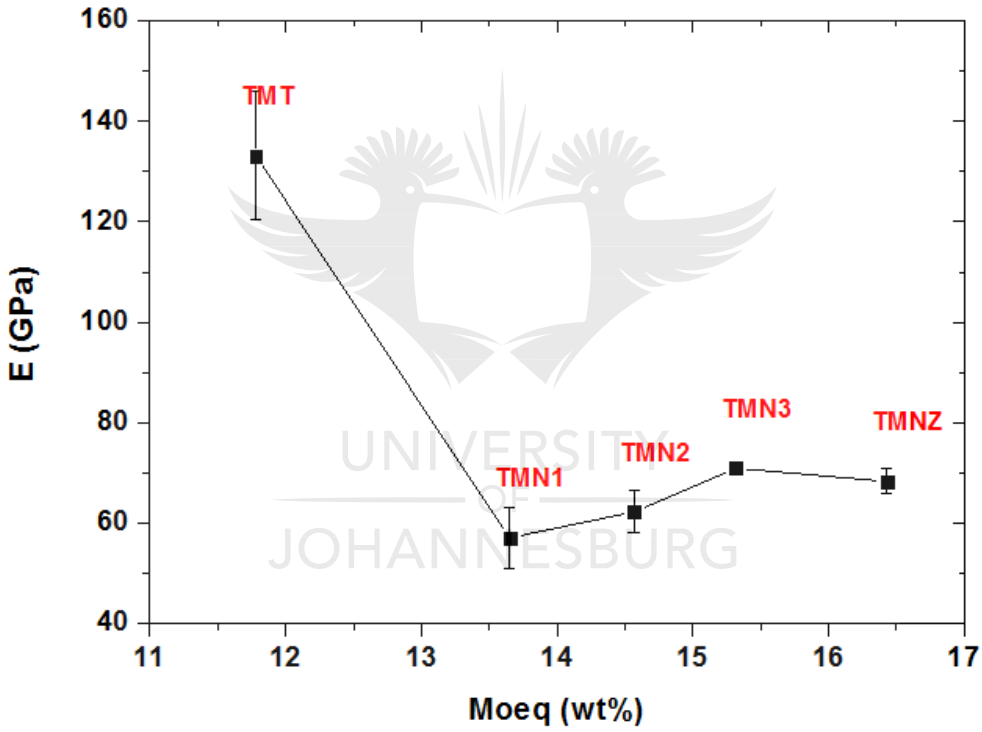

Figure 4-45: Variations of the elastic modulus of the AC alloy specimens with the molybdenum equivalence.

In the case of the ST alloy specimens, the variation tendency of *Moeq* vs. the elastic modulus (E) is depicted in Figure 4-46, where all the *Moeq* values exceed β_c (11.78 wt%). It is evident that with increasing *Moeq*, the elastic modulus of the ST alloy specimens showed no significant difference from TMT up to TMN1, but significantly decreased at TMN2, and became comparable up to TMNZ. Generally, the elastic moduli of the ST alloy specimens (multicomponent alloys only) show a decreasing tendency with the *Moeq*. These variations in the elastic moduli of the ST alloy specimen with *Moeq* also resulted from the variation of the

proportions of the phase constituents, specifically the ω phase, which increases the elastic modulus of metastable β-type Ti alloys. Despite the scattered behaviour of the data, the elastic moduli of both the AC and ST alloys generally exhibit a decreasing tendency with increasing molybdenum equivalence.

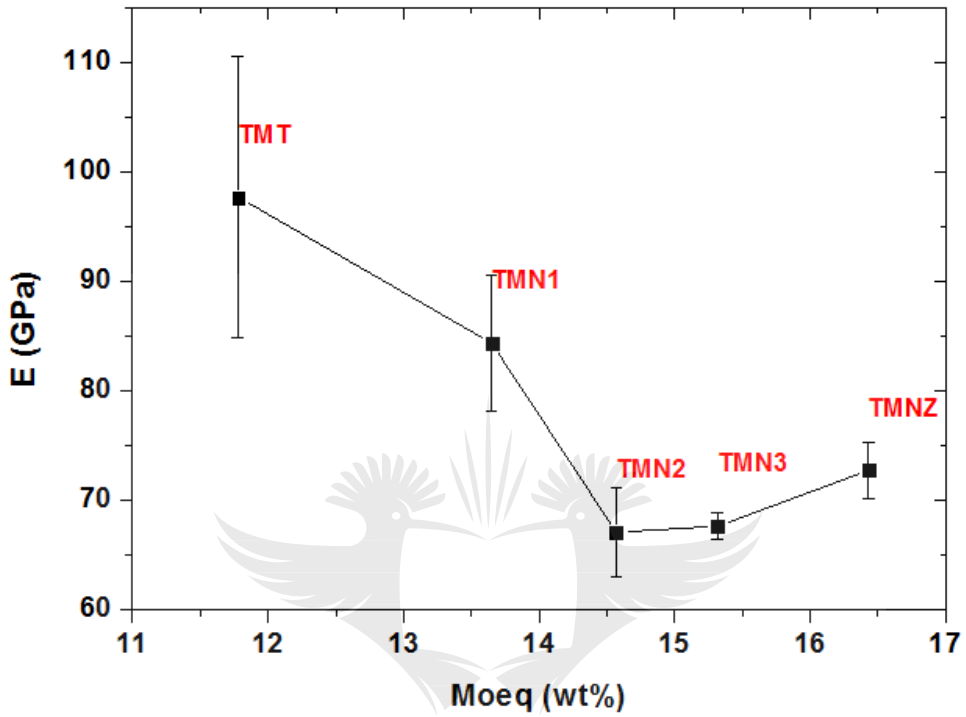

Figure 4-46: Variations of the elastic modulus of the ST alloy specimens with the molybdenum equivalence.

- **Variation of the elastic modulus of the alloy specimens with e/a ratio.**

Figure 4-47 illustrates the variation of elastic moduli of the AC alloy specimens with the *e/a* ratio. With increasing *e/a* ratio, a significant drop in elastic modulus of the alloys is observed up to TMN1, which became comparable at TMN2 and significantly increased at TMN3. Generally, a clear decreasing tendency of the elastic modulus with the *e/a* ratio of the ST alloys is evident. However, with the exclusion of the TMT binary alloy, the TMN and TMNZ alloys exhibit an increasing tendency of the elastic modulus with the e/a ratio, which is consistent with the findings reported in the literature [53].

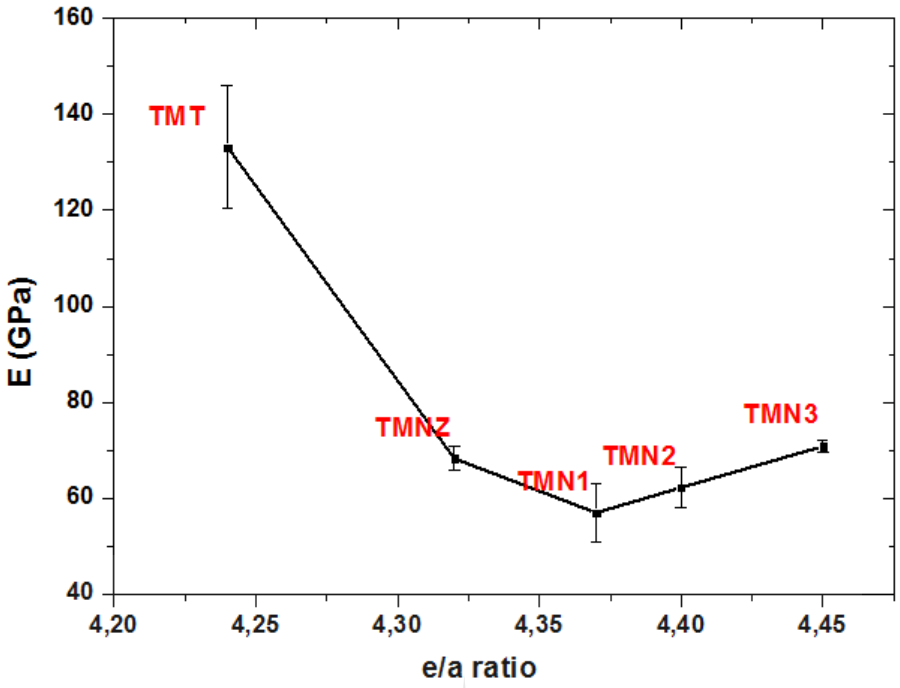

Figure 4-47: Variations of the elastic modulus of the AC alloy specimens with e/a ratio.

The variation of elastic moduli of the ST alloy specimens with the *e/a* ratio is shown in Figure 4-48. With increasing *e/a* ratio, the elastic modulus was significantly decreased, followed by a significant increase, a significant decrease, and it then became comparable. The ST alloys show a decreasing tendency of the elastic modulus with the *e/a* ratio even when the TMT binary alloy is excluded, which is not similar to trend in the AC alloy specimens.

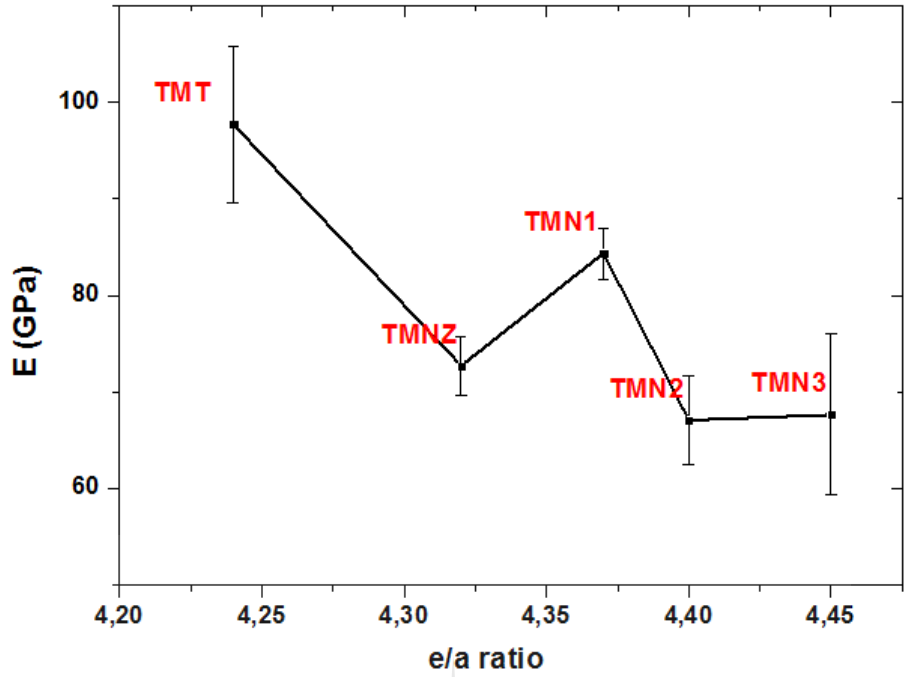

Figure 4-48: Variations of the elastic modulus of the ST alloy specimens with e/a ratio.

- **D-electron theory**

The elastic modulus is correlated with the Bo and Md parameters of the d-electron design theory. The elastic modulus generally decreases with increasing average Bo and Md values in the β-Ti region in the Bo-Md phase stability map. The average Bo and Md values of the designed $[(Mo)Ti_{14-x}Zr_x]Ti_yNb_z$ alloy series are given in Table 3-3**.** It can be established that the Bo of the TMT alloy specimen (Bo= 2.81) increased after the substitution of the Ti with Nb atom(s) (Bo= 2.83). The average Bo also increased with increasing Nb content (Nb1= 2.83, Nb2= 2.84 and Nb3= 2.86), whereas the substitution of one Ti atom in the cluster shell with one Zr atom in TMN1 alloy increased the average Bo value to 2.84. It is noteworthy that the average Md values of the TMT, TMN1, TMN2, and TMN3 alloy specimens were the same, whereas the replacement of one Ti atom in the cluster shell with one Zr atom in TMN1 alloy resulted in the increase in average Md value from 2.42 to 2.45 in TMNZ alloy specimen. It is found that the Bo of the TMN2, TMN3 and TMNZ alloy specimens were reasonably higher, hence they possessed the lowest elastic modulus values. Similar observations were reported by Li et al. [75] in their investigation on as-sintered Ti-Nb-Zr-Ta-Si alloy series.

- **Elastic admissible strain**

In orthopaedic applications, it is a requirement for ideal biomedical implant materials to have greater elastic admissible strain. The elastic admissible strain is defined as the ratio of the strength over the elastic modulus of a material and it is a useful parameter in orthopaedic applications. The greater the elastic admissible strain, the more desirable the material is for such applications [20,40,50,59]. Figure 4-49 displays the elastic admissible strain of the AC TMT, TMN1, TMN2, TMN3 and TMNZ alloy specimens and CP Ti Gr4, Ti6Al4V, Co-Cr and 316L Stainless steel (SS) considered for comparison [6]. It is evident that the TMT binary alloy specimen showed elastic admissible strain that is lower than the commercial CP Ti Gr4, Ti6Al4V and 316 L stainless steel alloys, but higher than that of Co-Cr alloy. Contrary to that, the substitution of the Ti glue atom with Nb(s) resulted in elastic admissible strains that were far greater than those of the conventional alloys and the designed TMT alloy.

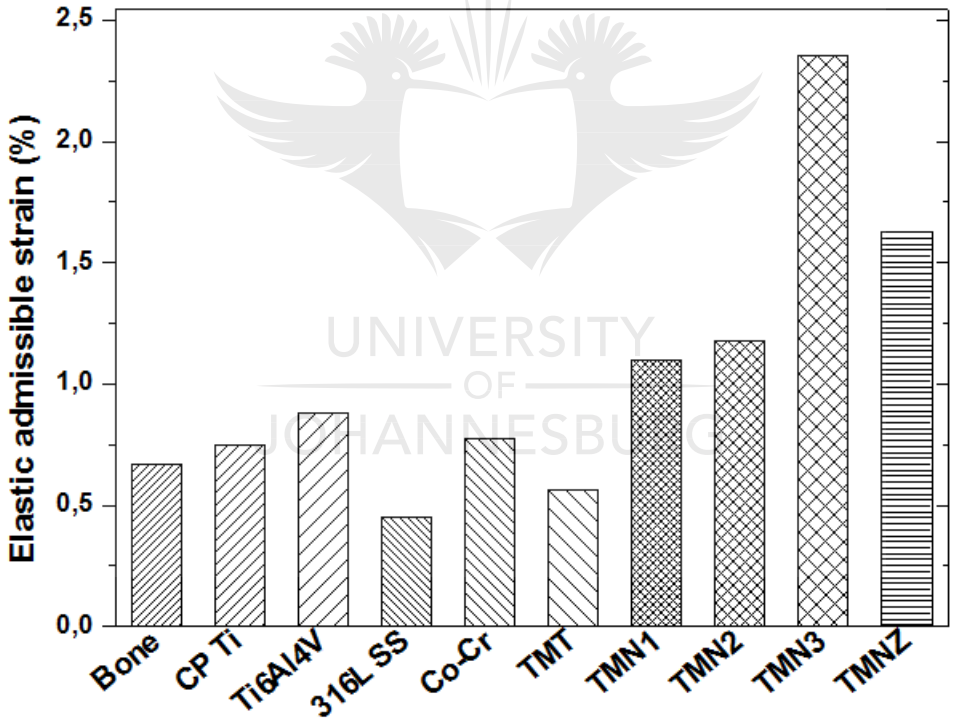

Figure 4-49: Elastic admissible strains of the AC alloy specimens and conventional orthopaedic implant materials considered for comparison [20].

In the case of the ST alloy specimens exhibited in Figure 4-50, similar observations were revealed regarding the binary TMT alloy. Conversely, TMN1, TMN2, TMN3 and TMNZ alloy specimens exhibited greater elastic admissible strains than the conventional orthopaedic materials.

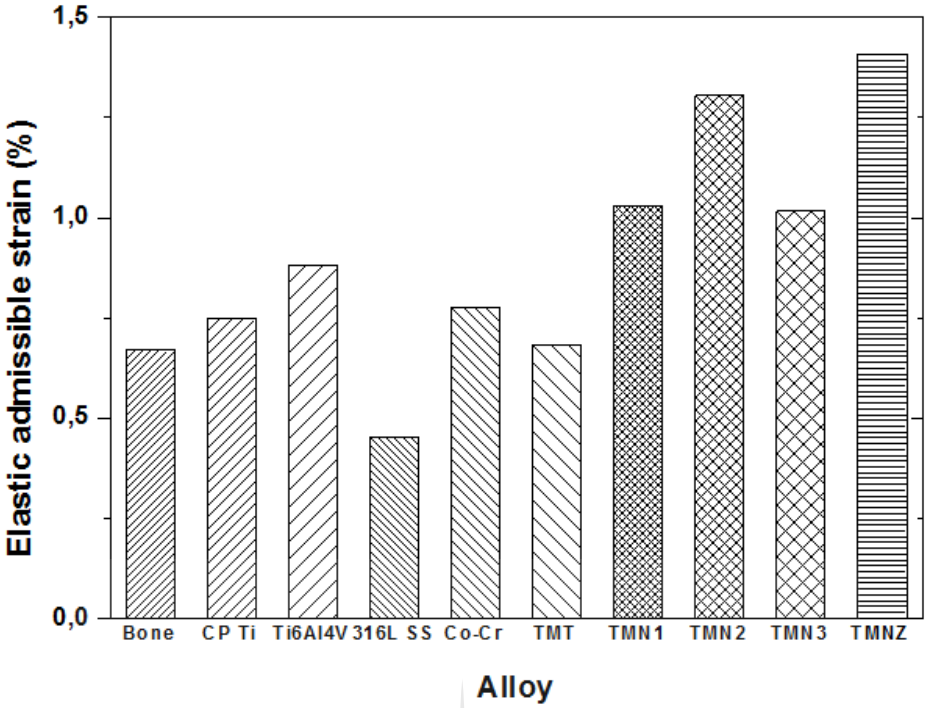

Figure 4-50: Elastic admissible strain of the ST alloy specimens and the conventional orthopaedic implant materials [20].

Furthermore, it can be seen in Table 4-10, that the solution treatment of the as-cast alloy specimens enhanced the elastic admissible strains of the alloys. Therefore, it can be concluded that the developed TMN1, TMN2, TMN3 and TMNZ alloy specimens would offer promising performance in practical applications in terms of mechanical compatibility.

Table 4-10. Comparison of the elastic admissible strains of the AC and ST alloys investigated in this study.

Alloy	EAS (AC)	EAS (ST)
TMT	0,56444	0,683946
TMN1	1,10091	1,030907
TMN2	1,17721	1,304282
TMN3	2,35513	1,016524
TMNZ	1,62744	1,407592

4.4.3 Bending test results

- **Bending stress-deflection curves**

The typical bending stress-deflection profiles of the designed alloys in as-cast condition are depicted in Figure 4-51. It can be seen that AC TMT binary and TMN2 ternary alloy specimens failed in a brittle fracture manner with the average deflections of about 1 mm and 2mm, respectively. This brittle fracture behaviour could be attributed to the large volume fractions of the ω phase in both alloys compared with the other alloy specimens, which is known to induce embrittlement in metastable β-type Ti alloys [8]. It is noteworthy that this kind of ω-induced embrittlement was also observed in AC Ti-10Mo alloy specimen, due to a large amount of the ω phase. It should also be noted that the brittle fracture in AC TMT binary alloy specimen was so premature, that no plastic deformation was noticeable in comparison with the TMN1 alloy specimen. This brittle fracture could be attributed to localized precipitation of the athermal ω phase, which is brittle in nature. Xu *et al.* [126] attributed the brittle fracture behaviour in Ti-Mo-Nb alloys to the existence of pores formed during casting. AC TMN3 alloy specimen showed a combination of brittle and little ductile fracture behaviour, with an average deflection of about 2.5 mm. Contrarily, AC TMN1 and TMNZ alloy specimens exhibited ductile fracture properties with average deflections of about 4 and 4.5mm, respectively. This could be ascribed to the large volume fraction of the β phase (high β phase stability) in comparison with the ω phase in both alloy specimens. The embrittling/weakening effect by the ω phase was found to be very sensitive to the number of atoms in the glue site, e.g. strong embrittling/ weakening effect in TMT and TMN1 alloy specimen. Similar fracture behaviour was expected in TMNZ alloy specimen because it comprises one Nb glue atom, but the presence of Zr alloying element could have hindered the effect. Similar observations were reported by Lin *et al.* [106] in the Ti-7,5Mo-xFe alloy series, whereby the weakening effect was largely diminished when the Fe content was only a little higher or lower than 1 wt%.

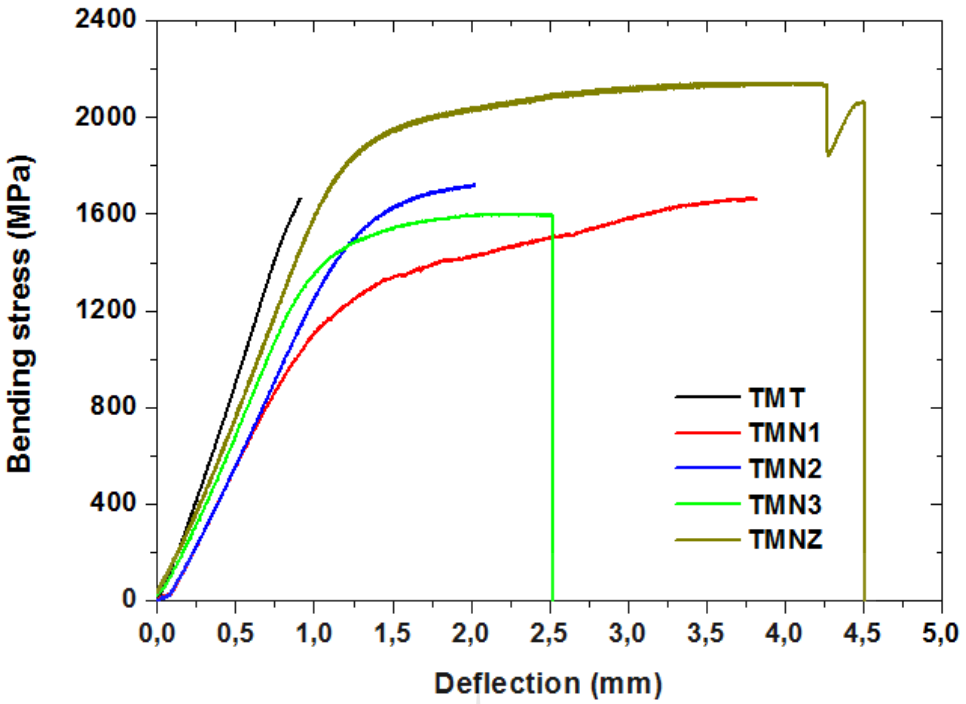

Figure 4-51: Bending stress-deflection curves of the AC alloy specimens.

Figure 4-52 displays the typical bending stress-deflection profiles of the ST alloy specimens. It is also evident that all the alloy specimens exhibited a ductile fracture behaviour. This suggests that solution treatment enhanced the ductility of the alloy specimens compared to the as-cast condition. The average deflections of TMT, TMN1, TMN2, TMN3 and TMNZ alloy specimens are ≈ 7mm, 5mm, 7.5 mm, 6mm and 7mm, respectively. Ho *et al.* [113] also observed ductile properties in Ti–10Zr– xMo alloys, even in the alloy containing the highest amount of the ω phase (Ti– 10Zr–7.5Mo alloy). When comparing the fracture behaviour of the ST with the AC alloy specimens, it is evident that solution treatment induced considerable plasticity in all the alloys. When the ω_{ath} phase precipitates are present in an alloy, they can get clustered at the grain boundaries during the mechanical test and cause stress concentration. This may result in a brittle fracture behaviour. Therefore, the plasticity observed after solution treatment indicates the considerable amount of the ω_{ath} phase that was precipitated during casting was transformed into the β phase during solution treatment. As a result, the amount of ω_{ath} phase that was precipitated during quenching following solution treatment was so small, that the β phase retained enhanced the ductility of the alloys.

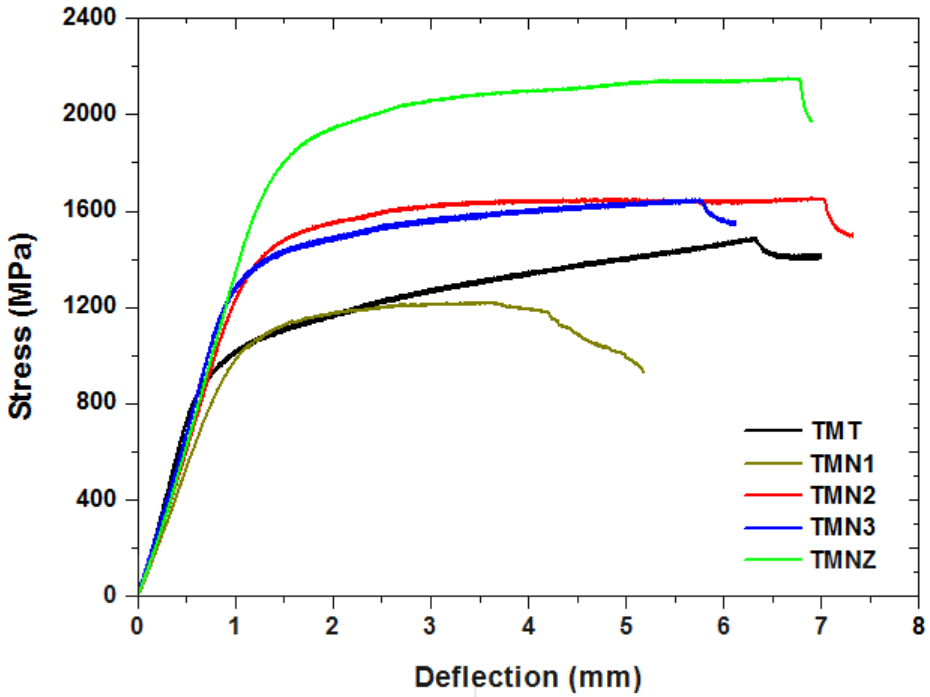

Figure 4-52: Bending stress-deflection curves of the ST alloy specimens.

- **Bending strengths**

The bending strengths of AC TMT, TMN1, TMN2, TMN3 and TMNZ alloy specimens are exhibited in Figure 4-53 and listed in Table 4-11. It is interesting to note that, despite the strong hardening effect of ω phase, the bending strength of the AC TMT and TMN1 alloy specimens consisting of the largest volume fraction of the ω phase was comparable to those of the alloy specimens comprising a small amount of the ω phase. This was attributable to the premature, brittle fracture that occurred in both alloy specimens. Similar observations were reported in Ti–7.5Mo–xFe [106] and Ti–10Zr–xMo alloys [113]. The highest bending strength is evident in AC TMNZ alloy specimen, which could be stemmed from the joint effect of solid solution strengthening of Mo, Nb and Zr and the nano-sized ω phase precipitates in the β matrix. Similar results were reported by Hsu et al. [22], whereas Ti-25Nb-8Sn alloy had the lowest ending strength which was attributed to the high volume fraction of the β phase in the alloy. TMN2 alloy specimen exhibited significantly higher bending strength than TMN3 alloy specimen.

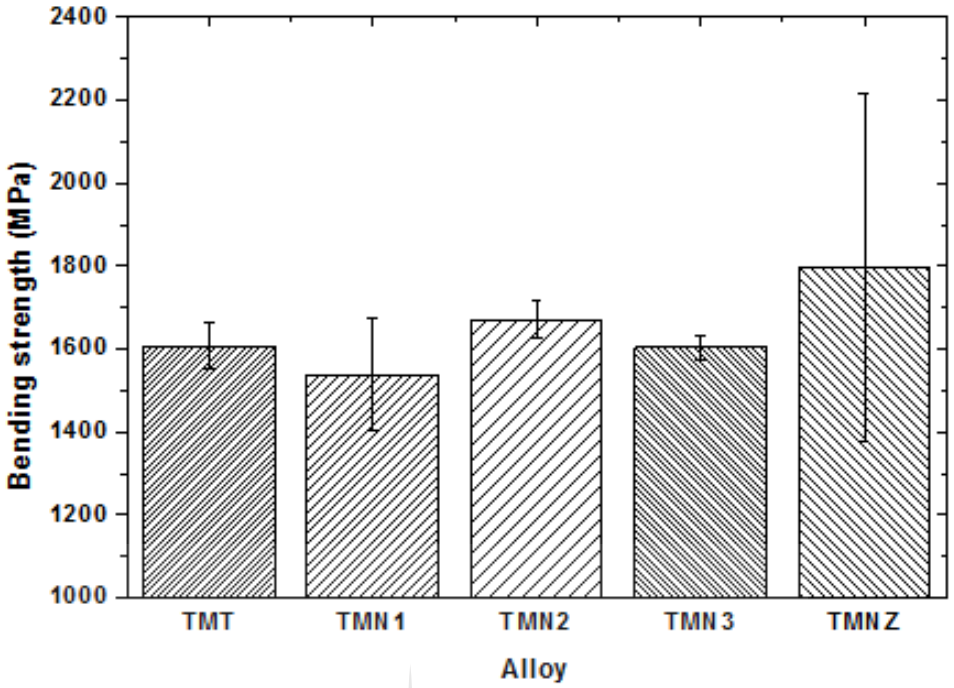

Figure 4-53: Bending strength of the AC alloy specimens.

Table 4-11. Bending strengths of AC alloys.

Alloy	Bending Strength (MPa)
TMT	1606 ± 55.7
TMN1	1536 ± 135.5
TMN2	1671 ± 46.4
TMN3	1603 ± 30.8
TMNZ	1797 ± 419.8

Fehler! Verweisquelle konnte nicht gefunden werden. and Table 4-12 illustrates the bending strengths of the ST TMT, TMN1, TMN2, TMN3 and TMNZ alloy specimens. It can be seen that the ST TMT alloy specimen had the lowest bending strength, whereas TMNZ ST alloys possessed the highest bending strength. Similar to the bending strength of the AC TMT alloy specimen, the largest amount of the ω phase in the ST TMT alloy induced premature, brittle fracture. The highest bending strength in TMNZ alloy specimen was attributable to the combined solid solution strengthening effect of Mo, Nb and Zr and the nano-sized ω phase precipitates in the β matrix.

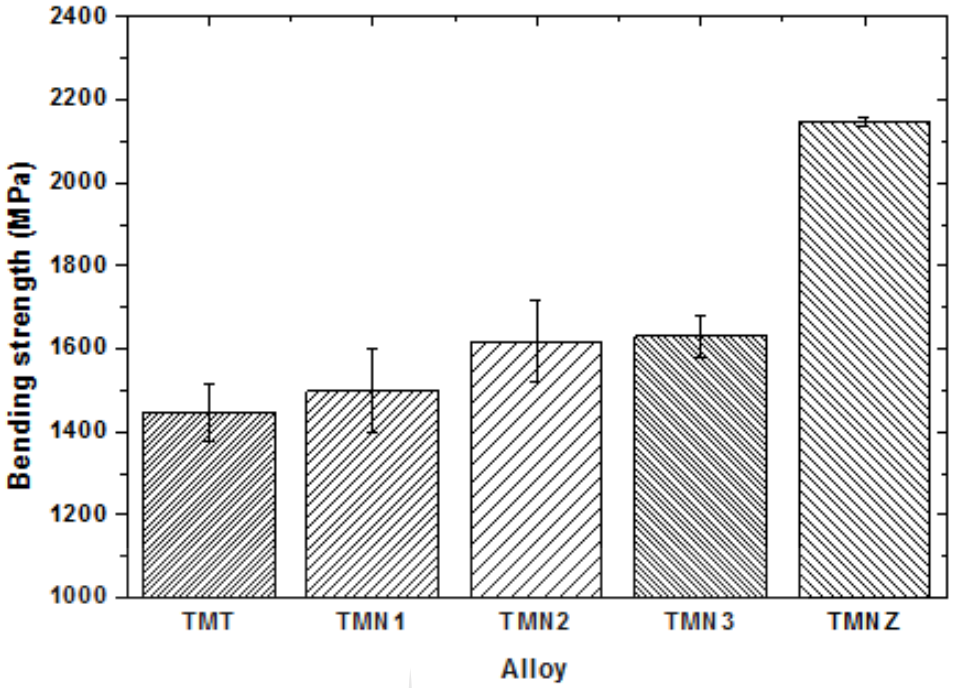

Figure 4-54: Bending strength of the ST alloy specimens.

Table 4-12. Bending strengths of ST alloys.

Alloy	Bending Strength (MPa)
TMT	1446 ±67.4
TMN1	1498 ± 99.9
TMN2	1618 ± 97.9
TMN3	1630 ± 51.3
TMNZ	2147 ± 11.6

The designed alloys in both AC and ST conditions exhibited bending strengths that were far greater than that of CP Ti (844 MPa) [21,113]. Except for the bending strength of the TMNZ alloy, the bending strength of the designed AC and ST alloys was lower than that of Ti6Al4V alloy (1860MPa) [126]. Mohan *et al.* [127] reported bending strengths in the range 1313-1440 MPa in sintered Ti-Mo-Zr-Cr alloys, which are substantially lower than those obtained in this study in both AC and ST conditions. Conversely, Ho et al. [113] obtained bending strengths in the range 1472–2098 MPa in Ti-10Zr-xMo alloys, which were similar to those obtained in this study. Hsu *et al.* [22] measured bending strengths in Ti-25Nb-xSn alloy ranging between 962 and 1908 MPa, whereby the minimum strength was substantially low, whereas the maximum strength was similar to the maximum strengths obtained in this study.

4.4.3.1 Bending Modulus

The bending modulus results of the Ti-Mo binary alloy specimens indicated that the bending modulus was strongly dependent on the alloy composition and phase constituents formed. The lowest bending modulus was observed in the Ti-15Mo alloy specimen comprising a large volume fraction of the β phase, while the Ti-10Mo alloy specimen consisting high proportion of the ω phase exhibited the highest bending modulus.

The bending modulus of the AC alloy specimens is shown in Figure 4-55. The bending moduli of TMT AC, TMN1 AC, TMN2 AC, TMN3 AC and TMNZ AC alloys are 91 ± 0.6 GPa, 91 ± 5.8 GPa, 65 ± 1.0 GPa, 70 ± 1.7 GPa and 72 ± 4.2 GPa, respectively. AC TMT and TMN1 alloy specimens exhibited high and close bending moduli, due to the high proportion of the ω phase. The TMN2 alloy specimen had the lowest bending modulus, which was attributed to the large volume fraction of the β phase, which led to the significant suppression of the ω phase precipitation. Similar results were reported by [22] in Ti–25Nb–8Sn and Ti–25Nb–9Sn with bending moduli of 52 and 53 GPa, respectively, which were related to the β phase. No significant difference was observed between the elastic moduli of AC TMN3 and AC TMNZ alloys. The TMN2 alloy specimen had a significantly lower bending modulus than the other alloy specimens. This suggests that the increase in Nb glue atoms to three promoted the retention of a large volume fraction of the β phase and the suppression of the large volume fraction of the ω phase compared to the other alloy specimens. The effect of the ω phase on modulus was not influenced by its weakening effect. Therefore, the AC TMT and TMN1 alloy still showed the highest bending moduli, despite their relatively lowest bending strength compared to the other alloys. Similar results were reported in AC Ti– 7.5Mo–xFe [106] and Ti–10Zr–xMo [113] alloy series.

Table 4-13. Bending moduli of AC alloys.

Alloy	Bending Modulus (GPa)
TMT	91 ± 0.6
TMN1	91 ± 5.8
TMN2	65 ± 1.0
TMN3	70 ± 1.7
TMNZ	72 ± 4.2

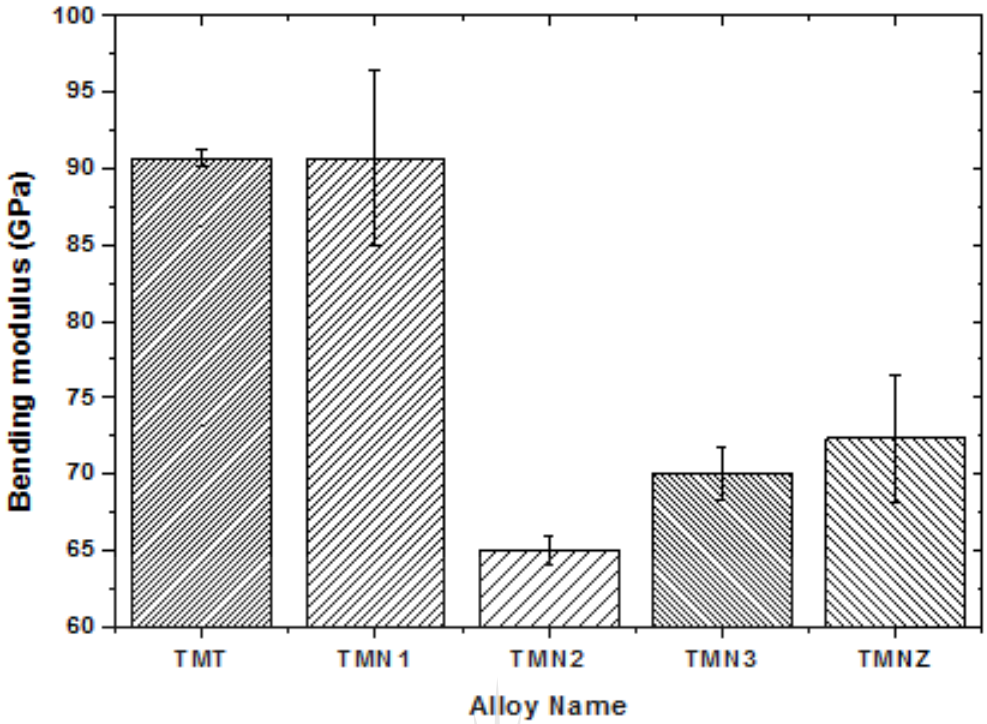

Figure 4-55: Bending modulus of the AC alloy specimens.

Figure 4-56 and Table 4-14 show the bending moduli of the ST alloy specimens, which are 78 ± 3.9 GPa, 68 ± 1.7 GPa, 64 ± 1.5 GPa, 66 ± 2.4 GPa and 67 ± 1.7 GPa, for ST TMT, TMN1, TMN2, TMN3 and TMNZ alloy specimens, respectively. It is evident that the TMT alloy specimen had the highest bending modulus, whereas the TMN2 alloy specimen showed the lowest bending modulus. The substitution of the Ti glue atom with one Nb atom led to a significant reduction in the bending modulus of TMN1 alloy specimen, which was further significantly decreased after the addition of one more Nb atom in TMN2 alloy specimen. It can be seen that no significant difference exists among the bending moduli of TMN2, TMN3 and TMNZ alloy specimens.

Table 4-14. Bending moduli of ST alloys.

Alloy	Bending Modulus (GPa)
TMT	78 ± 3.9
TMN1	68 ± 1.7
TMN2	64 ± 1.5
TMN3	66 ± 2.4
TMNZ	67 ± 1.7

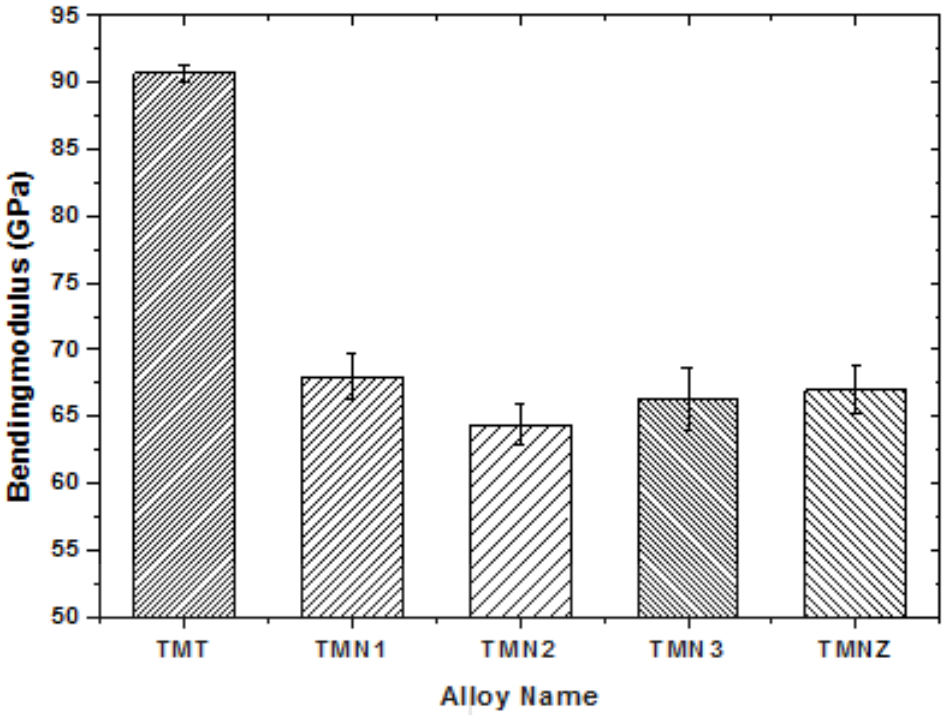

Figure 4-56: Bending modulus of ST alloy specimens.

The AC and ST designed alloys exhibited higher bending moduli than that of CP Ti (99 GPa). Mohan *et al.* [127] obtained bending moduli in sintered Ti-Mo-Zr-Cr ranging between 86-99 GPa. With the exception of AC TMT and TMN1 alloy specimens, these bending moduli were substantially higher than those of the other AC and ST alloy specimens in this study. Hsu et al. [22] reported the lowest bending modulus of 52 GPa in Ti-25Nb-8Sn alloy.

Figure 4-57 compares the bending moduli of the AC alloy specimens with the ST alloy specimens. It can be seen that the bending moduli of the TMT and TMN1 alloy specimen were significantly reduced after solution treatment. Contrarily, the bending moduli of AC and ST TMN2, AC and ST TMN3 as well as AC and ST TMNZ alloy specimens showed no significant difference. In general, there was a decreasing trend of the bending moduli although not significant for certain alloys, which would better justify the argument that solution treatment significantly suppressed the precipitation of the ω phase.

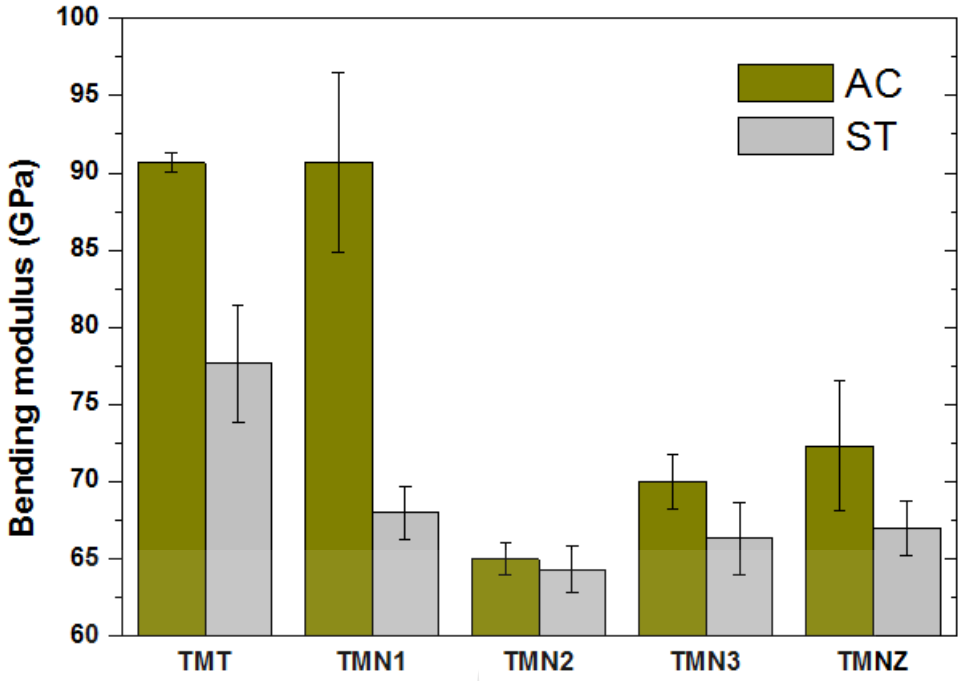

Figure 4-57. Comparison of the bending moduli of the AC and ST alloy specimens.

4.4.4 Compression test results

- **Compressive stress-strain curves**

The compressive properties of the developed alloy specimens are given in Table 4-15. It is noteworthy that the test was stopped just after the alloy specimen were strained about 12%, before the densification/ parabola stage could be reached, because of the limitations of measurements of the equipment. The ductile feature of the alloy specimens under compression loading is ascribed to the propagation behaviour of the cracks, i.e., cracks prone to remain closed under compression stress [59]. It is evident that the compressive strength of AC TMT, TMN1 and TMNZ alloy specimens are far greater than the strengths of 316L stainless steel (170-310 MPa) and CP Ti orthopaedic implant materials. Furthermore, the compressive strength of the TMT alloy specimen is comparable to the highest strength of CoCr, whereas TMN1 and TMNZ alloy specimens had strengths that fell within the CoCr strength range (450-1896 MPa). Contrarily, the compressive strengths of TMN2 and TMN3 alloy specimens were slightly lower than the highest strength of CP Ti (590-1117 MPa), but substantially lower than the highest strength of CoCr implant material.

Table 4-15: Compressive properties of the ST Ti-Mo binary alloys

Alloy	Compressive strength (MPa)	Yield strength (MPa)	E (GPa)	Reference
AC TMN1	1542	1234	26	This study
AC TMN2	1050	865	23	This study
AC TMN3	1075	828	22	This study
AC TMNZ	1358	1116	27	This study
ST TMT	1002	512	27	This study
ST TMN1	1146	856	21	This study
ST TMN2	1049	876	17	This study
ST TMN3	1022	818	14	This study
ST TMNZ	1319	1041	22	This study
CP Ti	590-1117	-	-	[6,26]
CoCr	(450-1896	-	-	[6,26]
316L Stainless steel	170-310	-	-	[6,26]

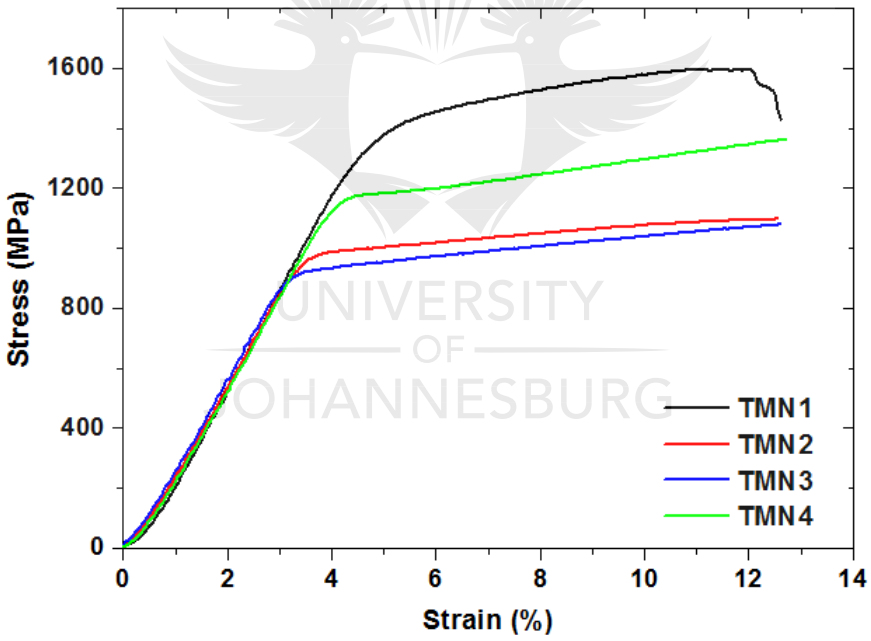

Figure 4-58: Compressive stress-strain curves of the AC alloy specimens.

The AC TMN1 alloy specimen exhibited the highest compressive strength and yield strength among the developed AC alloy specimens, meanwhile, TMN3 showed the lowest strengths. Similar to the bend test results, the highest strengths in AC TMT was attributed to the large volume fraction of the ω nano-particles. Both the compressive strength and yield strength of TMN2 alloy specimen were slightly higher than those of TMN3 alloy specimen, which consisted of a high proportion of the β phase with lower strength than the ω and the martensitic

α" phases. It is clearly visible that both the compressive strength and yield strength decreased with the increasing number of Nb atoms in the glue site.

These results are similar to the work of Zhang *et al.* [44], who observed a decrease in the compressive strength with increasing Nb concentration in the as-cast Ti-15Mo-xNb alloy series. Xu et al. [126] also demonstrated that the compressive strength and yield strength of Ti-0MoxNb alloys reduced with increasing Nb content.

Figure 4-59 depicts typical room temperature compressive stress-strain curves of the ST alloy specimens. It is clearly shown that the alloy specimens had undergone considerable plastic deformation. ST TMT alloy specimen exhibited the lowest compressive strength and yield strength, meanwhile, the elastic modulus was the highest. This was attributable to a large amount of the ω phase precipitated in the β phase matrix. The yield strengths of TMN1, TMN2 and TMN3 ternary alloy specimens were substantially improved, which was ascribed to the combined solid solution strengthening effect of the Mo and Nb. TMN3 alloy specimen showed the lowest elastic modulus, due to the high volume fraction of the β phase in the alloy. It is clearly shown that the presence of Zr in the TMNZ alloy specimen contributed towards the increase in both compressive strength and yield strength, whereas the elastic modulus was similar to that of TMN1 alloy specimen.

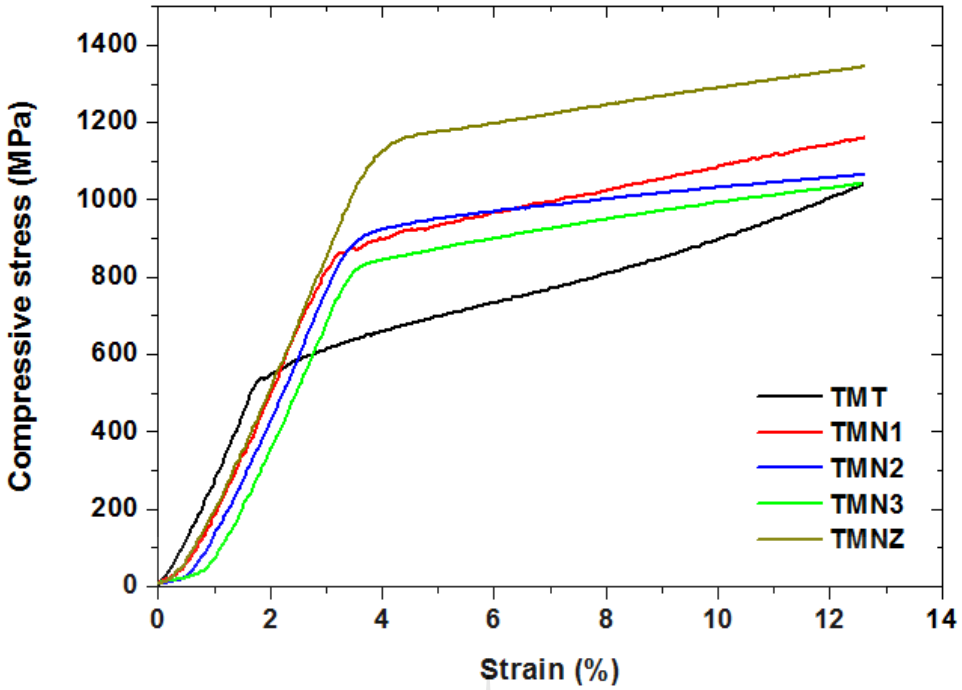

Figure 4-59: Compressive stress-strain curves of the ST alloy specimens.

It is also evident that the compressive strengths of ST TMN1 and TMNZ alloy specimens are substantially higher than those of 316L stainless steel (170-310 MPa) and CP Ti (590-1117 MPa) orthopaedic implant materials. However, both alloys were substantially lower than the highest compressive strength of CoCr implant material. TMT, TMN2 and TMN3 alloy specimens possessed compressive strength that was slightly lower than the highest strength of CP Ti, but far greater than the strength of 316L stainless steel. The compressive elastic moduli of TMN1 and TMNZ alloy specimens were similar and both higher than those of TMN2 and TMN3 alloy specimens, which were also comparable. The lower elastic moduli in TMN2 and TMN3 alloy specimens were ascribed to the higher β stability in both alloy specimens than in the TMN1 and TMNZ alloy specimens.

5 Conclusion and Recommendations

5.1 Conclusions

In this work, a series of metastable β-type Ti-Mo-Nb-Zr alloys were studied. The alloys were formulated using a suite of approaches including the cluster-plus-glue-atom model and the β stability predicting approaches including molybdenum equivalence, d-electron method and the average electron concentration (e/a) ratio). The feasibility of the synergic combination of the approaches was experimentally validated by investigating the microstructural and phase evolution and their mechanical properties of the alloys.

The following conclusions can be drawn based on the set objectives outlined for this study (see Chapter 1.5):

- The correlation between alloy composition, microstructure and mechanical properties of Ti-Mo binary alloys was studied. The microstructures of all the Ti-Mo binary alloys comprised primarily the β phase and secondary martensitic α" and athermal ω nano-particles. The stability of the β phase generally increased with increasing Mo content; however, with the increasing β stability, the precipitation of the secondary martensitic α" and ω phases in the β matrix was suppressed. The mechanical properties including microhardness, tensile properties, bending properties and compressive properties were strongly influenced by the amount of the ω phase precipitated in the alloys. Except for the elastic modulus, the mechanical properties were superior in alloys containing a large amount of the ω phase. The study finds that the presence of a large amount of the ω phase also induced embrittlement in the Ti-Mo alloys.
- Multicomponent alloy compositions were formulated using the cluster-plus-glue-atom model with the cluster formula $[(Mo)(Ti_{14-x}Zr_x)]Ti_yNb_z$ and their β phase stability was also determined using the Mo equivalence, d-electron method and the e/a ratio approaches. The molybdenum equivalence and e/a ratio values of the designed alloys in the range between 11.78 to 16.65 wt%, and 4.24 and 4.45, respectively, were all above the critical values, suggesting that the designed alloys would form a single β phase. The d-electron theory projected the formation of the predominantly β phase after the substitution of the Ti glue atoms with the Nb atom(s), while the substitution of one Ti glue atom in the cluster shell with a Zr atom would lead to the nucleation orthorhombic α" martensitic phase.
- Experimentally, the influence of Nb and/or Zr β stabilizers on the microstructural evolution and mechanical properties of the as-cast designed Ti-Mo-Nb-Zr alloys was determined.

- The microstructures generally exhibited primary BCC β phase and secondary precipitates of the orthorhombic martensitic α" and athermal ω phase. High microhardness was observed in alloys containing one Nb glue atom due to the large amount of the ω phase, which induced precipitation hardening effect on the β matrix, and/or one Zr atom in the cluster shell due to solid solution strengthening by the alloying elements.

- The mechanical properties are strongly dependent on the number of Nb atoms in the glue site of the cluster formula as well the Zr atom that substituted the Ti atom in the cluster shell. Generally, the addition of two to three Nb atoms and/ or the Zr in the cluster shell resulted in higher tensile and yield strengths, while the one Nb glue atom resulted in the lowest elastic modulus. All the as-cast alloys failed in a brittle manner. The variations of Nb and Zr atoms in the cluster formula did not cause a significant difference in the bending properties; however, two Nb glue atoms resulted in the lowest bending modulus, while one Nb glue atom and/ or one Zr atom in the cluster shell, ductile properties were observed. The highest compressive and yield strengths were obtained at one Nb and/ Zr atoms, while two Nb atoms resulted in the lowest compressive modulus.

- The effect of solution treatment with subsequent quenching on microstructural evolution and mechanical properties of the as-cast designed alloys was investigated. Similar to the AC alloys, the ST alloys comprised primarily β phase and secondary martensitic α" and ω nanoparticles. Generally, ST alloys precipitated larger volume fractions of the secondary phases than the AC alloys.

- After solution treatment, the tensile strength and elongation at rupture were generally enhanced, whereas the yield strength was decreased. A general increase in the elastic modulus was also observed, meanwhile the elastic admissible strain was considerably high. The bending strength was higher at Nb_1 and Nb_2 glue atom(s) as well as Zr_1 cluster shell atom. The ductility of the alloys was improved, while the bending modulus was generally reduced after solution treatment. The compressive strengths and yield strengths at Nb_1 glue atom was decreased, whereas at Nb_1 and Nb_2 glue atom as well as Zr_1 cluster shell atom, t both the compressive

strengths and yield strengths were similar to those of the AC alloys. The compressive modulus of elasticity was generally reduced.

- The accuracy of the theoretical prediction tools, with reference to the experimentally obtained results, for the alloys was evaluated. According to the experimental findings, the *Moeq* and e/a ratio approaches overestimated the β-stabilizing effect of alloying elements Mo, Nb and Zr in the designed multicomponent alloy. In the case of the d-electron theory approach, an overestimation of the β-stabilizing effect of the Mo and Nb was observed in the TMN alloys, respectively. Meanwhile, the β-stabilizing effect of Mo, Nb and Zr in TMNZ alloy was underestimated.
- The microstructural and mechanical characteristics have indicated that the combinatorial use of the cluster-plus-glue atom model and β-stability predicting approaches to design metastable β-type Ti-Mo-Nb-Zr alloys with low elastic modulus for orthopaedic applications is feasible. Furthermore, the superior mechanical properties of the designed alloys, obtained in the absence of thermo-mechanical processing, indicate that these alloys are suitable candidates for orthopaedic applications.

5.2 Contribution to knowledge

This Ph.D. study demonstrates the utility of combinatorial predicting approaches, and particularly the cluster-plus-glue-atom model in predicting and explaining the microstructural evolution and properties of as-cast and solution treated Ti-Mo and Ti-Mo-Nb-Zr alloys. This Ph.D. study has shown that high β stability and elastic moduli that are closer to that of the human bone in metastable β-type Ti-Mo-Nb-Zr alloy series can be achieved by the use of the cluster-plus-glue-atom model and the β phase predicting approaches. The challenge of theoretically predicting the undesirable α" and ω phases were resolved by the use of the predicting tools, which minimized the number of trials for alloy development and also simplified the optimization process. This study has also demonstrated the influence of Mo, Nb and Zr stabilizers on the microstructural evolution in as-cast and solution treated Ti-Mo and Ti-Mo-Nb-Zr alloys which to the best knowledge of the author, has been underreported. The mechanical properties of metastable β-type Ti alloys such as tensile strength, yield strength, elongation and elastic admissible strains were generally improved by solution treatment above the β-transus with subsequent ice water quenching.

5.3 Recommendations

Following the findings and the conclusions drawn from this study, the author makes the following recommendations:

- Further study on EBSD analysis to identify the secondary phases in the designed alloys and studying their morphology using transmission electron microscopy (TEM).
- Enhance the mechanical properties by performing more heat treatment procedures.
- Intensive study of the effect of the ω phase on the mechanical properties.
- Corrosion tests to investigate behaviour of the alloys in different simulated body fluids.

References

[1] A. Almeida, D. Gupta, C. Loable, and R. Vilar, "Laser-assisted synthesis of Ti – Mo alloys for biomedical applications," *Mater. Sci. Eng. C*, vol. 32, no. 5, pp. 1190–1195, 2012, doi: 10.1016/j.msec.2012.03.007.

[2] K. S. Katti, "Biomaterials in total joint replacement," *Colloids Surfaces B Biointerfaces*, vol. 39, no. 3, pp. 133–142, 2004, doi: 10.1016/j.colsurfb.2003.12.002.

[3] G. Radenković and D. Petković, "Metallic Biomaterials," in *Biomaterials in Clinical Practice*, Cham: Springer International Publishing, 2018, pp. 183–224.

[4] S. Guo, Q. Meng, X. Zhao, Q. Wei, and H. Xu, "Design and fabrication of a metastable β-type titanium alloy with ultralow elastic modulus and high strength," *Sci. Rep.*, vol. 5, no. September, pp. 1–8, 2015, doi: 10.1038/srep14688.

[5] M. Navarro, A. Michiardi, O. Castaño, and J. A. Planell, "Biomaterials in orthopaedics," *J. R. Soc. Interface*, vol. 5, no. 27, pp. 1137–1158, 2008, doi: 10.1098/rsif.2008.0151.

[6] M. Kaur and K. Singh, "Review on titanium and titanium based alloys as biomaterials for orthopaedic applications," *Mater. Sci. Eng. C*, vol. 102, no. December 2018, pp. 844–862, 2019, doi: 10.1016/j.msec.2019.04.064.

[7] D. Kuroda, M. Niinomi, M. Morinaga, Y. Kato, and T. Yashiro, "Design and mechanical properties of new β type titanium alloys for implant materials," *Mater. Sci. Eng. A*, vol. 243, no. 1–2, pp. 244–249, 1998, doi: 10.1016/s0921-5093(97)00808-3.

[8] P. S. Nnamchi, C. S. Obayi, I. Todd, and M. W. Rainforth, "Mechanical and electrochemical characterisation of new Ti-Mo-Nb-Zr alloys for biomedical applications," *J. Mech. Behav. Biomed. Mater.*, vol. 60, pp. 68–77, 2016, doi: 10.1016/j.jmbbm.2015.12.023.

[9] M. L. Raganya, N. M. Moshokoa, B. Obadele, P. A. Olubambi, and R. Machaka, "The microstructural and mechanical characterization of the β-type Ti-11.1Mo-10.8Nb alloy for biomedical applications," *IOP Conf. Ser. Mater. Sci. Eng.*, vol. 655, no. 1, p. 012025, Nov. 2019, doi: 10.1088/1757-899X/655/1/012025.

[10] C. Marker, S. L. Shang, J. C. Zhao, and Z. K. Liu, "Effects of alloying elements on the elastic properties of bcc Ti-X alloys from first-principles calculations," *Comput. Mater. Sci.*, vol. 142, pp. 215–226, 2018, doi: 10.1016/j.commatsci.2017.10.016.

[11] N. Moshokoa, L. Raganya, B. Obadele, P. Olubambi, and R. Machaka, "Effects of Mo content on the microstructural and mechanical properties of as-cast Ti-Mo alloys," *IOP Conf. Ser. Mater. Sci. Eng.*, vol. 655, no. 1, 2019, doi: 10.1088/1757-

899X/655/1/012015.

[12] S. Bahl, S. Das, S. Suwas, and K. Chatterjee, “Engineering the next-generation tin containing β titanium alloys with high strength and low modulus for orthopedic applications,” *J. Mech. Behav. Biomed. Mater.*, 2018, doi: 10.1016/j.jmbbm.2017.11.014.

[13] M. B. Nasab, M. R. Hassan, and B. Bin Sahari, “Metallic biomaterials of knee and hip - A review,” *Trends Biomater. Artif. Organs*, vol. 24, no. 2, pp. 69–82, 2010.

[14] D. McCutchen, E. Dibble, and M. M. Blount, “Phonemic effects in reading comprehension and text memory,” *Appl. Cogn. Psychol.*, vol. 8, no. 6, pp. 597–611, 1994, doi: 10.1002/acp.2350080606.

[15] M. Geetha, A. K. Singh, R. Asokamani, and A. K. Gogia, “Ti based biomaterials, the ultimate choice for orthopaedic implants - A review,” *Prog. Mater. Sci.*, vol. 54, no. 3, pp. 397–425, 2009, doi: 10.1016/j.pmatsci.2008.06.004.

[16] H. J. Rack and J. I. Qazi, “Titanium alloys for biomedical applications,” *Mater. Sci. Eng. C*, vol. 26, no. 8, pp. 1269–1277, 2006, doi: 10.1016/j.msec.2005.08.032.

[17] K. KATTI, D. VERMA, and D. KATTI, “Materials for joint replacement,” in *Joint Replacement Technology*, Elsevier, 2008, pp. 81–104.

[18] G. Manivasagam, D. Dhinasekaran, and A. Rajamanickam, “40RPTCS.pdf,” no. i, pp. 40–54, 2010.

[19] C. Kenesi, “Biomaterials in orthopedic surgery,” *Concours Med.*, vol. 106, no. 20, pp. 1879–1890, 1984.

[20] M. Abdel-Hady Gepreel and M. Niinomi, “Biocompatibility of Ti-alloys for long-term implantation,” *J. Mech. Behav. Biomed. Mater.*, vol. 20, pp. 407–415, 2013, doi: 10.1016/j.jmbbm.2012.11.014.

[21] A. Bansiddhi and D. C. Dunand, “Titanium and NiTi foams for bone replacement,” in *Bone Substitute Biomaterials*, Elsevier, 2014, pp. 142–179.

[22] H. C. Hsu, S. C. Wu, S. K. Hsu, J. Y. Syu, and W. F. Ho, “The structure and mechanical properties of as-cast Ti-25Nb-xSn alloys for biomedical applications,” *Mater. Sci. Eng. A*, vol. 568, pp. 1–7, 2013, doi: 10.1016/j.msea.2013.01.002.

[23] K. Prasad *et al.*, “Metallic biomaterials: Current challenges and opportunities,” *Materials (Basel).*, vol. 10, no. 8, 2017, doi: 10.3390/ma10080884.

[24] L. C. Zhang and L. Y. Chen, “A Review on Biomedical Titanium Alloys: Recent Progress and Prospect,” *Adv. Eng. Mater.*, vol. 21, no. 4, pp. 1–29, 2019, doi:

10.1002/adem.201801215.

[25] I. Kopova, J. Stráský, P. Harcuba, M. Landa, M. Janeček, and L. Bačákova, "Newly developed Ti-Nb-Zr-Ta-Si-Fe biomedical beta titanium alloys with increased strength and enhanced biocompatibility," *Mater. Sci. Eng. C*, vol. 60, pp. 230–238, 2016, doi: 10.1016/j.msec.2015.11.043.

[26] M. T. Mohammed, "Beta Titanium Alloys: The Lowest Elastic Modulus for Biomedical Applications: A Review Surface Modifications through FSP View project MACHINING View project," no. August, 2014, [Online]. Available: https://www.researchgate.net/publication/265396160.

[27] K. K. Sankaran and R. S. Mishra, "Titanium Alloys," in *Metallurgy and Design of Alloys with Hierarchical Microstructures*, Elsevier, 2017, pp. 177–288.

[28] P. J. Bania, "Beta titanium alloys and their role in the titanium industry," *Jom*, vol. 46, no. 7, pp. 16–19, 1994, doi: 10.1007/BF03220742.

[29] V. Brailovski *et al.*, "Bulk and porous metastable beta Ti-Nb-Zr(Ta) alloys for biomedical applications," *Mater. Sci. Eng. C*, vol. 31, no. 3, pp. 643–657, 2011, doi: 10.1016/j.msec.2010.12.008.

[30] R. Kolli and A. Devaraj, "A Review of Metastable Beta Titanium Alloys," *Metals (Basel).*, vol. 8, no. 7, p. 506, 2018, doi: 10.3390/met8070506.

[31] P. Sochacka, A. Miklaszewski, and M. Jurczyk, "Development of β-type Ti-x at. % Mo alloys by mechanical alloying and powder metallurgy: Phase evolution and mechanical properties ($10 \leq x \leq 35$)," *J. Alloys Compd.*, vol. 776, pp. 370–378, 2019, doi: 10.1016/j.jallcom.2018.10.217.

[32] M. Abdel-Hady, "Texturing Tendency in β-Type Ti-Alloys," *Recent Dev. Study Recryst.*, 2013, doi: 10.5772/53588.

[33] W. F. Ho, C. P. Ju, and J. H. C. Lin, "Structure and properties of cast binary Ti } Mo alloys," vol. 20, no. May, pp. 2115–2122, 1999.

[34] X. R. Hq, "(IIHFW RI 2PHJD 3KDVH RQ 0HFKDQLFDO 3URSHUWLHV RI 7L 0R $ OOR \ V IRU % LRPHGLFDO $ SSOLFDWLRQV," pp. 3–7.

[35] B. S. Sung, T. E. Park, and Y. H. Yun, "Microstructures and electrochemical behavior of Ti-Mo alloys for biomaterials," *Adv. Mater. Sci. Eng.*, vol. 2015, 2015, doi: 10.1155/2015/872730.

[36] F. F. Cardoso, P. L. Ferrandini, E. S. N. N. Lopes, A. Cremasco, and R. Caram, "Ti-Mo alloys employed as biomaterials: Effects of composition and aging heat treatment on

microstructure and mechanical behavior," *J. Mech. Behav. Biomed. Mater.*, vol. 32, pp. 31–38, 2014, doi: 10.1016/j.jmbbm.2013.11.021.

[37] M. Sabeena, A. George, S. Murugesan, R. Divakar, E. Mohandas, and M. Vijayalakshmi, "Microstructural characterization of transformation products of bcc β in Ti-15 Mo alloy," *J. Alloys Compd.*, vol. 658, pp. 301–315, 2016, doi: 10.1016/j.jallcom.2015.10.200.

[38] C. M. Lee, C. P. Ju, and J. H. C. Lin, "Structure ± property relationship of cast Ti ± Nb alloys," pp. 314–322, 2002.

[39] G. T. Aleixo, C. R. M. Afonso, A. A. Coelho, and R. Caram, "Effects of Omega Phase on Elastic Modulus of Ti-Nb Alloys as a Function of Composition and Cooling Rate," *Solid State Phenom.*, vol. 138, no. July 2018, pp. 393–398, 2008, doi: 10.4028/www.scientific.net/SSP.138.393.

[40] Y. L. Zhou, M. Niinomi, and T. Akahori, "Effects of Ta content on Young's modulus and tensile properties of binary Ti-Ta alloys for biomedical applications," *Mater. Sci. Eng. A*, 2004, doi: 10.1016/j.msea.2003.12.011.

[41] W. F. Ho, T. Y. Chiang, S. C. Wu, and H. C. Hsu, "Mechanical properties and deformation behavior of cast binary Ti-Cr alloys," *J. Alloys Compd.*, vol. 468, no. 1–2, pp. 533–538, 2009, doi: 10.1016/j.jallcom.2008.01.046.

[42] H. C. Hsu, S. C. Wu, Y. S. Hong, and W. F. Ho, "Mechanical properties and deformation behavior of as-cast Ti-Sn alloys," *J. Alloys Compd.*, 2009, doi: 10.1016/j.jallcom.2008.12.064.

[43] S. Guo, J. Zhang, X. Cheng, and X. Zhao, "A metastable β-type Ti–Nb binary alloy with low modulus and high strength," *J. Alloys Compd.*, vol. 644, pp. 411–415, 2015, doi: 10.1016/j.jallcom.2015.05.071.

[44] L. B. Zhang, K. Z. Wang, L. J. Xu, S. L. Xiao, and Y. Y. Chen, "Effect of Nb addition on microstructure, mechanical properties and castability of β-type Ti-Mo alloys," *Trans. Nonferrous Met. Soc. China (English Ed.*, vol. 25, no. 7, pp. 2214–2220, 2015, doi: 10.1016/S1003-6326(15)63834-1.

[45] L. You and X. Song, "A study of low Young′s modulus Ti-Nb-Zr alloys using d electrons alloy theory," *Scr. Mater.*, vol. 67, no. 1, pp. 57–60, 2012, doi: 10.1016/j.scriptamat.2012.03.020.

[46] A. Mehjabeen, W. Xu, D. Qiu, and M. Qian, "Redefining the β-Phase Stability in Ti-Nb-Zr Alloys for Alloy Design and Microstructural Prediction," *Jom*, vol. 70, no. 10,

pp. 2254–2259, 2018, doi: 10.1007/s11837-018-3010-1.

[47] H. Hsu, S. Wu, S. Hsu, W. Kao, and W. Ho, "Materials Science & Engineering A Structure and mechanical properties of as-cast Ti – 5Nb-based alloy with Mo addition," *Mater. Sci. Eng. A*, vol. 579, pp. 86–91, 2013, doi: 10.1016/j.msea.2013.05.004.

[48] E. S. N. Lopes, A. Cremasco, C. R. M. Afonso, and R. Caram, "Effects of double aging heat treatment on the microstructure, Vickers hardness and elastic modulus of Ti-Nb alloys," *Mater. Charact.*, vol. 62, no. 7, pp. 673–680, 2011, doi: 10.1016/j.matchar.2011.04.015.

[49] T.-K. Jung, S. Semboshi, N. Masahashi, and S. Hanada, "Mechanical properties and microstructures of β Ti–25Nb–11Sn ternary alloy for biomedical applications," *Mater. Sci. Eng. C*, vol. 33, no. 3, pp. 1629–1635, Apr. 2013, doi: 10.1016/j.msec.2012.12.072.

[50] X. Zhao, M. Niinomi, M. Nakai, T. Ishimoto, and T. Nakano, "Development of high Zr-containing Ti-based alloys with low Young's modulus for use in removable implants," *Mater. Sci. Eng. C*, vol. 31, no. 7, pp. 1436–1444, 2011, doi: 10.1016/j.msec.2011.05.013.

[51] P. A. B. Kuroda, M. A. R. Buzalaf, and C. R. Grandini, "Effect of molybdenum on structure, microstructure and mechanical properties of biomedical Ti-20Zr-Mo alloys," *Mater. Sci. Eng. C*, vol. 67, pp. 511–515, 2016, doi: 10.1016/j.msec.2016.05.053.

[52] C. F. Liu *et al.*, "A unique hybrid-structured surface produced by rapid electrochemical anodization enhances bio-corrosion resistance and bone cell responses of β-type Ti-24Nb-4Zr-8Sn alloy," *Sci. Rep.*, vol. 8, no. 1, pp. 1–14, 2018, doi: 10.1038/s41598-018-24590-x.

[53] Y. L. Hao, S. J. Li, S. Y. Sun, C. Y. Zheng, and R. Yang, "Elastic deformation behaviour of Ti-24Nb-4Zr-7.9Sn for biomedical applications," *Acta Biomater.*, 2007, doi: 10.1016/j.actbio.2006.11.002.

[54] J. Lin *et al.*, "Novel Ti-Ta-Hf-Zr alloys with promising mechanical properties for prospective stent applications," *Sci. Rep.*, vol. 6, no. June, pp. 1–11, 2016, doi: 10.1038/srep37901.

[55] A. W. Nugroho, G. Leadbeater, and I. J. Davies, "Processing and properties of porous Ti-Nb-Ta-Zr alloy for biomedical applications using the powder metallurgy route," *Aust. J. Mech. Eng.*, vol. 8, no. 2, pp. 169–175, 2011, doi: 10.1080/14484846.2011.11464608.

[56] M. J. Bermingham, S. D. McDonald, A. J. Buddery, D. H. Stjohn, and M. S. Dargusch, "Processing considerations for cast Ti-25Nb-3Mo-3Zr-2Sn biomedical alloys," *Mater.*

Sci. Eng. C, vol. 31, no. 7, pp. 1520–1525, 2011, doi: 10.1016/j.msec.2011.06.011.

[57] B. Jiang *et al.*, "Effects of Nb and Zr on structural stabilities of Ti-Mo-Sn-based alloys with low modulus," *Mater. Sci. Eng. A*, vol. 687, no. December 2016, pp. 1–7, 2017, doi: 10.1016/j.msea.2017.01.047.

[58] Q. Wang *et al.*, "Microstructures and Stability Origins of β-(Ti,Zr)-(Mo,Sn)-Nb Alloys with Low Young's Modulus," *Metall. Mater. Trans. A Phys. Metall. Mater. Sci.*, vol. 46, no. 9, pp. 3924–3931, 2015, doi: 10.1007/s11661-015-3011-4.

[59] S. Ozan, J. Lin, Y. Li, and C. Wen, "New Ti-Ta-Zr-Nb alloys with ultrahigh strength for potential orthopedic implant applications," *J. Mech. Behav. Biomed. Mater.*, vol. 75, no. May, pp. 119–127, 2017, doi: 10.1016/j.jmbbm.2017.07.011.

[60] P. Laheurte, F. Prima, A. Eberhardt, T. Gloriant, M. Wary, and E. Patoor, "Mechanical properties of low modulus β titanium alloys designed from the electronic approach," *J. Mech. Behav. Biomed. Mater.*, vol. 3, no. 8, pp. 565–573, 2010, doi: 10.1016/j.jmbbm.2010.07.001.

[61] Q. Wang, C. Dong, and P. K. Liaw, "Structural Stabilities of β-Ti Alloys Studied Using a New Mo Equivalent Derived from [β/(α + β)] Phase-Boundary Slopes," *Metall. Mater. Trans. A Phys. Metall. Mater. Sci.*, vol. 46, no. 8, pp. 3440–3447, 2015, doi: 10.1007/s11661-015-2923-3.

[62] M. Morinaga, "The molecular orbital approach and its application to biomedical titanium alloy design," in *Titanium in Medical and Dental Applications*, Elsevier, 2018, pp. 39–64.

[63] Q. Wang, C. Ji, Y. Wang, J. Qiang, and C. Dong, "β-Ti alloys with low young's moduli interpreted by cluster-plus-glue-atom model," *Metall. Mater. Trans. A Phys. Metall. Mater. Sci.*, vol. 44, no. 4, pp. 1872–1879, 2013, doi: 10.1007/s11661-012-1523-8.

[64] K. Tulugan, C. Park, W. Qing, and W. Park, "Composition design and mechanical properties of BCC Ti solid solution alloys with low Young's modulus," *J. Mech. Sci. Technol.*, vol. 26, no. 2, pp. 373–377, 2012, doi: 10.1007/s12206-011-1207-0.

[65] M. Buzatu *et al.*, "Obtaining and characterization of the Ti15Mo5W alloy for biomedical applications," *Mater. Plast.*, vol. 54, no. 3, pp. 596–600, 2017, doi: 10.37358/mp.17.3.4905.

[66] M. Morinaga and H. Yukawa, "Alloy design with the aid of molecular orbital method," *Bull. Mater. Sci.*, vol. 20, no. 6, pp. 805–815, 1997, doi: 10.1007/BF02747420.

[67] M. Morinaga and N. Yukawa, "Alloy design based on molecular orbital method," *Mater.*

Trans., vol. 57, no. 3, pp. 213–226, 2016, doi: 10.2320/matertrans.M2015418.

[68] M. Abdel-Hady, K. Hinoshita, and M. Morinaga, "General approach to phase stability and elastic properties of β-type Ti-alloys using electronic parameters," *Scr. Mater.*, vol. 55, no. 5, pp. 477–480, 2006, doi: 10.1016/j.scriptamat.2006.04.022.

[69] J. Du, C. Dong, R. Melnik, Y. Kawazoe, and B. Wen, "Hidden electronic rule in the ' cluster-plus-glue-atom ' model," *Nat. Publ. Gr.*, no. September, pp. 1–11, 2016, doi: 10.1038/srep33672.

[70] Q. Wang, X. D. Zhang, X. N. Li, C. J. Ji, and C. Dong, "Designing Multi-Component β-Ti Alloys with Low Young's Modulus," *Mater. Sci. Forum*, vol. 747–748, pp. 885–889, 2013, doi: 10.4028/www.scientific.net/MSF.747-748.885.

[71] C. Pang, B. Jiang, Y. Shi, Q. Wang, and C. Dong, "Cluster-plus-glue-atom model and universal composition formulas [cluster](glue atom)<inf>x</inf> for BCC solid solution alloys," *J. Alloys Compd.*, vol. 652, pp. 63–69, 2015, doi: 10.1016/j.jallcom.2015.08.209.

[72] Q. Wang, C. Pang, B. Jiang, Y. Shi, Q. Wang, and C. Dong, "Cluster-plus-glue-atom model and universal composition formulas [cluster] (glue atom) x for BCC solid solution alloys Cluster-plus-glue-atom model and universal composition formulas [cluster](glue atom) x for BCC solid solution alloys," *J. Alloys Compd.*, vol. 652, no. August, pp. 63–69, 2015, doi: 10.1016/j.jallcom.2015.08.209.

[73] D. Kuroda, M. Niinomi, M. Morinaga, Y. Kato, and T. Yashiro, "Design and mechanical properties of new β type titanium alloys for implant materials," *Mater. Sci. Eng. A*, vol. 243, no. 1–2, pp. 244–249, 1998, doi: 10.1016/S0921-5093(97)00808-3.

[74] S. B. Gabriel *et al.*, "Characterization of a new beta titanium alloy , Ti – 12Mo – 3Nb , for biomedical applications," *J. Alloys Compd.*, vol. 536, pp. S208–S210, 2012, doi: 10.1016/j.jallcom.2011.11.035.

[75] Y. Y. H. Li *et al.*, "Biomedical TiNbZrTaSi alloys designed by d-electron alloy design theory," *Mater. Des.*, vol. 85, pp. 7–13, 2015, doi: 10.1016/j.matdes.2015.06.176.

[76] T. Ozaki, H. Matsumoto, S. Watanabe, and S. Hanada, "Beta Ti Alloys with Low Young's Modulus," *Mater. Trans.*, vol. 45, no. 8, pp. 2776–2779, 2004, doi: 10.2320/matertrans.45.2776.

[77] H. Matsumoto, S. Watanabe, and S. Hanada, "α′ Martensite Ti-V-Sn alloys with low Young's modulus and high strength," *Mater. Sci. Eng. A*, vol. 448, no. 1–2, pp. 39–48, 2007, doi: 10.1016/j.msea.2006.11.022.

[78] T. Akahori, M. Niinomi, H. Fukui, and M. Ogawa, “Mechanical Properties and Microstructures of Beta-Type Titanium Alloy for Biomedical Applications,” *Mater. Sci. Forum*, vol. 539–543, no. 3, pp. 557–562, 2007, doi: 10.4028/www.scientific.net/MSF.539-543.557.

[79] X. Zhao, M. Niinomi, M. Nakai, and J. Hieda, “Acta Biomaterialia Beta type Ti – Mo alloys with changeable Young ’ s modulus for spinal fixation applications,” *Acta Biomater.*, vol. 8, no. 5, pp. 1990–1997, 2012, doi: 10.1016/j.actbio.2012.02.004.

[80] J. Lin *et al.*, “Effects of solution treatment and aging on the microstructure, mechanical properties, and corrosion resistance of a β type Ti-Ta-Hf-Zr alloy,” *RSC Adv.*, vol. 7, no. 20, pp. 12309–12317, 2017, doi: 10.1039/c6ra28464g.

[81] S. Hanada, N. Masahashi, T. K. Jung, M. Miyake, Y. S. Sato, and H. Kokawa, “Effect of swaging on Young[U+05F3]s modulus of β Ti-33.6Nb-4Sn alloy,” *J. Mech. Behav. Biomed. Mater.*, vol. 32, pp. 310–320, 2014, doi: 10.1016/j.jmbbm.2013.10.027.

[82] S. B. Gabriel, M. C. Rezende, L. H. de Almeida, C. A. Nunes, J. Dille, and G. de A. Soares, “Control of the Microhardness to Young Modulus Ratio by Mechanical Processing of a Ti-10Mo-20Nb Alloy,” *Mater. Res.*, vol. 18, no. suppl 2, pp. 39–42, 2015, doi: 10.1590/1516-1439.343514.

[83] Y. Guo, D. Chen, M. Cheng, W. Lu, L. Wang, and X. Zhang, “The bone tissue compatibility of a new Ti35Nb2Ta3Zr alloy with a low Young’s modulus,” *Int. J. Mol. Med.*, vol. 31, no. 3, pp. 689–697, 2013, doi: 10.3892/ijmm.2013.1249.

[84] M. Tane *et al.*, “Peculiar elastic behavior of Ti–Nb–Ta–Zr single crystals,” *Acta Mater.*, vol. 56, no. 12, pp. 2856–2863, Jul. 2008, doi: 10.1016/j.actamat.2008.02.017.

[85] G. Ryan, A. Pandit, and D. P. Apatsidis, “Fabrication methods of porous metals for use in orthopaedic applications,” *Biomaterials*, vol. 27, no. 13, pp. 2651–2670, 2006, doi: 10.1016/j.biomaterials.2005.12.002.

[86] X. Wan, C. Wu, C. Tan, and J. Lin, “Structure Stability and Elastic Properties of β Type Ti-X (X=Nb, Mo) Alloys from First-Principles Calculations,” *Rare Met. Mater. Eng.*, vol. 43, no. 3, pp. 553–558, Mar. 2014, doi: 10.1016/S1875-5372(14)60075-8.

[87] P. Cao, F. Tian, and Y. Wang, “Effect of Mo on the phase stability and elastic mechanical properties of Ti-Mo random alloys from ab initio calculations,” *J. Phys. Condens. Matter*, vol. 29, no. 43, 2017, doi: 10.1088/1361-648X/aa87d3.

[88] S. Guo, Q. Meng, X. Cheng, and X. Zhao, “Microstructural evolution and mechanical behavior of metastable β-type Ti-30Nb-1Mo-4Sn alloy with low modulus and high

strength," *Prog. Nat. Sci. Mater. Int.*, vol. 25, no. 5, pp. 414–418, 2015, doi: 10.1016/j.pnsc.2015.09.008.

[89] D. M. Gordin *et al.*, "Development of a β-type Ti-12Mo-5Ta alloy for biomedical applications: Cytocompatibility and metallurgical aspects," *J. Mater. Sci. Mater. Med.*, vol. 15, no. 8, pp. 885–891, 2004, doi: 10.1023/B:JMSM.0000036276.32211.31.

[90] W. D. Zhang *et al.*, "Elastic modulus of phases in Ti-Mo alloys," *Mater. Charact.*, vol. 106, pp. 302–307, 2015, doi: 10.1016/j.matchar.2015.06.008.

[91] P. S. Nnamchi, "First principles studies on structural, elastic and electronic properties of new TiMoNbZr alloys for biomedical applications," *Mater. Des.*, vol. 108, pp. 60–67, 2016, doi: 10.1016/j.matdes.2016.06.066.

[92] Y. Abdelrhman, M. A. H. Gepreel, S. Kobayashi, S. Okano, and T. Okamoto, "Biocompatibility of new low-cost (α + β)-type Ti-Mo-Fe alloys for long-term implantation," *Mater. Sci. Eng. C*, vol. 99, no. June, pp. 552–562, 2019, doi: 10.1016/j.msec.2019.01.133.

[93] P. Slopes, Q. Wang, C. Dong, and P. K. Liaw, "Structural Stabilities of β -Ti Alloys Studied Using a New Mo Equivalent Structural Stabilities of b -Ti Alloys Studied Using a New Mo Equivalent Derived from [b /(a + b)] Phase- Boundary Slopes," *Metall. Mater. Trans. A*, vol. 46, no. 8, pp. 3440–3447, 2015, doi: 10.1007/s11661-015-2923-3.

[94] A. Biesiekierski, J. Lin, K. Munir, S. Ozan, Y. Li, and C. Wen, "An investigation of the mechanical and microstructural evolution of a TiNbZr alloy with varied ageing time," *Sci. Rep.*, vol. 8, no. 1, pp. 1–12, 2018, doi: 10.1038/s41598-018-24155-y.

[95] N. T. C. Oliveira, G. Aleixo, R. Caram, and A. C. Guastaldi, "Development of Ti-Mo alloys for biomedical applications: Microstructure and electrochemical characterization," *Mater. Sci. Eng. A*, vol. 452–453, pp. 727–731, 2007, doi: 10.1016/j.msea.2006.11.061.

[96] R. Davis, H. M. Flower, and D. R. F. West, "Martensitic transformations in Ti-Mo alloys," *J. Mater. Sci.*, vol. 14, no. 3, pp. 712–722, 1979, doi: 10.1007/BF00772735.

[97] W. . Ho, C. . Ju, and J. . Chern Lin, "Structure and properties of cast binary Ti–Mo alloys," *Biomaterials*, vol. 20, no. 22, pp. 2115–2122, Nov. 1999, doi: 10.1016/S0142-9612(99)00114-3.

[98] W. F. Ho, "A comparison of tensile properties and corrosion behavior of cast Ti-7.5Mo with c.p. Ti, Ti-15Mo and Ti-6Al-4V alloys," *J. Alloys Compd.*, vol. 464, no. 1–2, pp. 580–583, 2008, doi: 10.1016/j.jallcom.2007.10.054.

[99] C. Li, Y. Zhan, and W. Jiang, "β-Type Ti-Mo-Si ternary alloys designed for biomedical applications," *Mater. Des.*, vol. 34, pp. 479–482, 2012, doi: 10.1016/j.matdes.2011.08.012.

[100] Y. Zhou and D. Luo, "Corrosion behavior of Ti – Mo alloys cold rolled and heat treated," *J. Alloys Compd.*, vol. 509, no. 21, pp. 6267–6272, 2011, doi: 10.1016/j.jallcom.2011.03.045.

[101] J. W. Lu, Y. Q. Zhao, P. Ge, and H. Z. Niu, "Microstructure and beta grain growth behavior of Ti-Mo alloys solution treated," *Mater. Charact.*, vol. 84, no. 96, pp. 105–111, 2013, doi: 10.1016/j.matchar.2013.07.014.

[102] G. S. Dyakonov, E. Zemtsova, S. Mironov, I. P. Semenova, R. Z. Valiev, and S. L. Semiatin, "An EBSD investigation of ultrafine-grain titanium for biomedical applications," *Mater. Sci. Eng. A*, vol. 648, pp. 305–310, 2015, doi: 10.1016/j.msea.2015.09.080.

[103] Y. Danard, L. Lilensten, C. Brozek, F. Sun, P. Vermaut, and F. Prima, "Development of New Titanium Alloys with High Strain Hardening Thanks to Combined TRIP and TWIP Effects: Microstructure/Mechanical Properties Relationships," *TMS 2018 147th Annu. Meet. Exhib.*, no. March, p. 961, 2018, doi: 10.1007/978-3-319-72526-0.

[104] E. Mihalcea, H. V. Hernández, L. Olmos, and O. Jimenez, "Semi-solid sintering of Ti6Al4V/CoCrMo composites for biomedical applications," *Mater. Res.*, vol. 22, no. 2, pp. 2–9, 2019, doi: 10.1590/1980-5373-MR-2018-0391.

[105] C. H. Wang *et al.*, "Martensitic microstructures and mechanical properties of as-quenched metastable β-type Ti–Mo alloys," *J. Mater. Sci.*, vol. 51, no. 14, pp. 6886–6896, 2016, doi: 10.1007/s10853-016-9976-6.

[106] D. J. Lin, J. H. Chern Lin, and C. P. Ju, "Structure and properties of Ti-7.5Mo-xFe alloys," *Biomaterials*, vol. 23, no. 8, pp. 1723–1730, 2002, doi: 10.1016/S0142-9612(01)00233-2.

[107] H. C. Hsu, S. C. Wu, S. K. Hsu, Y. C. Li, and W. F. Ho, "Structure and mechanical properties of as-cast Ti-Si alloys," *Intermetallics*, vol. 47, pp. 11–16, 2014, doi: 10.1016/j.intermet.2013.12.004.

[108] H.-C. Hsu, S.-C. Wu, Y.-S. Hong, and W.-F. Ho, "Mechanical properties and deformation behavior of as-cast Ti–Sn alloys," *J. Alloys Compd.*, vol. 479, no. 1–2, pp. 390–394, Jun. 2009, doi: 10.1016/j.jallcom.2008.12.064.

[109] S. Ehtemam-Haghighi, Y. Liu, G. Cao, and L. C. Zhang, "Phase transition,

microstructural evolution and mechanical properties of Ti-Nb-Fe alloys induced by Fe addition," *Mater. Des.*, vol. 97, pp. 279–286, 2016, doi: 10.1016/j.matdes.2016.02.094.

[110] X. Lu, B. Sun, T. F. Zhao, L. N. Wang, C. C. Liu, and X. H. Qu, "Microstructure and mechanical properties of spark plasma sintered Ti-Mo alloys for dental applications," *Int. J. Miner. Metall. Mater.*, vol. 21, no. 5, pp. 479–486, 2014, doi: 10.1007/s12613-014-0932-7.

[111] S. Li, Y. Hao, R. Yang, Y. Cui, and M. Niinomi, "Effect of Nb on Microstructural Characteristics of Ti-Nb-Ta-Zr Alloy for Biomedical Applications Effect of Nb on Microstructural Characteristics of Ti – Nb – Ta – Zr Alloy for Biomedical Applications," no. December, 2002, doi: 10.2320/matertrans.43.2964.

[112] S. Sadeghpour, S. M. Abbasi, M. Morakabati, A. Kisko, L. P. Karjalainen, and D. A. Porter, "On the compressive deformation behavior of new beta titanium alloys designed by d-electron method," *J. Alloys Compd.*, 2018, doi: 10.1016/j.jallcom.2018.02.212.

[113] W. F. Ho, S. C. Wu, S. K. Hsu, Y. C. Li, and H. C. Hsu, "Effects of molybdenum content on the structure and mechanical properties of as-cast Ti-10Zr-based alloys for biomedical applications," *Mater. Sci. Eng. C*, 2012, doi: 10.1016/j.msec.2011.12.003.

[114] C.-W. Lin, C.-P. Ju, and J.-H. Chern Lin, "A comparison of the fatigue behavior of cast Ti–7.5Mo with c.p. titanium, Ti–6Al–4V and Ti–13Nb–13Zr alloys," *Biomaterials*, vol. 26, no. 16, pp. 2899–2907, Jun. 2005, doi: 10.1016/j.biomaterials.2004.09.007.

[115] S. Ozan, J. Lin, Y. Li, R. Ipek, and C. Wen, "Development of Ti-Nb-Zr alloys with high elastic admissible strain for temporary orthopedic devices," *Acta Biomater.*, vol. 20, pp. 176–187, 2015, doi: 10.1016/j.actbio.2015.03.023.

[116] J. Wei, H. Sun, D. Zhang, L. Gong, J. Lin, and C. Wen, "Influence of heat treatments on microstructure and mechanical properties of Ti-26Nb alloy elaborated in situ by laser additive manufacturing with Ti and Nb mixed powder," *Materials (Basel).*, vol. 12, no. 1, 2018, doi: 10.3390/ma12010061.

[117] D. R. N. Correa *et al.*, "Effect of the substitutional elements on the microstructure of the Ti-15Mo-Zr and Ti-15Zr-Mo systems alloys," *J. Mater. Res. Technol.*, vol. 4, no. 2, pp. 180–185, 2015, doi: 10.1016/j.jmrt.2015.02.007.

[118] S. F. Jawed *et al.*, "Mechanical characterization and deformation behavior of β-stabilized Ti-Nb-Sn-Cr alloys," *J. Alloys Compd.*, vol. 792, pp. 684–693, 2019, doi: 10.1016/j.jallcom.2019.04.079.

[119] G. Choi and K. Lee, "Materials Characterization Effect of cold rolling on the

microstructural evolution of new β -typed Ti – 6Mo – 6V – 5Cr – 3Sn – 2 . 5Zr alloys," *Mater. Charact.*, vol. 123, pp. 67–74, 2017, doi: 10.1016/j.matchar.2016.11.007.

[120] A. Helth *et al.*, "Effect of thermomechanical processing on the mechanical biofunctionality of a low modulus Ti-40Nb alloy," *J. Mech. Behav. Biomed. Mater.*, vol. 65, pp. 137–150, 2017, doi: 10.1016/j.jmbbm.2016.08.017.

[121] E. L. Pang, E. J. Pickering, S. I. Baik, D. N. Seidman, and N. G. Jones, "The effect of zirconium on the omega phase in Ti-24Nb-[0–8]Zr (at.%) alloys," *Acta Mater.*, vol. 153, pp. 62–70, 2018, doi: 10.1016/j.actamat.2018.04.016.

[122] K. Endoh, M. Tahara, T. Inamura, and H. Hosoda, "Effect of Sn and Zr content on superelastic properties of Ti-Mo-Sn-Zr biomedical alloys," *Mater. Sci. Eng. A*, vol. 704, no. March, pp. 72–76, 2017, doi: 10.1016/j.msea.2017.07.097.

[123] J. Ruzic, S. Emura, X. Ji, and I. Watanabe, "Mo segregation and distribution in Ti–Mo alloy investigated using nanoindentation," *Mater. Sci. Eng. A*, vol. 718, no. January, pp. 48–55, 2018, doi: 10.1016/j.msea.2018.01.098.

[124] Y. L. Zhou and D. M. Luo, "Microstructures and mechanical properties of Ti-Mo alloys cold-rolled and heat treated," *Mater. Charact.*, vol. 62, no. 10, pp. 931–937, 2011, doi: 10.1016/j.matchar.2011.07.010.

[125] L. J. Xu, Y. Y. Chen, Z. G. Liu, and F. T. Kong, "The microstructure and properties of Ti–Mo–Nb alloys for biomedical application," *J. Alloys Compd.*, vol. 453, no. 1–2, pp. 320–324, Apr. 2008, doi: 10.1016/j.jallcom.2006.11.144.

[126] L. J. Xu, Y. Y. Chen, Z. G. Liu, and F. T. Kong, "The microstructure and properties of Ti-Mo-Nb alloys for biomedical application," *J. Alloys Compd.*, vol. 453, no. 1–2, pp. 320–324, 2008, doi: 10.1016/j.jallcom.2006.11.144.

[127] P. Mohan, T. A. Osman, and V. Amigó, "Microstructure and Mechanical Properties of Ti-Mo-Zr-Cr Biomedical Alloys by Powder Metallurgy," *J. Mater. Eng. Perform.*, no. February, 2017, doi: 10.1007/s11665-017-2531-z.